Dissertation zur Erlangung des Doktorgrades
der Fakultät für Geowissenschaften
der Ludwig-Maximilians-Universität München


# *Active Tectonics of the Lower Rhine Graben (NW Central Europe) Based on New Paleoseismological Constraints and Implications for Coseismic Rupture Processes in Unconsolidated Gravels*

***Simon Kübler***

München
September 2012

**Eingereicht am 19. September 2012**

1. Gutachterin:Prof. Dr. Anke Friedrich

2. Gutachterin:Prof. Dr. Claudia Trepmann

Tag der mündlichen Prüfung: 07. Februar 2013

# Table of Contents

# List of Figures and Tables

# Summary

Identification of active seismogenic faults in low-strain intraplate regions is a major challenge. The understanding of intraplate earthquakes is hampered by the spatiotemporal scattering of large earthquakes and by barely detectable strain accumulation. In populated humid regions, both hillslope and anthropogenic processes are important challenges to the recognition of potentially active faults.

The Lower Rhine Graben is the NW segment of the European Cenozoic Rift System. It is a prime example of a seismically active low-strain rift situated in a humid and densely populated region. The approximate location of potentially active fault segments in this region is well known, but knowledge of the recurrence of large earthquakes and of the dominant fault slip mode is still rudimentary. The current debate ranges from slip dominated by repeated large earthquakes to slip dominated by aseismic creep.

The purpose of this thesis is to determine whether the Lower Rhine Graben is an exception to the usually observed deformational behaviour of the upper crust, whereby active faults fail by brittle behaviour. The thesis addresses the Holocene, historical and present-day tectonic activity of the Lower Rhine Graben. It examines the signs of coseismic deformation in the geological record, and the surface expression of active fault segments. I analyzed high-resolution LiDAR terrain models of segments of the Erft and Wissersheimer faults, in order to understand the preservation potential of active fault scarps in populated, humid settings. Results of the LiDAR analysis illustrate that the central part of the Lower Rhine Graben is characterized by severe degradation and modification of suspected seismogenic structures. Degradation is due to fluvial erosion, hillslope processes and anthropogenic overprint. This analysis shows, also for the first time, the severity of surface modification of the region resulting from aerial bombing during World War II.

A large trench excavation at the Schafberg fault in Holocene sediments yielded a broadly distributed fault zone with a peculiar abundance of fractured clasts. A particular question at this site is whether or not the fault ruptured in the 1756 AD Düren event. The excavation reveals the first evidence of historical seismogenic faulting in the Lower Rhine Graben. Coseismic deformation at this site is expressed by a net vertical displacement of 1 ± 0.2 m and complex gravel fracturing. Analysis of the faulted strata and radiocarbon ages of event horizons reveal evidence of at least one, possibly two coseismic events since the Holocene. The youngest of them overlaps with the 1756 AD Düren earthquake. The complex deformation pattern in the trench included a range of features such as liquefaction, rotated,

and fractured clasts in the fault zone. I developed a new analysis technique based on "fractured-clasts", which allows insight into coseismic rupture and fracture processes in unconsolidated gravel deposits.

Results of this paleoseismic study show that faults in the Lower Rhine Graben do not move dominantly by aseismic creep. They further support the observation that faults in low-strain intraplate rifts can produce large surface-breaking earthquakes. The results of this thesis further imply that specific patterns of fractured clasts in fault zones may be a detector of coseismic rupture, and could in principle be used to calculate the energy involved in the rupture process.

# Zusammenfassung

In der Erdbebengeologie stellt die Identifizierung und Charakterisierung von seismogenen Strukturen in Intraplattenregionen mit niedrigen Deformationsraten eine große Herausforderung dar. Die stark variable, räumliche und zeitliche Verteilung von großen Erdbeben sowie kaum mit geodätischen Messmethoden erfassbare Verformungsraten erschweren das Verständnis von Intraplattenbeben. In dicht besiedelten, humiden Gebieten sind potenziell aktive Störungen noch schwerer zu erkennen, da diese, durch Hangprozesse und anthropogene Überprägung, intensiven Veränderungen unterworfen sind.

Die Niederrheinische Bucht, das nordwestliche Segment des Europäischen Känozoischen Graben Systems, ist ein erstklassiges Beispiel für ein seismisch aktives Intraplattenrift in einem humiden und dicht besiedelten Gebiet. Obwohl die Lokationen potenziell aktiver Störungen bekannt sind, ist die Kenntnis bezüglich der Rekurrenzintervalle von großen Erdbeben sowie der Art der Störungsbewegungen nach wie vor rudimentär. Die derzeitige Debatte reicht von Störungsbewegungen durch starke Erdbeben, bis hin zu aseismischem Kriechen.

Ziel dieser Arbeit ist es zu klären, ob der Niederrheingraben eine Ausnahme in Bezug auf das grundsätzlich beobachtete Deformationsverhalten der oberen Kruste darstellt, wo aktive Störungen durch sprödes Bruchverhalten charakterisiert sind. Hierbei befasst sich die Studie mit der Holozänen, historischen und heutigen tektonischen Aktivität des Niederrheingrabens und legt den Fokus auf die Erforschung koseismischer Prägung der Geologie sowie der Oberflächenexpression potenziell aktiver Störungen. Es wurden hochauflösende LiDAR-Geländemodelle an Segmenten der Erft- und Wissersheimer Störung in der zentralen Niederrheinischen Bucht untersucht, um das Erhaltungspotenzial aktiver Störungen in besiedelten, humiden Gebieten zu charakerisieren. Die Ergebnisse der LiDAR-Analyse offenbaren, dass seismogene Strukturen im zentralen Teil des Niederrheingrabens starker Degradation und Modifikation unterworfen sind. Hauptursachen hierfür sind fluviatile Erosion, Hangprozesse, sowie anthropogene Überprägung. In dieser Analyse konnte zudem erstmals die Schwere der Oberflächenveränderung in der Region, ausgelöst durch Fliegerbomben aus dem Zweiten Weltkrieg, dargestellt werden.

In einer groß angelegten Schürfgrabenanalyse in Holozänen Sedimenten an der Schafbergstörung, wurde eine breite Deformationszone, die eine auffallend große Anzahl zerbrochener Klasten enthielt, freigelegt. Insbesondere ist es wichtig zu klären, ob diese Störung während des Dürener Bebens von 1756 AD gebrochen ist. Die Ergebnisse der

Schürfgrabenanalysen an der Schafbergstörung liefern den ersten Beweis dafür, dass Erdbeben im Niederrheingraben in historischer Zeit die Oberfläche gebrochen haben. An diesem Störungssegment äußert sich die koseismische Deformation durch einen Gesamtversatz von 1 ± 0.2 m und komplexem verbreitetem Brechen von Klasten. Die Analyse mit-verworfener Schichten sowie Radiokarbondatierungen von Ereignishorizonten beweisen mindestens ein, möglicherweise zwei Holozäne koseismische Ereignisse. Das Jüngste der Beiden deckt sich hierbei mit dem Dürener Beben von 1756 AD. In der im Schürfgraben freigelegten Störungszone wurden komplexe Deformationsmuster wie Liquefaktion sowie rotierte und gebrochene Klasten dokumentiert. Basierend auf den gebrochenen Klasten habe ich in meiner Arbeit eine neue Analysetechnik entwickelt, die es ermöglicht, detaillierte Einblicke in koseismische Bruchprozesse in unverfestigten Geröllen zu erhalten.

Die Ergebnisse dieser paläoseismologischen Studie weisen darauf hin, dass Störungen im Niederrheingraben nicht aseismisch kriechen. Darüber hinaus festigen sie die Beobachtung, dass Störungen in Intraplattenrifts mit niedrigen Deformationsraten, in der Lage sind, große Erdbeben mit Oberflächenruptur zu erzeugen.

Die Daten dieser Studie zeigen des Weiteren, dass spezifische Muster gebrochener Klasten in Störungszonen ein möglicher Detektor koseismischer Rupturen sein können und demzufolge zur Energieberechnung des Rupturprozesses genutzt werden können.

Well, it took years to climb that hill... and now we look up to the mountains
*Fury in the Slaughterhouse, Hannover 1992*

# Acknowledgments

Starting my Acknowledgements with a citation taken from a rock song is something I always wanted to do. Besides, the two lines above describe in a good way the feelings I probably share with many other young researchers who have just finished their PhD theses - something that feels so big and overwhelming has now come to an end and now that you see what comes after that you feel pretty small again. Nevertheless, I want to express my gratitude to a great number of people who made the last years in Munich easier, more intense and more valuable.

First of all, I want to thank my thesis advisor Anke Friedrich for her inspiration and support over the last years. Thanks for the confidence and the freedom that enabled me to develop my own ideas. Her expertise and endless motivation as well as her ability to get across an exemplary enthusiasm towards research problems will always be an example for me.

I had the opportunity to present and discuss my work at numerous international conferences, workshops and research seminars, which enabled me to benefit from the expertise and criticism of specialists in the field of earthquake geology, seismology and tectonic geomorphology. To name a few, I would like to thank Seth Stein, Kris Vanneste, Jim McCalpin, Kurt Decker, Klaus Reicherter, Klaus Hinzen, Geoffrey King, George Davis, as well as "the young trenchers" Angela Landgraf, Esther Hintersberger and Petra Stepancikova.

The core my PhD thesis is based on is the trench excavation and analysis at the Untermaubach site in the Lower Rhine Graben. This study has been carried out in the framework of the DFG funded research project "Active intraplate deformation in central Europe: paleoseismology of the Lower Rhine Graben" (research grant FR 1673 awarded to Anke Friedrich, Manfred Strecker and Frank Scherbaum). I want to thank everybody who helped me during my fieldwork in the Lower Rhine Graben, and during the process of developing, preparing, and writing this thesis. It has been an exceptional and wonderful experience!

# Danksagung

Auch wenn eine Doktorarbeit am Ende einer einzelnen Person zugesprochen wird so ist es doch klar, dass eine solche Arbeit nicht ohne die Zusammenarbeit mit und Unterstützung von zahlreichen Personen möglich ist.

Im Besonderen möchte mich bei der Betreuerin meiner Dissertation, Anke Friedrich bedanken. Sie hat mir von Beginn an großes Vertrauen, Freiheit in der Entfaltung eigener Ideen sowie in der Planung und Durchführung meiner Arbeit, aber auch Inspiration und Kritik entgegen gebracht. Ihr Fachwissen und im Speziellen ihre Begeisterung wissenschaftlichen Problemen gegenüber waren, sind und werden mir immer ein Vorbild sein.

Der zentrale Kern meiner Arbeit ist die von der DFG finanzierte Trench-Studie in Untermaubach (Förderungsnr. AF 1673, vergeben an Anke Friedrich, Manfred Srecker und Frank Scherbaum). Diese Studie war ein organisatorisches Monstrum, sowohl in der fast ein Jahr dauernden Vorbereitung als auch in der Durchführung. Mein besonderer Dank hierzu gilt meinen Kollegen am Lehrstuhl für Geologie an der LMU München, Allen voran Markus Hoffmann, der sich nicht nur durch ein bemerkenswertes Organisationstalent auszeichnet, sondern in den letzten Jahren auch ein hervorragender Büronachbar, Mitbewohner und Freund gewesen ist, und der während der Trenchsaison im Speziellen großen Anteil an der komplizierten Organisation des Fahrzeugtransfer München-Untermaubach-München getragen hat. Vielen Dank auch für die große Hilfe bei der Überarbeitung der Abildungen für diese Arbeit. Großer Dank gilt auch Stefanie Rieger für die Unterstützung im Trench sowie bei unzähligen Konferenzen und manchmal sehr schmerzhaften und arbeitsamen, geophysik-lastigen Seminaren. Beiden wünsche ich viel Kraft und Durchhaltevermögen für die nächsten Monate und einen baldigen und erfolgreichen Abschluss ihrer Doktorarbeiten.

Großer Dank gilt auch Ramona Baran, die mir fachlich, im Besonderen durch das aufwendige Scannen des Untermaubach-Trenches als auch persönlich sehr geholfen hat. Es war mitunter sehr, sehr lustig. Im gleichen Zuge auch noch einen speziellen Dank an Amir Abolghasem, der mir sehr bei der Aufnahme und Auswertung der Scans geholfen hat und im Laufe der Jahre zu einem wichtigen Ansprechpartner am Lehrstuhl geworden ist.

Vielen, vielen Dank an alle weiteren Helfern am Lehrstuhl für Geologie und im Untermaubach Trench: Robert Gerlach (auch für die Hilfe beim Fertigstellen der Abbildungen für diese Arbeit), Florian Hofmann, Diana Schmid, Mohamed El-Kashab, Sara Carena, sowie einer großen Anzahl an fleißigen Bachelor-Studenten, die hunderte von Kieseln eingemessen und zentnerweise Sand und Kies geschaufelt haben. Es war eine schöne Zeit! Danke auch an

den Eigentümer und den Pächter der Ackerfläche in Untermaubach, Mariano Graf von Spee und Johannes Kempen, sowie an die Mitarbeiter des Rheinischen Amts für Bodendenkmalpflege, im Speziellen Petra Tutlies, die mir während der Herbst- und Winterwochen im Trench ein Dach über dem Kopf gegeben haben. Danke auch an die Mitarbeiter des GD NRW, Martin Salamon, Klaus Buschüter, Klaus Lehmann und Georg Schollmeyer für Tipps in der Schürfgrabenplanung und für Anregungen während der Geländearbeit.

Ich danke meiner Mutter dafür, dass sie mich im rechten Zeitpunkt daran erinnert hat, dass ich mit 7 Jahren bereits Geologe werden wollte - auch wenn mir damals vermutlich noch nicht klar war, was das eigentlich ist - und mir jederzeit die Freiheit gegeben und gelassen hat, mich persönlich und beruflich so zu entwickeln wie es mein Wunsch gewesen ist.

Ich möchte mich zu guter Letzt bei Kathi bedanken. Danke dafür, dass Du mir in stressigen Augenblicken eine seelische Stütze war und nie den Glauben an mich und das Gelingen dieser Arbeit verloren hast. Danke auch für das geduldige Ausharren wenn ich wochenlang im Gelände verschwunden war und das gute Gefühl zu Dir nach Hause zu kommen. Ohne Dich und Deine Liebe, Geduld und ständige Motivation, hätte das hier so nicht geklappt!

# Chapter 1

## *Introduction*

Our perception and knowledge of the location, magnitude and recurrence of earthquakes has been largely influenced by frequent large-magnitude events situated along plate boundaries. However, ongoing research in continental interiors and regions of low deformation rates shows increasing evidence for earthquakes involving ground rupture, and demonstrates that such regions may also be subject to considerable seismic hazard.

Although seismic events in the interior of continents only represent a small fraction of the total number of earthquakes and normally do not reach magnitudes as high as those at plate boundaries, they still pose a significant hazard to the society and infrastructure (England and Jackson, 2011). Part of the reason for this is simply that many seismogenic sources in intraplate settings were unknown prior to rupture due to a lack of exposure and thus, did not occur in previous hazard estimates of the region. For example, the Canterbury (New Zealand) earthquake of 2010 occurred on an unknown fault in a region where no large historical earthquakes were known (Gledhill et al., 2010), just like the 2012 Emilia earthquake in the Bologna region, Northern Italy (Alessio et al., 2010) and the 2012 Pernik earthquake in Western Bulgaria (Radulov et al., 2012). Liu et al. (2011) impressively demonstrated how earthquakes in Central China have migrated over the last 2000 years, and concluded that no fault in this region has ruptured twice in this time span.

Accordingly, one of the most pressing and enigmatic problems in earthquake geology is the spatiotemporal distribution of large earthquakes in low-strain intraplate regions. Unfortunately, understanding intraplate earthquakes is challenged by long recurrence intervals of surface rupturing earthquakes that often exceed several thousands of years, and slip rates on individual faults below or barely at geodetic measurability. Even in areas with dense space-geodetic coverage, the relationship between strain accumulation and strain release is poorly understood (Friedrich et al., unpublished data).

Even in densely populated regions with long historical records, such as China or central Europe, earthquake catalogues do not cover more than one or two thousand years and thus, are not sufficient to correctly assess seismicity and associated hazards in time and space (Liu et al., 2011; Stein and Liu, 2009; Stein and Mazotti, 2007). It is therefore important to extend records of seismicity into the past and combine paleoseismological, historical and

instrumental data to decipher meaningful neotectonic histories and assessments of seismic activity for those regions.

This thesis aims to shed light on the Holocene and historical rupture history of the Lower Rhine Graben, the NW sector of the seismically active Central European Rift System. Although paleoseismic studies in the Lower Rhine Graben have gained importance over the last 15 years, particularly after the $M_W$ 5.4 Roermond earthquake from 1992, central questions regarding the general slip behaviour of faults in this low-strain intraplate region remain unanswered. The current debate ranges from slip accommodated by repeated large coseismic events (Camelbeeck, 2007; Camelbeeck and Meghraoui, 1996, 1998; Vanneste et al., 1999; Vanneste et al., 2001) to slip dominated by aseismic or postseismic creep (Ahorner, 1968, 2001; Houtgast, 2005, 2003).

Reasons for this controversy are the low fault-slip rates on individual faults on the order of 0.06 - 0.23 mm/yr (Ahorner, 1968; Camelbeeck, 2007; Geluk et al., 1994; Meghraoui et al., 2000; Vanneste et al., 2001) in the face of erosion rates that are on the same order of magnitude (Bork and Lang, 2003; Meyer et al., 2008). Significantly higher (up to several cm/yr) aseismic subsidence rates of the Lower Rhine Graben monitored by levelling campaigns and GPS measurements (Görres, 2008a, b; Kümpel et al., 2001) additionally hamper the detection of a potential tectonic signal in the Lower Rhine Graben.

The Lower Rhine Graben is presumably one of the most challenging regions worldwide to identify unambiguous evidence for coseismic surface rupture. Anthropogenic processes including urbanization, large-scale groundwater disposal in the vicinity of open pit lignite mines, and abundant bomb craters from aerial bombs of World War II, have significantly modified the landscape of this region within a few decades. As a result, many potentially active faults and their associated hazards remain unknown.

Successful trenching studies in such densely populated regions require careful and sensible pre-planning. In this case, trench site selection typically includes negotiations with landowners, nature and water conservation authorities, as well as archaeologists and bomb disposal experts. Also, due to the subtle surface expression of fault scarps traditional approaches for trench site selection such as field mapping, orthophoto analysis, drilling and shallow geophysical surveys need to be enhanced by modern approaches to successfully localize possible trench sites. A promising approach that gained increasing importance in tectonic geomorphology and paleoseismology over the last years is the analysis of high-resolution digital elevation models derived from LiDAR (Light Detecting And Ranging) data sets. In my thesis, I have tested the applicability of such tools to identify fault scarps in the

Lower Rhine Graben, and importantly, any non-seismic obliteration of coseismic features on such structures.

A further important point concerning paleoseismical research in both intraplate and plate boundary settings is the differentiation between coseismic rupture and aseismic creep in the geologic record. In paleoseismology, certain sediment deformation features are usually considered as either primary (due to rupture) or secondary (due to shaking) evidence for coseismic activity (McCalpin, 2009). Most of the listed deformation features, however, may also result from non-seismic processes such as landslides, permafrost or fault creep. Consequently, former studies (Cowan, 1999) concluded that with the exception of pseudotachylites, no deformation features in the geologic record preserve unambiguous evidence for coseismic slip. This problem is enhanced in low-strain regions overprinted by climatic and anthropogenic processes, namely the Lower Rhine Graben.

Historical documents reveal information on several damaging earthquakes in the Lower Rhine Graben, the largest of which appears to have been the $M_L$ 6.2 Düren earthquake of 1756 AD. Historic damage related to the 1755/56 events implies that any of five recently active faults in the epicentral area may have ruptured. Possible seismogenic faults are the Rurrand-, Sandgewand-, Münstergewand-, Stockheimer-, and Schafberg faults. The Schafberg fault, a 16 km long NE-dipping normal fault, is the only one of these faults showing signs for surface deformation in Holocene sediments and thus, has emerged to be a prime location for studying possible Holocene and historical seismogenic activity in this part of the Lower Rhine Graben.

Following the introductory part of this thesis, I give an overview of the thesis layout and briefly explain the main research objectives addressed in the different chapters. Furthermore, I explain the tectonic framework of the Central European Rift System as well as the Lower Rhine Graben with special focus on the seismic activity assessed by instrumental and historical data as well as former paleoseismic studies.

The overarching issue that led to writing this thesis would be whether the LRG constitutes an exception from the generally observed deformational behavior of the upper crust - that active faults fail by brittle mechanisms. To better understand the tectonic deformation mechanisms of the LRG, the main research questions pursued in this thesis are:
(1) Is the surface expression of tectonic activity detectable in a densely populated humid intraplate region?

(2) Are faults in the Lower Rhine Graben capable of producing large earthquakes and associated coseismic surface ruptures? If yes, what are the recurrence rates and maximum magnitudes?
(3) Did the Schafberg fault rupture in the 1756 Düren event?
(4) Can fractured clasts in fault zones be used to determine coseismic deformation processes?

I address these questions in four main chapters:

In Chapter 3, I analyzed high-resolution digital elevation models derived from LiDAR (Light Detecting and Ranging) data. I focused on two study sites located in the central Lower Rhine Graben, which were proposed as possible paleoseismic trench sites by former DFG- and EC-funded studies (Friedrich et al., 2002; Strecker et al., 2002b). The LiDAR analysis focuses on the detection of non-seismic surface modification such as fluvial erosion, agricultural and urban land use, and the occurrence of abundant bomb craters derived from aerial bombs of World War II in the vicinity of large cities. I used results of this study to reevaluate the suitability of the proposed sites for the trenching project.

Results of this study as well as additional reconnaissance studies (Strecker et al., 2002a; Streich, 2003) reveal that trenching was most promising at the Untermaubach site. Therefore, Chapter 4 focuses on results of the paleoseismic trench study carried out across the Schafberg fault. This normal fault is situated in the SW portion of the Lower Rhine Graben in the vicinity of Germany's largest historical event that occurred close to the city of Düren (ML 6.2 ± 0.2, 1756 AD). The Untermaubach site is located outside of the area affected by mining-induced subsidence, and has also not been stricken by aerial bombing. The trench reveals first evidence for Holocene and historical coseismic rupture in the Lower Rhine Graben. More detailed results of this trenching analysis are presented and discussed in Chapter 5.

The DFG-funded paleoseismic study carried out along the Schafberg fault at the Untermaubach site provided data on Holocene fault slip rates and earthquake recurrence intervals. It includes detailed stratigraphical and geochronological data of the trench analysis as well as new approaches regarding the analysis of coseismically deformed gravels. Furthermore, I discuss in particular the seismogenic potential of the Schafberg fault as well as a possible connection of the observed surface rupture with the 1756 Düren event. I also consider different mechanisms that may have triggered increased Holocene fault activity in this region including glacial unloading and static stress change due to the major earthquake of Lisbon, Portugal, in 1755 AD.

Mapping of the Untermaubach trench site yielded an anomalously high number of deformed (fractured and rotated) clasts. Chapter 6 provides a detailed study on deformed

gravels exposed in the trench at the Untermaubach site. I developed a new approach to systematically analyze the deformed clasts. The numerous distribution and orientation measurements of the deformed clasts provide clear information on coseismic rupture processes in unconsolidated near-surface gravels. Apparently, the fractured clasts along fault exposures are an excellent diagnostic feature to detect coseismic rupture. To test whether this hypothesis holds true or not, we examined thin sections and polished cross-sections of the fractured clasts that provide additional information on the fracture process.

# Chapter 2

## *Geological Framework*

Most likely, most of the present-day seismicity in Central Europe is related to the reactivation of inherited zones of crustal weakness in the European Late Variscan, Permo–Carboniferous and Mesozoic fault systems (Dèzes et al., 2004b; Schumacher, 2002; Ziegler, 1992, 1994). Cenozoic intraplate deformation in Central Europe is the result of far-field stresses resulting from the continent-continent collision in the Alps and Pyrenees as well as the opening of the Atlantic Ocean (Illies, 1975; Illies and Greiner, 1978; Reicherter et al., 2008; Şengör et al., 1978; Ziegler, 1992, 1994), and effects due to the rise of mantle plumes (Cloething et al., 2005; Goes et al., 1999; Hoernle et al., 1995; Ritter et al., 2001).

During the Late Eocene to Oligocene, a phase of ESE-WNW directed extension led to the formation of the European Cenozoic Rift System (Figure 2.1), which extends over a distance of more than 1100 km from the North Sea to the western Mediterranean (Ahorner, 1975; Illies, 1975; Reicherter et al., 2008; Ziegler, 1992). It includes from north to south the Rhine and Rhône Valley Rift Systems, which are linked by the Burgundy and the eastern Paris Basin transfer zones with the grabens of the Massif Central. The southern part of the rift system consists of the Bresse Graben and the grabens of the lower Rhône Valley and their prolongation into the Western Mediterranean (Dèzes et al., 2004a; Jolivet et al., 1999; Michon et al., 2003; Ziegler, 1992, 1994).

The Rhine Rift System represents the northern part of the European Cenozoic Rift System including the Upper Rhine Graben, the Lower Rhine Graben, and the Hessian Graben system (Figure 2.2). The seismically active shallow Eger Graben of the Bohemian Massif is the easternmost graben of the European Cenozoic Rift System (Ziegler, 1992). In particular, the Upper Rhine Graben and the Lower Rhine Graben correspond to a zone of increased seismicity as demonstrated by large historical and recent earthquakes (Figure 2.2). The largest historical earthquake in the region, and one of the largest earthquakes reported for Central Europe, has been the $M_L \sim 6.5$ Basel earthquake of 1356 AD near the southern end of the Upper Rhine Graben, Switzerland, which resulted in severe destruction of the city of Basel including several hundred fatalities (Mayer-Rosa and Cadiot, 1979). For the Lower Rhine Graben, the largest documented earthquake has been the $M_L \sim 6.2$ Düren earthquake of 1756 AD. This event occurred only a few weeks after the $M \sim 9$ Lisbon earthquake of 1755 AD, which has been the largest historical earthquake of the European continent.

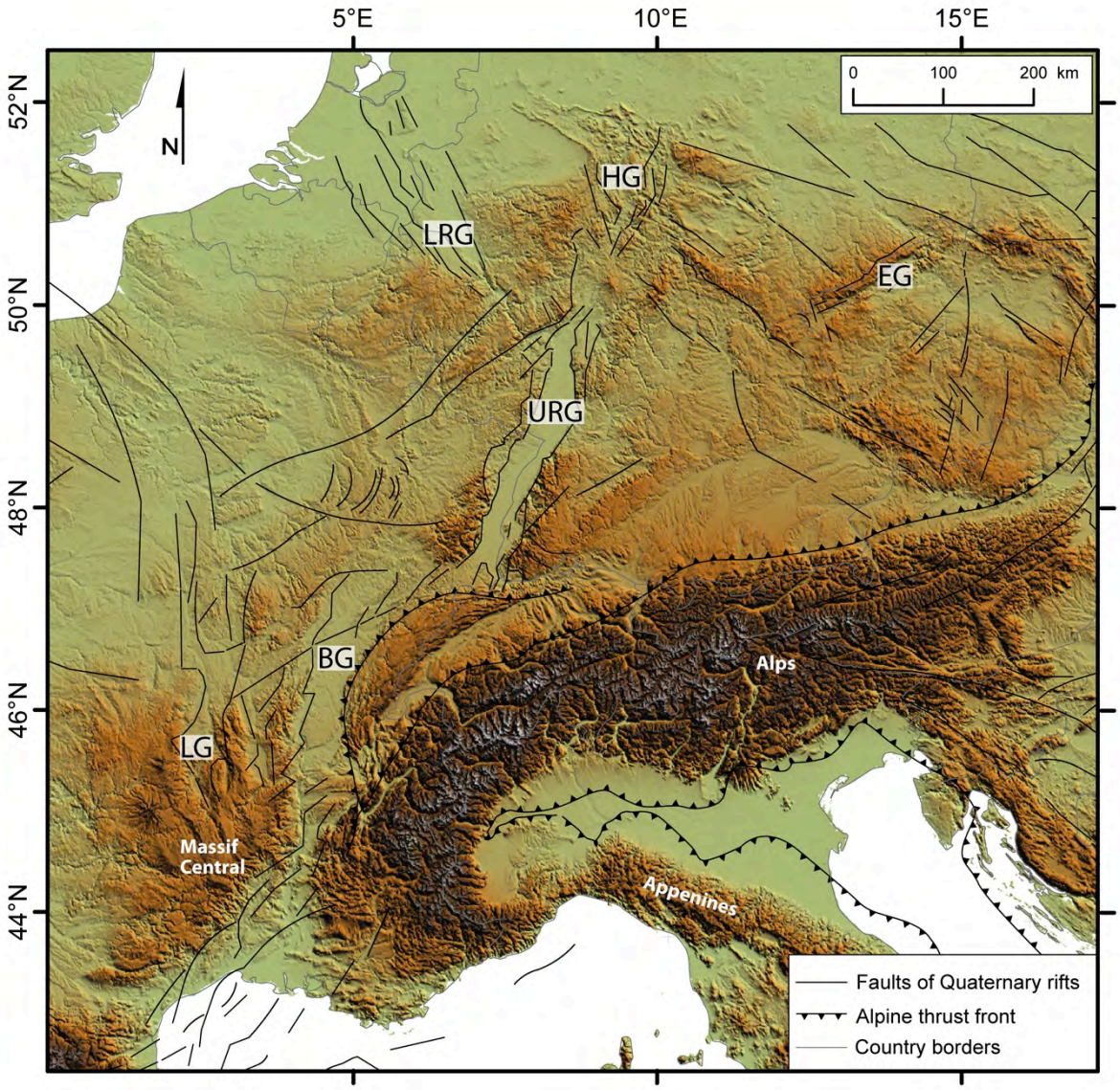


Figure 2.1: Digital Elevation Model of Central Europe showing the main structural and tectonic units. BG: Bresse Graben; EG: Eger Graben; HG: Hessian Graben; LG: Limange Graben; LRG: Lower Rhine Graben; URG: Upper Rhine Graben (modified from Ziegler, 1992). Map projection for this and the following maps: UTM Zone 31, Datum: WGS84. DEM derived from Shuttle Radar Mission data, 90 m resolution.

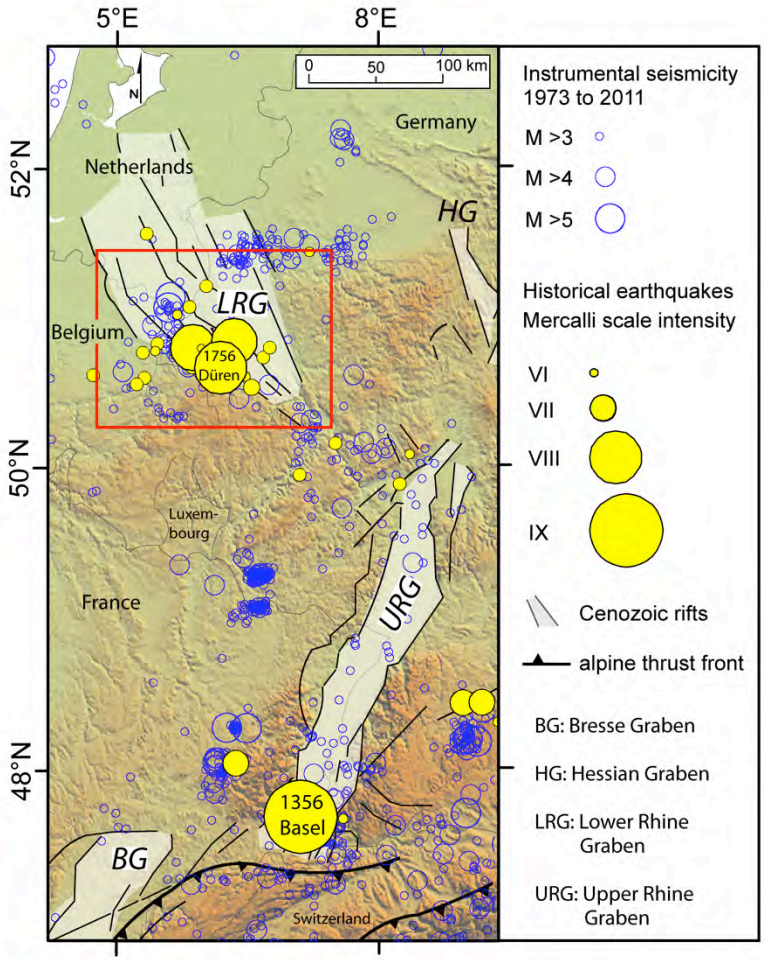


Figure 2.2: Seismotectonic map of the Rhine Graben System showing major rift faults and historical and present-day seismicity. Red box depicts the area covered by Figure 3. Solid yellow circles: Historical earthquakes (Leydecker, 2004; Hinzen, 2003), open blue circles: instrumentally recorded earthquakes (Leydecker, 2004; NEIC data base, USGS, for earthquakes after 2004).

## 2.1 The Lower Rhine Graben

The Lower Rhine Graben (LRG) covers an area of ~ 3600 km² and encompasses Northeastern Belgium, the Southern Netherlands and WNW Germany (Figure 2.3). It is characterized by basin-wide subsidence and frequent normal faulting along NW-SE striking faults (Ahorner, 1962; Hinzen, 2007). Graben-related structures cut into the Rhenish Shield to the south, where they produced a wedge-shaped structure striking roughly NW-SE (Figure 3).

The area is subdivided into several major blocks each bounded by NW-SE striking normal faults. The southwestern sectors are the Western and Eastern Campine blocks. They are bounded to the NE by the Roer Valley Graben and the Erft block, which represent the tectonically and seismically most active region of the LRG. The northeastern blocks are the Peel, Cologne, Venlo and Krefeld blocks (Ahorner, 1962; Geluk et al., 1994).

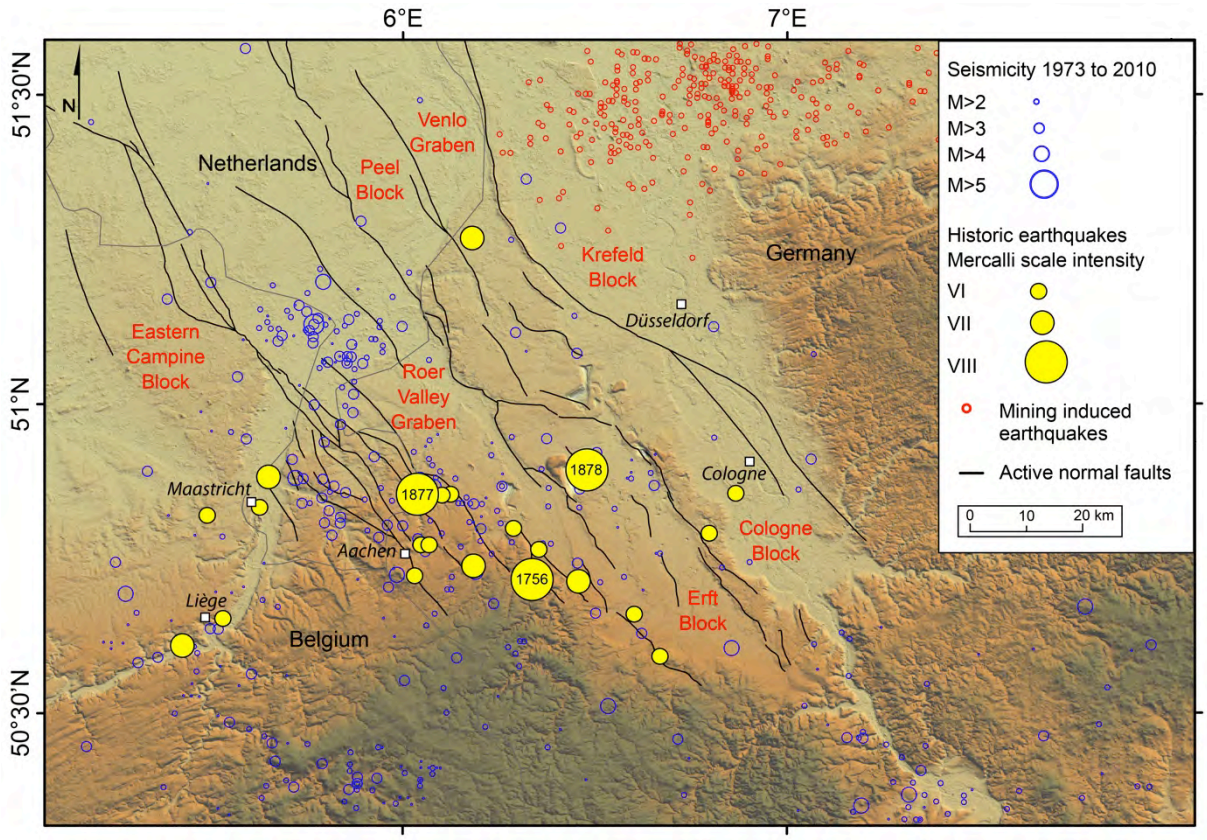


Figure 2.3: Seismotectonic map of the Lower Rhine Graben superimposed on digital elevation model. The map shows the main structural units, major faults, as well as historical (solid yellow circles) and instrumental (open blue circles) earthquakes (Leydecker, 2004, NEIC data base, USGS, for earthquakes after 2004). Numbers in yellow circles correspond to the years of occurrence of historical earthquakes with Mercalli scale intensities > VIII (Leydecker, 2004; Hinzen, 2003). 1756: Düren earthquake; 1873: Herzogenrath earthquake; 1878: Tollhausen earthquake. Elevation data derived from AsterDEM, 30 m resolution.

In the Lower Rhine Graben, Cenozoic taphrogenesis started in the Early Oligocene at around 36 Ma BP (Zijerveld et al., 1992). The initiation of rifting along NW-SE oriented basement faults presumably resulted from a counterclockwise rotation of the regional stress field from a NE-SW to a NW-SE directed maximum horizontal stress (Ahorner, 1975). The deepest part of the graben structure is located in the North Sea reaching a maximum depth of ~ 3.5 km, as revealed by the analysis of exploration wells (Kooi et al., 1989). Onshore graben depths reach a maximum of ~ 3.0 km in the central part of the Roer Valley Graben (Zijerveld et al., 1992).

The total crustal extension in Quaternary times is estimated at 90 to 180 m (Ahorner, 1962; Hinzen, 2007), maximum fault offsets of the LRG are 100 - 180 m observed at the Erft and Rurrand faults, respectively.

### 2.1.1 Present-Day Deformation

The Lower Rhine Graben is one of the most seismically active zones onshore NW Europe (Figure 2.3). The present-day stress field in the shallow lithosphere, as determined by fault-plane solutions of 110 instrumentally recorded earthquakes (Hinzen, 2003), is characterized by a subvertical $\sigma_1$ and a subhorizontal NE-SW oriented $\sigma_3$ indicating almost pure dip-slip for the predominately NW-SE striking normal faults. Almost pure extension across the LRG is also supported by the analysis of broad-scale space-geodetic measurements in Central and Western Europe (Tesauro et al., 2005), as well as tilt, gravity and GPS measurements in the LRG (Campbell et al., 2002).

### 2.1.2 Instrumental Seismicity

A significant portion of the present-day seismicity recorded in the Lower Rhine Graben is related to coal mining. Collapsed mines in the main coal mining area (Ruhrgebiet) have caused local subsidence of several tens of meters with local subsidence rates of more than 1 m/yr during the last 60 years (Spreckels, 2000; Wegmuller et al., 2000), and triggered numerous shallow mining earthquakes (Hinzen, 2007). In the Ruhr area alone about 1000 mining induced seismic events with local magnitudes between $0.7 \leq M_L \leq 3.3$ are recorded every year (Bischoff et al., 2010).

Mining induced earthquakes usually occur at very shallow depths (< 1 km) and may thus be easily distinguished from tectonically induced earthquakes, which in the LRG

predominately occur at depths of 12 - 18 km (Hinzen, 2003). Tectonically induced earthquakes in the LRG reveal some clustering of events, sometimes clearly associated with fault traces and some seismically quiet areas (Hinzen and Oemisch, 2001; Hinzen, 2007; Leydecker, 2004). During the last 100 years, the LRG has been struck by four $M_L > 5.0$ events including the $M_L$ 5.0 Uden earthquake of 1932 AD, the $M_L$ 5.7 Euskirchen earthquake of 1951 AD, the $M_L$ 5.8 Roermond earthquake of 1992 AD, and the $M_L$ 5.1 Alsdorf earthquake of 2002 AD (Hinzen, 2007; Leydecker, 2004).

The 1992 AD Roermond earthquake was one of the largest events of the last century in Central and Northwestern Europe. It was felt within a radius of about 450 km around the epicenter, notably in the Netherlands, Belgium, Germany and parts of the United Kingdom, France and Czech Republic (Meidow, 1994).

The 2002 AD Alsdorf earthquake occurred on the western border of the LRG in a region that showed clustering of seismic events within a time span of about ten years, including an earthquake swarm from December 2000 until August 2001. This swarm had a total of about 150 earthquakes with maximum magnitudes of 3.9 (Hinzen and Oemisch, 2001; Leydecker, 2004).

Studies on the frequency-magnitude distribution of earthquakes in the Lower Rhine Graben (Hinzen, 2007; Schmedes et al., 2005) revealed that the area is characterized by relatively high frequency-low magnitude seismicity (Figure 2.4) and *b*-values ranging from 0.8 to 1.2 depending on the seismic catalogue used for the calculation (Schmedes et al., 2005).

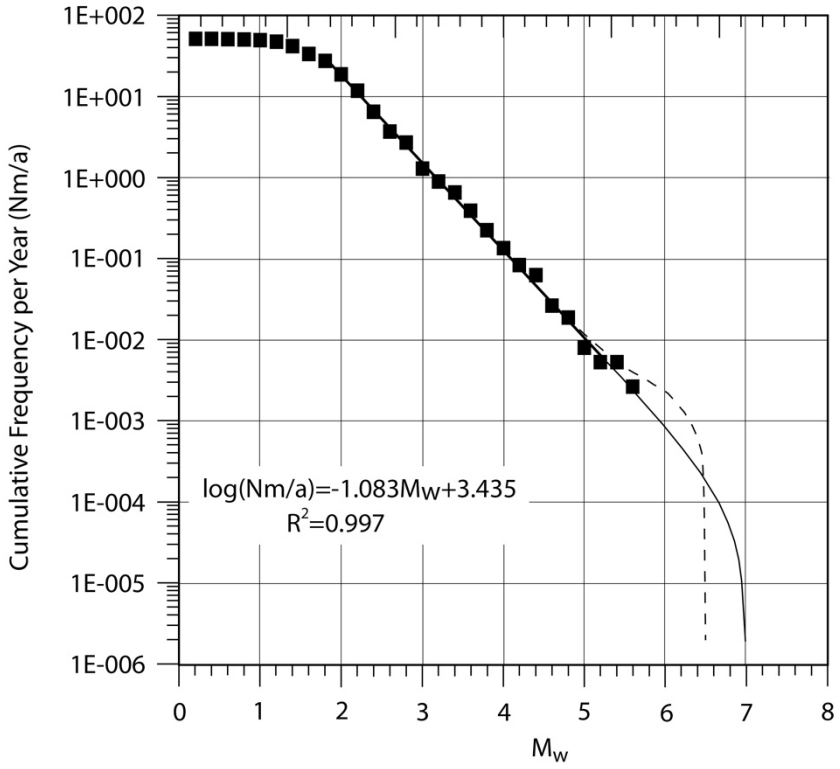


Figure 2.4: Cumulative frequency of earthquakes per year in the Lower Rhine Graben. The thin line is a truncated Gutenberg Richter model assuming a maximum magnitude of MW 7.0. The dashed line is a characteristic earthquake model with a recurrence interval for the characteristic event (MW 6.5) of 5000 years (modified from Hinzen and Reamer, 2003).

### 2.1.3 Historical Seismicity

Strong and damaging earthquakes have also occurred in pre-instrumental times, particularly in the southern part of the Lower Rhine Graben. Since 1350 AD, seven earthquakes with $M_S$ between 5.0 and 6.0 have been documented (Leydecker, 2004). The strongest known historical earthquake of the region, which is also a central part of this thesis, occurred on February 18$^{th}$ 1756 AD south of the city of Düren in the German part of the Lower Rhine Graben (Meidow, 1994). This earthquake with an estimated magnitude of $M_L$ = 6.2 ($M_S$ = 5.7) was part of an earthquake series lasting from 1755 till 1760 AD with more than 240 documented earthquakes (Hinzen and Oemisch, 2001; Leydecker, 2004). Other important historical earthquakes were situated near Aachen (earthquakes of 1504, 1640, 1690, and 1755 AD), and near Herzogenrath (earthquakes of 1873 and1877 AD), close to the boundary with the Liège Gulpen Zone. In the northern part of the Roer Valley Graben, there are no known historical events documented by earthquake catalogues of the region (Leydecker, 2004).

### 2.1.4 Paleoseismicity

The tectonic activity of the Lower Rhine Graben from the Quaternary until present-day has been the scope of research for almost 60 years, e.g., (Ahorner, 1962, 1968, 1975, 2001; Camelbeeck and Meghraoui, 1996; Geluk et al., 1994; Quitzow and Vahlensieck, 1955; Richter, 1962; Van Balen et al., 2005). Especially owing to ongoing open-pit mining in the central part of the Lower Rhine Graben, the Quaternary and Upper Tertiary stratigraphy of the LRG basin fill and the location and strike of many faults is known.

First seismotectonic studies in the Lower Rhine Graben (Ahorner, 1962, 1968, 1975; Quitzow and Vahlensieck, 1955) provide detailed information about the structure as well as the Quaternary displacement of most of the known fault structures. However, the possibility of coseismic surface ruptures had not been addressed in these studies. Ahorner (1968) suggested that the maximum possible earthquake magnitude would be similar in size to the largest known historical events (M ~ 6). However, after the 1992 Roermond earthquake geologists started to investigate the Lower Rhine Graben with the aim to identify surface ruptures related to large past earthquakes.

Since 1995, the seismological research group of the Royal Observatory of Belgium has conducted several paleoseismic studies across presumably active faults in the Belgian part of the Roer Valley Graben (Camelbeeck and Meghraoui, 1996, 1998; Vanneste et al., 2001; Figure 2.3). Results of these studies clearly support the hypothesis of repeated ground-rupturing earthquakes since the Early Pleistocene along this fault with recurrence intervals on the order of $10^4$ - $10^5$ years. However, no historical or Holocene surface rupture could be identified, because all the trenches were excavated in Pleistocene deposits. The scarcity of Holocene deposits visibly cut by faults is a general problem in the LRG and will also be addressed in Chapter 5 of this thesis.

Paleoseismic studies carried out along the Dutch part of the Roer Valley Graben (Figure 2.3) revealed no signs of coseismic rupture (Houtgast, 2005, 2003). Simultaneously, former trenching studies (Meghraoui et al., 2000; Vanneste et al., 2001) were reevaluated by the aforementioned authors concluding that the differentiation between coseismic and aseismic fault slip is not possible along the Bree fault with the results presented. A similar debate has originated in the framework of a trench study carried out across the Rurrand fault in the German part of the Lower Rhine Graben. Here, trench observations have first been interpreted to not reveal unambiguous proof for differentiating coseismic from aseismic fault slip (Lehmann et al., 2001). Later, the same trench has been analyzed by different researchers

concluding that the observed sediment deformation and offset of Pleistocene strata support the hypothesis of coseismic rupture (Vanneste and Verbeeck, 2001).

In addition to the problems concerning ambiguous results on coseismic rupture vs. aseismic creep, no prior paleoseismic study has found clear evidence for Holocene rupture activity. Furthermore, prior to the studies carried out in the framework of this thesis no historical earthquake could be associated with coseismic surface rupture in the Lower Rhine Graben. In summary, this thesis aims to shed light on the coseismic nature and rupture history of the Lower Rhine Graben.

## 2.2 References

Ahorner, L., 1962, Untersuchungen zur Quartären Bruchtektonik der Niederrheinischen Bucht: Eiszeitalter und Gegenwart, Quaternary Science Journal, v. 13, no. 1, p. 24-105.

-, 1968, Erdbeben und jüngste Tektonik im Braunkohlenrevier der Niederrheinischen Bucht: Zeitschrift der Deutschen Geologischen Gesellschaft v. 118, p. 150-160.

-, 1975, Present-day stress field and seismotectonic block movements along major fault zones in central Europe: Tectonophysics, v. 29, p. 233-249.

-, 2001, Abschätzung der statistischen Wiederkehrperiode von starken Erdbeben im Gebiet von Köln auf Grund von geologisch-tektonischen Beobachtungen an aktiven Störungen: DGG Mitteilungen, v. 2, p. 2-9.

Alessio, G., Alfonsi, L., Brunori, C. A., Cinti, F. R., Civico, R., Cucci, L., D'Addezio, G., De Ritis, R., Falcucci, E., Fracassi, U., Gasparini, A., Gori, S., Lisi, A., Mariano, S., Mariucci, M. T., Montone, P., Nappi, R., Pantosti, D., Patera, A., Pierdominici, S., Pignone, M., Pinzi, S., Pucci, S., Vannoli, P., Venuti, A., and Villani, F., 2010, Evidence for surface rupture associated with the Mw 6.3 L'Aquila earthquake sequence of April 2009 (central Italy): Terra Nova, no. 1/22 (2010).

Bischoff, M., Cete, A., Fritschen, R., and Meier, T., 2010, Coal Mining Induced Seismicity in the Ruhr Area, Germany: Pure and Applied Geophysics, v. 167, no. 1, p. 63-75.

Bork, H. R., and Lang, A., 2003, Quantification of past soil erosion and land use/land cover changes in Germany: Lecture Notes in Earth Sciences, v. 101, p. 231-239.

Camelbeeck, T., K. Vanneste, P. Alexandre, K. Verbeeck, T. Petermans, P. Rosset, M. Everaerts, R. Warnant, M. Van Camp, 2007, Relevance of active faulting and seismicity studies to assessments of long-term earthquake activity and maximum magnitude in intraplate northwest Europe, between the Lower Rhine Embayment and the North Sea, In: Stein, S. and Mazotti, S., ed., Continental Intraplate Earthquakes: Science, Hazard, and Policy Issues: The Geological Society of America Special Paper, v. 425, no. 14, p. 193-224.

Camelbeeck, T., and Meghraoui, M., 1996, Large Earthquakes in Northern Europe More Likely Than Once Thought: EOS, v. 77, no. 42, p. 405-409.

-, 1998, Geological and geophysical evidence for large palaeo-earthquakes with surface faulting in the Roer Graben (northwest Europe): Geophys. J. Int., v. 132, p. 347-362.

Campbell, J., Kümpel, H. J., Fabian, M., Fischer, D., Görres, B., Keysers, C. J., and Lehmann, K., 2002, Recent movement pattern of the Lower Rhine Embayment from tilt, gravity and GPS data: Netherlands Journal of Geosciences, v. 81, no. 2, p. 223-230.

Cloething, S., Ziegler, P. A., Beekman, F., Andriessen, P. A. M., Hardebol, N., and Dèzes, P., 2005, Intraplate deformation and 3D rheological structure of the Rhine Rift System and adjacent areas of the northern Alpine foreland: Int. J. Earth Sci. , v. 94, p. 758-778.

Cowan, D., S., 1999, Do faults preserve a record of seismic slip? A field geologist's opinion: Journal of Structural Geology, v. 21, p. 995-1001.

Dèzes, P., Schmid, S. M., and Ziegler, P. A., 2004a, Evolution of the European Cenozoic Rift System: interaction of the Alpine and Pyrenean orogens with their foreland lithosphere: Tectonophysics, v. 389, no. 1–2, p. 1-33.

-, 2004b, Evolution of the European Cenozoic Rift System: interaction of the Alpine and Pyrenean orogens with their foreland lithosphere: Tectonophysics, v. 389.

England, P., and Jackson, J., 2011, Uncharted seismic risk: Nature Geoscience, v. 4, p. 348-349.

Friedrich, A. M., Strecker, M. R., and Scherbaum, F., 2002, Active intraplate deformation in central Europe: paleoseismology of the Lower Rhine Embayment: DFG New Grant Application, p. 1-42.

Geluk, M. C., Duin, E. J., Dusar, M., Rijkers, R., van den Berg, M. W., and van Rooijen, P., 1994, Stratigraphy and tectonics of the Roer Valley Graben: Geologij en Mijnbouw, v. 73, no. 2-4, p. 129-141.

Gledhill, K., Ristau, J., Reyners, M., Fry, B., and Holden, C., 2010, The Darfield (Canterbury) Earthquake of september 2010: Preliminary Seismological Report: Bulletin of the New Zealand Society for Earthquake Engineering, v. 43, no. 4, p. 215-221.

Goes, S., Spakman, W., and Bijwaard, H., 1999, A Lower Mantle Source for Central European Volcanism: Science, v. 286, no. 5446, p. 1928-1931.

Görres, B., 2008a, Recent Site Motions in the Lower Rhine Embayment and the Eifel from 15 years of GPS data: Abstract Swiss Geoscience Meeting, Lugano, p. 1.

Görres, B., H. Kuhlmann, 2008b, How groundwater withdrawal and recent tectonics cause damages of the earth's surface: Monitoring of 3D site motions by GPS and terrestrial measurements: Journal of Applied Geodesy, no. 1(2007), p. 223-232.

Hinzen, K. G., 2003, Stress field in the Northern Rhine area, Central Europe, from earthquake fault plane solutions: Tectonophysics, v. 377, p. 325-356.

Hinzen, K. G., and Oemisch, M., 2001, Location and Magnitude from Seismic Intensity Data of Recent and Historic Earthquakes in the Northern Rhine Area, Central Europe: Bulletin of the Seismological Society of America, v. 91, no. 1, p. 40-56.

Hinzen, K. G., S. K. Reamer 2007, Seismicity, seismotectonics, and seismic hazard in the northern Rhine area. In: Stein, S. and Mazotti, S., ed., Continental Intraplate Earthquakes: Science, Hazard, and Policy Issues: Geological Society of America Special Paper, v. 425, p. 225-242.

Hoernle, K., Zhang Yu, S., and Graham, D., 1995, Seismic and geochemical evidence for large-scale mantle upwelling beneath the eastern Atlantic and western and central Europe: Nature, v. 374, p. 34-39.

Houtgast, R. F., R.T. Van Balen, C. Kasse, 2005, Late Quaternary evolution of the Feldbiss Fault (Roer Valley Rift System, the Netherlands) based on trenching, and its potential relation to glacial unloading: Quaternary Science Reviews, v. 24, p. 491-510.

Houtgast, R. F., R.T. Van Balen, C. Kasse, J. Vandenberghe, 2003, Late Quaternary tectonic evolution and postseismic near surface fault displacement along the Geleen Fault (Feldbiss Fault Zone - Roer Valley Rift System, the Netherlands), based on trenching: Geologie en Mijnbouw, v. 82, no. 2, p. 177-196.

Illies, H., 1975, |ntraplate tectonics in stable Europe as related to plate tectonics in the Alpine system: Int. J. Earth Sci., v. 64, p. 677-699.

Illies, H., and Greiner, G., 1978, Rhinegraben and the Alpine system: GSA Bulletin, v. 89, p. 770-782.

Jolivet, L., Frizon de Lamotte, D., Mascle, A., and Séranne, M., 1999, The Mediterranean Basins: Tertiary Extension within the Alpine Orogen — an introduction: Geological Society, London, Special Publications, v. 156, no. 1, p. 1-14.

Kooi, H., Cloetingh, S., and Remmelts, G., 1989, Intraplate stresses and the stratigraphic evolution of the North Sea Central Graben.: Geologie en Mijnbouw, v. 68, p. 49-72.

Kümpel, H. J., Lehmann, K., Fabian, M., and Mentes, G., 2001, Point stability at shallow depths: experience from tilt measurements in the Lower Rhine Embayment, Germany, and implications for high-resolution GPS and gravity recordings: Geophysical Journal International, v. 146, p. 699-713.

Lehmann, K., Klostermann, J., and Pelzing, R., 2001, Paleoseismological Investigations at the Rurrand Fault, Lower Rhine Embayment: Netherlands Journal of Geosciences, v. 80, no. 3-4, p. 139-154.

Leydecker, G., 2004, Erdbebenkatalog für die Bundesrepublik Deutschland mit Randgebieten für die Jahre 800 - 2003. Datenfile, BGR Hannover.: Datenfile, BGR Hannover.

Liu, M., Stein, S., and Wang, H., 2011, 2000 years of migrating earthquakes in North China: How earthquakes in midcontinents differ from those at plate boundaries: Lithosphere, v. 3, p. 128–132.

Mayer-Rosa, D., and Cadiot, B., 1979, A review of the 1356 Basel earthquake: Basic data: Tectonophysics, v. 53, no. 3–4, p. 325-333.

McCalpin, J. P., 2009, Paleoseismology: International Geophysics Series, v. 95, p. 1-613.

Meghraoui, M., Camelbeeck, T., Vanneste, K., M., B., and Jongmans, D., 2000, Active faulting and paleoseismology along the Bree fault, lower Rhine graben, Belgium: Journal of Geophysical Research v. 105, no. B6, p. 13809-13841.

Meidow, H., 1994, Comparison of the macroseismic field of the 1992 Roermond earthquake, the Netherlands, with those of large historical earthquakes in the Lower Rhine Embayment and its vicinity: Netherlands Journal of Geosciences, v. 73, no. 2-4, p. 282-289.

Meyer, H., Hetzel, R., and Strauss, H., 2008, Erosion rates on different time scales derived from cosmogenic 10Be and river loads: implications for landscape evolution in the Rhenish Massif, Germany: International Journal of Earth Science, v. 99, no. 2, p. 395-412.

Michon, L., Van Balen, R., Merle, O., and Pagnier, H., 2003, The Cenozoic evolution of the Roer Valley Rift System integrated at a European scale: Tectonophysics, v. 367, p. 101-126.

Quitzow, H. W., and Vahlensieck, O., 1955, Ober Pleistozäne Gebirgsbildung und rezente Krustenbewegungen in der Niederrheinischen Bucht: Int. J. Earth Sci., p. 56-67.

Radulov, A., Yaneva, M., Shanov, S., Nikolov, V., Kostov, K., Nikolov, N., Hristov, V., Dobrev, N., and Mitev, A., 2012, Report on field survey after May 22, 2012 Pernik earthquake: Bulgarian Academy of Sciences, Geological Institute, p. 1-12.

Reicherter, K., Froitzheim, N., Jaronsinski, M., Badura, J., Franzke, H. J., Hansen, M., Hübscher, C., Müller, R., Poprawa, P., Reinecker, J., Stackebrandt, W., Voigt, T., von Eynatten, H., and Zuchiewicz, W., 2008, Alpine Tectonics North of the Alps. In: McCann, T. (ed.) The Geology of Central Europe, Volume 2: Mesozoic and Cenozoic: The Geological Society, London, p. 1233-1285.

Richter, D., 1962, Die Hochflächen-Treppe der Nordeifel und ihre Beziehungen zum Tertiär und Quartär der Niederrheinischen Bucht: Geologische Rundschau, v. 52, no. 1, p. 376-404.

Ritter, J. R. R., Jordan, M., Christensen, U. R., and Achauer, U., 2001, A mantle plume below the Eifel volcanic fields, Germany: Earth and Planetary Science Letters, v. 186, no. 1, p. 7-14.

Schmedes, J., Hainzel, S., Reamer, S. K., Scherbaum, F., and Hinzen, K. G., 2005, Moment release in the Lower Rhine Embayment, Germany: seismological perspective of the deformation process: Geophys. J. Inr., v. 160, p. 901-909.

Schumacher, M. E., 2002, Upper Rhine Graben: the role of preexisting structures during rift evolution: Tectonics, v. 21, no. 6-1, p. 6-17.

Şengör, A. M. C., Burke, K., and Dewey, J. F., 1978, Rifts at High Angles to Orogenic Belts - Tests for their Origin and Upper Rhine Graben as an Example: American journal of science, v. 278, no. 1, p. 24-40.

Spreckels, V., 2000, Monitoring of Coal Mining Subsidence by HRSC-A Data: Proceedings of IAPRS, Amsterdam, v. 33, p. 13-15.

Stein, S., and Liu, M., 2009, Long aftershock sequences within continents and implications for earthquake hazard assessment: Nature v. 462, p. 87-89.

Stein, S., and Mazotti, S., 2007, Continental Intraplate Earthquakes: Science, Hazard, and Policy Issues: Geological Society of America, Special Paper, v. 425, p. 1-16.

Strecker, M. R., Hilley, G., Lück, E., Scherbaum, F., and Spangenberg, U., 2002a, S.A.F.E. Annual Report. Searching for surface ruptures associated with the Düren 1755/56 earthquakes, Germany: unpublished data, Potsdam University, p. 1-45.

Strecker, M. R., Streich, R., Lück, E., Scherbaum, F., and Schäbitz, F., 2002b, S.A.F.E. annual report. Holocene fault ruptures along the Erft Fault, Southern Lower Rhine Embayment?: unpublished data, Potsdam University, p. 1-66.

Streich, R., 2003, Geophysical Prospecting of Suspected Holocene Fault Activity in the Lower Rhine Embayment, Germany: Diploma Thesis, University of Potsdam, Germany, p. 1-125.

Tesauro, M., Hollenstein, C., Egli, R., Geiger, A., and Kahle, H. G., 2005, Continuous GPS and broad-scale deformation across the Rhine Graben and the Alps: International Journal of Earth Science, v. 94, p. 525–537.

Van Balen, R. T., Houtgast, R. F., and Cloething, S. A. P. L., 2005, Neotectonics of The Netherlands:a review: Quaternary Science Reviews, v. 24, p. 439-454.

Vanneste, K., Meghraoui, M., and Camelbeeck, T., 1999, Late Quaternary earthquake-related soft-sediment deformation along the Belgian portion of the Feldbiss Fault, Lower Rhine Graben system: Tectonophysics, v. 309, p. 57-79.

Vanneste, K., and Verbeeck, K., 2001, Paleoseismological analysis of the Rurrand fault near Jülich, Roer Valley graben, Germany: Coseismic or aseismic faulting history?: Geologie en Mijnbouw, v. 80, no. 3-4, p. 155-169.

Vanneste, K., Verbeeck, K., Camelbeeck, T., Paulissen, E., Meghraoui, M., Renardy, F., Jongmans, D., and Frechen, M., 2001, Surface-rupturing history of the Bree fault scarp, Roer Valley

graben: Evidence for six events since the late Pleistocene: Journal of Seismology, v. 5, p. 329-359.

Wegmuller, U., Strozzi, T., Werner, C., Wiesmann, A., Benecke, N., and Spreckels, V., 2000, Monitoring of mining-induced surface deformation in the Ruhrgebiet (Germany) with SAR interferometry Geoscience and Remote Sensing Symposium, 2000. Proceedings. IGARSS 2000. IEEE 2000 International, v. 6, p. 2771-2773.

Ziegler, P. A., 1992, European Cenozoic rift system: Tectonophysics, v. 208, no. 1–3, p. 91-111.

-, 1994, Cenozoic rift system of western and central Europe: an overview: Geologie en Mijnbouw, p. 99-127.

Zijerveld, L., Stephenson, R., Cloetingh, S., Duin, E., and van den Berg, M. W., 1992, Subsidence analysis and modelling of the Roer Valley Graben (SE Netherlands): Tectonophysics, v. 208, no. 1–3, p. 159-171.

# Chapter 3

## *Using High-Resolution Digital Elevation Data to Detect Non-Seismic Overprint on Suspected Fault Scarps: Implications for Trench Site Selections*

## 3.1 Abstract

The recognition of the surface expression of potential seismogenic structures is a major challenge in densely populated humid regions, because high erosion rates, urbanization and agricultural land use disguise the tectonic signal at the surface over wide areas. This problem is enhanced in low-strain regions like Central Europe, where recurrence intervals of large earthquakes are typically on the order of $10^3$ - $10^5$ years and fault slip rates are well below 1 mm/yr. Despite the infrequency of large earthquakes in low-strain regions, such events nevertheless have the potential for catastrophic damage if they struck poorly prepared metropolitan areas. The Lower Rhine Graben, the NW branch of the Central European Rift System is a seismically active intraplate rift. However, although instrumental records and historical documents reveal the occurrence of large earthquakes, the question of whether earthquakes large enough to rupture the surface have occurred in the Lower Rhine Graben is still a matter of debate. Reasons for this are severe surface modifications due to climatic and anthropogenic overprint. Additionally, subsidence effects triggered by coal mining and abundant surface craters caused by aerial bombs from World War II hamper the recognition of seismogenic surface structures. Moreover, potentially unexploded World War II bombs pose a significant hazard and turn prospecting and trench excavation into a dangerous task. To successfully select suitable trench sites for paleoseismic studies and importantly, preclude sites that are located in strongly disturbed regions, high-resolution digital elevation models such as LiDAR (Light Detection And Ranging) data sets provide meaningful information. The goal of this chapter is to assess to what degree the surface expression of potentially active faults in the Lower Rhine Graben may be pastured by non-seismic surface modifications, and if coseismic deformation can be differentiated from non-seismic disturbance. Two case studies carried out along the presumably active segments of the Erft and Wissersheimer faults in the Central Lower Rhine Graben demonstrate the challenges of paleoseismic research in densely populated humid intraplate rifts. In the Erft-fault area, the geomorphic expression of

the fault is clearly recognizable. Significant scarp degradation due to soil erosion and farming has been known already, but LiDAR analysis helps to more clearly convey the situation. Most importantly, LiDAR data show a dense pattern of bomb craters that have caused severe surface deformation and pose a potential hazard for trenching purposes. In the Wissersheimer-fault area, the fault scarp is intensively modified by fault-parallel fluvial erosion due to an active drainage. Furthermore, the study site is characterized by significant local subsidence of up to 10 cm/yr due to adjacent open pit mining and associated groundwater disposal. Here, a clear differentiation between coseismic and non-seismic fault slip would be a challenging task during trench analysis. Results of this study demonstrate that paleoseismic research in the Lower Rhine Graben needs careful and judicious preplanning to minimize potential hazards as well as ambiguity of the interpretation of sediment deformation in trench excavation studies. Furthermore, results of LiDAR analysis have proven that such techniques are a useful additional tool for trench-site selection.

## 3.2 Introduction

Research in paleoseismology and tectonic geomorphology has initiated and advanced mainly in arid regions, barely affected by anthropogenic overprint (e.g. Crone et al., 1997; McCalpin and Nishenko, 1996; Schwartz and Coppersmith, 1984; Sieh, 1978; Sieh et al., 1989; Wallace, 1977; Wallace, 1986). Here, seismogenic surface structures are exposed over several kilometers and preserve over long periods of time, due to low erosion rates and generally negligible anthropogenic landscape modification (Figure 3.1a). Thus, also low-strain intraplate fault systems in remote arid regions usually preserve seismogenic surface structures, e.g. fault scarps or offset gullies, in a way that they are easily recognizable in the field as well as on remote sensing data such as orthophotos and digital elevation models (DEM).

In contrast to remote arid regions, fault scarps formed in humid and densely populated regions are subject to a much higher degree of scarp degradation related to meteorological and anthropogenic processes. In particular, urbanization and farming may lead to rapid degradation of fault scarps as the "sharp edges" produced by coseismic surface ruptures are often systematically flattened immediately after the earthquake (Figure 3.1b). Meteorologically induced processes causing degradation and/or obliteration of fault scarps include solifluction (downslope movement of water-saturated soil in periglacial environments), fluvial erosion as well as a dense vegetation cover (Table 3.1). In low-strain regions with tectonic deformation rates well below 1mm/yr, seismogenic deformation is often barely distinguishable from fluvial and erosion processes and in many cases entirely obliterated. Consequently, the worst-case scenario regarding the preservation potential of fault scarps are densely populated low-strain fault systems situated in humid or moderately humid climate zones, a setting for which the Lower Rhine Graben in Central Europe is a prime example for (Figure 3.2).


Figure 3.1: Examples for the preservation potential of coseismic surface ruptures in in different climatic settings. a) Fault scarp of the MW 7.3 Fairview Peak earthquake, located in a remote arid region of Northern Nevada; b) Surface rupture of the MW 7.1 Canterbury earthquake, in a region characterized by moderately humid climate and intensive farming, Christchurch, New Zealand. Note the immediate flattening of the surface scarps by a tractor a few days after the earthquake.

We have selected two sites located in the central part of the Lower Rhine Graben (Figure 3.2), a region that has experienced severe regional and local subsidence due to groundwater disposal in the vicinity of large open-pit lignite mines (Figure 3.3). We have tested the potential of high-resolution LiDAR (Light Detection And Ranging) data as a tool for identifying both possible seismogenic structures as well as non-seismic processes leading to obliteration of surface faulting. The study sites have been the scope of the EC-funded research project S.A.F.E. (**S**low Active Faults in Central Europe), and have been proposed as potential trench sites for future research campaigns (Friedrich et al., 2002; Strecker et al., 2002). A third site, proposed for trenching studies at the Schafberg fault in the SW part of the Lower Rhine Graben, is discussed in Chapter 4-6 of this thesis. Mining-induced subsidence does not affect this site.

Table 3.1: Examples of intraplate fault zones of different climatic and population settings and their preservation potential of coseismic surface ruptures.

| **Climate** | **Mean Population Density (inhabitants/km²)** | **Example** | **Preservation potential of Coseismic Surface Ruptures** | **References** |
|---|---|---|---|---|
| Semi-arid, Arid | Very low (7-20) | Rio Grande Rift, Southern USA | Good, but degradation of fault scarps due to long recurrence intervals ($10^3$-$10^5$ years) | McCalpin, 2005; Bauer and Kelson, 2004 |
| Semi-arid | High (>500) | Northern Tehran fault, Northern Central Iran | Good in rural areas, lack of known seismogenic structures in the city due to rapid population growth and related surface modifications | Bachmanov et al., 2009; Nazari et al., 2010 |
| Humid | Low (20-50) | Cariatá trough, Northeastern Brazil | Poor, due to the dense vegetation cover, as well as mudflows and other processes associated with high precipitation rates | Bezerra et al., 2008; Rossetti et al., 2008 |
| (Moderately) Humid | High (>300) | Lower Rhine Embayment, Central Europe | Very poor, due to intensive farming, urbanization, mining and the dense vegetation cover | Vanneste and Verbeeck, 2001; this study |

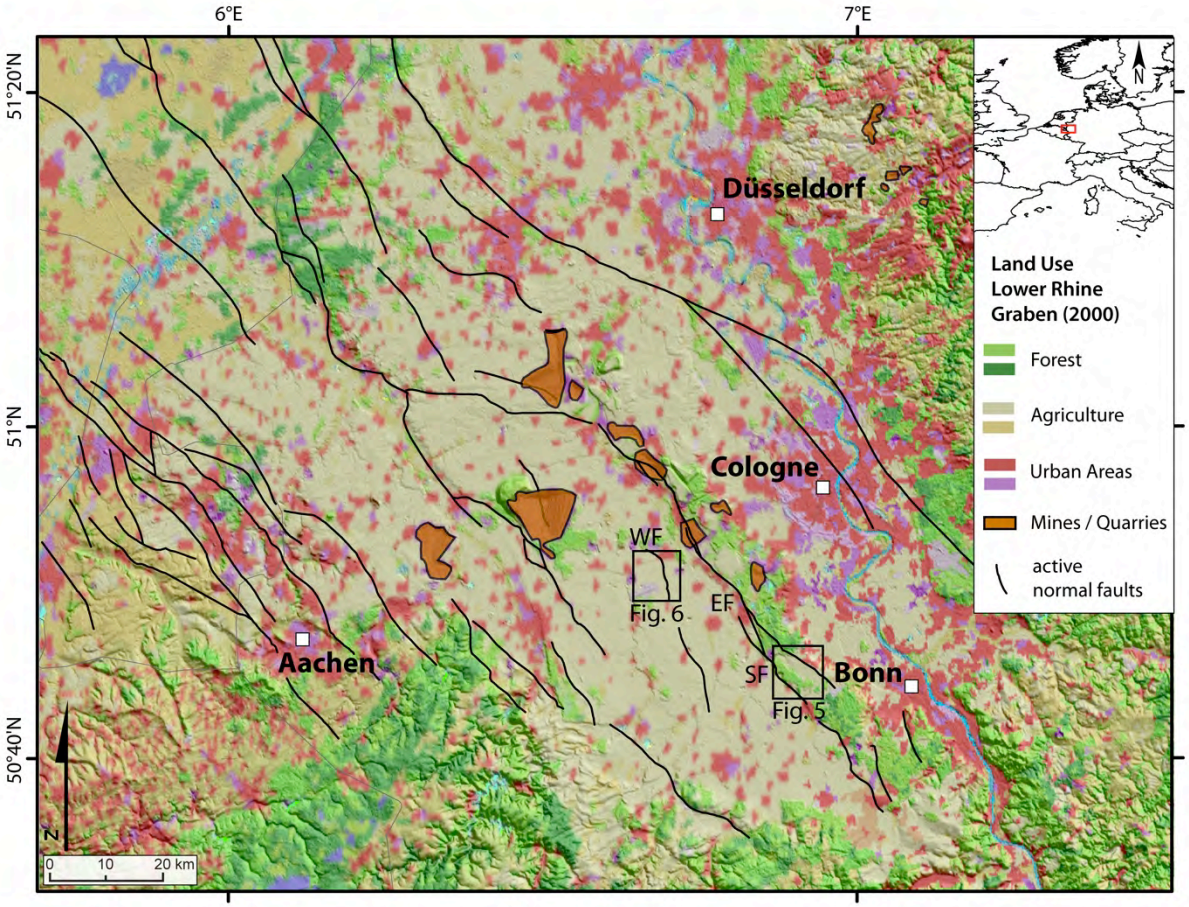


Figure 3.2: Digital elevation model of the Lower Rhine Graben showing the land use distribution and potentially active faults. (a) Erft-fault area; (b) Wissersheimer-fault area. EF: Erft fault; SF: Swist fault; WF: Wissersheimer fault; elevation data derived from Shuttle Radar Topographic Mission (SRTM), resolution 90 m, transparency 40 percent. (Source: SCAG, *ESRI* World Imagery, Tele *Atlas*)

In this chapter, we aim to establish new criteria for evaluating the viability of study sites for trenching approaches. A further intention of this study is to elucidate the challenges and pitfalls scientists face when planning paleoseismical studies in the Lower Rhine Graben and analog regions.

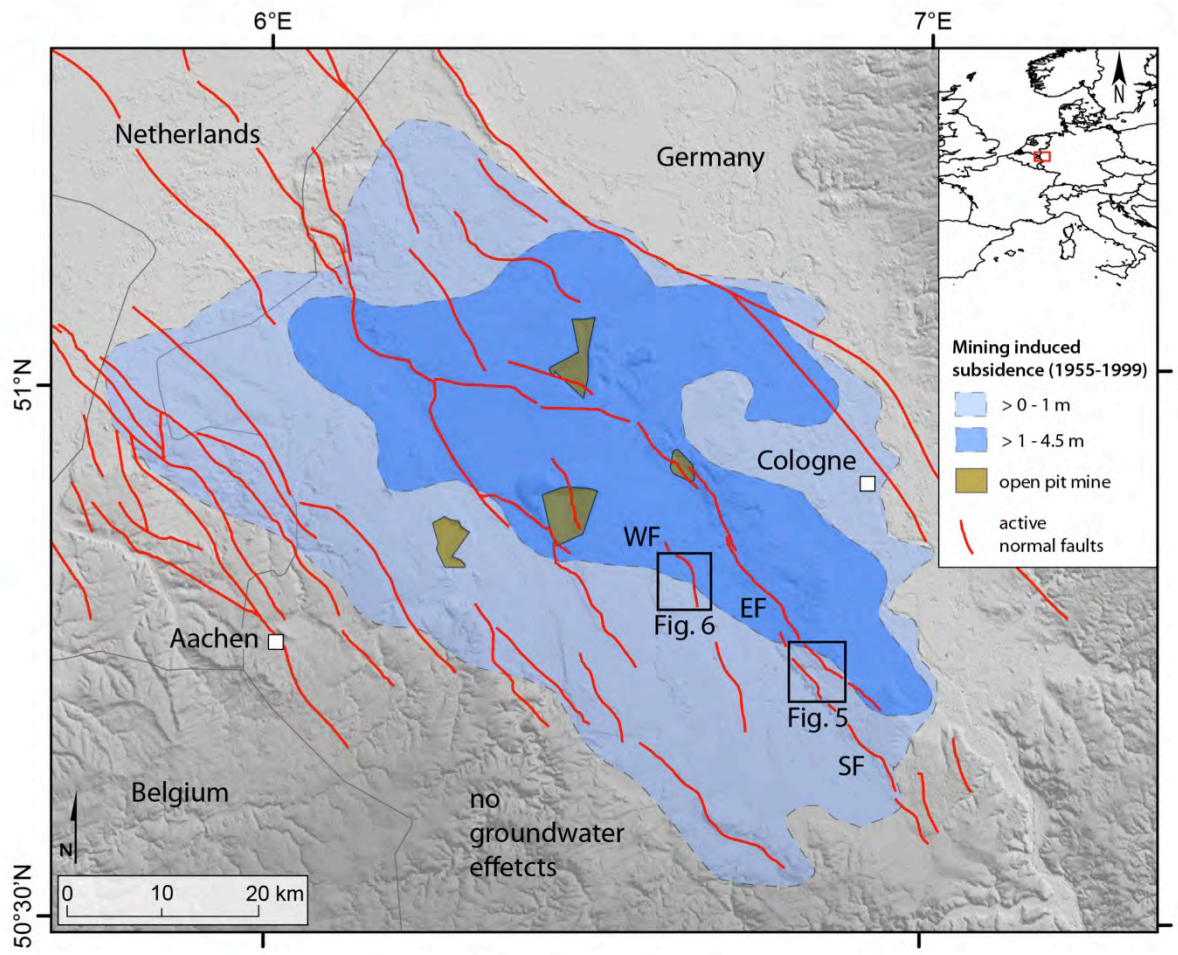


Figure 3.3: Digital elevation model of the Lower Rhine Graben showing the area affected by extensive subsidence triggered by groundwater disposal in the vicinity of open pit lignite mines. Red lines depict the surface trace of potentially active normal faults; black quadrangles depict the location of the two case studies discussed in this study; (a) Erft-fault area; (b) Wissersheimer-fault area. EF: Erft fault; SF: Swist fault; WF: Wissersheimer fault; subsidence data from Schäfer (1999).

## 3.3 LiDAR Analysis

One promising technique that gained increasing importance in tectonic geomorphology and paleoseismic research is the application of high-resolution elevation LiDAR (Light Detection And Ranging) data (e.g. Arrowsmith and Zielke, 2009; Baran et al., 2010; Salisbury et al., 2012). LiDAR data are composed of a large number (up to several millions) of distant measurements between a laser scanner and the ground surface. Depending on the quality of the scanner sub-centimeter accuracy is possible. Data acquisition can be performed by a laser scanner either from the ground surface (terrestrial LiDAR), or from an airplane (airborne LiDAR). The data used in this study are exclusively airborne LiDAR data.

Airborne LiDAR data are not only useful for mapping previously unrecognized surface ruptures in detail, but they also provide the opportunity to detect fault scarps in regions with a dense vegetation cover by using "virtual deforestation" software applications. During data acquisition each laser pulse measures a multiple number of distance measurements (returns), with the first return usually from the top of local vegetation and the last return from the ground surface. Here, digital terrain models (DTM) are produced using exclusively the last return of the single laser beams. This technique has successfully been used for the detection of fault scarps in densely forested regions in Southern Alaska and Northwestern Washington, United States (McCalpin, 2011), and Northeastern Germany (Kupetz, 2003). However, for certain cases in paleoseismic research information on the vegetation cover may be useful. For example, in arid regions with sparse annual precipitation plants often tend to grow along active fault traces, which may act as groundwater aquifer (Guest et al., 2007). Furthermore, in regions with highly variable coverage of forest and cropland, information on the vegetation cover are important for planning purposes regarding e.g. trench-site selection and geophysical prospecting.

During the last decade, the geodetic surveys of many German federal states carried out extensive acquisition of airborne LiDAR data. As a result some states such as North Rhine Westphalia, where the sites of this study are located, provide an almost statewide coverage of commercial LiDAR DTMs at a resolution ranging from 10 to 1 $m^2$/pixel. Paleoseismic research in North Rhine Westphalia is mainly focused on the potentially active faults of the Lower Rhine Graben. Here, airborne LiDAR data reveal the opportunity to study in detail suspected fault scarps and evaluate study sites regarding their suitability for trenching studies.

LiDAR data used in this study are part of a data set that was collected by the geodetic survey of North Rhine Westphalia. For the Erft-fault area, we used the DGM1 data subset

characterized by a regular point distribution, a resolution (point density in points/m²) of 1 $m^2$/pixel and a vertical precision of ± 0.2 m (Figure 3.4). For the Wissersheimer-fault area, we used the DGM1L data subset, which is in contrast to the DGM1 data composed of point clouds with irregular point distribution and a minimum resolution of 1 $m^2$/pixel with vertical precision of ± 0.2 m, which is the highest-resolution DTM available for the region (Figure 3.5). We used the geo-information software Global Mapper© (version 10) to produce hillshades, slope maps and topographic profiles, ArcMap© (version 10) to produce geo-referenced and projected maps, and Adobe Illustrator© (version 5.1) for final mapping purposes.

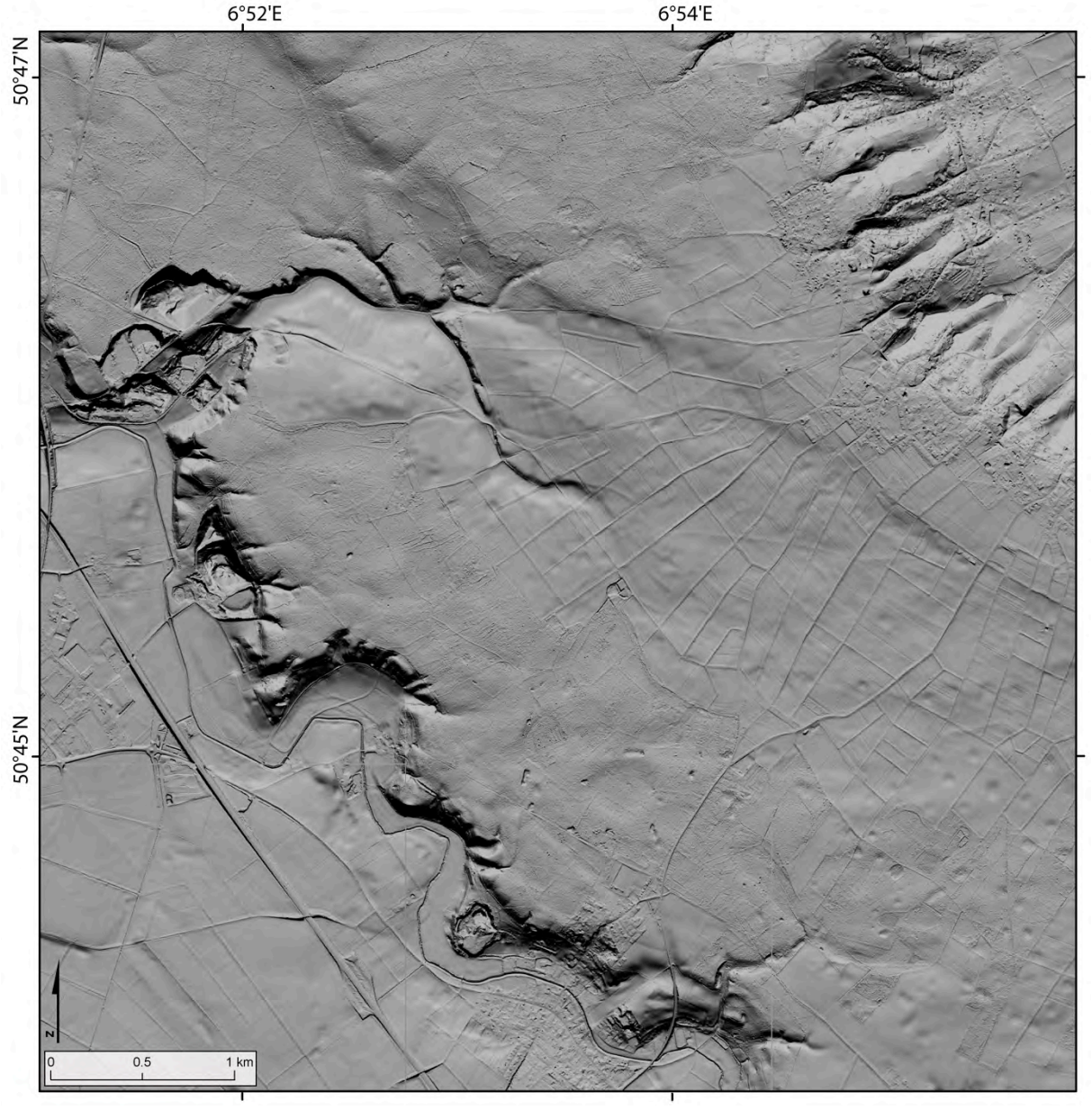

Figure 3.4: Digital Terrain Model (DTM) of the Erft-fault area derived from airborne LiDAR data. LiDAR data are produced and processed by the geodetic survey of Northrhine Westphalia (Landesvermessungsamt Nordrhein Westfalen). Data are displayed using hillshade effect with illumination from the NE. Resolution: max. 1m/pixel, vertical accuracy ± 0.2 m. Projection: Gauß-Krüger, Potsdam, Zone 2.

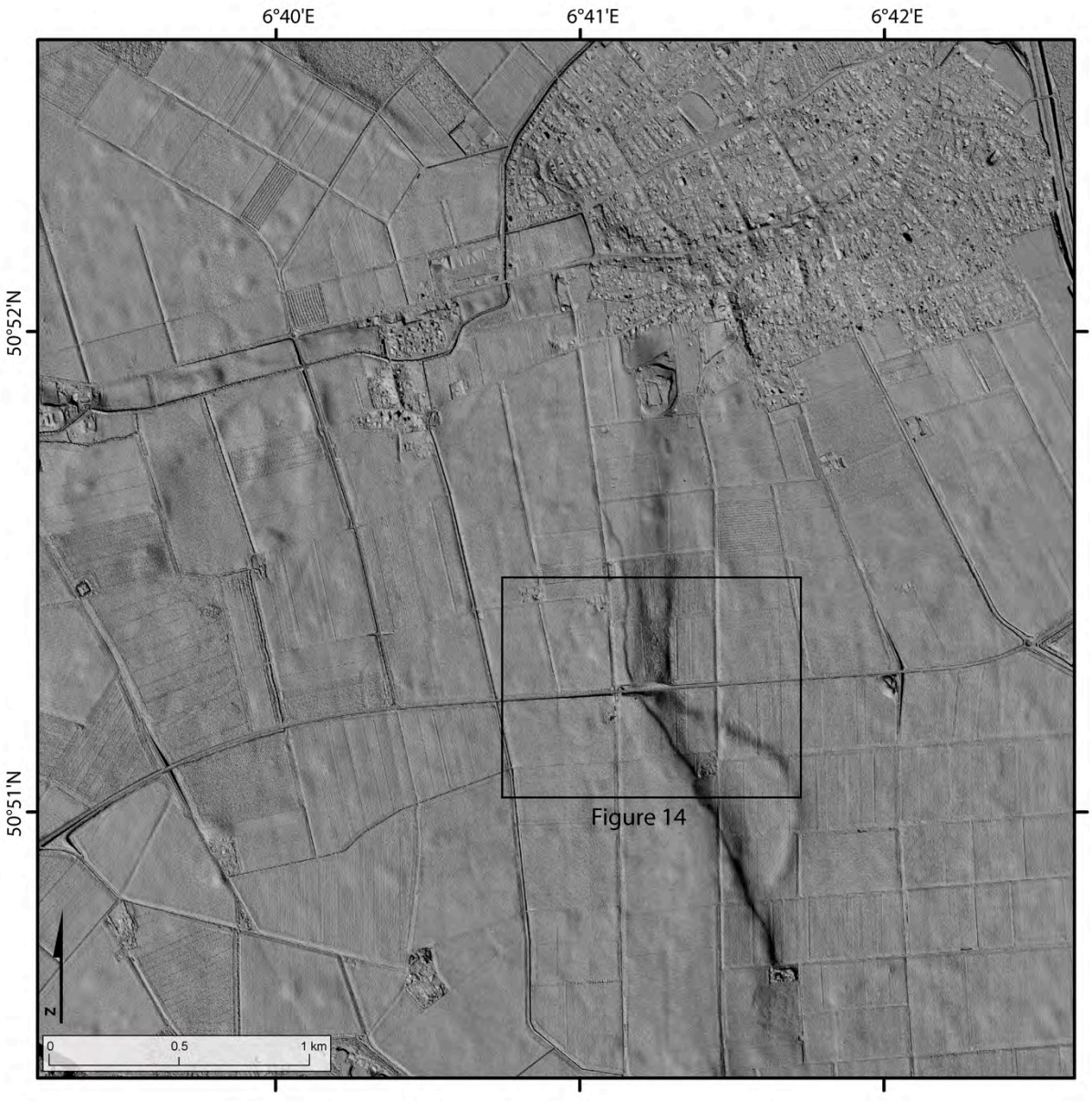


Figure 3.5: Hillshade DTM of the Wissersheimer-fault area derived from airborne LiDAR data. Illumination from the NE. Resolution: 1m/pixel, vertical precision ± 0.2 m. Projection: Gauß-Krüger, Potsdam, Zone 2.

## 3.4 Regional Setting

The study sites are located in the Central Lower Rhine Graben (Figure 3.2), a tectonically active intraplate rift structure situated in a densely populated and moderately humid region. Former seismotectonic studies revealed very small Pleistocene and Holocene slip rates on active faults ranging from 0.06 to 0.23 mm/yr (Ahorner, 1968; Geluk et al., 1994; Meghraoui et al., 2000; van den Berg, 1994). In contrast, long-term denudation rates are on the order of 0.05 mm/yr (Meyer et al., 2008) and regional present-day soil erosion rates range from 0.5 to 1 mm/yr (Bork and Lang, 2003).

Therefore, both long- and short-term erosion rates are on the same order of magnitude as tectonic slip rates, and thus potentially counterbalance tectonically induced surface effects. Furthermore, the Lower Rhine Graben has one of the highest population densities in Europe with an average of 576 inhabitants/km$^2$ (LÖGD-Report, 2010; Strohmeier et al., 2007). Due to the relatively warm temperatures (mean annual temperature of 9 - 11°C) and high precipitation values (600 - 800 mm/yr) as well as the dense cover of loess soils, the Lower Rhine Graben is considered an agriculturally favorable area. More than 50% of the region is used as farmland. Forests cover about 20% of the region and are predominately planted for commercial use (Figure 3.2).

One important factor for drastic surface modifications in the area of the Lower Rhine Graben is the extensive coal and open-pit lignite mining in its central and NE parts. Collapsed mines in the main coal mining area (Ruhr area) have caused local subsidence of several tens of meters with local subsidence rates exceeding 1 m/yr during the last 60 years (Spreckels, 2000; Wegmuller et al., 2000), and triggered numerous shallow mining earthquakes (Hinzen, 2007). In the Ruhr area alone about 1000 mining induced seismic events with local magnitudes between $0.7 \leq M_L \leq 3.3$ are recorded every year (Bischoff et al., 2010).

Additionally, open-pit lignite mining in the central part of the Lower Rhine Graben requires large-scale groundwater disposal, which in turn leads to sagging effects due to the collapse of previously water-filled cavities and peat-lenses (Figure 3.3). The consequence is large-scale subsidence of the entire German part of the Lower Rhine Graben with subsidence rates of locally more than 10 cm/yr (Schaefer, 1999). This process also induced continuous creeping rates on the order of 1 cm/year (Figure 3) on some segments of the Erft and Rurrand faults (Camelbeeck et al., 2001; Görres, 2008b; Görres et al., 2006; Kümpel et al., 2001; Vanneste and Verbeeck, 2001a, b).

Other drastic surface modifications are abundant bomb craters derived from aircraft battles at the end of World War II, in particular in the vicinity of large cities and industrial key locations like Cologne or the Ruhr area (Blank, 2012; Gregory, 2011).

## 3.5 The Erft-Fault Area

The Erft-fault area is situated ~ 20 km south of Cologne on the Ville Horst, a NNW-SSE striking ridge in the eastern central Lower Rhine Graben (Figure 3.2). According to former studies (Ahorner, 1962), the Erft and Swist faults, two of the major boundary faults of the Lower Rhine Graben, traverse the central and SE parts of the study site at a NW-SE strike (Figure 3.6a). Fault offset measurements (Ahorner, 1962) yield a maximum of 140 m of vertical displacement for the base of the Early Pleistocene terrace gravels at the SE end of the Ville Horst. Here, the Swist fault accommodates the largest portion of Quaternary offset (~ 85 m, Ahorner, 1962). Towards the NW, the Erft fault increasingly accommodates displacement and accounts for the major portion of Quaternary offset (~ 100 m) about 8 km NW of the study site (Ahorner, 1962).

The most prominent sedimentary deposits covering the Ville Horst to a large extent are Early Pleistocene Terrace conglomerates of the Rhine River (Figure 3.6a). On the hanging-wall of the suspected fault scarp the terrace gravels are overlain by Late Pleistocene loess and reworked loess deposits. Tertiary deposits including Oligocene and Miocene sandstone, siltstone and lignite, as well as Pliocene sandstone are exposed at the flanks of the Rhine River and Swist Creek terraces as well as in several quarries, particularly along the SW flank of the Ville Horst.

Mining-induced fault creep has been reported for the Donatus fault, a segment of the Erft fault ~ 5 km NW of the study site (Figure 3.3). Here, displaced walls and roads as well as continuous GPS measurements reveal displacement rates of up to 22 mm/yr in vertical and 6 mm/yr in horizontal direction (Görres, 2008a, b). Prior to this study, reconnaissance mapping as well as shallow geophysical surveys (Strecker et al., 2002; Streich, 2003) revealed possible Late Pleistocene fault activity of the Erft fault segment south of Hemmerich (Figure 3.6a) which favored this site as a possible trench site for future research.

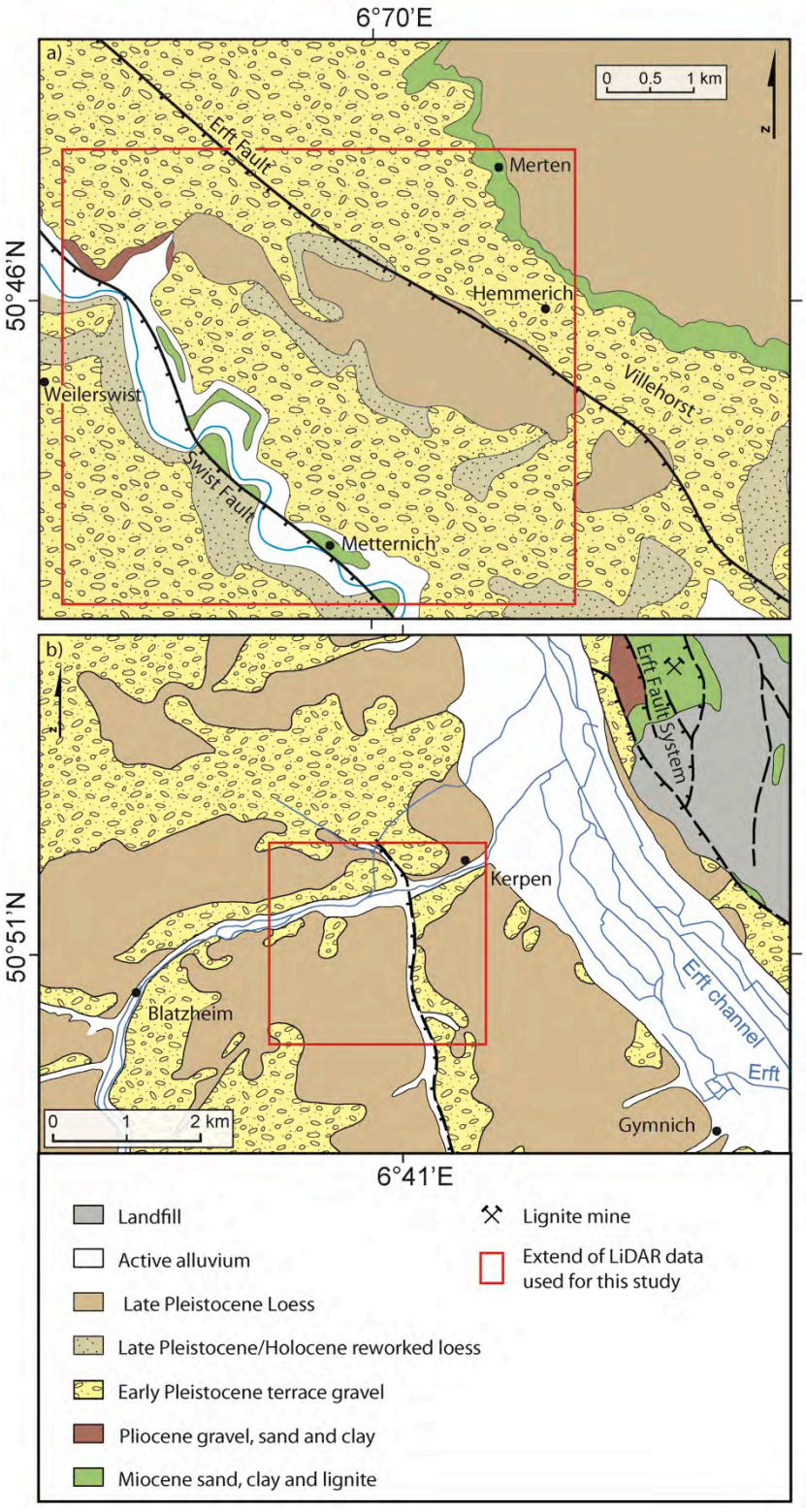


Figure 3.6: Geological maps of the study areas. (a) Erft-fault area, modified from the geological map of North Rhine Westphalia, map sheet C5506, Bonn (von Kamp, 1987); (b) Wissersheimer-fault area, modified from the geological map of Northrhine-Westphalia, map sheet C5106 Cologne (von Kamp, 1986); map style modified from Strecker et al., 2002.

## 3.6 The Wissersheimer-Fault Area

This study area is situated in the central part of the Lower Rhine Graben about 20 km SW of the city of Cologne The Wissersheimer fault, a west-dipping normal fault that is considered to represent the westernmost expression of the Erft fault system (Ahorner, 1962; Quitzow and Vahlensieck, 1955), is located in the central part of the study area traversing the city of Kerpen that is located at the NE end of the study area (Figure 3.6b).

The geology of the area is dominated mainly by Rhine River gravel deposits that stratigraphically belong to the Early Pleistocene Younger Main terrace 2 of the Rhine River (Klostermann, 1992). This gravel unit is commonly overlain by Late Pleistocene loess deposits with varying thickness of < 0.5 m to locally more than 4 m (Figure 3.6b). The westernmost part of the study area is highly affected by present-day fluvial activity and exposes active alluvial deposits of the Erft channel, and exhibited surface modifications due to past open-pit lignite mining of the former Frechen open-pit mine. The largest open-pit mine of the region, the Hambach mine, is located ~ 10 km west of the study area. As a result of large-scale groundwater disposal in the vicinity of the Hambach mine, the region has experienced strong regional subsidence of up to 3.3 m during the last 40 years (Schaefer, 1999; Figure 3.3). Thus, former studies (Streich, 2003) already pointed to the difficulty at this site regarding the differentiation of non-tectonic processes related to lignite mining from possible coseismic rupture processes.

## 3.7 Results

### 3.7.1 Erft-Fault Area

The LiDAR-DTM analysis reveals detailed information on the topographic structure, fluvial network, anthropogenic land use, and other morphologic features of the two study areas. The Erft-fault area can be separated into 4 - 5 main topographic elements that are each separated by NW-SE striking scarps (Figure 3.7). The NE corner of the map is the lowermost part of the area characterized by a flat plane situated at 95 - 100 m above sea level and inclined to the NE (inclination angle 4 - 5°). It corresponds to the Mid Pleistocene Rhine River terrace (Lower Middle Terrace, Quitzow, 1956; Winter; 1970) The topography rises abruptly towards the SW along a NW-SE striking scarp, which is intensively incised by sub-parallel small-scale gullies draining to the NE (Figure 3.7). For simplification reasons, which will become obvious in the later interpretation, we refer to this scarp as "Erft-scarp 1". Due to the intensive incision the trend of the scarp appears rather diffuse. The top of Erft-scarp 1 is at 155 - 160 m above sea level. SW of the scarp, the landscape is characterized by a plateau-like topography on a NW-SE striking ridge ("Ville" ridge, Ahorner, 1962).

Here, a subtle NW-SE striking, SW facing scarp separates the ridge (Erft-scarp 2, Figure 3.7). According to former studies (Ahorner, 1962; Strecker et al., 2002; Streich, 2003), this scarp represents the surface expression of the SW dipping Erft fault. At the SE end of the study area, Erft-scarp 2 is ~ 4 m high and does not show clear signs for fluvial incision. Towards the NW, the scarp height gradually increases reaching a maximum of ~ 10 m. A few small gullies draining to the SW incise the scarp. The SW part of the plateau in the central part of the study area is characterized by subtle topography with the exception of one deeply incised channel draining to the SW and three tributaries flowing from the north, northeast and southeast into this channel. Towards the SW, the topography descends rapidly 30 - 35 m along a steep meander-shaped scarp striking NW-SE (Erft-scarp 3). The lowermost point is situated at the recent course of the Swist Creek (110 m above sea level). Toward the SE of the creek, the topography gently rises again to a maximum of 125 m above sea level (Figure 3.7).

LiDAR analysis also facilitates the differentiation between farmland, forest and urban areas. Farmland is recognizable by a smooth surface grouped in clearly bordered sections each defining a single agricultural unit. In our study area, the largest portion (~ 70 % of the area) is used as farmland particularly covering the central and southwestern parts (Figure 3.8). In turn, forested areas are characterized by a higher surface roughness. About 20% of the

study area is covered by forest, predominately in the northeastern part and along the crest of the steep southwestern scarp. Here, the forested areas additionally exhibit shallow, irregular depressions, which we identified as wetlands once compared with satellite images and local topographic maps (Figure 3.8). Urban areas, in this case villages and small cities, are located, both, at the NE and SW corners of the study area. The LiDAR data allow for the differentiation between single houses as well as bridges and roads (Figure 3.8). Furthermore, the study area exposes a total of three quarries excavated in Tertiary sand deposits (von Kamp, 1987) along the steep southwestern scarp, the largest of which has a diameter of 1.2 km and is up to 45 m deep (Figure 3.8).

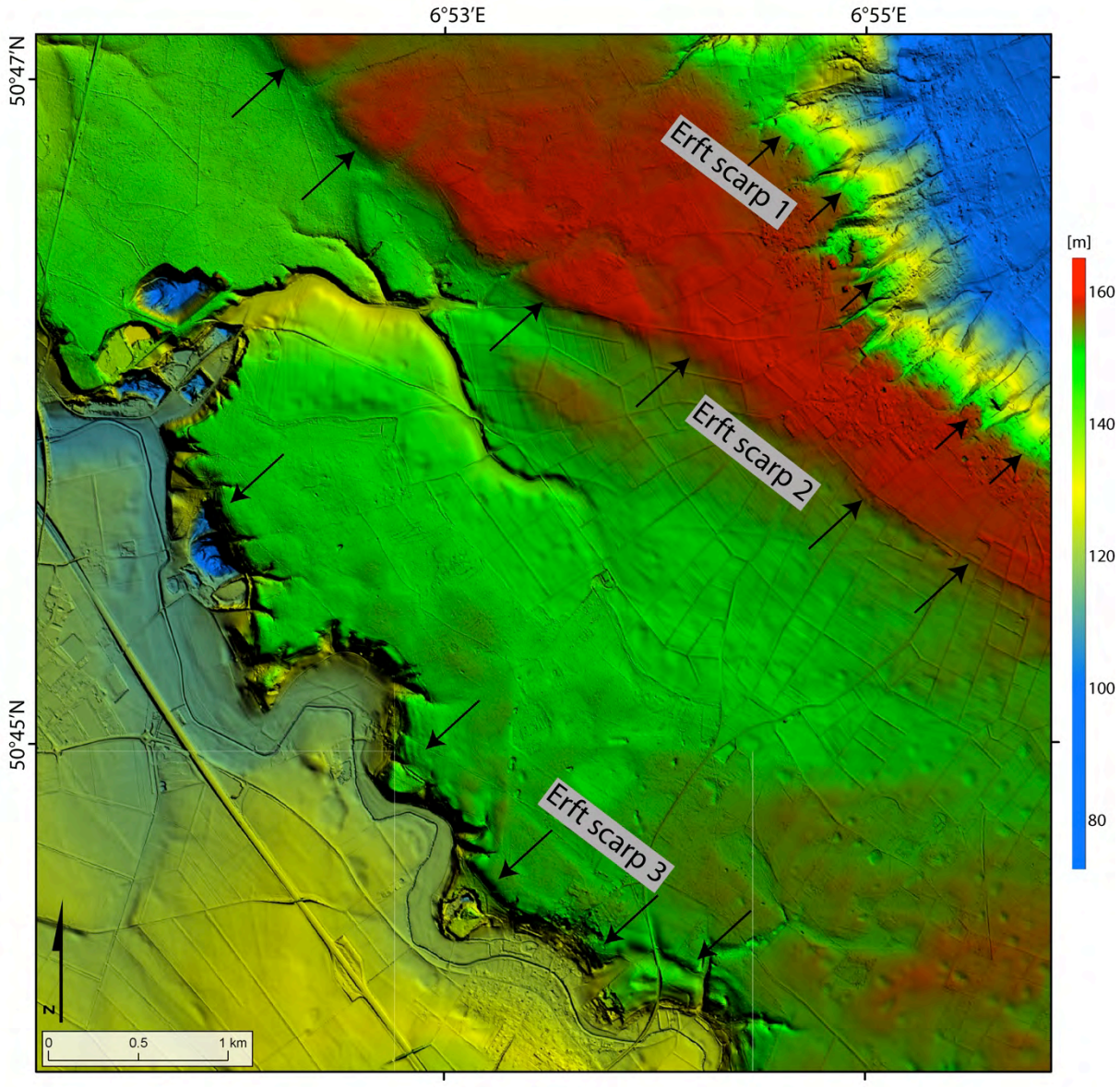


Figure 3.7: LiDAR DTM of the Erft-fault area using a color scheme adjusted to emphasizing the main topographic units.

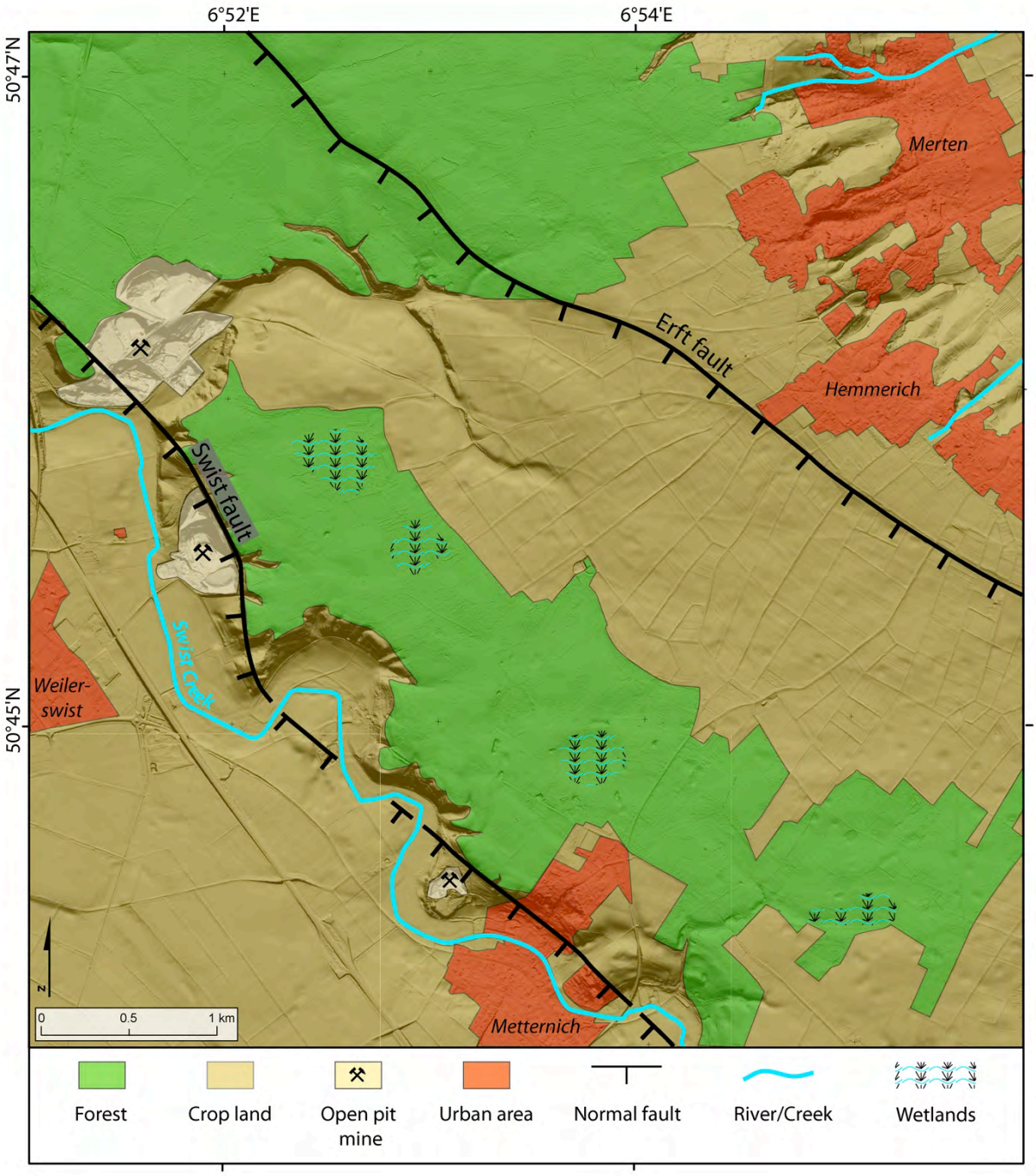


Figure 3.8: LiDAR DTM of the Erft-fault area showing the distribution of farmland, forest and urban areas, as well as the location of suspected faults.

A prominent geomorphic feature, which predominately occurs in the central and southeastern parts of the Ville horst is a dense pattern of crater-shaped depressions (Figure 3.9a). Craters are often almost perfectly circular, some are elliptical, few have a more irregular shape, but are still recognizable as craters (Figure 3.9b). Craters are predominately 20 - 50 m across (few have larger diameters of up to 100 m) and are up to 2 m deep (Figure

3.10). The highest density of craters is found at the SE edge of the study area almost exclusively on farmland where they form an irregular pattern. Farther north, craters are arranged in linear patterns located also along strike of the suspected Erft-fault scarp south of Hemmerich (Figure 3.9b).

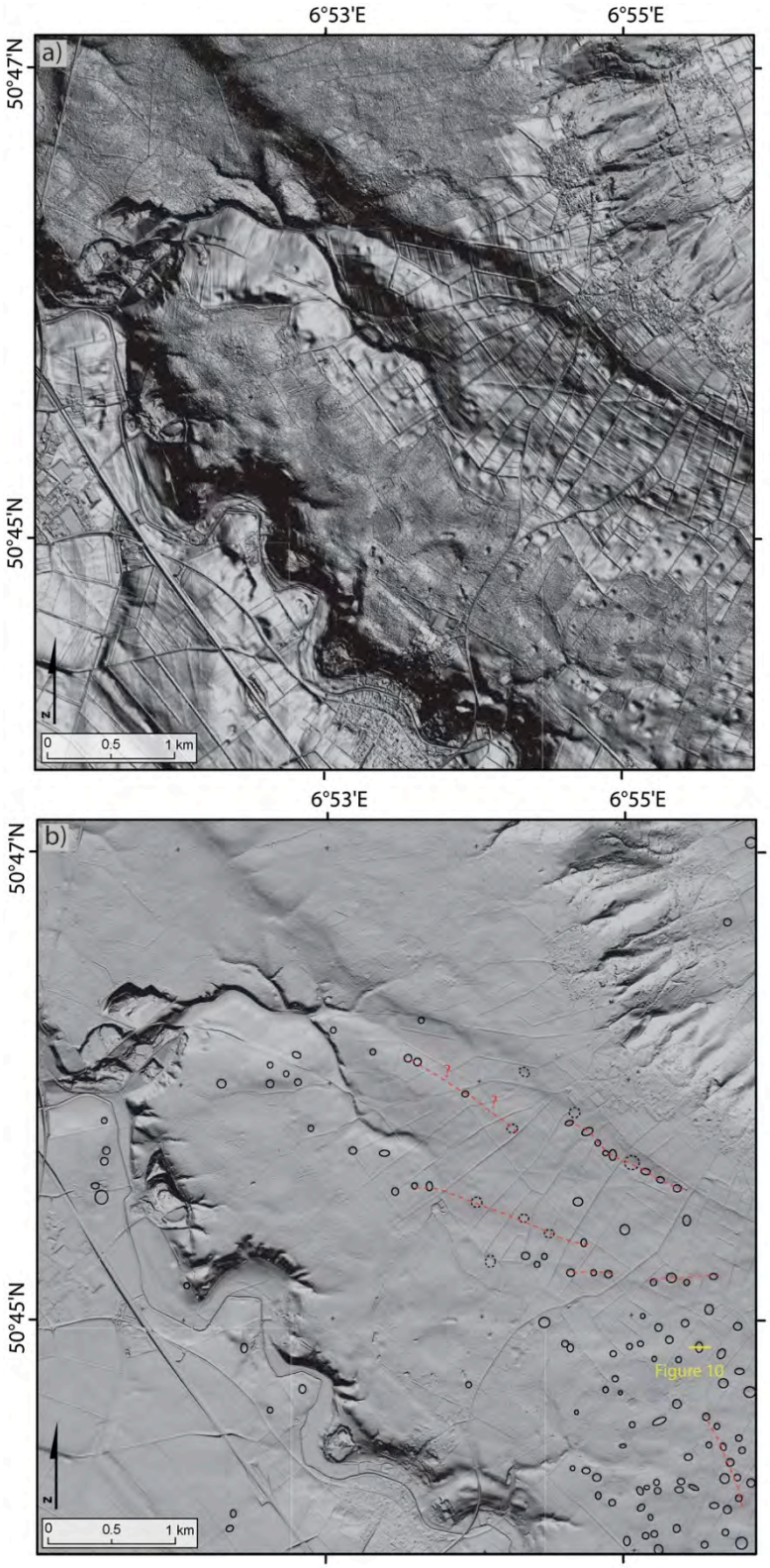


Figure 3.9: Distribution of craters in the Erft-fault area. (a) LiDAR DTM using a strongly exaggerated hillshade effect (vertical exaggeration factor 34.7; Global Mapper©) to emphasize the visibility of crater-shaped

depressions in the southeastern and central part of the map. (b) Crater map of the area overlaying LiDAR DTM (transparency 40%); note the linear crater patterns along and south of the suspected Erft-fault scarp. Yellow line depicts the position of the crater profile shown in Figure 10.

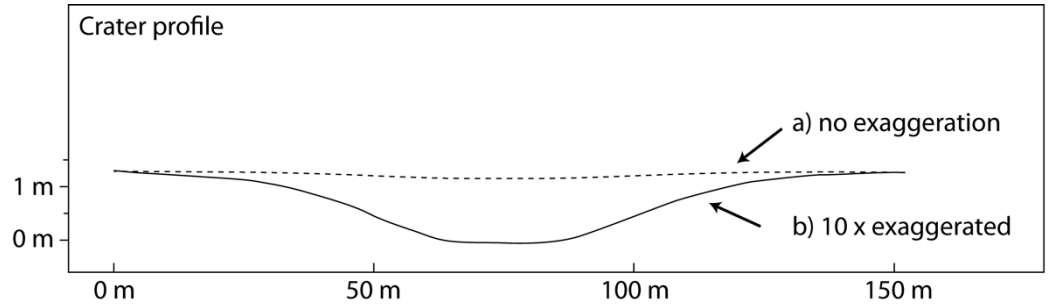


Figure 3.10: Exemplary topographic profile of a crater shaped depression located on the Ville Horst S of the Erft fault. The profile location is marked in Figure 9.

### 3.7.2 Wissersheimer-Fault Area

At the Wissersheimer fault, the region is characterized by a smooth morphology with maximum topographic variations of ~ 30 m. The most striking topographic element is a left-stepping scarp striking NW-SE to N-S in the central part of the study area (Figure 3.11), which according to former studies (Ahorner, 1962; Hinzen et al., 2004) represents the surface expression of the Wissersheimer normal fault.

The southern part of the west-facing scarp is clearly visible as a narrow and sharp, single step of ~ 6 m height (Profile A-A', Figure 3.11). Towards the NNW, the scarp turns into an almost pure northern strike, widens and branches into three smaller scarps. The eastern and central scarps are characterized by a smooth morphology and a vertical offset of 2.5 m and 1 m, respectively (Profile B-B', Figure 3.11). The western scarp appears sharper with a maximum height of 0.7 m. It is ~ 500 m long and dies out to the NNW. The central scarp is ~ 300 m long and dies out to the north. The easternmost scarp continues at a northern strike for ~ 1.3 km and then turns into a NW-SE strike for another ~ 1.5 km. Towards the NW the scarp gradually decreases with scarp heights of ~ 1.5 m at the northern edge of the study area.

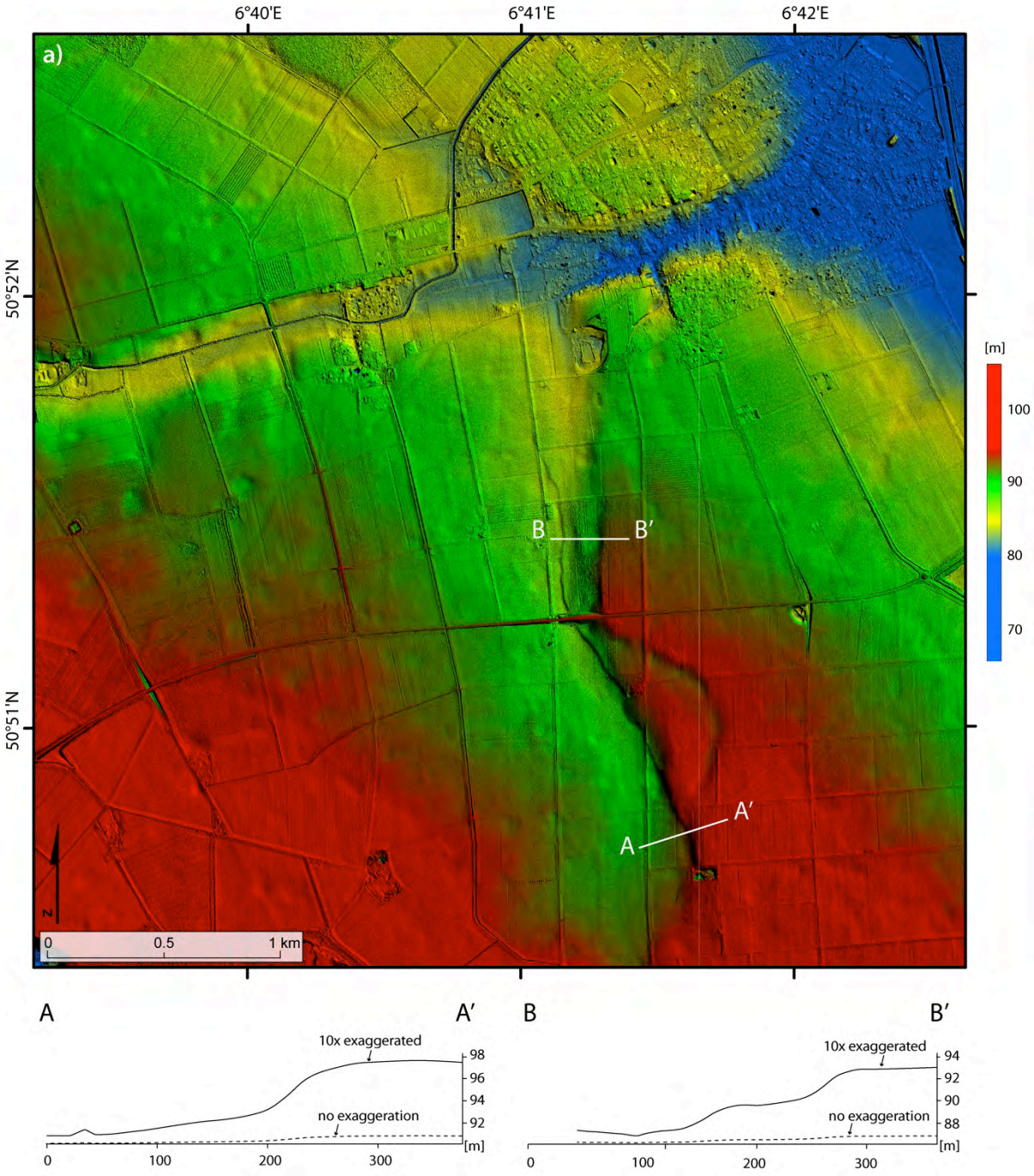


Figure 3.11: Topography of the Wissersheimer-fault area. Colored hillshade derived from LiDAR DTM, color scheme adjusted to emphasize the main topographic units; A-A': Topographic profile of the southern fault scarp segment; B-B': Topographic profile of the central fault scarp segment.

A color-coded hillshade adjusted to the topographic range of the study area, Figure 11a, clearly shows that the northern part exposes an ESE-WNW striking fluvial valley inclined to the east. The symmetric valley is 5 - 8 m deep, up to 300 m wide and incises the northern part of the Wissersheimer fault scarp.

The area is predominately covered by farmland (> 80%). Less than 5% of the area is covered by forest (Figure 3.12). The largest urban area is the city of Kerpen situated in the northern and northeastern part of the study area. Two quarries are situated in the study area, both along strike of the suspected fault scarp (Figure 3.12). However, as revealed by field inspections both quarries have recently been closed and refilled. Craters are visible predominately in the northeastern corner of the map ~ 1 km west of the city of Kerpen. Some isolated craters are also recognizable in the central and western part of the study area (Figure 3.12). The Craters are 20 - 50 m across and up to 1.5 m deep. In general, the crater density is lower compared to the Erft-fault area.

At some locations along roads as well as in the city of Kerpen, irregular 0.5 - 1 m deep depressions are reported to have formed during the last 10 to 20 years. The depressions are characterized by very subtle geomorphic expressions and are hardly recognizable even on LiDAR data. However, local farmers and citizens of the city of Kerpen confirmed the existence of such local subsidence phenomena leading to demolition of several houses and resulting in ongoing repair work along several roads. The presumable locations of reported local subsidence are indicated in Figure 3.12.

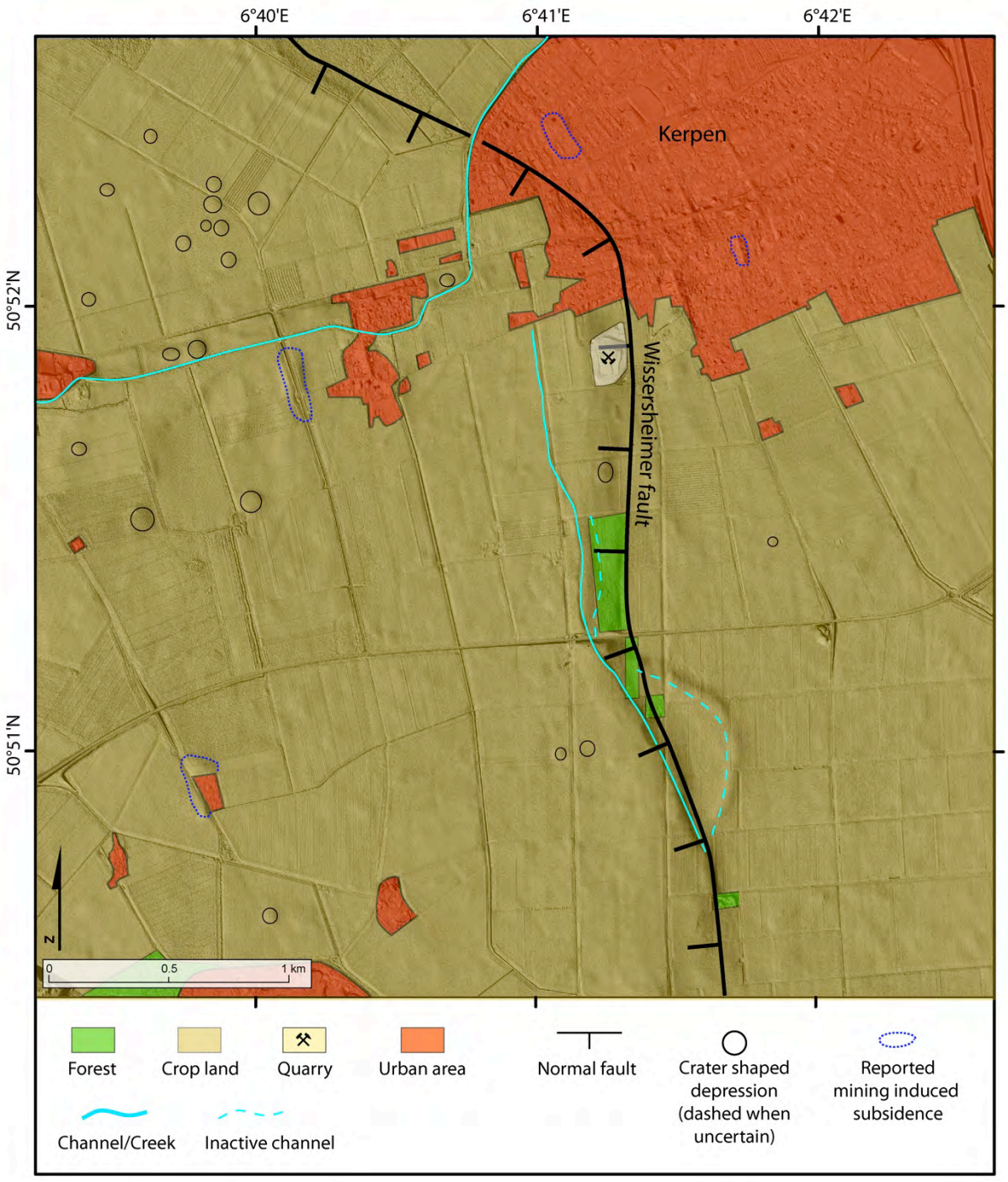


Figure 3.12: LiDAR DTM of the Wissersheimer-fault area illustrating the distribution of farmland, forest and urban areas, as well as the distribution of craters and the location of suspected faults.

## 3.8 Interpretation

In the Erft-fault area, it is difficult to distinguish between fault scarps and river terrace risers in regions of high fluvial activity. Furthermore, if large rivers flow sub-parallel to the suspected fault strike, as in this case, the topographic analysis may easily lead to ambiguous results. We therefore compared our data with the results of former studies that identified potentially active faults as well as fluvial terrace sequences in this sector (Ahorner, 1962, 1968; Hinzen, 2004, 2007; Klostermann, 1992; Quitzow, 1956; Quitzow and Vahlensieck, 1955; Strecker et al., 2002; Streich, 2003; Winter, 1970).

The NE-most scarp of the study area (Erft-scarp 1, Figure 3.7) represents the edge of the Early Pleistocene Rhine River terrace (*Jüngere Hauptterasse*) and is not associated with tectonic activity (Klostermann, 1992; Quitzow, 1956; Winter, 1970). Eastward incision of the scarp, however, most likely results from tectonically induced base-level-drop, and headward erosion along the Viersener fault, which represents the easternmost rift structure of the Lower Rhine Graben (Ahorner, 1962; Fliegel, 1922; Quitzow and Vahlensieck, 1955). Erft scarp 2 (Figure 3.7) is the surface expression of the Erft fault, one of the major boundary faults of the Lower Rhine Graben (Ahorner, 1962; Strecker et al., 2002; Streich, 2003), which offsets the Erft block to the SW against the Ville Horst to the NE. The increase of scarp height towards the NW is in accordance with the displacement of Tertiary and Quaternary strata, which also increases towards the NW along the Erft fault (Ahorner, 1962; Quitzow and Vahlensieck, 1955). According to the geological map of the area (von Kamp, 1987), as well as former tectonic studies (Ahorner, 1962; Quitzow and Vahlensieck, 1955), Erft-scarp 3 is the surface expression of the NW-SE striking Swist fault, the southernmost segment of the Erft fault system (Figure 3.8). At the study site, the fault scarp is intensively eroded and overprinted by the meandering Swist Creek, which strongly hampers the recognition of the tectonic origin of this scarp.

Crater-shaped depressions on the Ville-Horst may result from local subsidence induced by, e.g., karstification or groundwater disposal. In our study, the regular sizes and shapes of the craters suggest an anthropogenic rather than a geologic origin as formation process (Figure 3.9). Furthermore, karstification has not been observed in the sediments exposed in our study site, and groundwater disposal usually affects a larger area and does not produce circular depressions in such regular patterns as observed here. Considering the proximity of the Erft-fault area to the city of Cologne, which has been severely destroyed by aircraft bombs during World War II, surface damage exerted by warfare appears a likely

scenario to explain the cratered landscape at the study site. Crater-shaped damage of the Earth's surface due to the impacts of explosive munitions is referred to as bombturbation (Hupy and Koehler, 2012; Hupy and Schaetzl, 2008). As confirmed by orthophoto analysis carried out by the bomb disposal unit of Northrhine Westphalia (Kampfmittelräumdienst, NRW), the Ville Horst has been intensively targeted by aerial bombs during World War II in 1942. Furthermore, the crater shapes as well as the distribution pattern of craters coincide well with crater patterns observed during aerial bombing of western France during World War I (Figure 3.13a). Linear crater distribution patterns as observed e.g., along the Erft fault segment south of Hemmerich, have also been documented in Central Vietnam during the Vietnam War in the late 1960s (Figure 3.13b) indicating the flight path of warplanes. Bombturbation therefore appears to be the most likely explanation for the craters observed at the Erft fault site.

A more detailed analysis on the spatial distribution of bomb craters in this region may include the analysis of LiDAR data combined with historical orthophotos taken during the aerial bombing of World War II. Such historical data are available through the Aerial Reconnaissance Archives of the British Library. As the archive only provides unsorted images such analyses are beyond the scope of this thesis.

In the Wissersheimer-fault area the left-stepping NW-SE to N-S striking scarp is interpreted to represent the surface trace of the Wissersheimer fault. Here, the differentiation between fluvial and tectonic surface features is challenged by intensive fault-parallel fluvial erosion, which led to over-steepening of the southern scarp segment and complex scarp deviation farther north (Figure 3.11 and Figure 3.14). During high-precipitation events the fault-parallel drainage reactivates, which leads to flooding and present-day gully incision, as reported by local farmers. In the central part, the easternmost of the three scarps presumably represents the Wissersheimer-fault scarp. The westernmost and central scarps represent fluvial channels, which incise into the hanging wall of the Wissersheimer-fault scarp (Figure 3.14).

Local subsidence phenomena include sagging of roads, as well as houses and walls. They are hardly visible on the LiDAR DTM, but have been documented and drawn onto the data set according to damage reports given by local farmers and citizens of the city of Kerpen (Figure 3.12). Local subsidence rates reach values of 5 - 10 cm/yr resulting in total subsidence of up to 1 m. Since the entire region subsides at rates of up to 3.3 m during the last 40 years, a likely explanation for the small-scale sagging phenomena would therefore be mining related groundwater disposal and resulting collapse of previously water-filled cavities or water-saturated peat lenses.

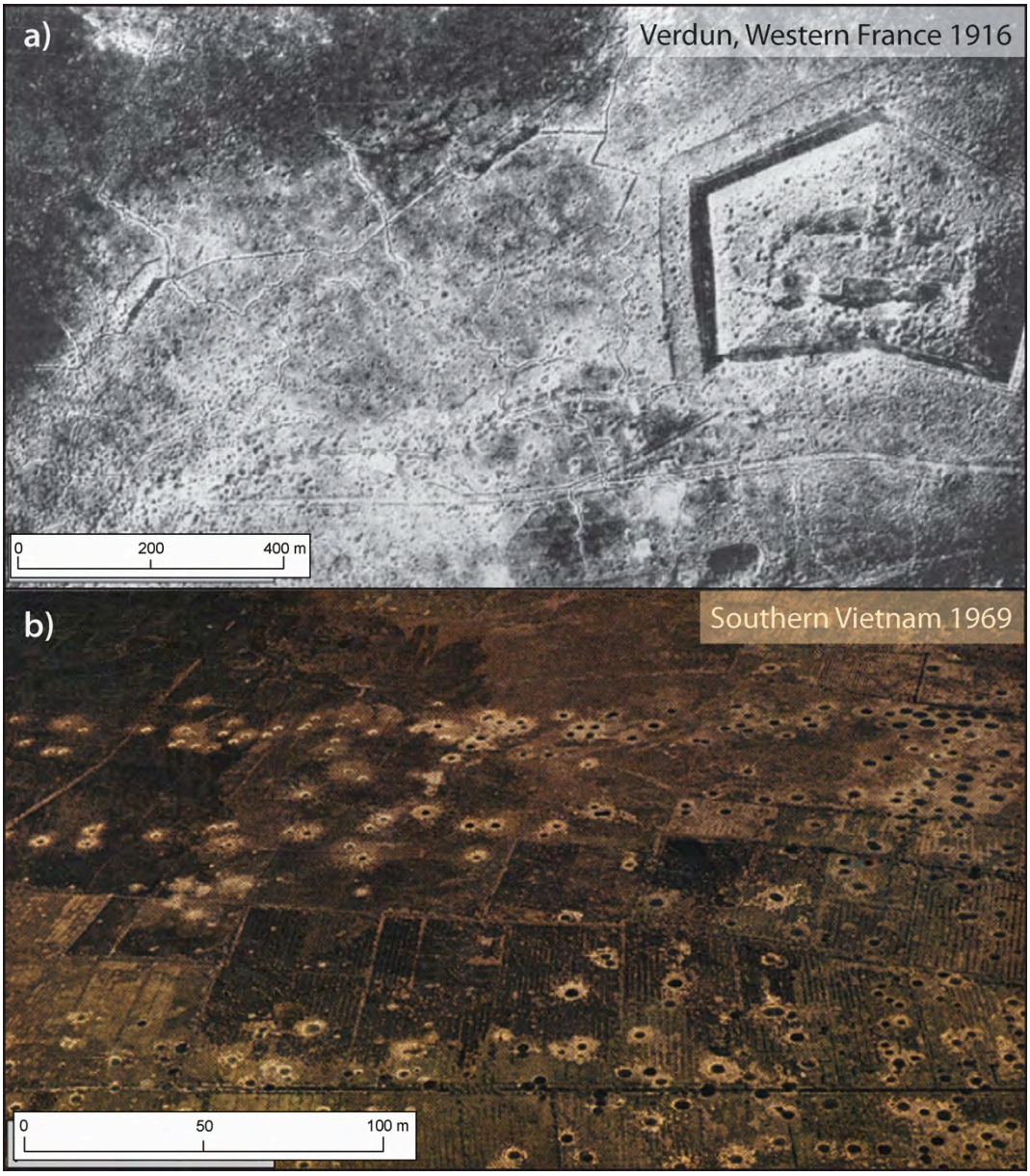


Figure 3.13: Examples of landscapes affected by aerial bombing. (a) Aerial reconnaissance image of 1916 of the Verdun, France battlefield showing dense pattern of bomb craters. Data source: International War Archive. (b) Southern Vietnamese agricultural fields targeted by aereal bombs in March 1969. The linear pattern of the craters results from the path of B52 bombers. Photo by A.H. Westing, 1972. Note the similarity of linear crater patterns compared to the ones observed at the Hemmerich site. Images modified from Hupy and Koehler, 2012.

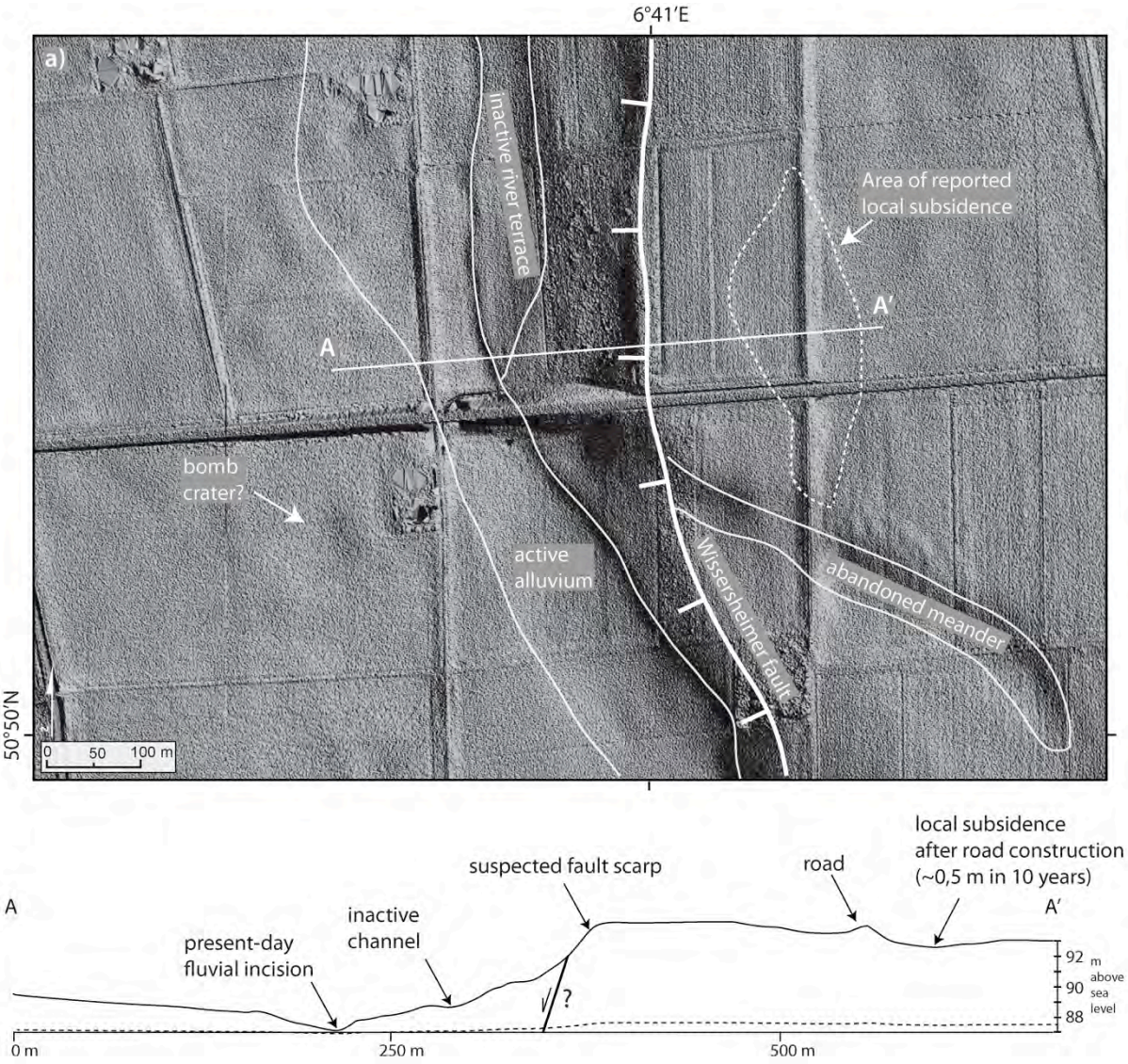


Figure 3.14: Close-up map of the Wissersheimer fault scarp. Mapping of the DTM shows the complex interaction of possible tectonic displacement with fluvial activity and mining induced local subsidence. Topographic profile (A-A', exaggeration factor 10, the dashed line shows the topographiy profile without exaggeration) reveals the multi-level morphology of the scarp. Figure extent is indicated in Figure 6.

## 3.9 Discussion

### 3.9.1 Suitability of the Study Areas for Trench Analysis

Both study areas are characterized by severe surface modifications caused by fluvial activity or anthropogenic overprint. In the following we aim to evaluate, to what degree the study sites are viable and permissible for future trench excavation in light of the information on non-seismic overprint at both sites.

In the Erft-fault area, the fault scarp is nicely exposed and can be traced along a narrow zone, approximately 30 - 100 m wide along strike over the entire study area. The abundance of bomb craters, however, covering both the hanging wall and the fault trace makes it difficult to select a site not affected by bombturbation. As the craters have presumably obliterated any earthquake-related damage, and the potential hazard related to excavation in the vicinity of potentially unexploded bombs is rather high the analyzed part of the Erft fault is not a viable trench site. In addition, none of the landowners of the sites traversed by the Erft-fault scarp granted permission for trench excavations.

At the Wissersheimer-fault area, fault-parallel fluvial incision has severely modified the southern fault segment. Farther north, the fluvial scarps can be more easily differentiated from the fault scarp, which would allow trench site selection at this location. However, mining-induced subsidence phenomena affect almost the entire region (up to 3.3 m over the last 40 years) and have caused local sagging on a meter-scale. It is therefore difficult to decide whether potential fault-slip observed in a trench across this fault segment can unambiguously be assigned to coseismic rupture. Thus, trenching at this fault is not recommendable unless future research will provide further diagnostic criteria that enable a clear differentiation between mining induced fault creep and coseismic rupture.

### 3.9.2 Bombturbation - A Disqualification Factor for Trenching?

LiDAR analysis of both study sites reveal that bombturbation is a major process leading to surface deformation and near-surface sediment disturbance. In particular at the Erft-fault, aerial bombing produced a dense crater pattern presumably also along the suspected fault scarp. Present-day craters are up to 2 m deep and up to 50 m in diameter. According to recent studies (Hupy and Koehler, 2012; Hupy and Schaetzl, 2008) and historical documentation (Great-Britain-War-Office, 1952), aerial bombs may penetrate and damage the uppermost 0.5

- 5 m of the surface, depending on the bomb weight (Table 3.2). Initial crater width may be as large as 15 m. The larger crater diameters (> 50 m) observed at the study site presumably result from degradation of the crater rims during the last decades, due to farming and fluvial processes.

To decipher a meaningful coseismic deformation history of the fault segment exposed at the Erft-fault area, it would be necessary to differentiate between sediment deformation derived from coseismic activity, from that resulting from bombturbation. Below the presumed penetration depth of aerial bombs, it may be possible to reach levels unaffected by bombturbation, however there exist no study yet on how sediment at deeper levels is deformed by the effect of an exploding bomb. Keeping in mind present-day examples of controlled remote detonations of previously unexploded bombs in urban construction pits (e.g., Munich Schwabing, 2012), one may easily imagine that such detonation processes may affect sediments several meters below the penetration depth of a bomb (Figure 3.15). Therefore, an overlap of fault-derived and bombturbation-derived sediment disturbance is likely at a fault site targeted by aerial bombing. To avoid ambiguity in interpreting trenching results, such sites should thus, if possible, be precluded for trench excavation purposes. Additionally, the hazard of potentially unexploded bombs at such sites requires careful preplanning including geophysical prospecting surveys by the local bomb disposal units (Kampfmittelräumdienst) - a factor that needs to be considered in general for excavation studies in regions that have been war zones in the past.

Nevertheless, considering results of this study as well as recent geomorphological studies carried out in Western France and Central Vietnam (Hupy and Koehler, 2012; Hupy and Schaetzl, 2008) bombturbation appears to be a significant geomorphologic process responsible for severe surface modification and thus, may open up a promising new field of research.

Table 3.2: Relation of bomb weight with initial crater dimensions. Increasing bomb weight implies increasing mass of explosive matter. Data from Great-Britain War Office, 1952, converted from feet to meters.

| Bomb Weight | Initial Crater Diameter | Initial Crater Depth |
|---|---|---|
| 50 kg | 2.5 - 4 m | 0.5 - 1.5 m |
| 100 kg | 6 - 10 m | 2 - 3 m |
| 250 kg | 7 - 12 m | 3 - 4 m |
| 500 kg | 10 -15 m | 3.5 - 5 m |

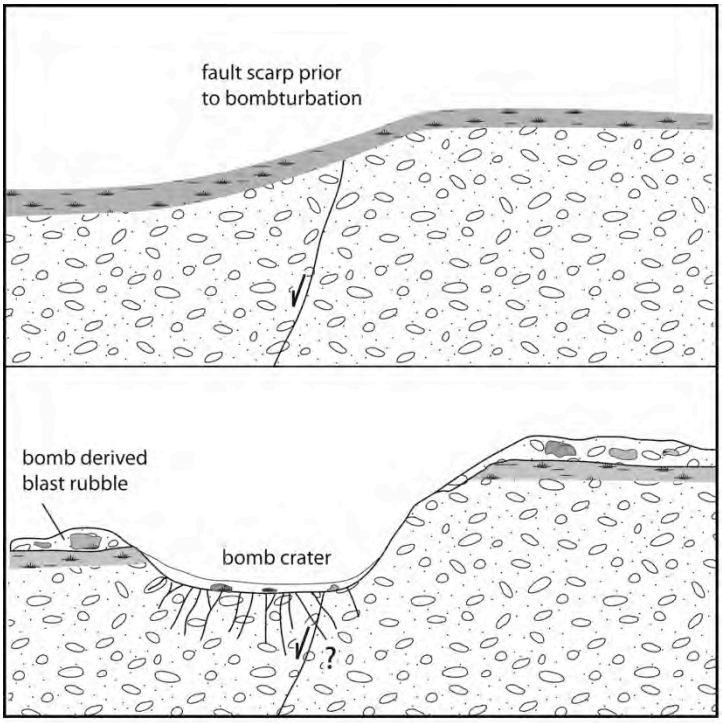


Figure 3.15: Potential fault scarp modification produced by bombturbative process. (a) Fault scarp in unconsolidated gravel deposits; present-day soil horizon indicated in grey. (b) Bombturbation producing a crater-shaped depression and sediment disturbance partly overlapping with fault deformation. Crater depth and width depends on the size and weight of the explosive munitions as well as soil properties and groundwater depth. Crater morphology modified from Hupy and Koehler, 2012. The sketch is not drawn to scale.

### 3.9.3 LiDAR Analysis in Paleoseismology

Results of this study reveal information on the local relief as well as land use and anthropogenic and fluvial surface processes in great detail. Due to the subtle expression of the geomorphic features, other techniques such as field mapping, or the analysis of satellite images and orthophotos, respectively, would not have provided comparable results. The inclusion of LiDAR analysis may therefore be considered as a promising tool for successful trench-site reconnaissance. However, in many cases trench-site selection purely based on LiDAR analysis would not be appropriate as this technique does not provide information on the lithology, sedimentology and stratigraphy of a given site and thus, should always be supplemented with surface field mapping, drilling and/or shallow geophysical surveys. Nevertheless, a combination of orthophoto and LiDAR analysis is recommended for the first evaluation of the suitability of a study site for trench excavation.

## 3.10 Conclusions

We have carried out analysis of airborne LiDAR data at two study sites located in the Central Lower Rhine Graben to evaluate their suitability for future trenching studies. Both sites have previously been proposed as potential trench sites using traditional mapping approaches as well as shallow geophysics and drilling (Strecker et al., 2002; Streich, 2003).

Results of our LiDAR analysis illustrate that the fault scarps at both sites underwent severe non-seismic surface modification due to fluvial erosion, mining induced sagging as well as bombturbation. Results of trenching studies at both sites would therefore most probably provide ambiguous results as a clear differentiation between coseismic rupture and non-seismic sediment disturbance would be challenging and presumably not possible. In addition, none of the landowners at the Erft-fault site granted permission to excavate trenches on their properties. In Chapter 4 and 5 of this thesis we present results on a trench study carried out along the Schafberg fault in the SW part of the Lower Rhine Graben, in an area unaffected by groundwater disposal and aerial bombing.

The abundance of bomb craters along the Erft fault also raises the question of how high the potential hazard related to unexploded munitions at such sites would be, and if researchers should expose themselves to such hazards. In any case, sites known to contain explosive munitions or to be situated in regions exposed to past warfare should be thoroughly inspected by local bomb disposal units before starting excavation studies. For this purpose, we have shown in this study that LiDAR analysis provides crucial information on the severeness of bombturbation possibly affecting a region.

Results of this study imply that the field of research dealing with the significance of bombturbation on the geomorphology of a region is a promising new field that should be investigated in more detail in the future. Additional research that would also be of significance for paleoseismology could include studies on sediment deformation related to exploded bombs, and how such deformation could be differentiated from earthquake-related deformation. The same concern accounts for study areas subject to mining related subsidence phenomena. If future studies could define diagnostic features for both aseismic and coseismic fault displacement, the evaluation of the seismogenic potential of faults would be much easier.

## 3.11 References

Ahorner, L., 1962, Untersuchungen zur Quartären Bruchtektonik der Niederrheinischen Bucht: Eiszeitalter und Gegenwart, Quaternary Science Journal, v. 13, no. 1, p. 24-105.

-, 1968, Erdbeben und jüngste Tektonik im Braunkohlenrevier der Niederrheinischen Bucht: Zeitschrift der Deutschen Geologischen Gesellschaft v. 118, p. 150-160.

Arrowsmith, J. R., and Zielke, O., 2009, Tectonic geomorphology of the San Andreas Fault zone from high resolution topography: An example from the Cholame segment: Geomorphology, v. 113, no. 1–2, p. 70-81.

Baran, R., Guest, B., and Friedrich, A. M., 2010, High-resolution spatial rupture pattern of a multiphase flower structure, Rex Hills, Nevada: New insights on scarp evolution in complex topography based on 3-D laser scanning Geological Society of America Bulletin, v. 122, p. 897-914.

Bischoff, M., Cete, A., Fritschen, R., and Meier, T., 2010, Coal Mining Induced Seismicity in the Ruhr Area, Germany: Pure and Applied Geophysics, v. 167, no. 1, p. 63-75.

Blank, R., 2012, The Battle of the Ruhr, 1943: Aerial Warfare against an Industrial Region: Labour history review, v. 77, no. 1, p. 35-48.

Bork, H. R., and Lang, A., 2003, Quantification of past soil erosion and land use/land cover changes in Germany: Lecture Notes in Earth Sciences, v. 101, p. 231-239.

Camelbeeck, T., Martin, H., Vanneste, K., Verbeeck, K., and M., M., 2001, Morphometric analysis of active normal faulting in slow-deformation areas : examples in the Lower Rhine Embayment: Geologie en Mijnbouw, v. 80, no. 3-4, p. 95-107.

Crone, A. J., Machette, M. N., and Bowman, J. R., 1997, Episodic nature of earthquake activity in stable continental regions revealed by palaeoseismicity studies of Australian and North American quaternary faults: Australian Journal of Earth Sciences, v. 44, no. 2, p. 203-214.

Fliegel, G., 1922, Der Untergrund der Niederrheinischen Bucht: Abh. preuß. geol. L.-A., v. 92, p. 1-155.

Friedrich, A. M., Strecker, M. R., and Scherbaum, F., 2002, Active intraplate deformation in central Europe: paleoseismology of the Lower Rhine Embayment: DFG New Grant Application, p. 1-42.

Geluk, M. C., Duin, E. J., Dusar, M., Rijkers, R., van den Berg, M. W., and van Rooijen, P., 1994, Stratigraphy and tectonics of the Roer Valley Graben: Geologij en Mijnbouw, v. 73, no. 2-4, p. 129-141.

Görres, B., 2008a, Recent Site Motions in the Lower Rhine Embayment and the Eifel from 15 years of GPS data: Abstract Swiss Geoscience Meeting, Lugano, p. 1.

Görres, B., H. Kuhlmann, 2008b, How groundwater withdrawal and recent tectonics cause damages of the earth's surface: Monitoring of 3D site motions by GPS and terrestrial measurements: Journal of Applied Geodesy, no. 1(2007), p. 223-232.

Görres, B., Sager, B., and Campbell, J., 2006, Geodätische Bestimmung von Bodenbewegungen im Bereich des Erftsprungsystems: Zeitschrift für Vermessungswesen, p. 16-24.

Great-Britain-War-Office, G. S., 1952, Bomb Reconnaissance and Protection against Unexploded Bombs: Field Engineering and Mine Warfare Pamphlet, v. 9, p. 1-15.

Gregory, D., 2011, "Doors into Nowhere": Dead Cities and the Natural History of Destruction Cultural Memories, *in* Meusburger, P., Heffernan, M., and Wunder, E., eds., Cultural Memories Knowledge and Space, Volume 4, Springer Netherlands, p. 249-283.

Guest, B., Niemi, N. A., and Wernicke, B., 2007, Stateline fault system: A new component of the Miocene-Quaternary Eastern California shear zone: Geological Society of America Bulletin, v. 119, no. 11-12, p. 1337-1247.

Hinzen, K. G., B. Weber, F. Scherbaum, 2004, On the Resolution of H/V Measurements to Determine Sediment Thickness: a Case Study Across a Normal Fault in the Lower Rhine Embayment, Germany Journal of Earthquake Engineering, v. 8, no. 6, p. 909-926.

Hinzen, K. G., S. K. Reamer 2007, Seismicity, seismotectonics, and seismic hazard in the northern Rhine area. In: Stein, S. and Mazotti, S., ed., Continental Intraplate Earthquakes: Science, Hazard, and Policy Issues: Geological Society of America Special Paper, v. 425, p. 225-242.

Hupy, J. P., and Koehler, T., 2012, Modern Warfare as a Significant Form of Zoogeomorphic Disturbance Upon the Landscape: Geomorphology, v. 157-158, p. 169-182.

Hupy, J. P., and Schaetzl, R. J., 2008, Soil Development on the WWI Battlefield of Verdun, France: Geoderma, v. 145, no. 1-2, p. 37-49.

Klostermann, J., 1992, Das Quartär der Niederrheinischen Bucht: Ablagerungen der letzten Eiszeit am Niederrhein. : Geological Survey of Northrhine-Westphalia, Krefeld, p. 1-200.

Kümpel, H. J., Lehmann, K., Fabian, M., and Mentes, G., 2001, Point stability at shallow depths: experience from tilt measurements in the Lower Rhine Embayment, Germany, and implications for high-resolution GPS and gravity recordings: Geophysical Journal International, v. 146, p. 699-713.

Kupetz, M., 2003, Der Muskauer Faltenbogen - Das Abbild tiefreichender glazialtektonischer Großstrukturen im hochauflösenden digitalen Geländemodell am Beispiel des Muskauer Faltenbogens: Berichte von der 23. Wissenschaftlich-Technischen Jahrestagung der DGPF vom 9. bis 11. September 2003 in Bochum, p. 9-10.

LÖGD-Report, 2010, Gesundheitliche und soziale Situation der Bevölkerung im Ruhrgebiet, p. 1-12.

McCalpin, J. P., 2011, Mapping and Measuring Holocene Fault Scarps in Dense Forests with LiDAR: In:Grützner, C., Fernández Steeger, T., Papanikolaou, I., Reicherter, K.,Silva, P.G., Pérez-López, R., Vött, A. (eds.): Proceedings 2nd INQUA-IGCP7International Workshop on Active Tectonics, Earthquake Geology,Archaeology and Engineering 19-24 September 2011, Corinth (Greece), ISBN:978-960-466-093-3, 111-113.

McCalpin, J. P., and Nishenko, S. P., 1996, Holocene palaeoseismicity, temporal clustering, and probabilities of future large (M>7) earthquakes on the Wasatch fault zone, Utah: Journal of Geophysical Research v. 101, no. B2, p. 6233-6253.

Meghraoui, M., Camelbeeck, T., Vanneste, K., M., B., and Jongmans, D., 2000, Active faulting and paleoseismology along the Bree fault, lower Rhine graben, Belgium: Journal of Geophysical Research v. 105, no. B6, p. 13809-13841.

Meyer, H., Hetzel, R., and Strauss, H., 2008, Erosion rates on different time scales derived from cosmogenic 10Be and river loads: implications for landscape evolution in the Rhenish Massif, Germany: International Journal of Earth Science, v. 99, no. 2, p. 395-412.

Quitzow, H. W., 1956, Die Terrassengliederung im niederrheinischen Tieflande: Geologie en Mijnbouw, v. 18, p. 357-373.

Quitzow, H. W., and Vahlensieck, O., 1955, Ober Pleistozäne Gebirgsbildung und rezente Krustenbewegungen in der Niederrheinischen Bucht: Int. J. Earth Sci., p. 56-67.

Salisbury, J. B., Rockwell, T. K., Middleton, T. J., and Hudnut, K. W., 2012, LiDAR and Field Observations of Slip Distribution for the Most Recent Surface Ruptures along the Central San Jacinto Fault: Bulletin of the Seismological Society of America, v. 102, no. 2, p. 598-619.

Schaefer, W., 1999, Bodenbewegungen und Bergschadensregulierung im Rheinischen Braunkohlerevier/Surface movement and mining damage adjustment in the Rhenish ignite mining area: Proceedings of the 42. DMV Meeting, Cottbus, September 1999, p. 1-10.

Schwartz, D. P., and Coppersmith, K. L., 1984, Fault behavior and characteristic earthquakes: examples from the Wasatch and the San Andreas faults: Journal of Geophysical Reasearch, v. 89, p. 5681-5698.

Sieh, K., 1978, Prehistoric Earthquakes Produced by Slip on the San Andreas Fault at Pallet Creek, California: Journal of Geophysical Reasearch, v. 83, no. B8, p. 3907-3939.

Sieh, K., Stuiver, M., and Brillinger, D., 1989, A More Precise Chronology of Earthquakes Produced by the San Andreas Fault in Southern California: J. Geophys. Res., v. 94, no. B1, p. 603-623.

Spreckels, V., 2000, Monitoring of Coal Mining Subsidence by HRSC-A Data: Proceedings of IAPRS, Amsterdam, v. 33, p. 13-15.

Strecker, M. R., Streich, R., Lück, E., Scherbaum, F., and Schäbitz, F., 2002, S.A.F.E. annual report. Holocene fault ruptures along the Erft Fault, Southern Lower Rhine Embayment?: unpublished data, Potsdam University, p. 1-66.

Streich, R., 2003, Geophysical Prospecting of Suspected Holocene Fault Activity in the Lower Rhine Embayment, Germany: Diploma Thesis, University of Potsdam, Germany, p. 1-125.

Strohmeier, K. P., Schultz, A., Bardehle, D., Annluss, R., and Lenz, A., 2007, Health indicator-based cluster analysis of districts and urban districts in north rhine-westphalia: Das Gesundheitswesen, v. 69, no. 1, p. 26-33.

van den Berg, M. W., 1994, Neotectonics of the Roer Valley rift system: Style and rate of crustal deformation inferred from syn-tectonic sedimentation: Geologij en Mijnbouw, v. 73, no. 2-4, p. 143-156.

Vanneste, K., and Verbeeck, K., 2001a, Detailed paleoseismic investigation of the Rurrand Fault in Hambach trench, Germany: Cahiers du Centre Européen de Géodynamique et de Séismologie v. 18, p. 153-156.

-, 2001b, Paleoseismological analysis of the Rurrand fault near Jülich, Roer Valley graben, Germany: Coseismic or aseismic faulting history?: Geologie en Mijnbouw, v. 80, no. 3-4, p. 155-169.

von Kamp, H., 1986, Geologische Karte von Nordrhein-Westfalen 1:100 000, Blatt C5106 Köln: Geological Survey of Northrhine-Westphalia, Krefeld, p. 1.

-, 1987, Geologische Karte von Nordrhein-Westfalen 1:100 000, Blatt C5506 Bonn: Geological Survey of Northrhine-Westphalia, Krefeld, p. 1.

Wallace, R. E., 1977, Profiles and ages of young fault scarps, north-central Nevada: Geological Society of America Bulletin, v. 88, p. 1267-1281.

Wallace, R. E., 1986, Active tectonics – studies in geophysics: National Academic Press, Washington, D. C., p. 266 pp.

Wegmuller, U., Strozzi, T., Werner, C., Wiesmann, A., Benecke, N., and Spreckels, V., 2000, Monitoring of mining-induced surface deformation in the Ruhrgebiet (Germany) with SAR interferometry Geoscience and Remote Sensing Symposium, 2000. Proceedings. IGARSS 2000. IEEE 2000 International, v. 6, p. 2771-2773.

Winter, K. P., 1970, Untere Mittelterrasse und Krefelder Mittelterrasse im Südteil der Niederrheinischen Bucht: Eiszeitalter und Gegenwart, Quaternary Science Journal, v. 21, p. 161-172.

# Chapter 4

## *Historical Coseismic Surface Rupture Identified in Intraplate Europe*

## 4.1 Abstract

An essential question for seismic hazard assessment in densely populated central Europe is whether the Quaternary faults of the Central European Rift are associated with ground-rupturing earthquakes, or instead with slow aseismic creep. In the framework of a paleoseismic study carried out in the epicentral area of Germany's largest historical earthquake ($M_L$ 6.2, 1756 AD) we have identified evidence of ground rupturing associated with historic coseismic activity in the Lower Rhine Graben. We developed a new fractured-clast approach that lead to identifying the first unambiguous evidence of coseismic surface rupture in this part of Europe on centennial timescales. Our observations further document repeated Holocene coseismic rupture along a normal fault that resulted in a cumulative offset of 1.0 ± 0.2 m. The possibility of such earthquakes in the future thus needs to be considered along the entire rift system.

## 4.2 Introduction

The poorly understood patterns of destructive earthquakes in intraplate regions pose an important challenge for earthquake hazard assessment and mitigation (Bilham, 2009; England and Jackson, 2011; Stein and Liu, 2009). Destructive intraplate earthquakes occur in virtually all continental interiors and mid-continental rifts and demonstrate that these regions may be subject to damaging earthquakes despite their great distance to plate boundaries (Bilham, 2009; England and Jackson, 2011; Gupta et al., 2001; Stein and Liu, 2009). Controversy centers on whether rift-bounding faults with known Quaternary offset may generate earthquakes large enough to cause surface rupturing or accommodate surface deformation by aseismic creep (Cattin et al., 2005; Sylvester, 2001), two end-member scenarios that are crucial for seismic risk and mitigation measures (Ahorner, 2001; Camelbeeck, 2007; Grünthal, 2006; Houtgast, 2005). Intraplate geological settings of great concern are densely populated continental rifts like the Central European Rift (Figure 1a). Instrumental Seismicity data (since about 1900 AD) record relatively frequent low (M<5) magnitude events and historic and paleoseismic data reveal rarer larger events in this region (Hinzen, 2007). Although the locations of neotectonic faults in this rift system are well known, the recurrence rate, size, and possible surface ruptures of past earthquakes on these faults has remained enigmatic due to degradation or burial of seismogenic features. Particularly, solifluction (flow of saturated soil) processes degraded fault scarps during Pleistocene periglacial climatic conditions, while anthropogenic influence has either obliterated or altered tectonic landforms. In the Lower Rhine Graben, the NW sector of the Central European Rift (Figure 4.1a), assessment of paleoseismic activity is further complicated by land subsidence related to mining and associated creep of some extensional faults (Görres, 2008; Kümpel et al., 2001). Here, fault displacement rates derived from leveling campaigns as well as GPS and tiltmeter measurements are on the order of 1 mm/yr to up to 10 mm/yr for some segments in the vicinity of large open pit mines (Ahorner, 1968, 1975; Schaefer, 1999). This discrepancy led to an ongoing debate concerning the dominant slip mode of faults in this region (Ahorner, 1968; Camelbeeck, 2007; Camelbeeck and Meghraoui, 1996, 1998; Houtgast, 2005, 2003; Lehmann et al., 2001; Vanneste and Verbeeck, 2001). First paleoseismic studies carried out on suspected fault segments in the Lower Rhine Graben (Camelbeeck and Meghraoui, 1996, 1998; Vanneste et al., 1999; Vanneste et al., 2001) reported repeated Late Pleistocene and possibly Holocene coseismic activity along the Bree fault. However, later studies challenged the observations by pointing out the possible ambiguity in correctly assessing inferred past

ground ruptures in this region (Houtgast, 2005, 2003; Lehmann et al., 2001). Thus, the determination of diagnostic features that unambiguously identify coseismic rupture in the sedimentary record would be an important step forward in paleoseismic research in the Lower Rhine Graben as well as other low-strain intraplate regions.

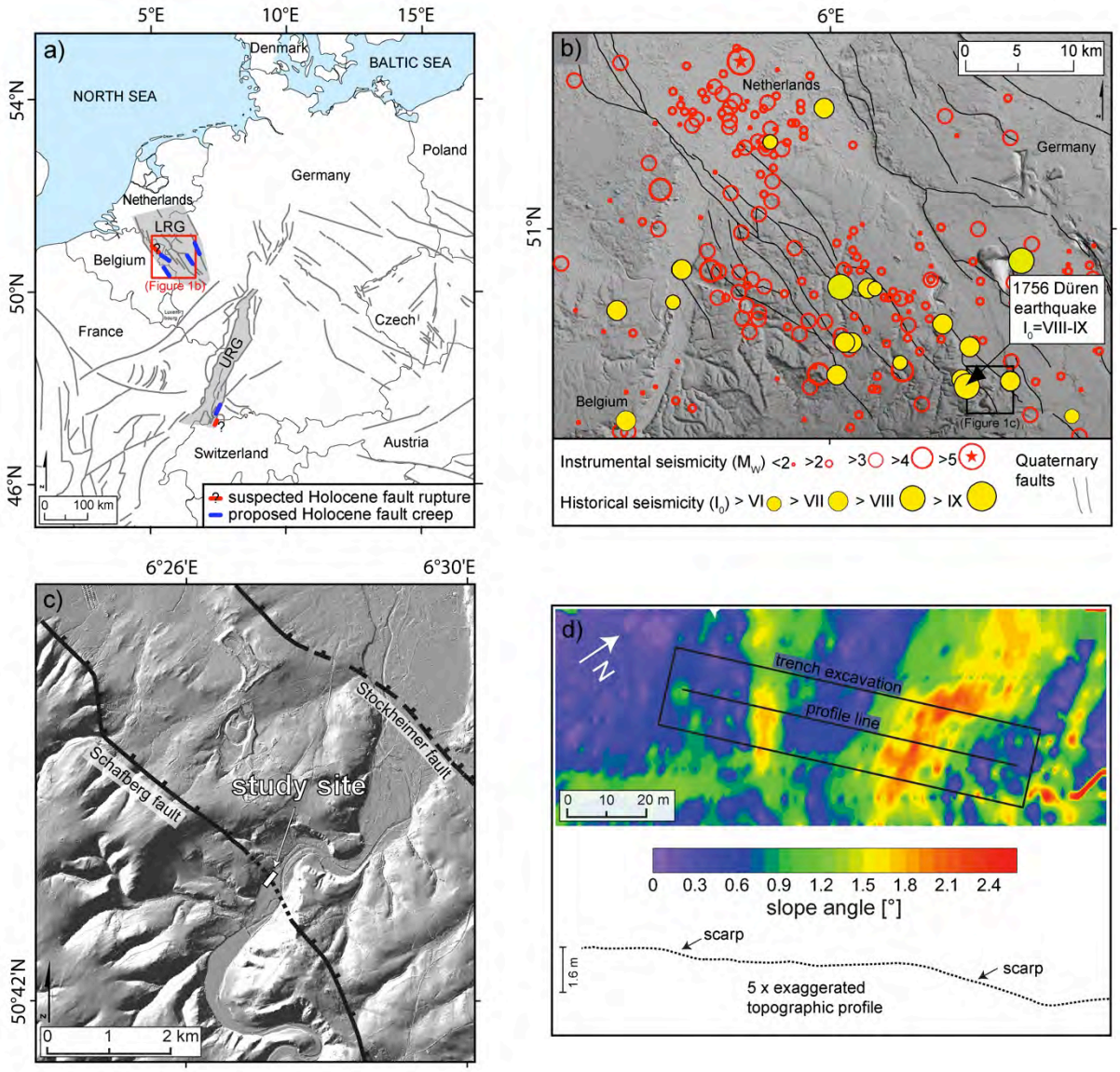


Figure 4.1: Seismotectonics of Central Europe and the Lower Rhine Graben and overview of the trench site. (a) Proposed slip behavior of central European faults. Blue lines depict areas where Holocene fault creep has been proposed (Demoulin, 2004, 1998; Houtgast, 2005, 2003); red lines depict areas where Holocene coseismic rupture has been suspected (Meghraoui, 2001; Vanneste, 2001b). LRG: Lower Rhine Graben; URG: Upper Rhine Graben; (b) Seismotectonic framework of the Lower Rhine Graben, covering area marked as a red box in (a). Red circles denote epicenters of instrumentally recorded earthquakes from 1973 to 2010. Yellow solid circles denote epicenter of historical events inferred from intensity data (Leydecker, 2004). Location of the trench site is indicated by the white rectangle; (c) Digital elevation model of the Schafberg fault (data source: DGM5, geodetic survey, North Rhine Westphalia); (d) Slope map of the study site, high slow angles shown in red, low slope angles shown in purple, covering area marked as a white box in (c); a Topographic profile of the excavation site is shown below.

Here, we explore the issue of slow, protracted aseismic fault motion vs. seismogenic ground rupture using a new fractured-clast approach in a paleoseismic study carried out in the SW sector of the Lower Rhine Graben (Figure 4.1b). We demonstrate that in a suspected fault zone fractured clasts exposed in near-surface gravels can be used as unambiguous feature for detecting coseismic rupture.

Our study across a Holocene fault scarp near the city of Düren in the inferred epicentral region of Germany's largest historical earthquake (1756 AD, Figure 4.1b) reveals morphologic, stratigraphic, and deformational evidence of repeated dynamic surface faulting during the last 6000 – 10.000 years. Our new approach clearly supports the notion of seismogenic surface rupture, rather than slow, aseismic creep along long-lived extensional faults in Central Europe. Historical seismic intensities of VIII-IX (Meidow, 1994), yield an estimated local magnitude of $M_L$ 6.2 ± 0.2 for the Düren earthquake. Documented damage included collapsed houses and castles, and the triggering of a landslide (Meidow, 1994). Surface rupture related to this earthquake has not been reported. Although events of such magnitude can be associated with surface rupture in other regions (Bonilla, 1988; McCalpin, 2009), the available historic documents do not provide adequate information to assess whether this occurred in Central Europe.

## 4.3 Results

The trench site analyzed in this study is located in the village of Untermaubach, at a small right-step in the prolongation of the NW-SE striking, 16-km long E-dipping, extensional Schafberg fault. We identified two gentle 0.5 to 1 m high scarps in late Holocene deposits in the continuation of the fault where it crosses the Rur River valley (Figure 4.1c,d). The trench reveals a thin (5-6 m) cover of unconsolidated fluvial deposits overlying Devonian sedimentary rocks (Figure 4.2a). The water table at the trench site is situated at 1.5 m below the surface and thus, was lowered during trench excavation and analysis. Due to groundwater fluctuation the sediments are coated with patinas consisting of Fe and Mn-Oxides. The patinas are visible as red and black horizons in the sediment exposure (Figure2a). The lowermost unit A comprises ~ 1.5-m clast-supported Holocene coarse gravel with predominately prolate clasts up to 60 cm in diameter in a silt- and clay-rich matrix. The top of this layer contains a reworked paleosoil with organic-rich clay lenses (Unit A', Figure 4.2b). Two plant remains from this horizon provide ages of 6545 ± 97 and 6708 ± 80 years BP, respectively. The superseding unit B is a 1-2.5 m thick clast and matrix-supported coarse gravel layer. Radiocarbon ages of this unit range from 1205 ± 155 to 394 ± 84 years BP. Unit B is in turn overlain by a matrix-supported clayey and sandy to fine gravel layer (unit C). The trench also exposes two asymmetric channels, which coincide with the position of the observed surface scarps (Figure 4.2b). The channel fill comprises sandy silt and clay-rich layers (unit D). At the base of both channels, a layer of organic matter provides highly diachronous radiocarbon ages, with the youngest sample dated at 700 ± 30 years BP.

We observed various deformation phenomena in the gravels. The most striking features are fractured and offset clasts of various sizes. The conglomeratic gravel consists of Triassic sandstone, as well as Devonian limestone and quartzite, with grain sizes ranging from < 1 cm to 60 cm. Clasts were locally fractured and rotated independent of size, lithology, and original layering. The deformation of the gravels is most prominent within an approximately 10-m-wide zone below the eastern scarp. This sector consists of shear zones with fractured, offset and rotated pebbles that traverse the entire gravel units A and B. Rose plots of the clast long-axis orientations illustrate that the majority of clasts are inclined between 70° and 90° from horizontal (Figure 4.2c).

Figure 2

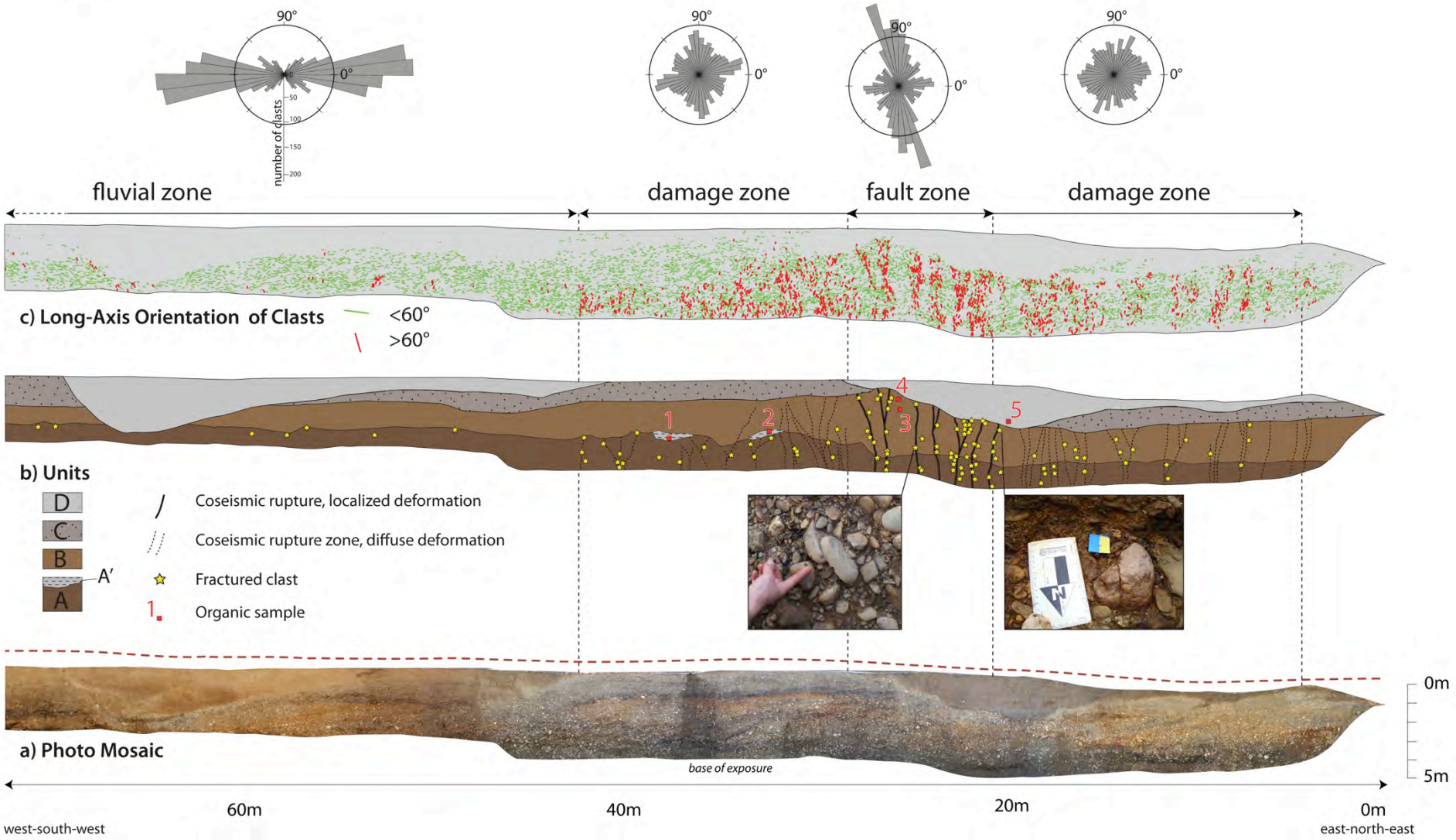
90°
0°
number of clasts
0
50
100
150
200
fluvial zone
damage zone
fault zone
damage zone
c) Long-Axis Orientation of Clasts
<60°
>60°
b) Units
D
C
B
A
A'
Coseismic rupture, localized deformation
Coseismic rupture zone, diffuse deformation
Fractured clast
Organic sample
1
2
3
4
5
a) Photo Mosaic
base of exposure
0m
5m
60m
40m
20m
0m
west-south-west
east-north-east

Figure 4.2: Results of trench analysis. a) Photo mosaic of the trench wall. b) Trench log of the main units and deformation features. Yellow stars depict locations of fractured clasts; red boxes denote positions of organic samples. c) Long-axis inclination angles of clasts. Green lines indicate inclination angles of 0-60°; red lines indicate inclination angles of 61-90°. Rose diagrams above c) show the distribution of the long- axis orientation of clasts at different locations.

The maximum vertical displacement across this zone ("fault core", Figure 4.2c) is 1.0 ± 0.2 m, based on three offset marker horizons, which correspond to the surface scarp, the contact of unit A and unit B, and units B and C, respectively (Figure 4.2a). Gravel deformation west of the fault core only affects unit A (Figure 4.2b,c). Gravel deposits in the proximity of the western scarp only contain few isolated fractured and rotated clasts (Figure 4.2b,c). A contour stereonet plot of the fracture planes of 237 pebbles (Figure 4.3) illustrates that the majority of fracture planes dip to the northeast and thus, match the orientation of the Schafberg fault plane.

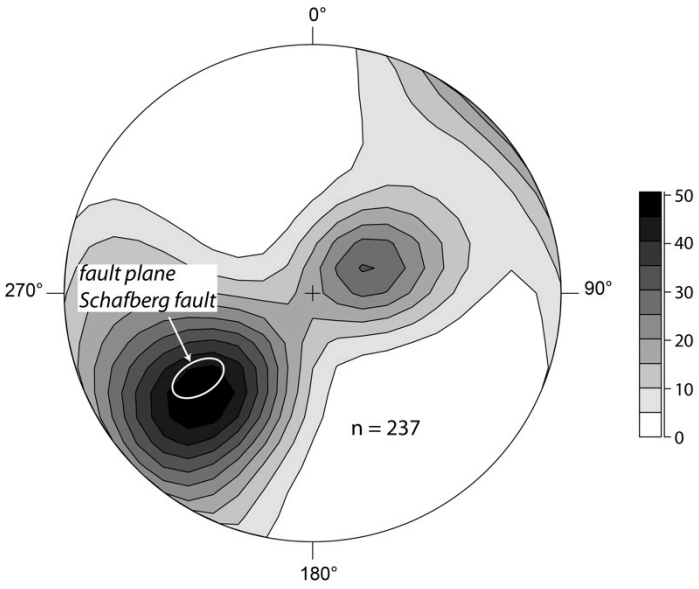


Figure 4.3: Contour stereographic plot of the fracture planes of 237 broken pebbles. The white ellipse depicts the approximate orientation of the Schafberg fault in prolongation of the trench site. The diagram is drawn in lower hemisphere, equal area projection.

In contrast to the tectonically overprinted gravel unit, the channel deposits of Unit D do not expose any deformation. The eastern channel clearly truncates the gravel units B and C and forms an erosional contact. The contact between unit C and B, or B and D, respectively, marks the most recent event horizon (Figure 4.2b). Plant remains taken from deformed deposits in unit B yield radiocarbon ages ranging from 1205 ± 155 to 394 ± 84 years BP (Figure 4.4, Table 4.1). West of the fault core deformation only affects Unit A (Figure 4.2b,

c). We thus interpret Unit A', as an older, less conspicuous event horizon dated at 6545 ± 97 and 6708 ± 80 years BP (Figure 4.4, Table 4.1).

Table 4.1: Radiocarbon ages of samples. The precise sample locations are shown in the trench log Figure 2b. Samples 1, 2 and 4 were prepared and analyzed by Leibniz-Laboratory for Radiometric Dating and Isotope Research, Max-Eyth-Str. 11-13, 24118 Kiel, Germany; samples 3 and 5 were prepared and analyzed by Gliwice Radiocarbon Laboratory, Krzywoustego 2, 44-100 Gliwice, Poland.

| Sample No.[a] | Lab No.[b] | Conventional 14C, Years B.P. | Calibrated Age (cal years B.P.) 2σ | Sample Description (in Stratigraphic Order) |
|---|---|---|---|---|
| 1 | KIA43737 (SK09-130) | 5839 ± 36 | 6743 - 6548 | Plant remains from clay and silt rich A' horizon, provides maximum age of A' |
| 2 | KIA43738 (SK09-152) | 5871 ± 37 | 6788 - 6629 | Plant remains from clay and silt rich A' horizon, provides a minimum date of penultimate event |
| 3 | GdS-1100 (SK09-56) | 1300 ± 80 | 1360 - 1050<br>1030 - 1010 | Plant remains from lower portion of fluvial gravel of Unit B, provides maximum age of Unit B |
| 4 | KIA43734 (SK09-86) | 338 ± 30 | 478 - 310 | Plant remains from upper portion of fluvial gravel of Unit B, approximates latest event age |
| 5 | GdA-2304 (SK09-159) | 760 ± 20 | 730 - 670 | Plant remains from lowermost portion of clay rich channel fill of Unit D, approximates latest event age |

The trench at the Untermaubach site reveals one, possibly two separate rupture events that affected Holocene gravels, accounting for a cumulative vertical offset of about 1 m (Figure 4.2a), which coincides with the surface scarp (Figure 4.1d). The gravels in the immediate vicinity of the fault inferred to be responsible for ground rupture are pervasively cataclasized with fracture orientations of clasts and shear zone inclinations parallel to the Schafberg fault. We thus interpret this fault to be seismogenic and capable of producing earthquake magnitudes large enough to cause surface rupture. Sample ages from the event horizons suggest at least one, possibly two rupture events along this fault during the Holocene with recurrence rates of 6 000 to 10 000 yrs.

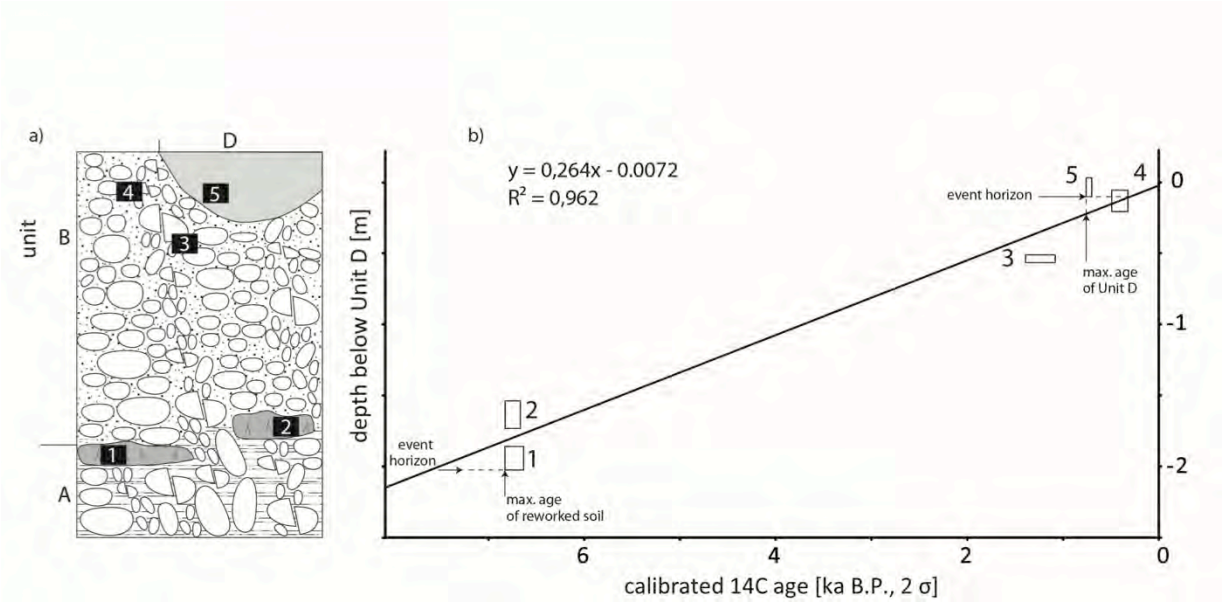


Figure 4.4: Relationship between sample ages and burial depth. a) Simplified stratigraphic context of organic samples. Rotated and fractured clasts indicate zones of coseismic deformation; b) Graph of stratigraphic position versus age of organic samples (Table 1). The sizes of the boxes represent uncertainties in age and depth.

## 4.4 Coseismic Rupture vs. Aseismic Creep

Importantly, our data also provide additional information on the issue of abrupt surface rupturing versus protracted, slow fault motion. First, deformation features in the gravels of units A and B, in particular the fractured and offset clasts, are key to understanding deformation at this site. The co-planar sets of fractured and rotated clasts affect the entire gravel unit, but do not reach the bottom layer of unit C and the bottom of the channel fill (unit D). One hypothesis to explain pebble fractures in this location is the effect of overburden. The minimum sedimentary thickness overlying the deformed gravel is 0.5 m, which would correspond to a minimum value of ~ 12 kPa for the lithostatic stress generated by the overburden (assuming sediment bulk density of 2500 kg/m³). This value, however, appears much too low to trigger the fracturing of clasts during slow aseismic creep. Earlier studies (Eidelmann and Reches, 1992) have concluded that a vertical overburden stress on the order of 10 MPa, corresponding to a sedimentary thickness of approximately 400 m, would be necessary to produce *in situ* fracturing of pebbles similar to those we observe in the trench. While this is highly unlikely, seismic shaking could alternatively generate fractures and overcome the shear resistance of the pebbles.

However, seismic shaking would have caused widely distributed deformation phenomena in the sandy and gravelly layers of unit A and B. Instead, the fractured pebbles are concentrated in the immediate vicinity of the scarp within these units, which is offset by 1 ± 0.2 m. These observations thus favor these features being due to the rupture itself rather than the resulting shaking. Second, alternative mechanisms for pebble fracturing, such as freeze-thaw cycles under permafrost conditions or rearrangement of pebbles during the formation of ice-wedges, are not viable because this region did not experience periglacial conditions during the Holocene (Davis et al., 2003). Finally, the scarp morphology favors a seismic rupture origin. If it reflected aseismic fault creep, the geometry of the deposits in the hanging wall should show decreasing offsets in progressively younger strata (McCalpin, 2009). Instead, offset measurements reveal that the thickness of the units in the hanging wall matches those of the corresponding units in the footwall, rather than indicating aseismic creep and syntectonic sedimentation.

Our results thus reveal unambiguous evidence for a historical coseismic rupture event in Central Europe. Considering the high population density, the concentration of values, and recent small to moderate earthquakes, regional earthquake hazard assessments should take into account surface-rupturing earthquakes with recurrence times on the order of thousands of

years. Further, our new fractured-clast approach allows general applicability on faults of unknown seismogenic potential, which is an essential step forward in paleoseismic research in intraplate settings.

## 4.5 References

Ahorner, L., 1968, Erdbeben und jüngste Tektonik im Braunkohlenrevier der Niederrheinischen Bucht: Zeitschrift der Deutschen Geologischen Gesellschaft v. 118, p. 150-160.

-, 1975, Present-day stress field and seismotectonic block movements along major fault zones in central Europe: Tectonophysics, v. 29, p. 233-249.

-, 2001, Abschätzung der statistischen Wiederkehrperiode von starken Erdbeben im Gebiet von Köln auf Grund von geologisch-tektonischen Beobachtungen an aktiven Störungen: DGG Mitteilungen, v. 2, p. 2-9.

Bilham, R., 2009, The seismic future of cities: Bull. Earthquake Eng., v. 7, p. 839-887.

Bonilla, M. G., 1988, Minimum earthquake magnitude associated with coseismic surface faulting: Bulletin of the Association of Engineering Geologists, v. 25, no. 1, p. 17-29.

Camelbeeck, T., K. Vanneste, P. Alexandre, K. Verbeeck, T. Petermans, P. Rosset, M. Everaerts, R. Warnant, M. Van Camp, 2007, Relevance of active faulting and seismicity studies to assessments of long-term earthquake activity and maximum magnitude in intraplate northwest Europe, between the Lower Rhine Embayment and the North Sea, In: Stein, S. and Mazotti, S., ed., Continental Intraplate Earthquakes: Science, Hazard, and Policy Issues: The Geological Society of America Special Paper, v. 425, no. 14, p. 193-224.

Camelbeeck, T., and Meghraoui, M., 1996, Large Earthquakes in Northern Europe More Likely Than Once Thought: EOS, v. 77, no. 42, p. 405-409.

-, 1998, Geological and geophysical evidence for large palaeo-earthquakes with surface faulting in the Roer Graben (northwest Europe): Geophys. J. Int., v. 132, p. 347-362.

Cattin, R., Doubre, C., de Chabalier, J. B., King, G., Vigny, C., Avouac, J. P., and Ruegg, J. C., 2005, Numerical modelling of quaternary deformation and post-rifting displacement in the Asal–Ghoubbet rift (Djibouti, Africa): Earth and Planetary Science Letters, v. 239, p. 352-367.

Davis, B. A. S., Brewer, S., Stevenson, A. C., and Guiot, J., 2003, The temperature of Europe during the Holocene reconstructed from pollen data: Quaternary Science Reviews, v. 22, no. 15-17, p. 1701-1716.

Eidelmann, A., and Reches, Z., 1992, Fractured pebbles - a new stress indicator: Geology, v. 20, p. 307-310.

England, P., and Jackson, J., 2011, Uncharted seismic risk: Nature Geoscience, v. 4, p. 348-349.

Görres, B., H. Kuhlmann, 2008, How groundwater withdrawal and recent tectonics cause damages of the earth's surface: Monitoring of 3D site motions by GPS and terrestrial measurements: Journal of Applied Geodesy, no. 1(2007), p. 223-232.

Grünthal, G., R. Wahlström, 2006, New Generation of Probabilistic Seismic Hazard Assessment for the Area Cologne/Aachen Considering the Uncertainties of the Input Data: Natural Hazards, v. 38, p. 159-176.

Gupta, H. K., Purnachandra Rao, N., Rastogi, B. K., and Sarkar, D., 2001, The Deadliest Intraplate Earthquake: Science, v. 291, no. 5511, p. 2101-2102.

Hinzen, K. G., S. K. Reamer 2007, Seismicity, seismotectonics, and seismic hazard in the northern Rhine area. In: Stein, S. and Mazotti, S., ed., Continental Intraplate Earthquakes: Science, Hazard, and Policy Issues: Geological Society of America Special Paper, v. 425, p. 225-242.

Houtgast, R. F., R.T. Van Balen, C. Kasse, 2005, Late Quaternary evolution of the Feldbiss Fault (Roer Valley Rift System, the Netherlands) based on trenching, and its potential relation to glacial unloading: Quaternary Science Reviews, v. 24, p. 491-510.

Houtgast, R. F., R.T. Van Balen, C. Kasse, J. Vandenberghe, 2003, Late Quaternary tectonic evolution and postseismic near surface fault displacement along the Geleen Fault (Feldbiss Fault Zone - Roer Valley Rift System, the Netherlands), based on trenching: Geologie en Mijnbouw, v. 82, no. 2, p. 177-196.

Kümpel, H. J., Lehmann, K., Fabian, M., and Mentes, G., 2001, Point stability at shallow depths: experience from tilt measurements in the Lower Rhine Embayment, Germany, and implications for high-resolution GPS and gravity recordings: Geophysical Journal International, v. 146, p. 699-713.

Lehmann, K., Klostermann, J., and Pelzing, R., 2001, Paleoseismological Investigations at the Rurrand Fault, Lower Rhine Embayment: Netherlands Journal of Geosciences, v. 80, no. 3-4, p. 139-154.

McCalpin, J. P., 2009, Paleoseismology in Extensional Tectonic Environments, In McCalpin, J., ed., Paleoseismology, International Geophysics Series, v. 95, p. 171-269.

Meidow, H., 1994, Comparison of the macroseismic field of the 1992 Roermond earthquake, the Netherlands, with those of large historical earthquakes in the Lower Rhine Embayment and its vicinity: Netherlands Journal of Geosciences, v. 73, no. 2-4, p. 282-289.

Schaefer, W., 1999, Bodenbewegungen und Bergschadensregulierung im Rheinischen Braunkohlerevier/Surface movement and mining damage adjustment in the Rhenish ignite mining area: Proceedings of the 42. DMV Meeting, Cottbus, September 1999, p. 1-10.

Stein, S., and Liu, M., 2009, Long aftershock sequences within continents and implications for earthquake hazard assessment: Nature v. 462, p. 87-89.

Sylvester, A. G., 2001, Search for contemporaneous fault creep in Death Valley: *in* Machette, M.N., Johnson, M.L., and Slate, J.L., eds., Quaternary and late Pliocene geology of the Death Valley region: Recent observations on tectonics, stratigraphy, and lake cycles, U.S. Geological Survey Open-File Report, v. 01-51, p. N217-224.

Vanneste, K., Meghraoui, M., and Camelbeeck, T., 1999, Late Quaternary earthquake-related soft-sediment deformation along the Belgian portion of the Feldbiss Fault, Lower Rhine Graben system: Tectonophysics, v. 309, p. 57-79.

Vanneste, K., and Verbeeck, K., 2001, Detailed paleoseismic investigation of the Rurrand Fault in Hambach trench, Germany: Cahiers du Centre Européen de Géodynamique et de Séismologie v. 18, p. 153-156.

Vanneste, K., Verbeeck, K., Camelbeeck, T., Paulissen, E., Meghraoui, M., Renardy, F., Jongmans, D., and Frechen, M., 2001, Surface-rupturing history of the Bree fault scarp, Roer Valley graben: Evidence for six events since the late Pleistocene: Journal of Seismology, v. 5, p. 329-359.

# Chapter 5

## *Paleoseismological Constraints on a Historically Active Intraplate Fault, Schafberg Fault, Lower Rhine Graben*

## 5.1 Abstract

Intraplate earthquakes pose a significant hazard in densely populated rift systems like the Lower Rhine Graben in Northern Central Europe. While the locations of most of the faults are well known, our database about the seismogenic potential and recurrence of earthquakes on these faults is rudimentary. In particular, the Holocene and historical rupture history of potentially active faults remains enigmatic in this region. We carried out a paleoseismic study along a subtle fault scarp that formed in Holocene deposits along the 16-km long Schafberg fault situated south of the city of Düren in the seismically active Lower Rhine Graben (NW Germany). The city is located in the epicentral area of the $M_L$ 6.2 ± 0.2 earthquake of February 18$^{th}$ 1756 AD, Germany's largest historical seismic event on record and one of the largest events in Central Europe. Trenching results across this fault revealed evidence for coseismic activity along the exposed fault strand and a cumulative fault displacement of 1 ± 0.2 m. We mapped several types of soft-sediment deformation features in the Holocene sandy and clayey deposits, including sand and clay intrusions as well as asymmetric folding of cm- to dm-scale related to liquefaction processes. Furthermore, the analysis of faulted strata revealed evidence for at least one, possibly two coseismic events since the Holocene resulting in surface rupture, the youngest of which overlaps with the 1756 AD event. Our study emphasizes that apparently quiescent faults in Central Europe are capable of producing large ground-rupturing earthquakes. This fact has to be taken into account for future attempts to improve earthquake hazard assessments of the region.

## 5.2 Introduction

Large (M > 6) earthquakes in continental rift zones occur with great surprise. In continental interiors, plate body forces commonly held responsible for strain accumulation, are generally very small and often below measurability. Therefore, inherited faults in such regions are apparently inactive due to their very long recurrence intervals of large earthquakes ($10^3$ to $10^5$ years). A prime example for this is the New Madrid earthquake series of 1811/12 AD, in the southeastern United States, where at least six M > 7 earthquakes occurred on previously quiescent faults within two years (e.g. Braile et al., 1982; Fuller, 1912; Johnston, 1996; Johnston and Schweig, 1996)

In the Lower Rhine Graben in NW central Europe, the location of most of the faults is fairly well known, however, due to long recurrence intervals of large earthquakes it remained challenging to find clear evidence for Holocene and/or historical earthquake activity along these structures. Another reason for this is the rare occurrence of Holocene sediments covering potential fault scarps.

Over the last two decades, seismotectonic and paleoseismic studies along the main boundary faults of the Upper Rhine Graben and the Lower Rhine Graben revealed increasing indications for large paleo-earthquakes since the Early Pleistocene (Bonjer, 1997; Camelbeeck and Meghraoui, 1996, 1998; Meghraoui et al., 2000; Meghraoui et al., 2001; Peters et al., 2005; Vanneste, 2008; Vanneste et al., 1999; Vanneste and Verbeeck, 2001; Vanneste et al., 2001; Wenzel and Brun, 1991). Yet, a large portion of potentially active fault segments in this region still needs to be analyzed to better understand the seismogenic potential and associated hazard of intraplate Europe.

The Lower Rhine Graben, the NW branch of the European Cenozoic Rift System, is currently one of the most tectonically active regions in central Europe. Historical records for the LRG document the occurrence of at least 21 M > 5 events. Probably the most significant earthquakes of this region have been the $M_L$ 6.2 Düren earthquake of February 18th 1756 AD and the $M_W$ 5.4 Roermond earthquake of April 23rd 1992 AD (Figure 5.1). The 1756 event is considered the strongest historical earthquake of Germany and - in line with the 1356 Basel earthquake ($M_L$6.0-6.5, Meghraoui et al. 2001) - one of the most destructive earthquakes of Central Europe. The 1992 AD event which occurred in the central sector of the Lower Rhine Graben is considered till this day as the largest instrumentally recorded earthquake in central Europe (Haak et al., 1994). In particular, this event has motivated several studies carried out in the Lower Rhine Graben addressing the question of how frequently large earthquakes

occurred in this region, and if any of those events have been large enough to rupture the surface (Camelbeeck, 2007; Camelbeeck and Meghraoui, 1996, 1998; Houtgast, 2005, 2003; Lehmann et al., 2001; Vanneste et al., 1999; Vanneste et al., 2001).

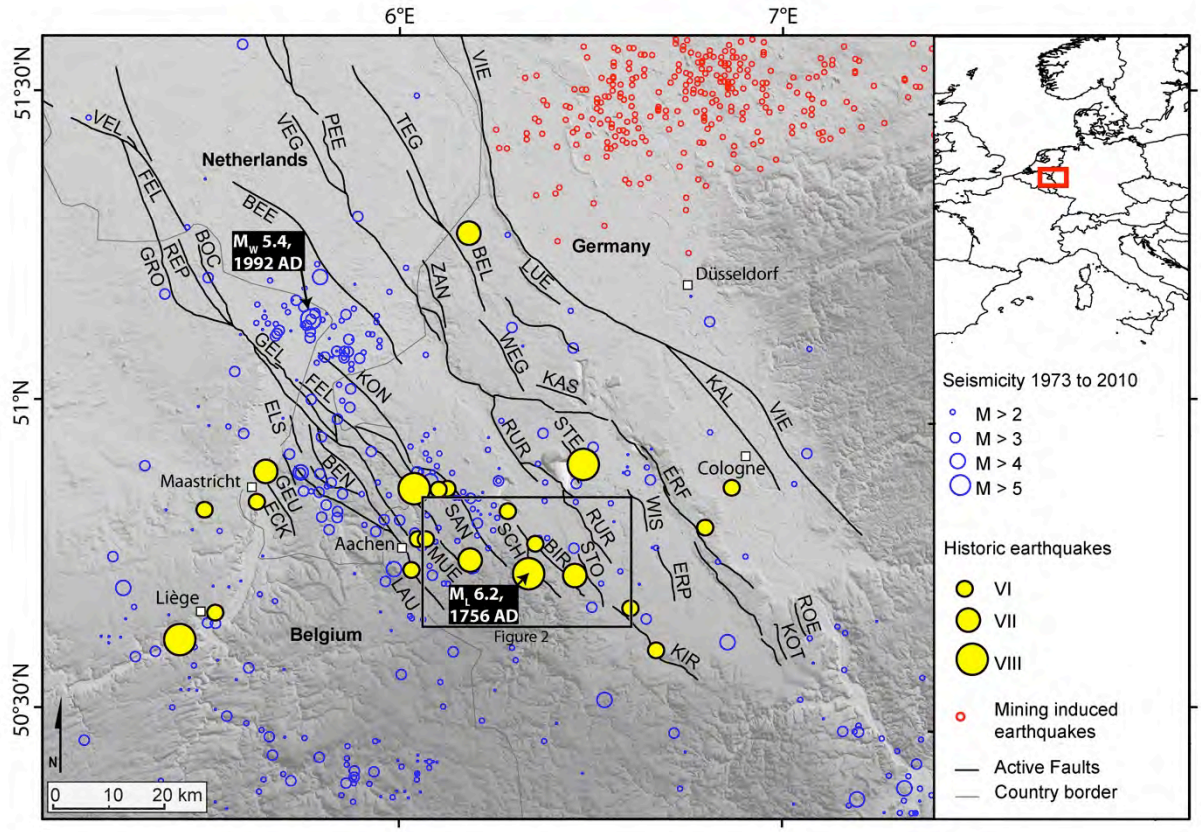


Figure 5.1: Seismotectonic framework of the Lower Rhine Graben. Covering area marked by a red box in the inset at the upper right corner of the map. Blue circles denote epicenters of instrumentally recorded earthquakes from 1973 to 2010. Yellow solid circles denote epicenter of historical events inferred from intensity data. Sizes increase with magnitude or maximum intensity. Black lines denote Quaternary faults. Small red circles mark the epicentral position of shallow, mining induced earthquakes of the Ruhr coal mining area. Black lines indicate the surface expression of active normal faults (Vanneste et al., 2010). BEE: Beegden fault, BEL: Belfeld fault, BEN: Benzenrade fault, BIR: Birgel fault, BOC: Bocholt fault, ECK: Eckelrade fault, ELS: Elsloo fault, ERF: Erft fault, ERP: Erp fault, FEL:Feldbiss fault, GEL: Geleen fault, GEU: Geulle fault, GRO: Grote Brogel fault, KAL: Kalken fault, KAS: Kaster fault, KIR: Kirspenpicher fault, KON: Koningsboscher fault, KOT: Kotenforst fault, LAU: Laurensberg fault, LUE: Luelkener fault, MUE: Muenstergewand fault, PEE: Peelrand fault, REP: Reppel fault, ROE: Roettgener fault, RUR: Rurrand fault, SAN: Sandgewand fault, SCH: Schafberg fault, STE: Steinstrass fault, STO: Stockheimer fault, TEG: Tegelen fault, VEG: Veghel fault, VEL: Veldhovenfault, VIE: Viersener fault, WEG: Wegberger fault, WIS: Wissersheimer fault, ZAN: Zandberg fault. Map projection for this and the following map: UTM Zone 31, Datum: WGS84. Digital elevation model derived from AsterDEM data, 30 m resolution.

In a previous study (Chapter 4), we reported on first evidence of coseismic rupture in the Lower Rhine Graben on centennial timescales and identified the Schafberg fault as a seismogenic structure and most likely the source of the $M_L$ 6.2 Düren earthquake of February 18$^{th}$ 1756 AD. In this study, we provide a summary of the Düren earthquake followed by a detailed description of the Schafberg fault and the observed coseismic deformation features

exposed in the trench. In contrast to the study sites addressed in Chapter 3, this trench is situated in a part of the Lower Rhine Graben unaffected by mining induced subsidence. As confirmed by the local bomb disposal unit, the site has also not been targeted by aerial bombing.

At the trench site we explore the recurrence of large earthquakes and the fault displacement rates in the Holocene along the 16-km long normal fault located at the southwestern border of the Lower Rhine Graben (Figure 5.1). We combined geomorphic, geologic and paleoseismic approaches to illuminate the surface faulting history along this structure that is located in the epicentral area of the Düren earthquake (Figure 5.2). Trenching across a Holocene fault scarp detected in prolongation of the Schafberg fault 9 km south of the city of Düren allowed the studying of the primary and secondary effects of past earthquakes at this location, as well as the nature of coseismic deformation related to the historic event of 1756 AD. Our results thus underline the importance of paleoseismic studies in this region and particularly on fault segments that have not previously been recognized as being potentially seismically active.

### 5.2.1 The 1756 Düren Earthquake

The $M_L$ 6.2 ± 0.2 earthquake (Hinzen, 2007; Meidow, 1994) that occurred in the vicinity of the city of Düren on February 18$^{th}$ 1756 AD (Figure 5.2), was the strongest event of an earthquake series that lasted from December 26$^{th}$ 1755 to December 15$^{th}$ 1756 AD, a few weeks after the $M_W$ 8.7 Lisbon earthquake of November 1$^{st}$ 1755 AD (Gutscher, 2004). With a total of 75 M > 3 events, the Düren event has been one of the most devastating earthquake series in central Europe and the $M_L$ 6.2 event is considered the strongest historical earthquake in Germany and one of the strongest in Central Europe (Meidow, 1994). Damage reports for this event include destroyed houses, churches and castles, as well as several physical injuries including one fatality (Meidow, 1994). Furthermore, the earthquake triggered a landslide in the epicentral area near the village of Hürtgenwald. Historical documentation does not reveal information on surface ruptures related to this event. However, in other regions events of this magnitude commonly rupture the surface producing offsets on a decimeter-scale (Bonilla, 1988; McCalpin, 2009a; Wells and Coppersmith, 1994). Meidow (1994) conducted extensive analyses of historical documents to estimate the magnitude, epicenter and hypocentral depth of the 1756 event. His study implies that any of five active faults in the epicentral area may have ruptured. Possible seismogenic faults are the Münstergewand-, Sandgewand-, Birgel-, Schafberg- and Rurrand faults (Figure 5.2). All five

faults are NW-SE striking normal faults that are capable for producing M ≥ 6 earthquakes based on their maximum surface rupture lengths and estimated rupture widths (Wells and Coppersmith, 1994). Reconnaissance mapping and geophysical prospecting (Strecker et al., 2002; Streich, 2003) revealed surface scarps and subsurface anomalies in Holocene deposits in the prolongation of the Schafberg fault which led to selecting this fault as trench and study site.

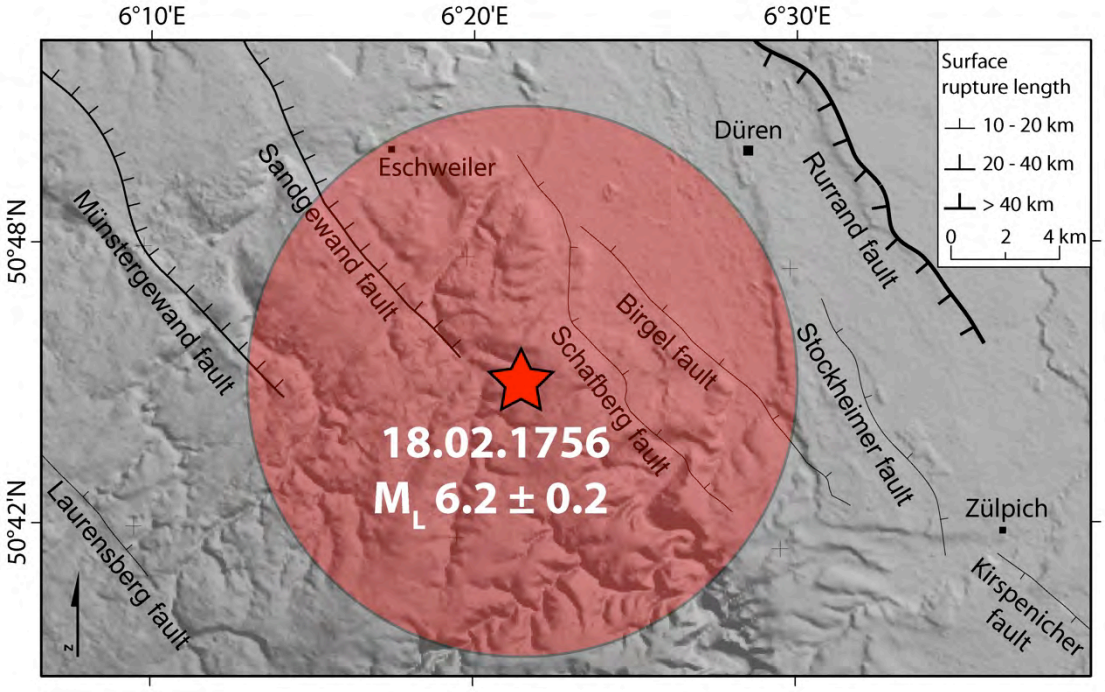


Figure 5.2: Estimated epicentral location of the 1756 Düren earthquake. The red star depicts the epicenter; the red circle indicates the approximate error in position of the epicenter of 10 km (Meidow, 1994). Faults are shown as black lines, strokes point to the downthrown side. Line width varies with maximum surface rupture length. Fault data from: seismic source catalogue of the Roer Valley Graben system (Vanneste et al., 2010).

## 5.2.2 Regional Geological Setting

The study is carried out at the SW boundary of the Lower Rhine Graben at the transition to the Northern Eifel, the NW part of the Rhenish Shield (Figure 5.3). This sector of the Lower Rhine Graben consists of complex normal fault systems including the Feldbiss-, Sandgewand, Münstergewand and Schafberg- Birgel fault systems (Ahorner, 1962; Fliegel, 1922; Holzapfel, 1904; Quitzow and Vahlensieck, 1955). In contrast to the eastern and central sectors of the Lower Rhine Graben, that are characterized by large SW-dipping boundary faults (Erft fault, Swist fault, Rurrand fault, Figure 1) and records of more than 100 m of

vertical offset since the Quaternary, the SW faults predominately dip to the NE and record < 50 m of Quaternary offset (Ahorner, 1962; Quitzow and Vahlensieck, 1955).

This study is conducted along and across the 16 km-long Schafberg fault, which is part of the Schafberg-Birgel fault system - a set of sub-parallel NE-dipping normal faults including the Schafberg fault to the west and the Birgel fault to the east (Figure 5.3). Ahorner (1962) reports that the faults combined offset the Devonian basement and Triassic cover rocks of the Eifel by several hundreds of meters. Between the villages of Bogheim and Untermaubach (Figure 3) offset measurements and drilling surveys revealed early to mid Pleistocene upper main terrace gravels with offsets ranging from 10 - 15 m (Ahorner, 1962; Quitzow and Vahlensieck, 1955; Richter, 1962).

### 5.2.3 Tectonogeomorphic Setting of the Study Site

The geomorphic expression of the Schafberg fault is most obvious south of the village of Straß (Figure 5.3) exhibiting a clear linear offset of several tens of meters. Along strike, the trace of the fault is also indicated by patch-like remnants of Tertiary sand- and siltstone that are deposited on the hanging-wall side of the fault (Figure 5.3). Quitzow and Vahlensieck (1955), suggested that the Tertiary sediments originally covered the entire region and are now mostly eroded. South of Untermaubach, the Schafberg fault traverses a narrow river valley surrounded by Devonian rocks of the Rhenish Shield and Triassic cover rocks (Knapp and Hager, 1980). The valley floor is covered by Late Pleistocene and Holocene fluvial deposits of the Rur River. Here, two sub-parallel NNE-trending scarps have been identified where the Schafberg fault projects into the valley (Figure 5.4). The scarps are visible as two pronounced eastward sloping segments in between flat surfaces. To the south the scarps disappear in the active river bed; to the north the scarps are overprinted by adjacent road construction and the dense vegetation cover. The trends of the two scarps are slightly different: the south-western scarp strikes 125° and is slightly curved, whereas the north-eastern scarp is almost perfectly straight striking 155°. The subtle scarps are 0.8 to 1.2 m high and also affect the hydrologic conditions at the study site. In summer, plants along the trend of the suspected fault often wilt due to local drought, whereas in spring the water table is high on the hanging wall side (Strecker et al., 2002). Satellite images also illustrate the difference in soil properties resulting in a different colouring of the plants and thus, indicating the location and strike of potentially tectonically induced subsurface anomalies (Figure 5.4). The deposits at the site comprise terrace gravel of the youngest terrace sequence (Lower Terrace) of the Rur valley

(Klostermann, 1992). The gravel deposits are overlain by a soil developed on Holocene flood deposits, which consist of silty sand with clay-rich layers and abundant organic material (Figure 5.3). The study site is situated on farmland very close to the recent channel bed of the active Rur river, therefore, the topography of the fluvial terrace and any possible tectonic imprint on the landscape are probably overprinted by both fluvial and anthropogenic processes.

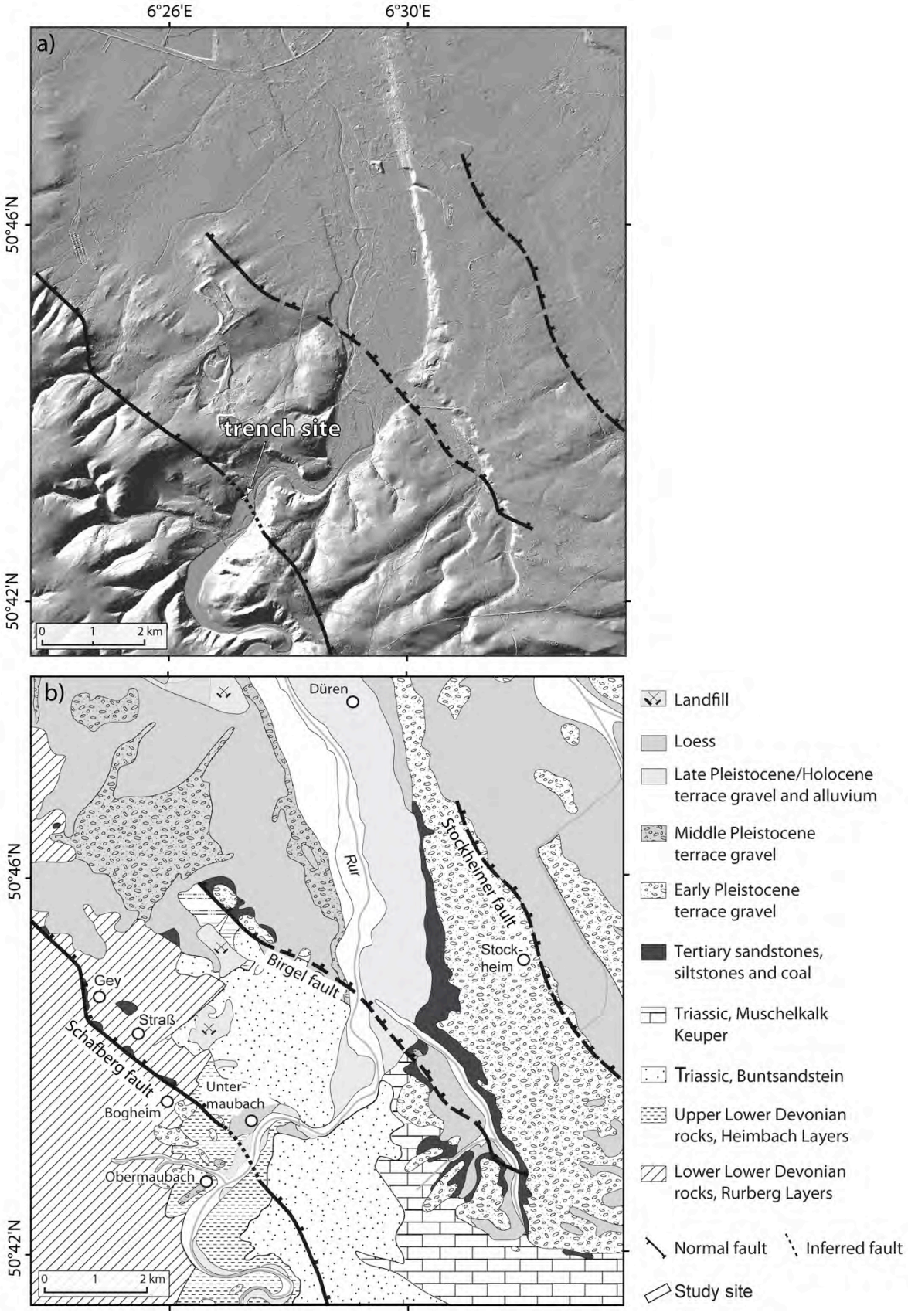
6°26'E
6°30'E
a)
50°46'N
50°42'N
trench site
0 1 2 km
b)
Düren
Rur
Stockheimer fault
Stock-
heim
Birgel fault
Gey
Straß
Schafberg fault
Unter-
maubach
Bogheim
Obermaubach
Landfill
Loess
Late Pleistocene/Holocene terrace gravel and alluvium
Middle Pleistocene terrace gravel
Early Pleistocene terrace gravel
Tertiary sandstones, siltstones and coal
Triassic, Muschelkalk Keuper
Triassic, Buntsandstein
Upper Lower Devonian rocks, Heimbach Layers
Lower Lower Devonian rocks, Rurberg Layers
Normal fault
Inferred fault
Study site

Figure 5.3: Geomorphical and geological setting of the trench site. (a) Shaded relief map of the Rur valley study area based on digital elevation data (5 m resolution, provided by the geodetic survey of Northrhine Westphalia). Black arrows depict the surface trace of the Schafberg fault; the trench site on the Rur river terrace is indicated by the white quadrangle. (b) Geological map of the Rur valley study area, modified after the geological map of the Northern Eifel (Knapp and Hager, 1980). The location of the trench site between the villages of Obermaubach and Untermaubach is marked by the black quadrangle.

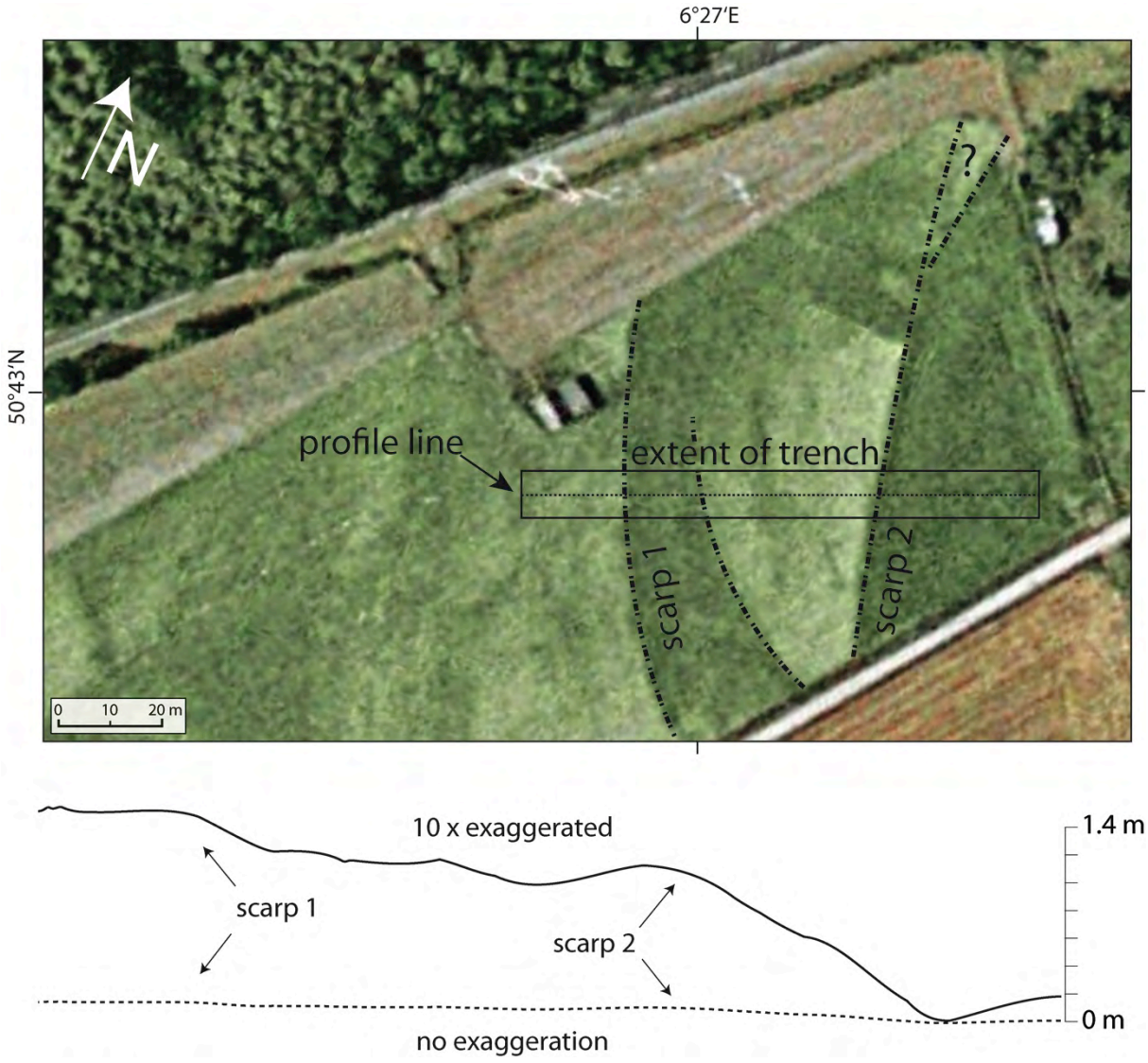


Figure 5.4: Satellite image of the Untermaubach site. Note the difference in color of the pasture corresponding to differences in conductivity (also indicated by the dashed-dotted lines). The extent of the excavation site is marked by the black quadrangle; the dashed line indicates the position of the topographic profile shown below the satellite image. Satellite image derived from SPOT/Cnes data (2009).

## 5.3 Methods

### 5.3.1 Trench Site Selection

The Untermaubach study site has been selected within the framework of the SAFE project (Slow Active Faults of Europe) funded by the EC (Strecker et al., 2002). Trench excavation and has been carried out in the framework of the DFG-funded research project "Active intraplate deformation in central Europe: paleoseismology of the Lower Rhine Graben" (Friedrich et al., 2002). Exploratory work prior to trench excavation included seismotectonic studies, geomorphic and geologic mapping, topographic leveling and shallow geophysical surveys (Friedrich et al., 2002; Schmedes et al., 2005; Strecker et al., 2002; Streich, 2003). The suspected fault scarps were inspected in cooperation with researchers from the Royal Observatory of Belgium, Brussels, who are working on related topics on the Belgian side of the Lower Rhine Graben (Camelbeeck et al., 2008; Vanneste et al., 2008; Verbeeck et al., 2000).

In contrast to two proposed trench sites at the Erft and Wissersheimer faults (Chapter 3), this trench site is not affected by mining-induced subsidence. In addition, excavation permits were only obtainable at the Untermaubach site.

### 5.3.2 Trenching Strategy

The trench site is located on farmland in a narrow river-valley close to the present-day river course. This is one of the few exceptional locations in the Lower Rhine Graben where a presumably active fault is covered by Holocene sediments. This provides the opportunity to study the latest rupture history of the fault segment, given that the Holocene sediments are affected by coseismic deformation. However, the proximity of the trench site to the active river-bed as well as its position on actively used farmland caused extensive pre-planning including permit applications (nature conservation authority; water conservation authority; city building authority; archeological survey; bomb disposal unit) and negotiations with the landowner and tenant of the farmland.

To place constrains on the age of scarp formation and to determine the offset across the fault, we excavated the trench perpendicular to the suspected fault scarps at a 65° strike (Figure 5.4). As requested by the landowner we first removed and separately deposited the upper humous soil horizon (Appendix, Figure I.1). To determine a possible anthropogenic

nature of the identified structures the archaeological survey of North Rhine Westphalia (Rheinisches Amt für Bodendenkmalpflege, Nideggen) analyzed the uppermost 0.5 to 1 m at the trench site by excavating several shallow trenches parallel and perpendicular to the location of the main trench. Due to its proximity to the current Rur-river bed (approximately 200 m to the east) the ground water table at the trench site is situated about 1.5 m below the surface, which led to a complex stepwise excavation strategy. First, we opened the trench to a depth of 2 m to uncover the current water table and to evaluate the required pumping system. Then a total of six 8 m deep wells were installed and equipped with wet-pit pumps (Figure I.1). The well logs were additionally used to determine the top of the Devonian basement. After the water table was lowered to a maximum of 5 m below the surface, we excavated the trench to its final maximum depth of up to 4.5 m at a length of 85 m and a maximum width of 9 m. At some locations, the trench was additionally excavated by hand to a depth of 5 m (Appendix, Figure I.1). The trench walls inclined at 45° to avoid collapsing of the water saturated gravel deposits. All trench logs are corrected to vertical from the 45° inclination angle to facilitate correct offset estimates.

We cleaned the trench walls using running water for the coarse-grained deposits and palette knifes and scrapers for the fine-grained deposits (Appendix, Figure I.1). This way, we removed the outermost 15 - 20 cm of the gravel deposits, so that backhoe-related deformation of the sediment deposits can be precluded. We intentionally left the gravel deposits uncovered to let erosion due to rain and wind carve out the sedimentary structures, which led to a better visibility of layering and deformation features.

### 5.3.3 Mapping Strategy

The main objective of the trenching study was to look for features indicating coseismic or aseismic faulting behaviour and if possible to identify and date individual coseismic events. For logging purposes, we produced several photo mosaics of both trench walls that consist of up to 100 single photo shots (Appendix, Figure II.1). We flagged all important contacts and sample locations and repeatedly scanned the trench walls with sub-centimeter resolution using a terrestrial laser-scanning device (Topcon GLS-1000©, Figure 5.5, Appendix, Figure I.1). We mapped the sedimentary deposits by describing the composition, lithology and sedimentary fabric in detail. We further mapped deformation features including fissures, joints and rotated and fractured clasts exposed in the gravel

deposits. For radiocarbon dating, we collected several samples including charcoal, plant remnants and wood from critical sediment contacts and suspected event horizons (Appendix, Figure II.1).

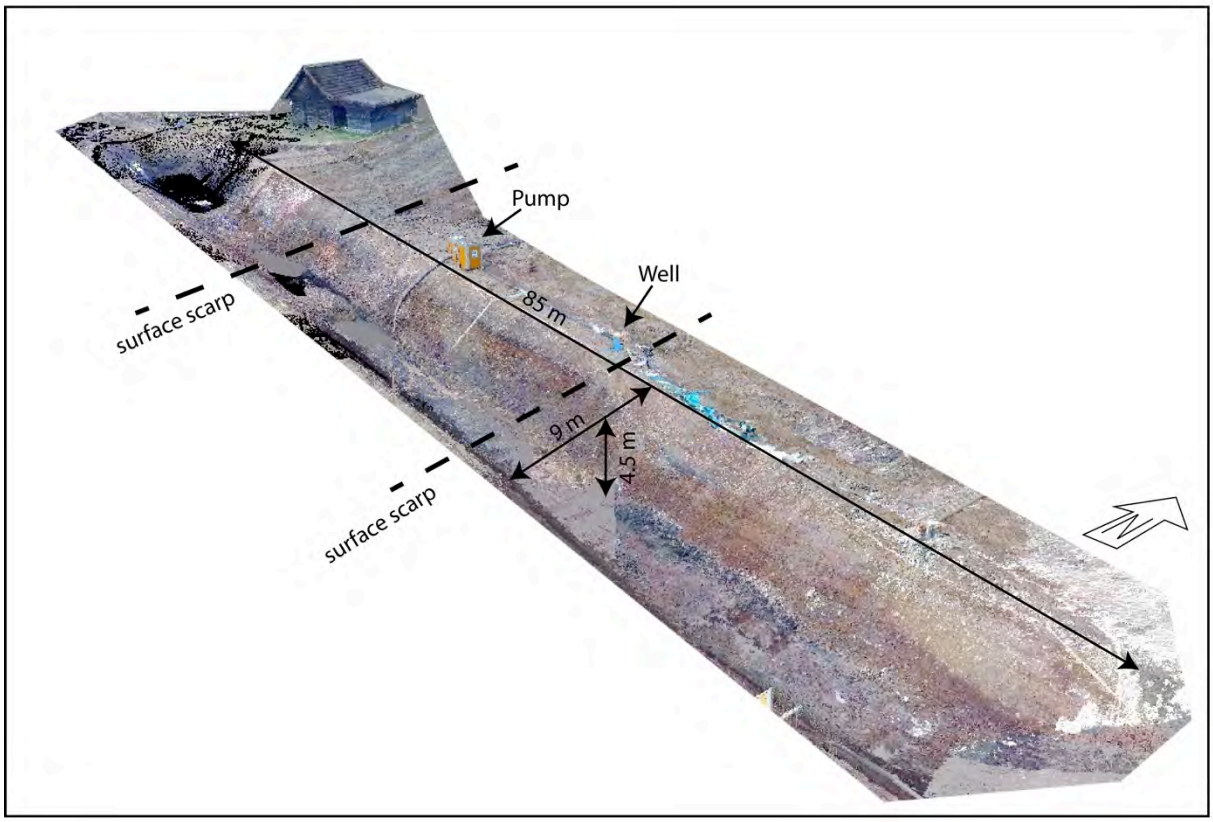


Figure 5.5: Perspectively reduced view of 3D scan of the Untermaubach trench, view to the NE. The scan has a minimum resolution of 1 point per 2 cm and consists of a total of ~ 11 million points gained from 8 single scan stations. The dashed lines depict the location and strike of the observed surface scarps.

## 5.4 Results

In the following we provide a detailed description of the trench stratigraphy and deformation features exposed in the Untermaubach trench. We further provide a detailed documentation of sample ages and associated event horizons.

### 5.4.1 Trench Stratigraphy

We have subdivided the sediments into four main units, from oldest to youngest (units A to D). The trench exposes a 5-6 m thick cover of unconsolidated fluvial deposits overlying Devonian sedimentary rocks. The basement rocks consist of platy mud- and sandstone of the Heimbach Formation (Upper Lower Devonian; Knapp and Hager, 1980). The lowermost unit A comprises a ~ 1.5 m thick layer of clast-supported coarse gravel with predominately prolate clasts up to 60 cm in diameter in a silt- and clay-rich matrix (Figure 5.6a). Clasts mainly consist of Triassic sandstone (Buntsandstein) or Devonian shale of the Heimbach Formation. Few clasts consist of Devonian quartzite, presumably of the Ems Formation (Upper Lower Devonian). The top of the unit A layer contains interspersed clay lenses containing organic material possibly related to a reworked soil horizon (unit A', Figure 5.6b). This horizon is overlain by unit B, a 1 - 2.5 m thick inhomogeneous clast and matrix-supported coarse gravel layer with interbedded sand and fine gravel lenses (Figure 5.6c). The lithological composition of clasts does not significantly differ from that of unit A, but here the clasts are smaller and more rounded. Maximum clast sizes do not exceed 30 cm. Unit B is in turn overlain by a matrix-supported clayey and sandy to fine gravel layer (unit C) with well-developed zones of cross-bedded sand lenses (Figure 5.6d). Furthermore, the trench exposes two asymmetric channels, which coincide with the position of the observed surface scarps (Figure 5.5 and Figure 5.7). The channel fill consists of sandy silt and clay-rich layers (unit D, Figure 5.6e).

The eastern channel has a total length of 12 ± 2 m and a maximum sediment thickness of 2.5 m (Figure 5.7). The channel exhibits an internal horizontal stratification characterized by variations in the content of organic matter, clay and Mn- and Fe-oxides. The base of the channel lies below the present groundwater table and shows the typical features of a reductive gley soil horizon (Gr), that is characterized by anoxic conditions exhibiting a greenish blue soil colour due to the presence of ferrous oxide ($Fe^{II}$) (Scheffer and Schachtschabel, 2002).

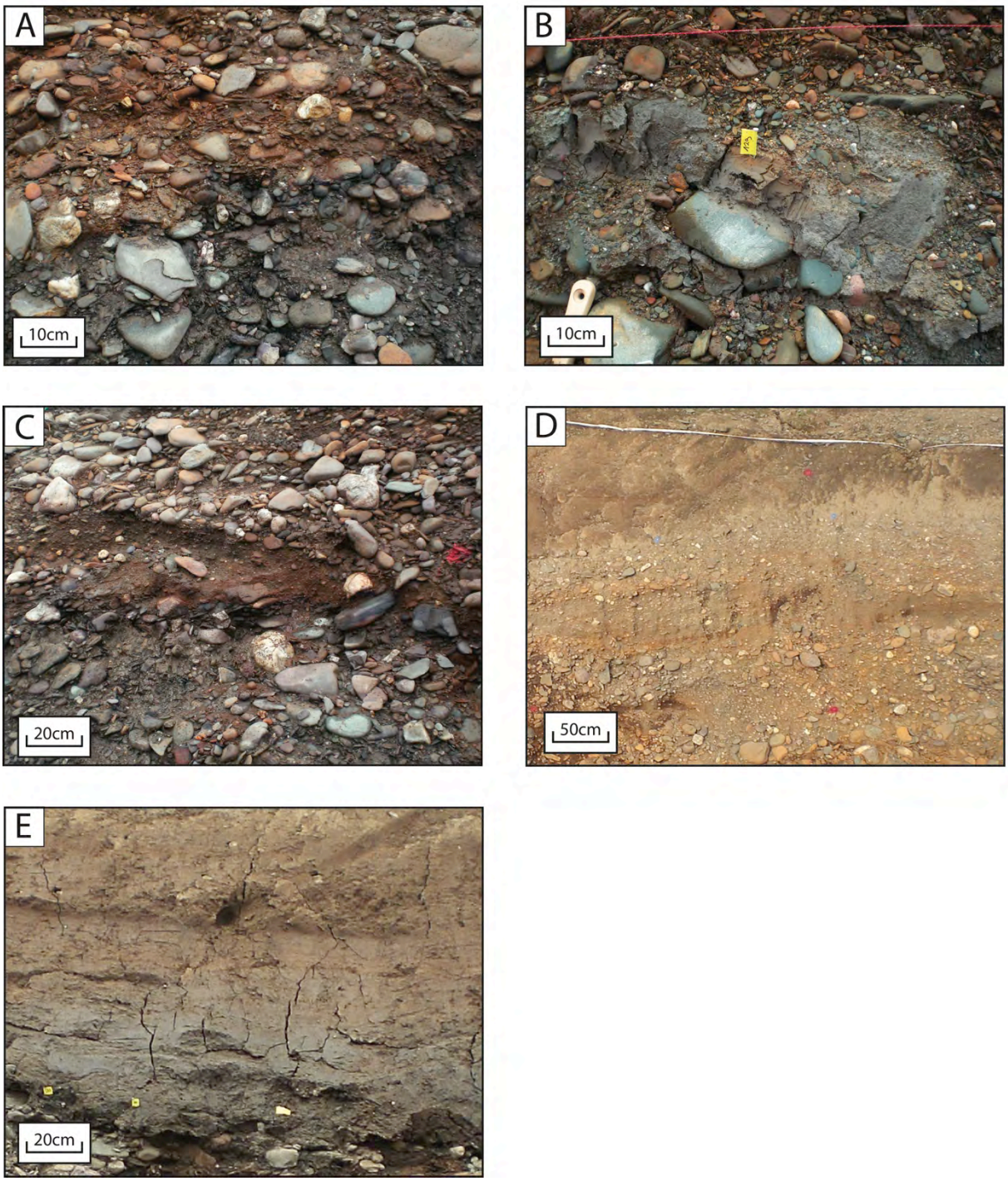


Figure 5.6: Photographs of typical sedimentary units exposed in the trench. (a) Clast-supported coarse gravel with dm-sized boulders in a silt and clay-rich matrix typical for unit A; (b) silty clay lens containing abundant plant remnants and roots typical for paleosoil at the top of unit A (unit A'); (c) clast-supported coarse gravel with cm- to dm-sized boulders with lenses of sandy clast supported fine- and medium gravel typical for unit B; (d) sand and fine gravel with cross-bedded sand and gravel lenses typical for unit C overlain by silt and clay rich flood deposits of unit D; (e) silt and clay rich flood deposit containing abundant plant remnants and charcoal at the base typical for unit D; note the greyish blue coloring of the lower part of the sediment unit reflecting typical features of a reductive gley soil-horizon.

This horizon further contains a high concentration of organic matter in the form of retransported plant remains, charcoal and wood. The overlaying horizon is characterized by the presence of Mn- and Fe-oxides in the form of black and reddish concretions ranging in diameter from < 1 mm to up to 2 cm.

The western channel had a total exposed length of 10 ± 1 m and a maximum sediment thickness of 3 m. The channel is highly asymmetric with a steep western flank (45 ± 5°) and a shallower eastern flank (15 ± 3°). The base of this channel lies also below the groundwater table exhibiting the same features as the eastern channel. The overlying deposits predominately consist of clayey silt with a few isolated clasts exhibiting different zones of vertical and lateral clay migration caused by fluctuations of groundwater and percolating water. Furthermore, a moderately well preserved sub-channel within the superior channel bed is exposed (Figure 5.7).

Figure 5.7: Results of the trench analysis. (a) Photo mosaic of the northern trench wall. The dashed brown line indicates the original surface before excavation and removal of the upper soil horizon. Trench log of the main units and deformation features of (b) the west-north-western part and (c) the east-south-eastern part of the northern trench wall. Yellow stars depict the locations of fractured clasts; red boxes denote the positions of organic samples. MRE: most recent event; PUE: penultimate event; the complete trench log including the southern trench wall is found on the CD-ROM attached to this thesis (Appendix, Figure II.1)

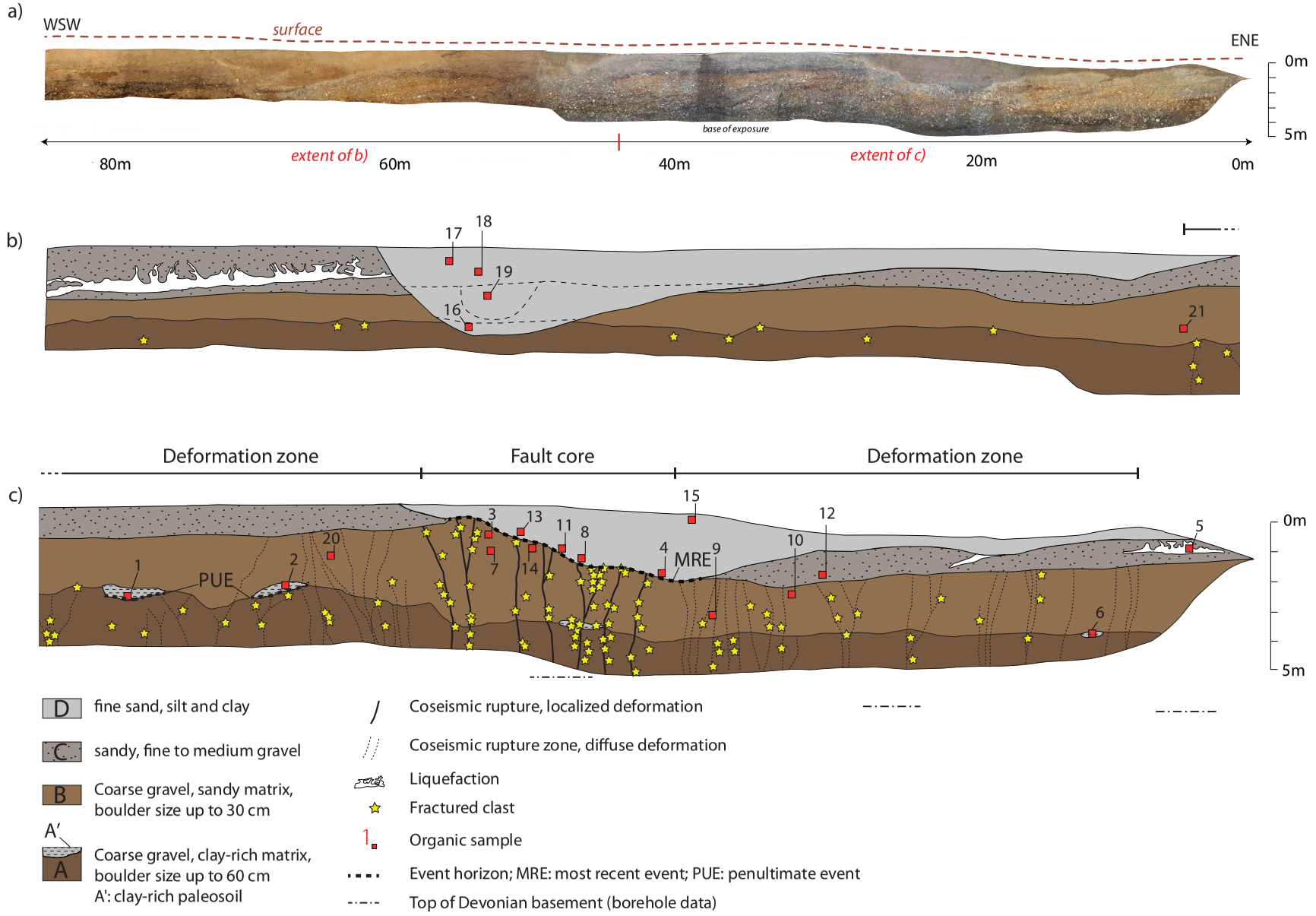
a)
WSW
surface
ENE
0m
5m
base of exposure
80m
extent of b)
60m
40m
extent of c)
20m
0m
b)
17
18
19
16
21
Deformation zone
Fault core
Deformation zone
c)
15
3
13
11
8
12
5
20
4
MRE
9
10
2
7
14
PUE
1
6
0m
5m
D
fine sand, silt and clay
C
sandy, fine to medium gravel
B
Coarse gravel, sandy matrix, boulder size up to 30 cm
A'
A
Coarse gravel, clay-rich matrix, boulder size up to 60 cm
A': clay-rich paleosoil
Coseismic rupture, localized deformation
Coseismic rupture zone, diffuse deformation
Liquefaction
Fractured clast
1
Organic sample
Event horizon; MRE: most recent event; PUE: penultimate event
Top of Devonian basement (borehole data)

### 5.4.2 Seismogenic Features

Due to the lack of laterally continuous layering within the gravel deposits and intense sediment alteration produced by groundwater fluctuation, the recognition of faulting related sediment deformation within the gravel deposits required extremely careful and detailed mapping of the trench walls. Sediment deformation in this fault exposure is not concentrated along a single fault plane, but is rather characterized by cataclasis (fractured and offset clasts) and shear fabric (rotated clasts) predominately across a ~ 10 m-wide fault core (Figure 5.7), and less prominent but still recognizable deformation across a ~ 30 - 40 m wide deformation zone coinciding with the eastern surface scarp (Figure 5.7). The cumulative offset across the fault core of 1.0 ± 0.2 m is taken up by numerous small fractures each accommodating a few centimeter of displacement.

Secondary evidence for coseismic activity at the trench site can be observed by several liquefaction phenomena exposed in both the hanging wall and footwall of the fault. Liquefaction occurs exclusively in fine sand and silt layers of unit C including sill- and dyke-structures (Obermeier, 1996), as well as small-scale folding of intact sand layers (Figure 5.10). Radiocarbon dating only provides inherited ages of charcoal samples for this horizon and thus, probably overestimates the age of the liquefaction event. Radiocarbon ages range from 862 ± 67 to 1308 ± 34 yrs BP (sample numbers 12 and 5, Table 5.1, Figure 5.8). The best-preserved liquefaction features are exposed at the westernmost portion of the trench (Figure 5.10).

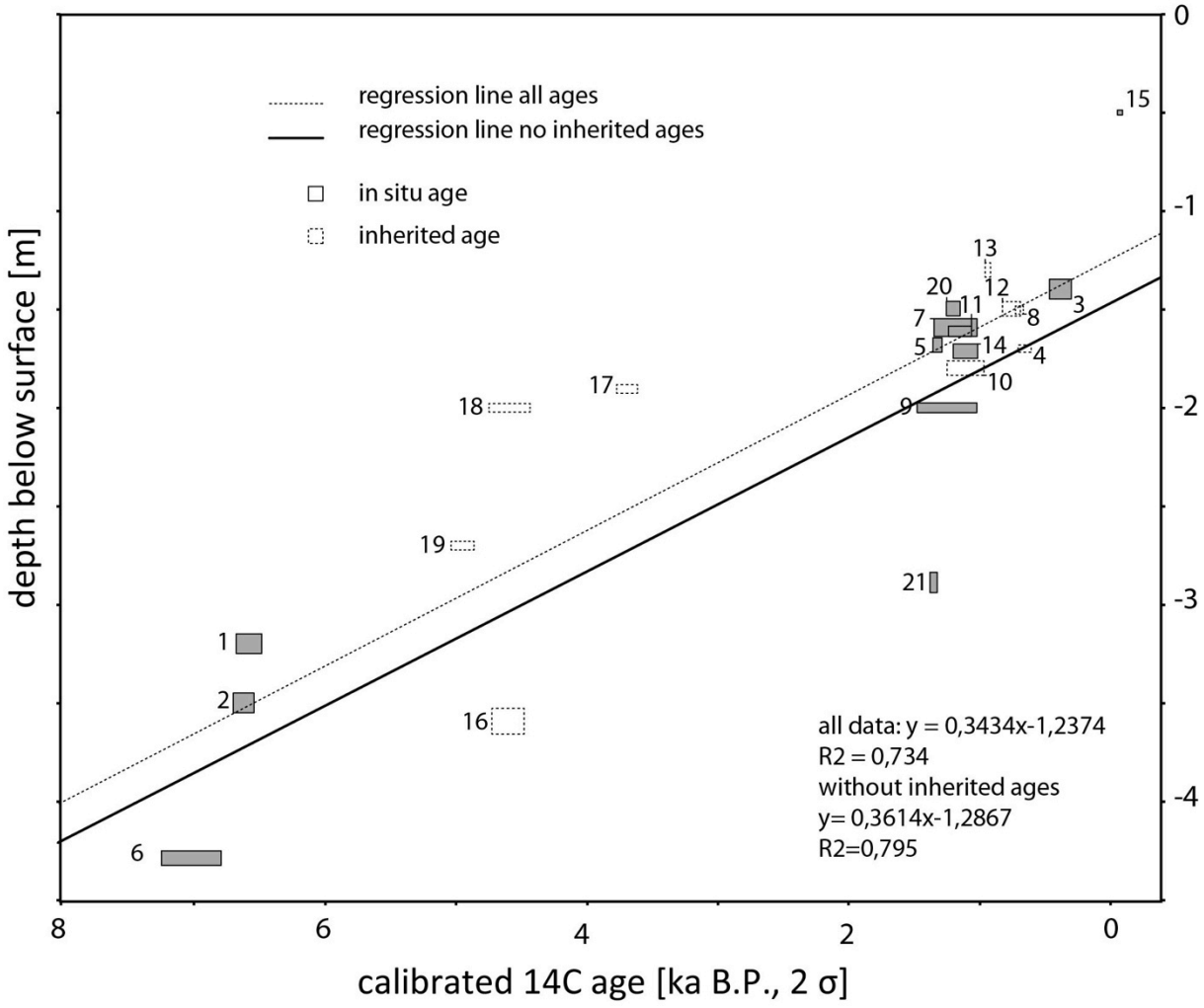


Figure 5.8: Graph of stratigraphic position versus age of samples used for radiocarbon dating. The sizes of the boxes represent uncertainties in age (Table 1) and depth. Solid grey boxes represent in-situ ages derived from samples preserved in paleoseoil horizons (plant remnants and roots). Dashed boxes represent inherited ages from charcoal and wood samples.

Fractured pebbles occur exclusively in unit A and B, while unit C exhibits liquefied sand deposits. Most of the clasts reveal pure dip-slip fractures, however, offset measurements on a few clasts indicate a left-lateral strike-slip component (Figure 5.9). Unit D shows no signs of deformation and clearly truncates the deformed gravels of unit B below the eastern scarp (Figure 5.7). We thus interpret the contact between unit B and the channel fill of unit D as the most recent event horizon (MRE). An older event horizon is preserved at the contact between unit A and the overlying soil horizon (unit A') west of the main fault zone. Here, the partly degraded soil horizon truncates sheared and cataclized pebbles of unit A (penultimate event horizon PUE, Figure 5.7).

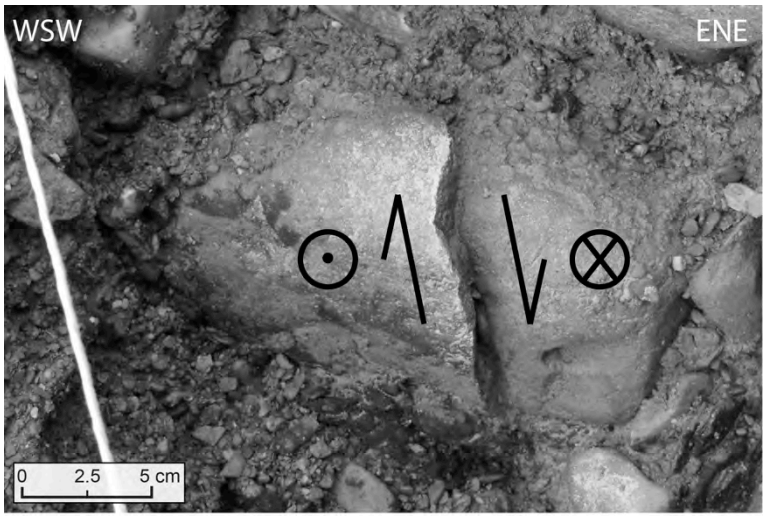


Figure 5.9: Fractured Buntsandstein clast exposed in gravel deposits of unit A. The clast exhibits both normal and left-lateral displacement.

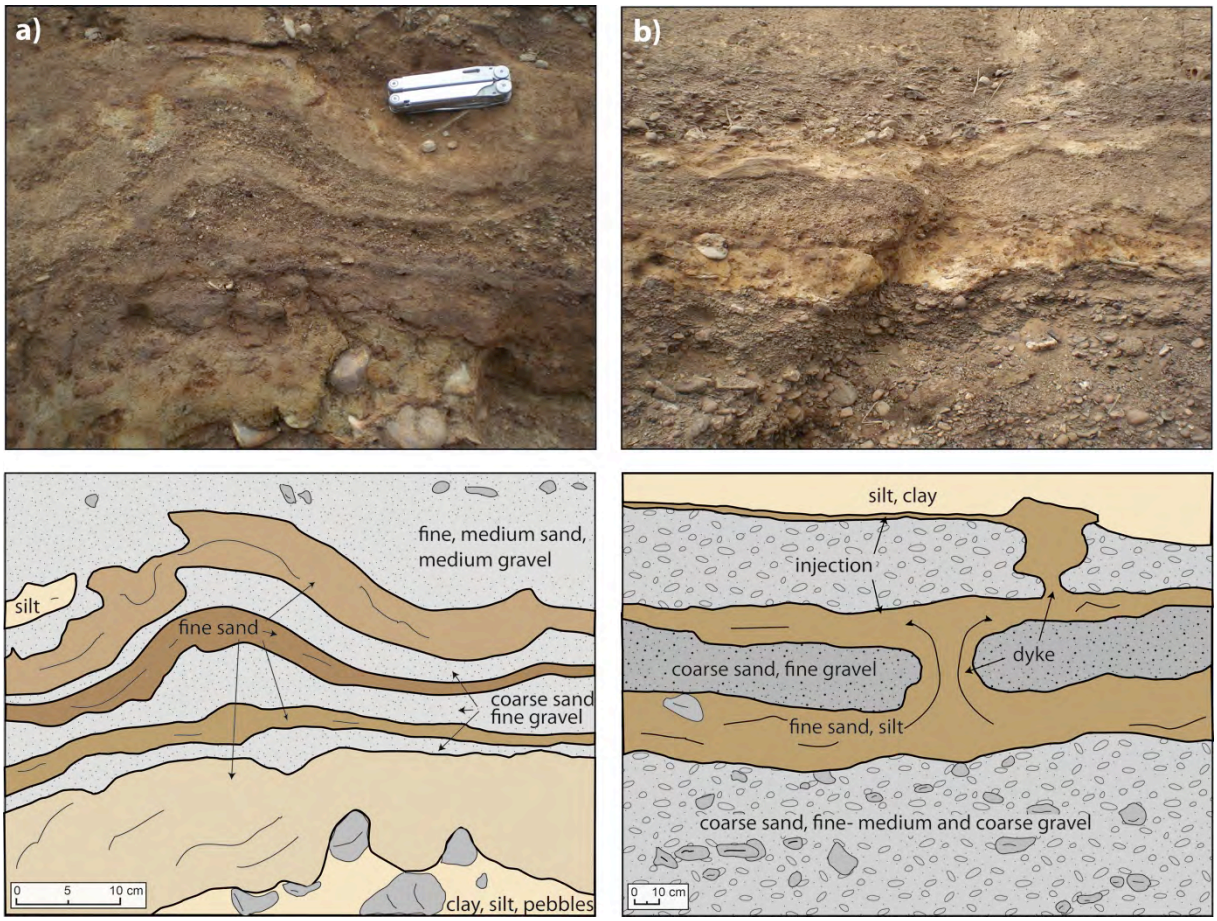


Figure 5.10: Liquefaction features of soft-sediment deposits exposed in unit C. (a) Dm-scale folding of fine-sand and silt deposits; (b) "sills-and-dykes" structure (Obermeier, 1996) of fine-sand and silt layer injected into gravel deposits.

### 5.4.3 Ages of Event Horizons

To determine the age of the event horizons we collected charcoal, wood and plant remnants from several stratigraphic levels (Figure 5.7, 5.8). Inherited ages of radiocarbon-dated material, i.e., time between carbon fixation in wood and its incorporation in a sediment deposit, can result in over-estimation of the ages of those deposits. Thus, it is essential to evaluate the robustness of determined radiocarbon ages and to differentiate between in-situ ages and inherited ages (Figure 5.8). We collected a total of 21 radiocarbon ages of organic samples including detrital charcoal, wood and plant remnants (Table 5.1). A likely source for the charcoal would be the burning of wood at several sites upslope from the trench site. The region has experienced intensive deforestation and charcoal production during the beginning of Roman occupation (50 BC) and during the 16$^{th}$ century related to the rising iron industry (Zolitschka, 1998). This suggests that the charcoal samples exposed in the trench have likely been transported downward from the hillslopes and reworked into the deposits and therefore, may yield $^{14}$C ages significantly older than their time of deposition.

We have found wood samples at the base of unit D at the western channel as well as within a sand lens at the top of unit B below the eastern channel (Figure 5.7). In both cases, the wood samples are several dm to 1 m long, and up to 10 cm thick branches. These are oriented parallel to the flow direction of the sediments suggesting that the wood has experienced fluvial transport and thus, $^{14}$C ages of these samples likely overestimate the age of the sediment.

In-situ ages are found in partly degraded soil horizons containing abundant organic material at the top of the gravel unit A (unit A'), as well as at the top of and within the gravel unit B (Figure 5.7). The age of the most recent event horizon (MRE, Figure 5.7) is best constrained by sample No. 3 (Table 5.1) - a plant remnant preserved in a degraded soil horizon at the top of unit B that is clearly affected by coseismic deformation yielding an age of 394 ± 84 years BP. The overlaying channel sediments of unit D provide older, highly diachronous radiocarbon ages ranging from 700 ± 30 to 1200 ± 65 years BP (sample numbers 4, 8 and 11, Table 1). $^{14}$C ages of detrital charcoal samples of unit D in the western channel are even older ranging from 3785 ± 80 to 4802 ± 23 years BP. The ages for unit D are exclusively derived from detrital charcoal samples and thus, likely overestimate the age of the sediment. Therefore, the 338 years age determination represents a maximum age of the most recent coseismic event.

The age of the penultimate event horizon (PUE) is best constrained by samples No. 1 and 2 (Table 5.1) determined from two plant fragments of a degraded soil horizon (unit A')

preserved at the top of unit A. The samples yield ages of 6545 ± 97 and 6708 ± 80 years BP, respectively. Unit A' clearly truncates sediment deformation features preserved in unit A and thus, most likely represent a minimum age of the penultimate event. A sample taken from unit A' east of the main fault zone yields a $^{14}C$ age of 7035 ± 229 yrs BP. Here, the relation between unit A and unit A' is less conspicuous as sediment deformation also appears to affect unit A'.

Table 5.1: Results of radiocarbon dating for 21 samples. Detailed reports on radiocarbon dating are found on the attached CD-ROM (Appendix, Figure II.1)

| Sample No.[a] | Lab No.[b] | Conventional 14C, Years B.P. | Calibrated Age, (cal years B.P.) 2σ[c] | Average, (cal years B.P.) 2σ[d] | Sample Description |
|---|---|---|---|---|---|
| 1 | KIA43737 (SK09-130) | 6545 ± 97 | 6743 - 6548 | 6545 ± 97 | Plant remains from clay and silt rich A' horizon, provides maximum age of A' |
| 2 | KIA43738 (SK09-152) | 5871 ± 37 | 6788 - 6629 | 6708 ± 80 | Plant remains from clay and silt rich A' horizon, provides a minimum date of penultimate event |
| 3 | KIA43734 (SK09-86) | 338 ± 30 | 478 - 310 | 394 ± 84 | Plant remains from clay rich horizon at the uppermost portion of fluvial gravel of Unit B, maximum age of the latest event |
| 4 | KIA43733 (SK09-59) | 825 ± 30 | 785 - 687 | 736 ± 49 | Plant remains from lowermost portion of clay rich channel fill of Unit D (eastern channel), approximates latest event age (inherited age) |
| 5 | KIA43735 (SK09-90) | 1382 ± 29 | 1342 - 1274 | 1308 ± 34 | Charcoal from sandy part of liquefaction feature in Unit C, Maximum date of liquefaction event (inherited age) |
| 6 | KIA43736 (SK09-117) | 6169 ± 85 | 7264 - 6806 | 7035 ± 229 | Charcoal from clay and silt rich A' horizon, provides a minimum age of penultimate event |
| 7 | GdS-1100 (SK09-56) | 1300 ± 80 | 1360 - 1050<br>1030 - 1010 | 1205 ± 155<br>1020 ± 10 | Plant remains from lower portion of fluvial gravel of Unit B, provides maximum age of Unit B |
| 8 | GdA-2304 (SK09-159) | 760 ± 20 | 730 - 670 | 700 ± 30 | Plant remains from lowermost portion of clay rich channel fill of Unit D (eastern channel), approximates latest event age |
| 9 | GdS-1104 (SK09-50) | 1385 ± 100 | 1520 - 1070 | 1295 ± 225 | Root from lower portion of fluvial gravel of Unit B, provides maximum age of Unit B |
| 10 | GdC-459 (SK09-49b) | 1180 ± 45 | 1250 - 1200<br>1190 - 970 | 1225 ± 25<br>1080 ± 110 | Branch of beech tree from upper portion of fluvial gravel of Unit B, provides minimum age of Unit B |
| 11 | GdA-2293 (SK09-24) | 1245 ± 15 | 1265 - 1135<br>1110 - 1090 | 1200 ± 65<br>1100 ± 10 | Plant remains from lowermost portion of clay rich channel fill of Unit D (eastern channel), approximates latest event age |
| 12 | GdA-2294 (SK09-26) | 950 ± 20 | 930 - 795 | 862 ± 67 | Plant remains from sand layer of the lower portion of Unit C, provides maximum age of Unit C |
| 13 | GdA-2295 (SK09-53) | 1030 ± 20 | 970 - 930 | 950 ± 20 | Charcoal from sand lens within the lower portion of Unit D, approximates latest event age |
| 14 | GdA-2296 (SK09-83) | 1240 ± 20 | 1265 - 1080 | 1172 ± 92 | Plant remnant from silty layer within the upper portion of fluvial gravel of Unit B, provides minimum age of Unit B |

| Sample No.[a] | Lab No.[b] | Conventional 14C, Years B.P. | Calibrated Age, (cal years B.P.) 2σ[c] | Average, (cal years B.P.) 2σ[d] | Sample Description |
|---|---|---|---|---|---|
| 15 | GdA-2297 (SK09-94) | 110.41 ± 0,2 pMC | *1957 - 1995 cal A. D.* | *1957 - 1995 cal A. D.* | Plant remnant from uppermost portion of channel fill of Unit D (eastern channel), probably maximum age of the cropping soil horizon |
| 16 | GdA-2298 (SK09-109) | 4155 ± 20 | 4825 - 4780<br>4770 - 4610<br>4600 - 4585 | 4802 ± 23<br>4690 ± 80<br>4592 ± 8 | Branch of oak tree from sandy layer within lowermost portion of Unit D (western channel), provides maximum age of western channel fill |
| 17 | GdA-2299 (SK09-144) | 3515 ± 25 | 3865 - 3705 | 3785 ± 80 | Charcoal from silty soil horizon of the upper portion of Unit D (western channel), inherited age |
| 18 | GdA-2300 (SK09-145) | 4070 ± 20 | 4790 - 4765<br>4620 - 4515<br>4475 - 4445 | 4777 ± 13<br>4567 ± 53<br>4460 ± 15 | Charcoal from clay rich horizon of the upper portion of Unit D (western channel), inherited age |
| 19 | GdA-2301 (SK09-147) | 4395 ± 20 | 5045 - 4990<br>4985 - 4870 | 5017 ± 28<br>4927 ± 58 | Charcoal from clay rich horizon of the upper portion of Unit D (western channel), inherited age |
| 20 | GdA-2302 (SK09-151) | 1280 ± 20 | 1280 - 1175 | 1227 ± 53 | Clay rich soil horizon within central portion of fluvial gravel of Unit B, provides minimum age of Unit B |
| 21 | GdA-2303 (SK09-158) | 1400 ± 20 | 1340 - 1285 | 1312 ± 28 | Plant remains from sandy soil horizon within fluvial gravel of central portion of Unit B, provides minimum age of Unit B |

[a] See trench log Figure 5.7 for precise sample locations

[b] Samples 1 - 5 were prepared and analyzed by Leibniz-Laboratory for Radiometric Dating and Isotope Research, Max-Eyth-Str. 11-13, 24118 Kiel, Germany; samples 5 - 21 were prepared and analyzed by Gliwice Radiocarbon Laboratory, Krzywoustego 2, 44-100 Gliwice, Poland

[c] To obtain the calibrated age, the conventional radiocarbon age in 14C years has been calibrated against calendar years (in years before present, which is before 1950) based on comparing the conventional age to a spline fit through the tree ring calibration curve of Reimer et al. (2009) and Hua and Barbetti (2004)

[d] Average of the age range from the calibrated age curve with 2σ uncertainties.

## 5.5 Interpretation

### 5.5.1 Reconstruction of Coseismic Events

Pre-Holocene activity along this fault segment cannot be reconstructed, as all sediments are younger than Holocene age. Thus, the initial stage of the trench site represented by undeformed early Holocene gravel above a fault that cuts Devonian basement rocks. The penultimate event (Figure 5.11a) ruptures unit A and leads to a displacement in range of cm to dm. During the interseismic period a clay-rich soil horizon (unit A') develops at the top of unit A (Figure 5.11b). Two plant fragments from this horizon provide ages of 6545 ± 97 and 6708 ± 80 years BP, respectively. Following the development of this soil horizon, a sedimentation period leads to the partial erosion of unit A' and deposition of unit B (Figure 5.11c). The most recent event ruptures all gravel layers and leads to a displacement of a few dm (Figure 5.11d). The rupture event occurred presumably after 394 ± 84 yrs BP, based on radiocarbon dating of plant fragments of the topmost portion of unit B (sample No. 3, Table 5.1). From trench observations it is not obvious whether unit C has been deposited before or after the most recent rupture event. Unit C does only expose liquefaction features, which can also result from a different coseismic event of a neighboring fault. Thus, the deposition of unit C after the most recent rupture event (Figure 5.11e) is one hypothesis that remains unproven. After the most recent coseismic event, units B and C are incised and unit D is deposited (Figure 5.11f).

### 5.5.2 Resolution of Displacement

The maximum offset across the fault zone is constrained by three offset markers (Figure 5.12) – the contact between units A and B (1.0 ± 0.2 m), the contact between units B and C (0.9 ± 0.2 m), and the surface scarp (0.8 ± 0.15 m). A fourth, less conspicuous offset marker is the contact between unit A and the basement rocks. This contact is exposed only at one location in the trench, at the eastern end of the main fault zone (Figure 5.7). However, drill cores derived from the installation of wells for groundwater lowering provide basement depth at two further locations east of the fault zone. These differences in basement depth indicate that the offset of the basement is ~ 1.2 m and thus, coincides with the offset measured in the displaced sediments.

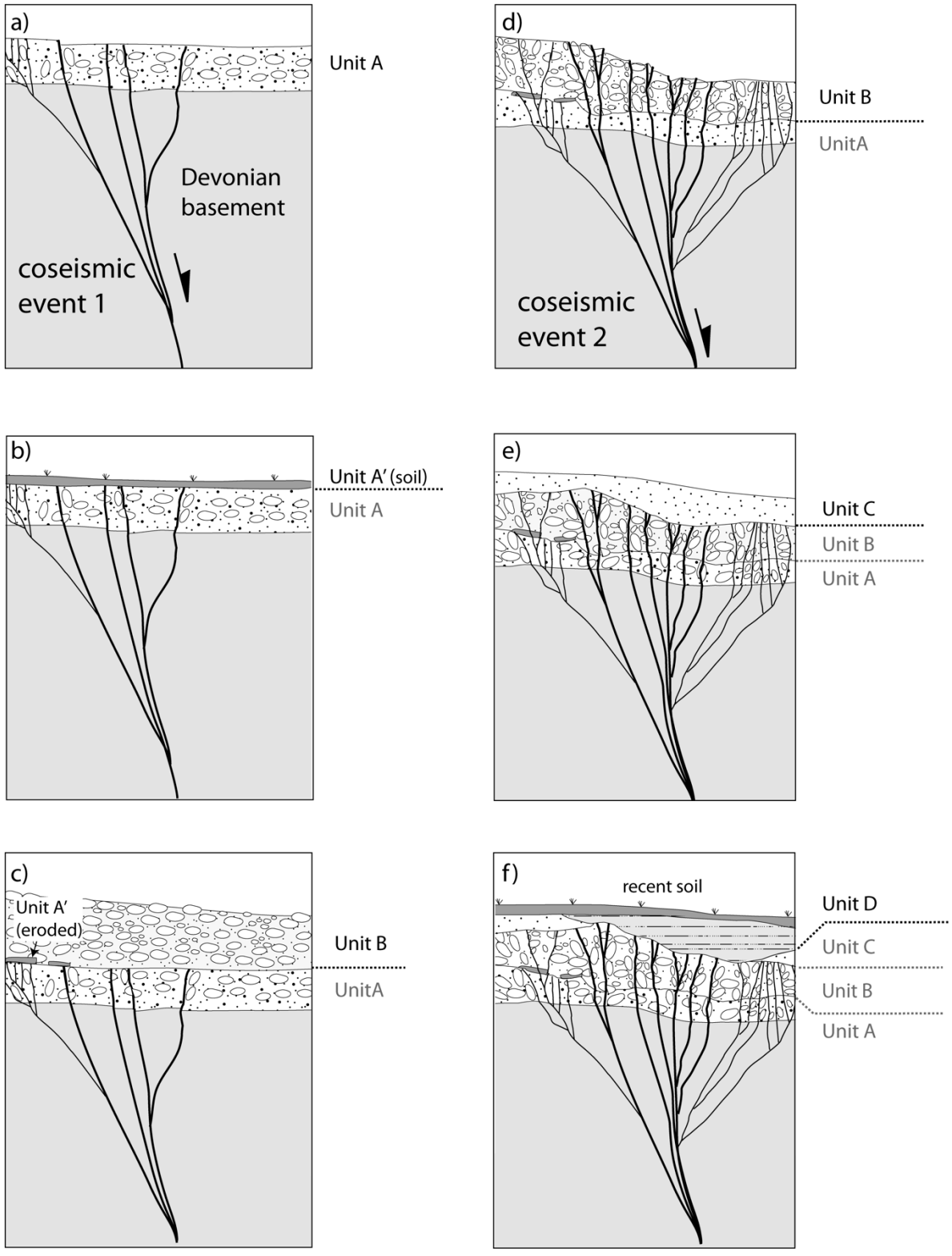


Figure 5.11: Reconstruction of rupture-, sedimentation-, and erosion events at the exposed fault segment. (a) penultimate rupture event affecting early to mid Holocene gravels of unit A. Gravel deformation is indicated by rotated and fractured pebbles; (b) soil formation (unit A') above unit A; (c) erosion of unit A' leading to patchwise preservation of this soil horizon; sedimentation of gravel deposit unit B; (d) most recent rupture event leading to repeated deformation of unit A and initial deformation of unit B. (e) sedimentation of unit C; (f) channel incision and sedimentation of unit D; present-day soil formation.

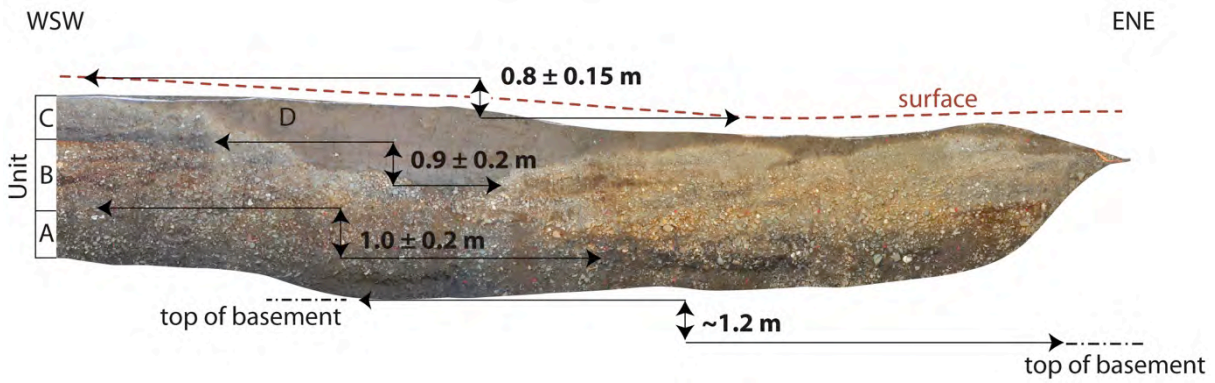


Figure 5.12: Photo mosaic of the eastern part of the northern trench wall showing four displaced marker horizons. The offset of basement rocks is determined by trench measurements and drilling.

### 5.5.3 Robustness of Event Horizons

We identified the contact between unit A and A' as the oldest exposed event horizon (Figure 5.7). Unit A' is a strongly degraded soil horizon and it is visible only at four locations in the trench (Figure 5.7). This horizon unconformably overlays unit A and clearly truncates the deformed gravels west of the main fault zone. The age of unit A' is well constrained by three radiocarbon ages (samples 1, 2 and 6, Table 5.1). We thus consider the contact between unit A and A' to be a robust event horizon that provides a minimum age of the penultimate rupture event.

The youngest event horizon is interpreted to be the contact between unit B and the incised channel deposits of unit D. It is not clear whether the rupture propagated coseismically through unit C, because this unit only displays liquefaction features. Unit D lacks any sediment deformation. On the other hand we need to consider that the sedimentary composition of this deposit (clayey silt, few sandy parts) and the high groundwater level and associated clay migration processes (Scheffer and Schachtschabel, 2002) may have masked any rupture-related sediment deformation. The age constraints of the event horizon are limited to one sample of the ruptured gravel unit B (sample 3, Table 5.1), because samples from the overlying units only provide inherited radiocarbon ages (Figure 5.8). We therefore consider the contact between units B and D an event horizon that represents a robust maximum age of the most recent rupture event.

### 5.5.4 Recurrence Intervals

We identified two event horizons in the deformed gravel deposits A and B (Figure 5.7). The most recent event most likely matches the 1756 AD earthquake. The penultimate event has a minimum age of 6708 ± 80 yrs BP and is likely not older than 10 000 years, based on the sedimentological interpretation of similar gravel deposits in the vicinity of the trench site (Klostermann, 1992). The cumulative offset of the exposed fault segment is 1 ± 0.2 m. This results in average Holocene fault displacement rates of 0.1 ± 0.02 to 0.17 ± 0.03 mm/yr and in recurrence intervals in the order of 6 000 to 10 000 years.

### 5.5.5 Complexity of the Fault Zone

In contrast to many normal faults, which produce simple surface ruptures along a single fault plane (McCalpin, 2009b), the fault rupture at the Untermaubach site is characterized by complex anastomosing fractures and distributed slip over a ~ 40 m wide fault zone. Deformation is best described by diffuse step faulting, with each minor fault accommodating a few mm-cm of vertical slip. Results from other studies (Crone, 1985; Crone et al., 1987; McCalpin, 1983) suggest that normal faults produce simple surface ruptures over the major portion of their entire length. Complex rupture patterns result from relatively unusual subsurface conditions that lead to fault branching (McCalpin, 2009b). With the exception of the Untermaubach site no further data exist for the Schafberg fault to evaluate rupture style and fault complexity. However, due to the clear expression of the fault morphology north of Untermaubach (Figure 5.3) simple fault geometry for most of the fault length is likely. The Untermaubach site is unusual compared to other localities along the Schafberg fault, because it is located at a right-step of the NW-SE trending normal fault, which implies a sinistral component for the total displacement (Figure 5.13). Strike-slip faults often form complex surface-rupture zones, so that the lateral component of this fault segment may have induced the formation of complex rupture patterns at the Untermaubach site.

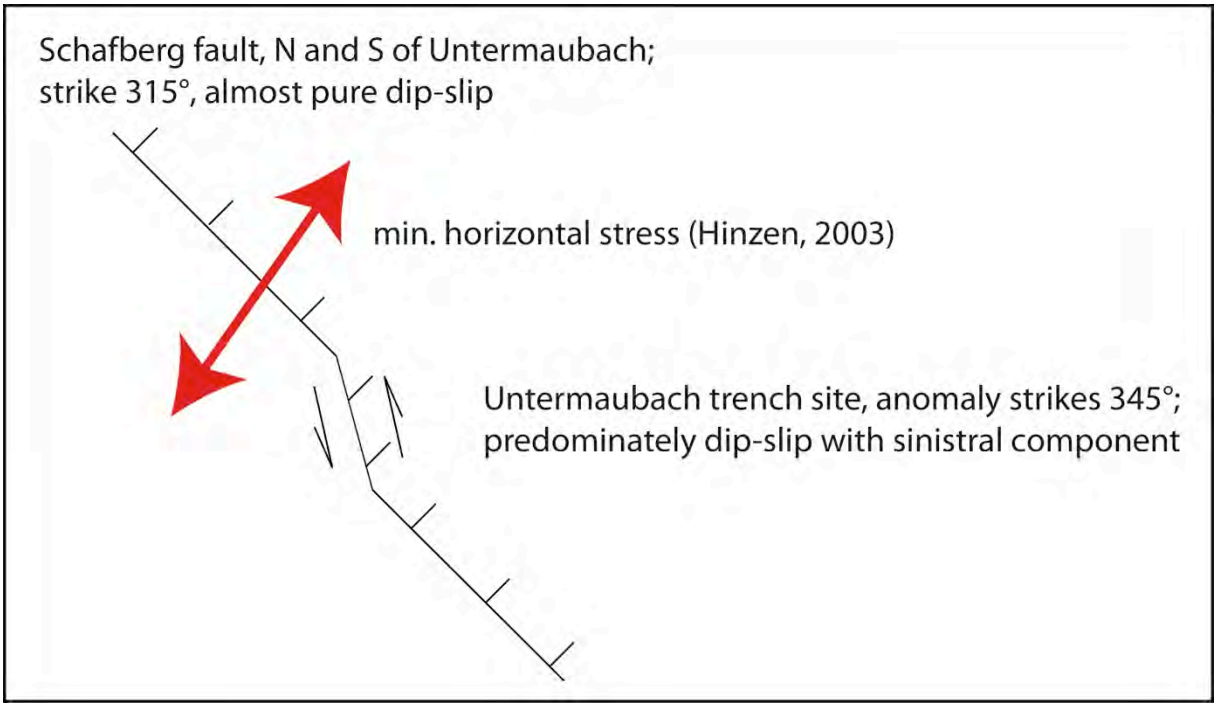


Figure 5.13: Schematic map view of the Schafberg fault with respect to the recent stress field. The red arrow indicates the direction of minimum horizontal stress as calculated by Hinzen et al. (2003).

## 5.6 Discussion

This study presents the first paleoseismic data for the Schafberg fault, a subsidiary fault in the Lower Rhine Graben whose seismically active character was previously unknown. In the following, we test the robustness of our results and discuss the significance of our study in light of the ongoing debates on spatiotemporal fault-slip patterns in low-strain regions. We also discuss possible triggering mechanisms for large intraplate earthquakes.

### 5.6.1 The Penultimate Event

The event horizon for the Penultimate event (PUE) is constrained by four patch-like remnants of a paleosoil horizon at the top of unit A (Figure 5.7). Fractured gravels west of the main fault zone are clearly truncated by this horizon. Furthermore, the measured ~1 m cumulative offset of sedimentary layers is unlikely to be the product of only one event considering a reasonable maximum earthquake magnitude ($M_W$ ~ 6.5) for the Schafberg fault. Because of its poor state of preservation, this event horizon is less conspicuous and more speculative compared to the event horizon of the most recent event. Also, a clear offset of layers cannot be associated with this horizon. Although the PUE at this fault exposure cannot unambiguously be proven, it appears a reasonable assumption supported by the trench observations and a possible explanation for the amount of fault displacement.

### 5.6.2 Seismogenic Potential of the Schafberg Fault

In order to evaluate the seismogenic potential of the Schafberg fault we assume a simple fault geometry with a constant fault dip and a planar fault surface. Using a large empirical database, Wells and Coppersmith (1994) developed a set of equations that relate $M_w$ to rupture length and maximum displacement. The empirically derived equation for $M_W$ on normal faults derived from surface rupture length (L) is:

$$M_W = 5.08 + 1.16 * \log(L)$$

Using this equation for the Schafberg fault, with a maximum rupture length of 16 km (Figure 2), the corresponding $M_{Wmax}$ would be 6.48 (~ 6.5). This is a reasonable magnitude for surface-rupturing earthquakes as reported in other regions (Bonilla, 1988; McCalpin, 2009a).

We can now calculate the maximum displacement with the empirically derived equation from Wells and Coppersmith (1994) for maximum displacement (MD) on normal faults derived from the Moment Magnitude ($M_W$):

$$MD = 10^{Mw-6.69/0.74}$$

For a maximum of $M_W$ 6.5, the maximum displacement would be 0.55 m. This implies that the maximum measured offset of 1.0 ± 0.2 m has likely been the product of multiple events along the exposed fault segment.

A further important point for evaluating the seismogenic potential of the Schafberg fault is also the orientation of the northeast dipping fault plane. Because no deep seismic data are available for the German portion of the Lower Rhine Graben, the dip of the Schafberg fault can only be estimated based on modeling results (Dirkzwager et al., 2000) and on seismic profiles from other locations of the rift system (Geluk et al., 1994; Michon et al., 2003; Remmelts and Duin, 1990). According to this, a reasonable dip for bordering faults of the Lower Rhine Graben is 58 ± 2°. Assuming this value for both the Schafberg fault and the southwest-dipping Rurrand fault, which crops out 11 km northwest of the Schafberg fault, both faults would merge at a depth of 8.8 ± 0.7 km. Calculations on the depth range of seismic events in the Lower Rhine Graben (Hinzen, 2003) are in the order of 12 to 18 km. Thus, depending on which fault acts as the superior structure in this part of the rift system, either the Schafberg or the Rurrand fault would not reach seismogenic depths (Figure 5.14).

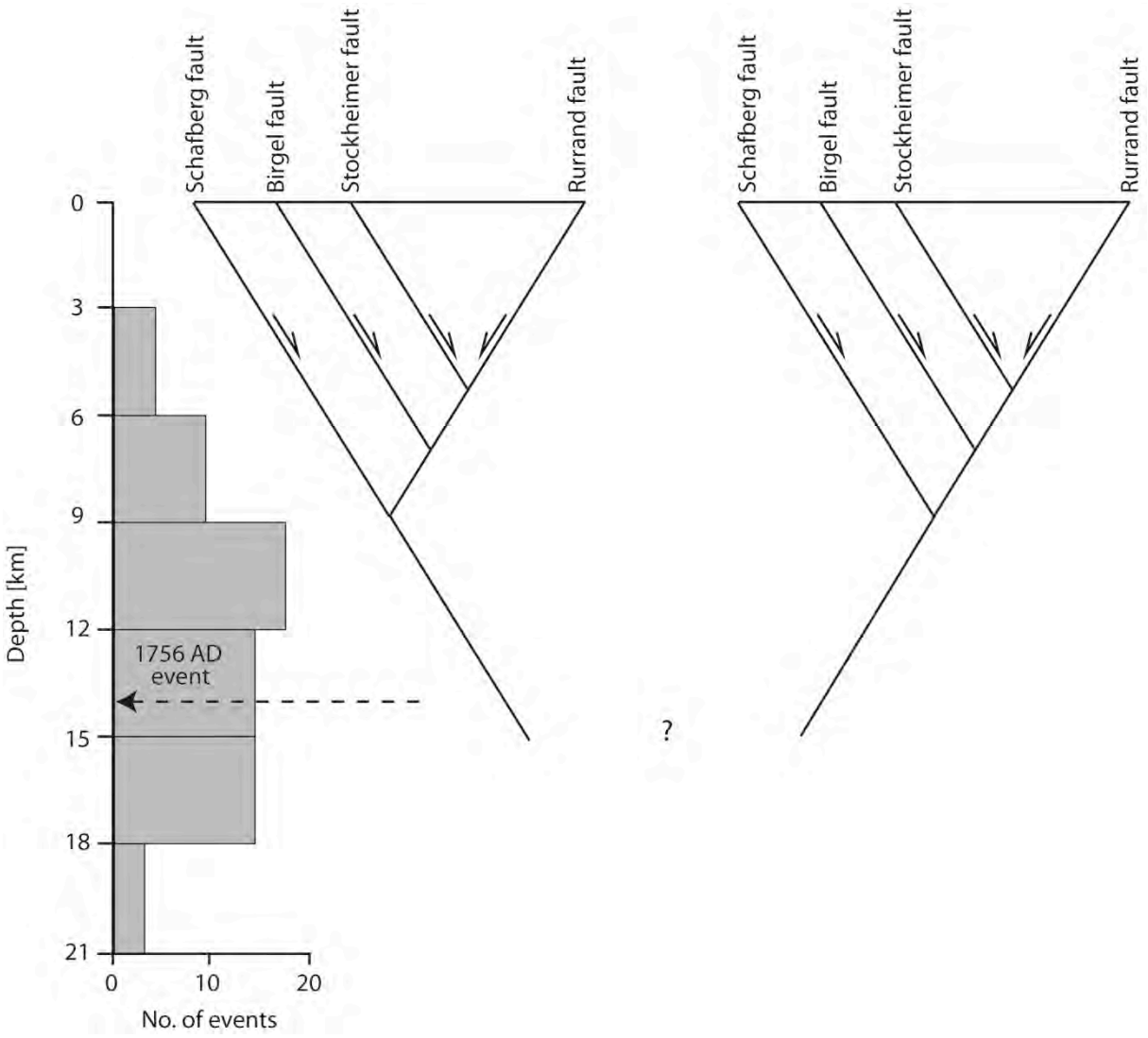


Figure 5.14: Simplified sketch of the fault-plane orientations of the Schafberg-, Birgel, Stockheimer- and Rurrand faults. The dashed lines in prolongation of the Schafberg and Rurrand faults indicate the uncertainty concerning the question which fault is the superior structure and traverses through the entire seismogenic layer. The block diagram on the left shows the hypocentral depth range of seismic events for the Lower Rhine Graben based on 61 instrumentally recorded earthquakes (modified from Hinzen, 2003). The dashed arrow depicts the estimated hypocentral depth of the 1756 AD Düren earthquake (Meidow, 1994).

### 5.6.3 Age of the Schafberg Fault

Like other faults in the Lower Rhine Graben and in the Rhine Graben system in general, the Schafberg fault most likely represents a reactivated structure originally formed during the Variscan orogeny (Ahorner, 1962; Dèzes et al., 2004; Fliegel, 1922; Schumacher, 2002; Ziegler, 1992). Along the Schafberg-Birgel fault system (Ahorner, 1962), reported offsets of Triassic and Devonian rocks are in the order of several hundred meters (Ahorner, 1962; Quitzow and Vahlensieck, 1955). Reported Quaternary offsets of 10 - 15 m are much

smaller than those of the major boundary fault in the eastern an central sector of the Lower Rhine Graben such as the Erft and Rurrand faults. The latter faults exhibit Quaternary displacements of > 150 m, and > 100 m, respectively (Ahorner, 1962). In contrast, the Holocene and historical displacment of the Schafberg fault reported in this study may exceed that of the Erft and Rurrand faults, on which Holocene activity has not been proven yet. This suggests that the Schafberg fault represents a structure reactivated during the latest rifting phase of the Lower Rhine Graben. This suggestion is supported by observations on the distribution of historical and present-day seismicity, which reveal a clustering of seismic events predominately in the SW sector of the Lower Rhine Graben (Camelbeeck, 2007; Hinzen, 2007). However, to better understand the complex spatiotemporal distribution of tectonic activity in this region, more paleoseismical studies are needed.

### 5.6.4 A Higher Holocene Slip Rate as a Response to Deglaciation?

The long-term slip rate on the Schafberg fault is only poorly constrained by displaced mid-Pleistocene gravel deposits (Upper Terrace gravel, 0.78 - 0.5 Ma, e.g., Klostermann, 1992; Kemna, 2008). The maximum displacement of the gravel terrace is 15 m (Quitzow, 1955), resulting in average Quaternary slip rates of 0.019 - 0.03 mm/yr.

Despite the large uncertainties in offsets and ages for the Quaternary slip rates of the Schafberg fault, the Holocene slip rates still appear to be up to ten times higher. A possible explanation for this may be clustering of seismic events over a relatively short period after a long period of tectonic quiescence, as suggested by previous studies in plate interiors and other low-strain regions (Crone et al., 1997; Friedrich et al., 2003). Another possibility for increased Holocene activity along this fault segment may be fault reactivation due to deglaciation and isotostatic unloading of the lithosphere after the last glacial maximum. This scenario has already been suggested in a former study conducted along the Feldbiss fault (Houtgast, 2005) and the Peel boundary fault in the Lower Rhine Graben (van den Berg et al., 2002). These authors suggest that glacial unloading of the Scandinavian ice sheet produced extensional stresses in the far field. These stresses could have triggered an increase in fault activity along the main faults of the Lower Rhine Graben during the initial phase of deglaciation. However, the increase of fault activity in the study by Houtgast et al. (2005) is observed around 15 000 yrs BP and it is thus significantly older than that observed at the Schafberg fault. Isostatic effects due to deglaciation around 15 000 yrs BP are interpreted to be the result of the rapid collapse of the fore-bulge, leading to fast unloading of the

lithosphere (Houtgast, 2005). However, since it is not clear how pronounced the lithospheric response due to deglaciation has been at 6 000 yrs BP compared to 15 000 yrs BP, an increase of seismicity due to deglaciation at the Untermaubach site cannot clearly be shown in the framework of this study.

### 5.6.5 Association with the 1756 Earthquake

Radiocarbon dating yields a maximum age of the latest rupture event of 394 ± 84 years BP (Table 5.1, Figure 5.7 and Figure 5.8). A minimum event age cannot be determined, because overlying deposits only yield inherited $^{14}C$ ages. As the radiocarbon ages may not unambiguously pinpoint that the 1756 AD event occurred on the Schafberg fault, we can still test a different scenario, e.g. the occurrence of an additional ground-rupturing event during the last 338 years. Based on the assumptions made in this study, a reasonable $M_W$ for an earthquake producing the observed offset is larger than 6.0. Historical documents do not give information on further large earthquakes in this region during the last 300-400 years (Leydecker, 2004). Therefore it is most likely that the identified sediment deformation in the trench represents the surface rupture of the 1756 AD earthquake.

### 5.6.6 Increased Seismic Activity in Central Europe after the 1755 Lisbon Earthquake?

On November 1$^{st}$ 1755 AD, three months prior to the 1756 AD Düren earthquake, an $M_W \sim 9$ earthquake occurred near the SW coast of Portugal, leading to catastrophic damage of the city of Lisbon and surrounding areas. As reported from different locations in Central Europe (Grünthal, 2001; Hinzen and Oemisch, 2001), the time after the major Lisbon earthquake is considered a period of increased seismic activity. The largest earthquakes that occurred within a few months after the Lisbon earthquake in Central Europe are the $M_W$ 6.1 Brig earthquake (Valais region, Switzerland) of December 9$^{th}$ 1755 AD (Gisler et al., 2004) and the $M_L$ 6.2 Düren earthquake (Lower Rhine Graben, Germany) of February 18$^{th}$ 1756 AD (Meidow, 1994; Figure 5.15).

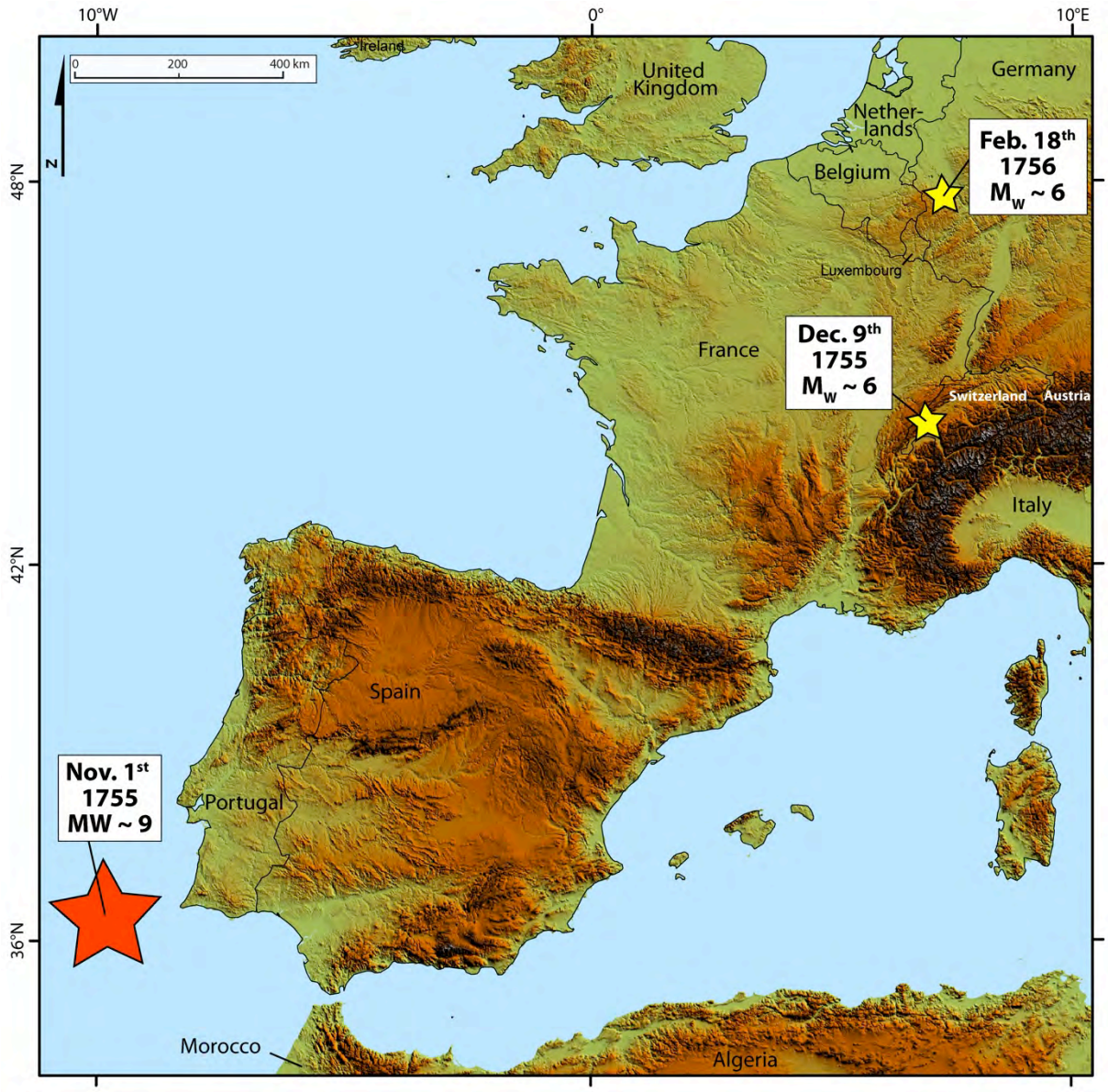


Figure 5.15: Seismicity of Western Europe of 1755/56 AD. The map shows the epicenter of the 1755 Lisbon earthquake, as well as the epicenters of the 1755 Brig earthquake (Valais region, Switzerland) and the 1756 Düren earthquake (Lower Rhine Graben, NW Germany). Map projection: UTM, Zone 30, Datum: WGS 84. Map derived from SRTM data, 90 m resolution.

Due to this clustering of large events it is reasonable to consider that the Brig and Düren earthquakes may have been linked to the Lisbon earthquake and triggered as a result of static stress transfer. To test this, we produced a series of simple stress transfer models to examine whether such a scenario is likely (Figure 5.16).

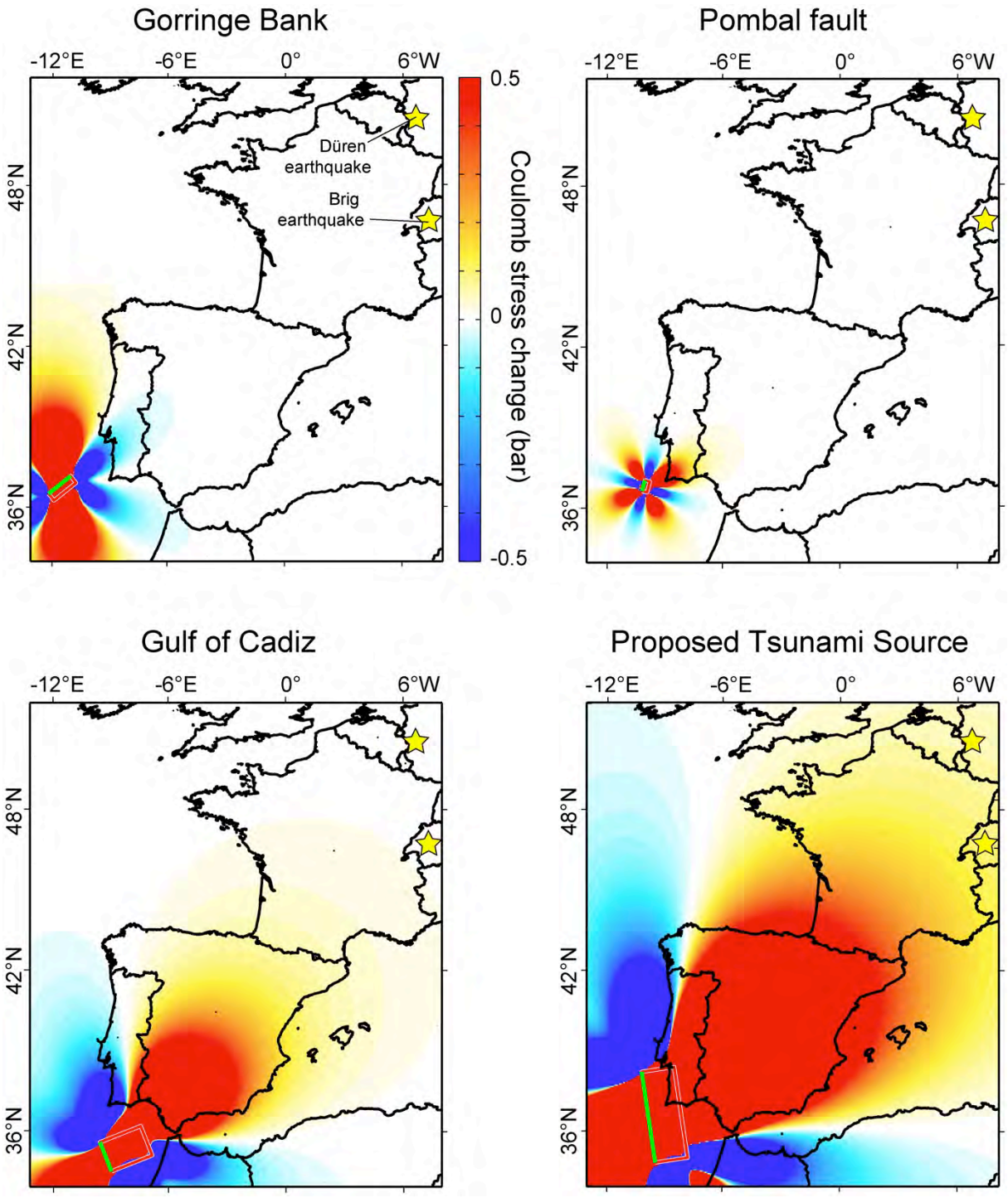


Figure 5.16: Static stress transfer models for the four proposed sources of the 1755 Lisbon earthquake. Input parameters: Average fault displacement: 25 m; friction coefficient: 0.6. Regional stress field: $\sigma_1$: 110° horizontal; $\sigma_2$: subvertical (89.1°); $\sigma_3$: 20° subhorizontal (1°); depth: 7.5 km.

According to recent studies, the actual fault that has been the seismic source for the $M_W \sim 9$ Lisbon earthquake is still a matter of debate. Proposed fault sources are: (1) the NE-SW striking Gorringe bank offshore the SW coast of Portugal e.g. (Babtista et al., 1998; Johnston, 1996), (2) the NNE-SSW striking Marquis de Pombal fault (Zitellini, 2001), (3) the

Gulf of Cadis overthrust (Gutscher, 2004), and (4) an unnamed fault proposed as most suitable tsunami source (Babtista et al., 1998). We tested different parameters for maximum coseismic displacement (12-25 m) based on previous studies (Johnston, 1996; Zitellini, 2001) and produced alternative models showing the static stress change for each proposed fault (Figure 5.16).

The results of our stress transfer models imply that, with the exception of the tsunami source fault (the largest proposed seismic source), none of the other faults would have caused a significant change in the static stress field in the Valais region and the Lower Rhine Graben. Additionally, only a coseismic scenario with average fault displacement of 25 m would cause a recognizable static stress change in these regions. Such large fault displacements usually only occur along subduction zones and whether the proposed subduction beneath the Gibraltar Arc is capable of producing such large displacement is still a matter of controversy (Gutscher, 2004; Johnston, 1996). With an average of 25 m of coseismic displacement and the 350 km long tsunami source proposed by Babtista et al. (1998), the static stress change would be on the order of 0.1 MPa for the Valais region and 0.2 MPa for the Lower Rhine Graben. Although this value still appears very low, it may still be sufficient to trigger earthquakes on faults that are on the threshold of failure as observed on faults in the Eastern California Shear Zone (e.g. King et al., 1994). However, to clearly demonstrate a connection between the Lisbon earthquake and smaller events in Central Europe further studies such as dynamic stress models would be necessary.

### 5.6.7 Relevance of the Trench Location for Slip Rate Measures

The Untermaubach trench site is located at the SW end of the Schafberg fault and it is the only site along strike where the fault is covered with Holocene sediments. Any constraints on slip rates and recurrence intervals are thus limited to one data point and may not be representative of the entire fault. Moreover, since it is likely that for $M > 6$ earthquakes the Schafberg fault has to rupture along its entire length, this study gives minimum rates rather than average or maximum rates, because the maximum coseismic slip is probably located in the central part of the rupture rather than at its end (Cowie and Roberts, 2001). The lack of more suitable trench sites along this fault segment does not allow for more precise offset and slip-rate estimates. And the trench site is located at a small right step with respect to the main strike of the Schafberg fault. As a consequence, displacement in this part of the fault is

probably a combination of dip-slip and left-lateral strike slip and therefore, the observed vertical displacement may be an underestimation of the true displacement (Figure 5.13).

### 5.6.8 Driving Mechanisms for Complex Deformation in Gravel

The widely-distributed sediment deformation in the studied fault exposure (Figure 5.7) represents a type of deformation that differs remarkably from those observed in many other trench studies carried out along intraplate normal faults in the Lower Rhine Graben and other regions (Camelbeeck and Meghraoui, 1998; McCalpin, 2009b; Peters et al., 2005; Vanneste et al., 2001). Reasons for this unusual setting are presumably rooted either in the local geology or in the coseismic rupture process. The geological setting of the trench site is unusual compared to the majority of trench studies in active rifts because of the relatively thin cover (5-6 m) of unconsolidated and water-saturated sediments above bedrock. This implies a large contrast in material properties for ruptures and waves when they reach the surface. At the Untermaubach site, although information on the fault structure at depth is missing, it is still reasonable to assume that a well-defined fault plane may exist in the basement rocks. During a coseismic event, however, once the earthquake rupture traverses the boundary between bedrock and unconsolidated sediment the rupture may disperse into numerous small fault branches due to enhanced damping processes in unconsolidated sediments. In contrast, in thick sedimentary deposits, as documented e.g. for the central Lower Rhine Graben, such boundary effects between bedrock and sediment are probably less significant due to higher confining pressure and less distinct damping processes at greater depth. In water-saturated sediments as observed at our study site, such dispersion effects may potentially be enhanced, as proposed in previous studies on sediment acoustics in water-saturated granular sediments (Sessarego et al., 2008; Stoll, 2002) and seismological studies on subaqueous reservoir dynamics (Cheng, 1986).

Another possibility for explaining the distributed deformation pattern may be that the observed deformation features are the surface expression of a coseismic rupture, which barely reached the surface. This seems a reasonable assumption considering the proposed maximum magnitude for the Schafberg fault ($M_{Wmax} \sim 6.5$) at a typical hypocentral depth range of 8 - 18 km.

Another possible mechanism for creating such complex fault zones is the formation of a monoclinal scarp, a process observed in cohesive gravels similar to those exposed at the Untermaubach trench site (Crone et al., 1987; McCalpin, 2009b). Importantly, such scarps

usually do not expose colluvial wedges as they accommodate displacement over numerous minor faults without exposing a free face large enough to produce recognizable colluvial wedges. This would be in agreement with the observations made in the Untermaubach trench, which lacks colluvial wedges in the fault zone. However, for a clear explanation of the complex deformation pattern at the Untermaubach site, further studies on the deeper fault structure of this and other faults in the Lower Rhine Graben, and further knowledge on deformation textures in unconsolidated sediments are needed.

## 5.7 Conclusions

The most significant lesson from our trench study is that the Schafberg fault is capable of producing large earthquakes with an associated ground rupture even though this fault is not a major boundary fault of the Lower Rhine Graben and has not accumulated significant amounts of Quaternary offsets. Surface faulting at the trench site is characterized by broad gravel deformation distributed over a ~ 10 m-wide fault zone and a ~ 30 m-wide damage zone expressed by abundant fractured and rotated pebbles.

Sample ages suggest that the youngest event occurred during the last 800 years (and probably during the last 340 years) and therefore likely matches the 1756 AD Düren earthquake, since no other event large enough occurred in the vicinity of the analyzed fault segment in this period of time (Hinzen, 2007; Leydecker, 2004; Meidow, 1994).

Based on the identification of two event horizons in the trench, we have evidence for at least one, possibly two large paleoearthquakes from 250 yrs BP to 6 -10 ka BP producing a maximum vertical displacement of 1.2 ± 0.2 m. Because the trench only exposes Holocene sediments, we have no constraints on older earthquakes on this fault segment and thus, we can only suggest recurrence intervals in the order of 6 -10 ka for the Schafberg fault.

The Schafberg fault is characterized by a relatively high seismic activity during the Holocene, but a relatively small total displacement. This suggests that the fault may be representative of the latest reactivation phase of basement faults implying a period of increased seismic activity in the SW part of the Lower Rhine Graben. To improve the knowledge on spatiotemporal distribution patterns of tectonic activity, more paleoseismical studies, e.g. in the eastern and central parts of the Lower Rhine Graben, will be necessary.

## 5.8 References

Ahorner, L., 1962, Untersuchungen zur Quartären Bruchtektonik der Niederrheinischen Bucht: Eiszeitalter und Gegenwart, Quaternary Science Journal, v. 13, no. 1, p. 24-105.

Babtista, M. A., Miranda, P. M. A., Miranda, J. M., and Mendes Victor, L. A., 1998, Constraints on the source of the 1755 Lisbon tsunami inferred from the numerical modelling of historical data: Journal of Geodynamics, v. 25, p. 159-174.

Bonilla, M. G., 1988, Minimum earthquake magnitude associated with coseismic surface faulting: Bulletin of the Association of Engineering Geologists, v. 25, no. 1, p. 17-29.

Bonjer, K. P., 1997, Seismicity pattern and style of seismic faulting at the eastern borderfault of the southern Rhine Graben: Tectonophysics, v. 275, no. 1–3, p. 41-69.

Braile, L. W., 1982, An Ancient Rift Complex and its Relation to Contemorary Seismicity in the New Madrid Seismic Zone: Tectonics, v. 1, no. 2, p. 225-237.

Camelbeeck, T., K. Vanneste, P. Alexandre, K. Verbeeck, T. Petermans, P. Rosset, M. Everaerts, R. Warnant, M. Van Camp, 2007, Relevance of active faulting and seismicity studies to assessments of long-term earthquake activity and maximum magnitude in intraplate northwest Europe, between the Lower Rhine Embayment and the North Sea, In: Stein, S. and Mazotti, S., ed., Continental Intraplate Earthquakes: Science, Hazard, and Policy Issues: The Geological Society of America Special Paper, v. 425, no. 14, p. 193-224.

Camelbeeck, T., and Meghraoui, M., 1996, Large Earthquakes in Northern Europe More Likely Than Once Thought: EOS, v. 77, no. 42, p. 405-409.

-, 1998, Geological and geophysical evidence for large palaeo-earthquakes with surface faulting in the Roer Graben (northwest Europe): Geophys. J. Int., v. 132, p. 347-362.

Camelbeeck, T., Vanneste, K., and Van Camp, M., 2008, The seismic activity in stable continental Europe: Seismic Risk 2008 - Earthquakes in North-Western Europe, p. 25-32.

Cheng, A. H. D., 1986, Effect of Sediment on Earthquake-Induced Reservoir Hydrodynamic Response: J. Eng. Mech., v. 112, no. 7, p. 654-665.

Cowie, P. A., and Roberts, G. P., 2001, Slip rates and spacings for active normal faults: Journal of Structural Geology, v. 23, p. 1901-1915.

Crone, A. J., 1985, Fault scarps, landslides and other features associated with the Borah Peak earthquake of October 28, 1983, central Idaho - a field trip guide, with a section on the Doublespring Pass road trench by Hait, M. M. Jr.: USGS Open-File Report, v. B 23, p. 85-290.

Crone, A. J., Machette, M. N., Bonilla, M. G., and Lienkaemper, J. J., 1987, Surface faulting accompanying the Borah Peak earthquake and segmentation of the Lost River fault, central Idaho: Bulletin of the Seismological Society of America, v. 77, p. 739-770.

Crone, A. J., Machette, M. N., and Bowman, J. R., 1997, Episodic nature of earthquake activity in stable continental regions revealed by palaeoseismicity studies of Australian and North American quaternary faults: Australian Journal of Earth Sciences, v. 44, no. 2, p. 203-214.

Dèzes, P., Schmid, S. M., and Ziegler, P. A., 2004, Evolution of the European Cenozoic Rift System: interaction of the Alpine and Pyrenean orogens with their foreland lithosphere: Tectonophysics, v. 389.

Dirkzwager, J. B., Van Wees, J. D., Cloething, A. A. P. L., Geluk, M. C., Dost, B., and Beekman, F., 2000, Geo-mechanical and rheological modelling of upper crustal faults and their near-surface expression in the Netherlands: Global and Planetary Change, v. 27, p. 67-88.

Fliegel, G., 1922, Der Untergrund der Niederrheinischen Bucht: Abh. preuß. geol. L.-A., v. 92, p. 1-155.

Friedrich, A. M., Strecker, M. R., and Scherbaum, F., 2002, Active intraplate deformation in central Europe: paleoseismology of the Lower Rhine Embayment: DFG New Grant Application, p. 1-42.

Friedrich, A. M., Wernicke, B., and Niemi, N. A., 2003, Comparison of geodetic and geologic data from the Wasatch region, Utah, and implications for the spectral character of Earth deformation at periods of 10 to 10 million years: Journal of Geophysical Research, v. 108, no. B4, p. 2199-2322.

Fuller, M. L., 1912, The New Madrid Earthquake, U. S. Geol. Surv. Bull., v. 494, p. 1-119.
Geluk, M. C., Duin, E. J., Dusar, M., Rijkers, R., van den Berg, M. W., and van Rooijen, P., 1994, Stratigraphy and tectonics of the Roer Valley Graben: Geologij en Mijnbouw, v. 73, no. 2-4, p. 129-141.
Gisler, M., Fah, D., and Deichmann, N., 2004, The Valais earthquake of December 9 1755: Eclogae geol. Helv., v. 97, p. 411-422.
Grünthal, G., Fischer, J., 2001, Eine Serie irrtümlicher Schadenbeben im Gebiet zwischen Nördlingen und Neuburg an der Donau vom 15. bis zum 18. Jahrhundert: Mainzer Naturwissenschaftliches Archiv, v. 39, p. 15-32.
Gutscher, M. A., 2004, What Caused the Great Lisbon Earthquake?: Science, v. 305, p. 1247-1248.
Haak, H. W., Meidow, H., Ahorner, L., Verbeiren, R., Hoang-Trong, P., Musson, R. M. V., Henni, P., Schenkova, Z., and Zimova, R., 1994, The macroseismic map of the Roermond earthquake of April 13, 1992: Geologij en Mijnbouw, v. 73, p. 265-270.
Hinzen, K. G., 2003, Stress field in the Northern Rhine area, Central Europe, from earthquake fault plane solutions: Tectonophysics, v. 377, p. 325-356.
Hinzen, K. G., and Oemisch, M., 2001, Location and Magnitude from Seismic Intensity Data of Recent and Historic Earthquakes in the Northern Rhine Area, Central Europe: Bulletin of the Seismological Society of America, v. 91, no. 1, p. 40-56.
Hinzen, K. G., S. K. Reamer 2007, Seismicity, seismotectonics, and seismic hazard in the northern Rhine area. In: Stein, S. and Mazotti, S., ed., Continental Intraplate Earthquakes: Science, Hazard, and Policy Issues: Geological Society of America Special Paper, v. 425, p. 225-242.
Holzapfel, E., 1904, Beobachtungen im Diluvium der Gegend von Aachen: Jb. preuß. geol. L.-A., v. 24, p. 483-502.
Houtgast, R. F., R.T. Van Balen, C. Kasse, 2005, Late Quaternary evolution of the Feldbiss Fault (Roer Valley Rift System, the Netherlands) based on trenching, and its potential relation to glacial unloading: Quaternary Science Reviews, v. 24, p. 491-510.
Houtgast, R. F., R.T. Van Balen, C. Kasse, J. Vandenberghe, 2003, Late Quaternary tectonic evolution and postseismic near surface fault displacement along the Geleen Fault (Feldbiss Fault Zone - Roer Valley Rift System, the Netherlands), based on trenching: Geologie en Mijnbouw, v. 82, no. 2, p. 177-196.
Johnston, A. C., 1996, Seismic moment assessment of earthquakes in stable continental regions, III New Madrid 1811-1812, Charleston 1886 and Lisbon 1755: Geophys. J. Inr., v. 126, p. 314-344.
Johnston, A. C., 1996, The Enigma of the New Madrid Earthquakes of 1811-1812: Annual Review of Earth and Planetary Sciences, v. 24, p. 339-384.
King, G., Stein, R., and Lin, J., 1994, Static Stress Changes and the Triggering of Earthquakes: Bulletin of the Seismological Society of America, v. 84, no. 3, p. 935-953.
Klostermann, J., 1992, Das Quartär der Niederrheinischen Bucht: Ablagerungen der letzten Eiszeit am Niederrhein. : Geological Survey of Northrhine-Westphalia, Krefeld, p. 1-200.
Knapp, G., and Hager, H., 1980, Geologische Karte der nördlichen Eifel: 1:100.000: Geological Survey of Northrhine-Westphalia, Krefeld.
Lehmann, K., Klostermann, J., and Pelzing, R., 2001, Paleoseismological Investigations at the Rurrand Fault, Lower Rhine Embayment: Netherlands Journal of Geosciences, v. 80, no. 3-4, p. 139-154.
Leydecker, G., 2004, Erdbebenkatalog für die Bundesrepublik Deutschland mit Randgebieten für die Jahre 800 - 2003. Datenfile, BGR Hannover.: Datenfile, BGR Hannover.
McCalpin, J. P., 1983, Quaternary geology and netoectonics of the west flank of the northern Sangre de Cristo Mountains, south-central Colorado: Colorado School Mines, v. 77, no. 3, p. 97 pp.
-, 2009a, Paleoseismology: International Geophysics Series, v. 95, p. 1-613.
-, 2009b, Paleoseismology in Extensional Tectonic Environments, In McCalpin, J., ed., Paleoseismology, International Geophysics Series, v. 95, p. 171-269.
Meghraoui, M., Camelbeeck, T., Vanneste, K., M., B., and Jongmans, D., 2000, Active faulting and paleoseismology along the Bree fault, lower Rhine graben, Belgium: Journal of Geophysical Research v. 105, no. B6, p. 13809-13841.

Meghraoui, M., Delouis, B., Ferry, M., Giardini, D., Huggenberger, P., Spottke, I., and Granet, M., 2001, Active Normal Faulting in the Upper Rhine Graben and Paleoseismic Identification of the 1356 Basel Earthquake: Science, v. 293, p. 2070-2073.

Meidow, H., 1994, Comparison of the macroseismic field of the 1992 Roermond earthquake, the Netherlands, with those of large historical earthquakes in the Lower Rhine Embayment and its vicinity: Netherlands Journal of Geosciences, v. 73, no. 2-4, p. 282-289.

Michon, L., Van Balen, R., Merle, O., and Pagnier, H., 2003, The Cenozoic evolution of the Roer Valley Rift System integrated at a European scale: Tectonophysics, v. 367, p. 101-126.

Obermeier, S., F., 1996, Use of liquefaction-induced features for paleoseismic analysis — An overview of how seismic liquefaction features can be distinguished from other features and how their regional distribution and properties of source sediment can be used to infer the location and strength of Holocene paleo-earthquakes: Engineering Geology, v. 44, no. 1-4, p. 1-76.

Peters, G., Buchmann, T. J., Connolly, P., Van Balen, R., Wenzel, F., and Cloething, S. A. P. L., 2005, Interplay between tectonic, fluvial and erosional processes along the Western Border Fault of the northern Upper Rhine Graben, Germany: Tectonophysics, v. 406, p. 39-66.

Quitzow, H. W., and Vahlensieck, O., 1955, Ober Pleistozäne Gebirgsbildung und rezente Krustenbewegungen in der Niederrheinischen Bucht: Int. J. Earth Sci., p. 56-67.

Remmelts, G., and Duin, E. J. T., 1990, Results of a regional deep seismic survey in The Netherlands. In: B. Pinet & C, Bois (eds): The potential of deep seismic profiling for hydrocarbon exploration: Proc. Inst. Franeois Petr. Expl. Res. Conf, p. 335-343.

Richter, D., 1962, Die Hochflächen-Treppe der Nordeifel und ihre Beziehungen zum Tertiär und Quartär der Niederrheinischen Bucht: Geologische Rundschau, v. 52, no. 1, p. 376-404.

Scheffer, F., and Schachtschabel, P., 2002, Lehrbuch der Bodenkunde: Spektrum Akademischer Verlag Heidelberg, v. 15. Auflage, p. 381-403.

Schmedes, J., Hainzel, S., Reamer, S. K., Scherbaum, F., and Hinzen, K. G., 2005, Moment release in the Lower Rhine Embayment, Germany: seismological perspective of the deformation process: Geophys. J. Inr., v. 160, p. 901-909.

Schumacher, M. E., 2002, Upper Rhine Graben: the role of preexisting structures during rift evolution: Tectonics, v. 21, no. 6-1, p. 6-17.

Sessarego, J. P., Ivakin, A. N., and Ferrand, D., 2008, Frequency Dependence of Phase Speed, Group Speed, and Attenuation in Water-Saturated Sand: Laboratory Experiments: Journal of Oceanic Engineering, v. 33, no. 4, p. 359-366.

Stoll, R. D., 2002, Velocity dispersion in water-saturated granular sediment Journal of the Acoustical Society of America, v. 111, no. 2, p. 785-793.

Strecker, M. R., Hilley, G., Lück, E., Scherbaum, F., and Spangenberg, U., 2002, S.A.F.E. Annual Report. Searching for surface ruptures associated with the Düren 1755/56 earthquakes, Germany: unpublished data, Potsdam University, p. 1-45.

Streich, R., 2003, Geophysical Prospecting of Suspected Holocene Fault Activity in the Lower Rhine Embayment, Germany: Diploma Thesis, University of Potsdam, Germany, p. 1-125.

van den Berg, M. W., Vanneste, K., Dost, B., Lokhorst, A., van Eijk, M., and Verbeeck, K., 2002, Paleoseismological investigations along the Peel Boundary Fault: geological setting, site selection and trenching results: Netherlands Journal of Geosciences, v. 81, p. 39-60.

Vanneste, K., F. Mees, K. Verbeeck 2008, Thin-section analysis as a tool to aid identification of palaeoearthquakes on the “slow”, active Geleen Fault, Roer Valley Graben: Tectonophysics, v. 453, p. 94-109.

Vanneste, K., Meghraoui, M., and Camelbeeck, T., 1999, Late Quaternary earthquake-related soft-sediment deformation along the Belgian portion of the Feldbiss Fault, Lower Rhine Graben system: Tectonophysics, v. 309, p. 57-79.

Vanneste, K., and Verbeeck, K., 2001, Detailed paleoseismic investigation of the Rurrand Fault in Hambach trench, Germany: Cahiers du Centre Européen de Géodynamique et de Séismologie v. 18, p. 153-156.

Vanneste, K., Verbeeck, K., and Camelbeeck, T., 2008, A decade of paleoseismic research in the Roer Valley graben: Seismic Risk 2008 - Earthquakes in North-Western Europe, p. 57-64.

Vanneste, K., Verbeeck, K., Camelbeeck, T., Paulissen, E., Meghraoui, M., Renardy, F., Jongmans, D., and Frechen, M., 2001, Surface-rupturing history of the Bree fault scarp, Roer Valley graben: Evidence for six events since the late Pleistocene: Journal of Seismology, v. 5, p. 329-359.

Vanneste, K., Verbeeck, K., Moreno, D. G., and Camelbeeck, T., 2010, A database of seismic sources for the Roer Valley Rift system: Proceedings of the European Seismological Commission 32nd General Assembly, September 6-10, Montpellier, France p. 1.

Verbeeck, K., Beatse, H., Vanneste, K., Renardy, F., Van der Meer, H., Roy-Chowdhury, K., and Camelbeeck, T., 2000, Geomorphic and geophysical reconnaissance of the Reppel and Bocholt faults, NE Belgium, p. 1-4.

Wells, D. L., and Coppersmith, K. J., 1994, New Empirical Relationships among Magnitude, Rupture Length, Rupture Width, Rupture Area, and Surface Displacement: Bulletin of the Seismological Society of America, v. 84, no. 4, p. 974-1002.

Wenzel, F., and Brun, J. P., 1991, A deep reflection seismic line across the Northern Rhine Graben: Earth and Planetary Science Letters, v. 104, no. 2–4, p. 140-150.

Ziegler, P. A., 1992, European Cenozoic rift system: Tectonophysics, v. 208, no. 1–3, p. 91-111.

Zitellini, N., 2001, Source of 1755 Lisbon earthquake and tsunami investigated: EOS (Transactions, American Geophysical Union), v. 82, p. 285-291.

Zolitschka, B., 1998, A 14,000 year sediment yield record from western Germany based on annually laminated lake sediments: Geomorphology, v. 22, p. 1-17.

# Chapter 6

# *Fractured Clasts in Unconsolidated Gravels Record Coseismic Rupture*

## 6.1 Abstract

Unconsolidated sediments subjected to tectonic loading may produce various deformation features including liquefaction as well as folding of sand deposits and fracturing of gravels. While the former usually displays deformation due to coseismic shaking, the formation process of fractured clasts is still a matter of debate. In this study, we propose that abundant fractured clasts and their fracture pattern are the result of coseismic rupture. The fault-zone exposure in our study consists of numerous fractured clasts in unconsolidated Holocene gravel deposits. Gravel deformation is most prominent within a ~ 10 m wide fault core and coincides with the fault scarp and offset of strata of ~ 1 m. The fracture planes are predominately oriented sub-parallel to the fault plane (strike NW-SE, dip angle ~ 60° NW). Thin-section analysis of fractured clasts reveals trans-granular fractures on secondary cracks as well as local crushing and complex fracturing at contact points of the gravels as well as radial fractures suggesting complex point-loading processes combined with impact forces presumably triggered by tectonic processes. Furthermore, the near-surface location of the gravel deposits excludes fracture formation under slow tectonic loading due to the lack of overburden stress and thus, dynamic loading triggered by the propagating rupture remains the only satisfying explanation. Our results imply that fractured clasts in fault zones are a detector of coseismic rupture, and could potentially be used for calculations on the energy involved in the rupture process.

## 6.2 Introduction

For several decades deformed gravels have been the scope of numerous studies in different geological settings (Decker and Peresson, 1996; Ernston et al., 2001; Harker, 1993; Hippolyte, 2001; Jerzykiewicz, 1985; Kupsch, 1955; Tapponier et al., 1986; Tokarski and Swierczewska, 2005; Tokarski et al., 2007; Zuchiewicz et al., 2002). In areas affected by glacial processes, the orientation of fracture patterns in gravels has been used to infer information on transport directions and sub-glacial deformation mechanisms (Hiemstra and van den Meer, 1997; Kupsch, 1955). Research on meteorite impacts have used fractured and cratered gravels as indicator for impact-related shock deformation (Ernston et al., 2001). In structural geology and tectonic research, fractured clasts in exhumed fault zones from great depths have long been recognized as indicator for paleo-stress conditions in tectonically active regions (Eidelmann and Reches, 1992; Hippolyte, 2001; Jerzykiewicz, 1985; Lee et al., 1996; Ramsay, 1964; Tanner, 1963, 1976).

In this study, we introduce a new paleoseismic approach to detect coseismic fault slip in unconsolidated gravel deposits using fractured and offset clasts. In contrast to former studies, the fractured clasts at our study site (Figure 6.1) are exposed in a fault zone formed in young unconsolidated sediments very close to the surface (up to 0.5 m). This challenges previous conclusions that the fracture process under tectonic loading is only possible at burial depths of several hundred meters (Eidelmann and Reches, 1992). Conceivable deformation processes leading to tectonic fracturing of unconsolidated gravels include dynamic loading of clast contacts or impact processes of colliding clasts triggered by propagating seismic waves or the coseismic rupture front.

Fractured clasts in loose gravel deposits are rarely described in paleoseismic studies yet seem to provide useful information on rupture dynamics and the general seismogenic potential of presumably hazardous fault segments. Among others, fractured clasts in unconsolidated near-surface gravels have also been observed in exposed fault segments on the Alhambra hill in the Eastern Granada Basin, southern Spain (Azanón et al., 2004), western Taiwan (Lee et al., 1996), the Feldbiss fault zone in northeastern Belgium (Demoulin, 1996), and the Rex Hills area in the Eastern California Shear Zone (Baran et al., 2010).

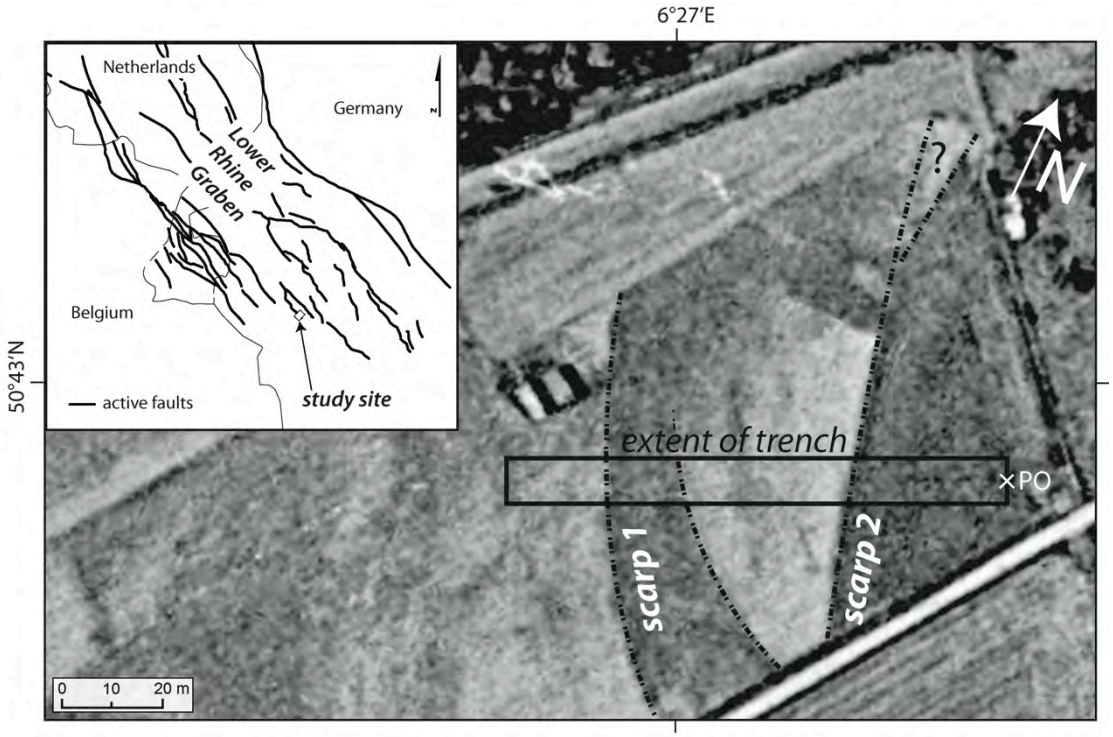


Figure 6.1: Satellite image of the study site. Shown are the trench location as well as the location and strike of the two surface scarps. PO: point of origin relevant for distance measurements in the trench log.

We present results from a detailed analysis of fractured clasts exposed in Holocene gravel deposits at the Untermaubach trench site (Figure 6.1, Chapter 4 and 5). The prime objectives of this study were to investigate the deformation processes leading to the fracture of gravels and determine whether or not the fractured clasts in this fault segment represent coseismic rupture. Furthermore, we aimed to examine whether fractured clasts in the near-surface exposure of fault zones can be generally used as a diagnostic tool to differentiate coseismic from aseismic fault displacement.

The clast study was carried out in a paleoseismic trench (Figure 6.2) installed across the Schafberg fault (Chapter 4 and 5), an E-dipping normal fault in the Lower Rhine Embayment. Gravel deposits at the study site predominately consist of unconsolidated and poorly sorted conglomerates (Figure 6.3). The sediments are situated below the present-day groundwater table and are thus water saturated. The gravels can be subdivided into two principal units. Unit A is the lowermost gravel unit consisting of predominately clast-supported gravel deposits. The matrix consists of silty clay commonly interspersed with both sand-rich lenses and sandy clay lenses. At the base of the exposure, clasts are up to 60 cm across. In the upper gravels, clasts have common diameters of 10 - 20 cm with isolated larger clasts of more than 40 cm across (Chapter 5).

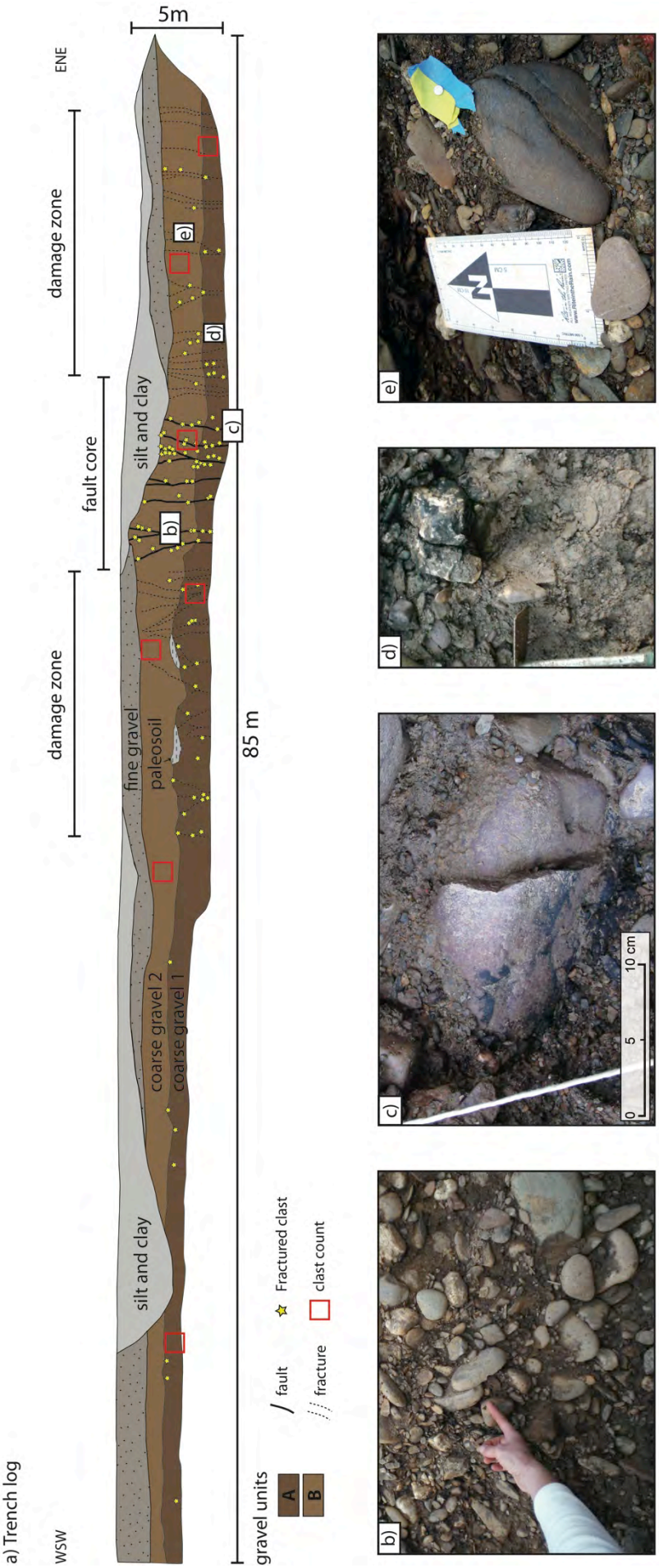
a) Trench log
WSW
ENE
5m
damage zone
fault core
damage zone
silt and clay
fine gravel
paleosoil
coarse gravel 2
coarse gravel 1
silt and clay
85 m
b)
c)
d)
e)
gravel units
A
B
fault
fracture
Fractured clast
clast count
0
5
10 cm

Figure 6.2: Overview of the trench log and examples of fractured clasts. (a) Trench log of the northern trench wall showing the main sedimentary units as well as faults, fractures and the location of fractured clasts; (b) fractured and offset Buntsandstein-pebble showing pure dip-slip displacement, offset ~ 5 cm; fracture plane dips to the NE; (c) fractured and offset Buntsandstein-pebble showing both dip-slip and left-lateral strike slip displacement, offset ~ 2 cm (strike slip), ~ 1 cm (dip-slip); (d) sub-vertically fractured quartzite pebble; (e) fractured Buntsandstein-pebble; fracture plane dips to the SW. Red quadrangles depict areas where clast counts were performed (Table 1).

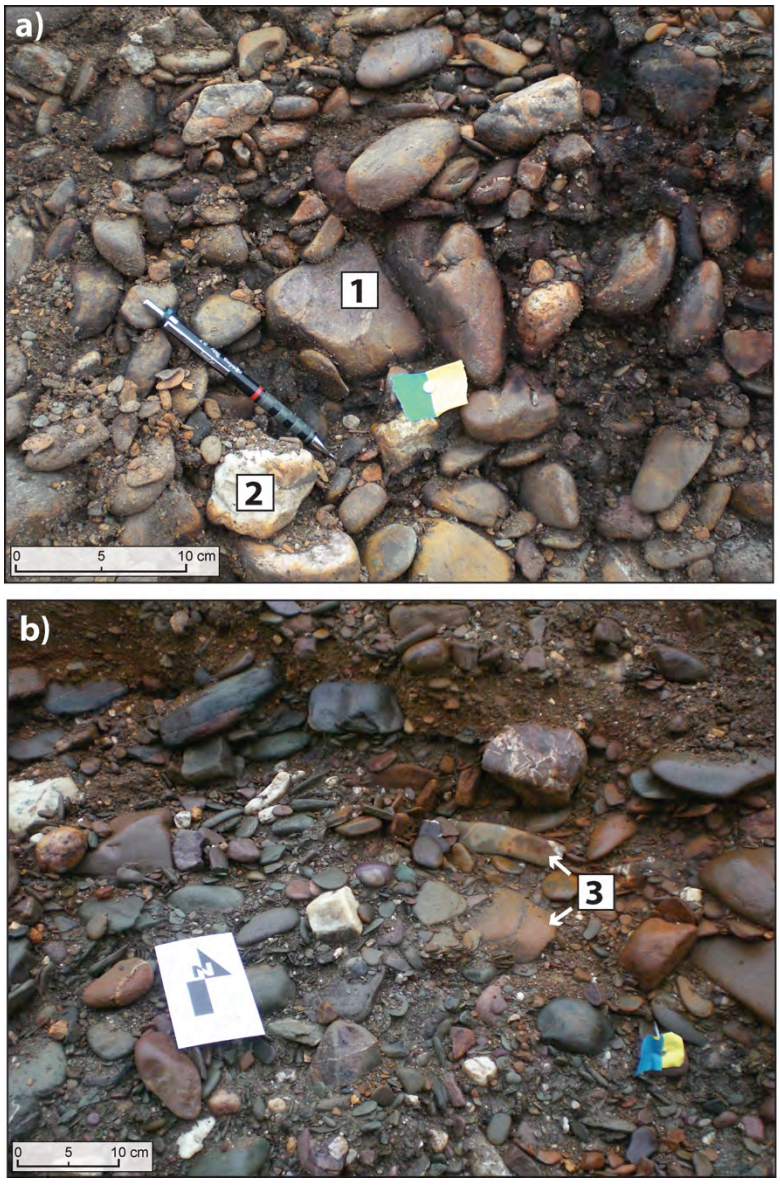


Figure 6.3: Photographs of typical gravels exposed in the Untermaubach trench. (a) Sub-rounded to well-rounded gravels of the oldest gravel unit in silt- and clay-rich matrix; 1: Buntsandstein clast (Lower Triassic); 2: quartzite clast (Ems Formation, Upper Lower Devonian); (b) sub-rounded and prolate gravels of the second oldest gravel unit with interbedded sand and fine-gravel lenses; 3: fine-sand and mudstone clasts (Heimbach Formation, Upper Lower Devonian).

## 6.3 Methods

To determine the different lithologies of the gravel units (Figure 6.3) and their frequency of occurrence, we conducted clast counts at seven different locations (1 $m^2$ quadrangles) along the trench wall (Figure 6.2; Table 6.1). We mapped 237 fractured pebbles and the orientation of fracture planes on both trench walls (Figure 6.2, Appendix, Table III.1). To avoid artificial clustering of observations we repeated the measuring campaigns three times performed by a different person. From the orientation data, we produced rose plots and stereo-net plots using stereo32©. On 91 of the 237 clasts we also measured the lengths of the long- and short-axes and their orientation with respect to the fracture planes. These measurements were not performable on fractured pebbles deeply buried in the gravel assemblage and thus we only obtained data on the clast orientation from fractured clasts sampled from the trench walls and well-exposed clasts with simple ellipsoidal shapes. We took several oriented samples of fractured clasts preserved in their original position by fixing them using epoxy resin and fiberglass tissue prior to sampling. From the sampled clasts we analyzed thin sections (Figure 6.4) and special-size thick sections (maximum size 20 x 15 cm, Figure 5) using a polarization microscope. We further analyzed high-resolution scans (4800 dpi) of sawed and polished cross-sections (Appendix, Figure III.1, III.2). For sample preparation, the clasts were fully cast in epoxy resin and cut after drying. We cut the oriented rock sample perpendicular to the main fracture.

Table 6.1: Results of clast counts at seven different locations in the Untermaubach trench.The point of origin is shown in Figure 1.

| Location (m) | No. of clasts | Sandstone | Mudstone | Quartzite | Unit |
|---|---|---|---|---|---|
| 12 | 212 | 176 (83%) | 21 (10%) | 15 (7%) | A |
| 25 | 189 | 147 (78%) | 23 (12%) | 19 (10%) | A |
| 40 | 223 | 198 (89%) | 23 (10%) | 2 (1%) | A |
| 65 | 279 | 237 (85%) | 33 (12%) | 9 (3%) | A |
| total | 903 | 758 (84%) | 100 (11%) | 45 (5%) | A |
| 5 | 241 | 176 (73%) | 32 (13%) | 33 (14%) | B |
| 35 | 263 | 160 (61%) | 66 (25%) | 37 (14%) | B |
| 78 | 318 | 198 (62%) | 66 (21%) | 54 (17%) | B |
| total | 822 | 534 (65%) | 164 (20%) | 124 (15%) | B |

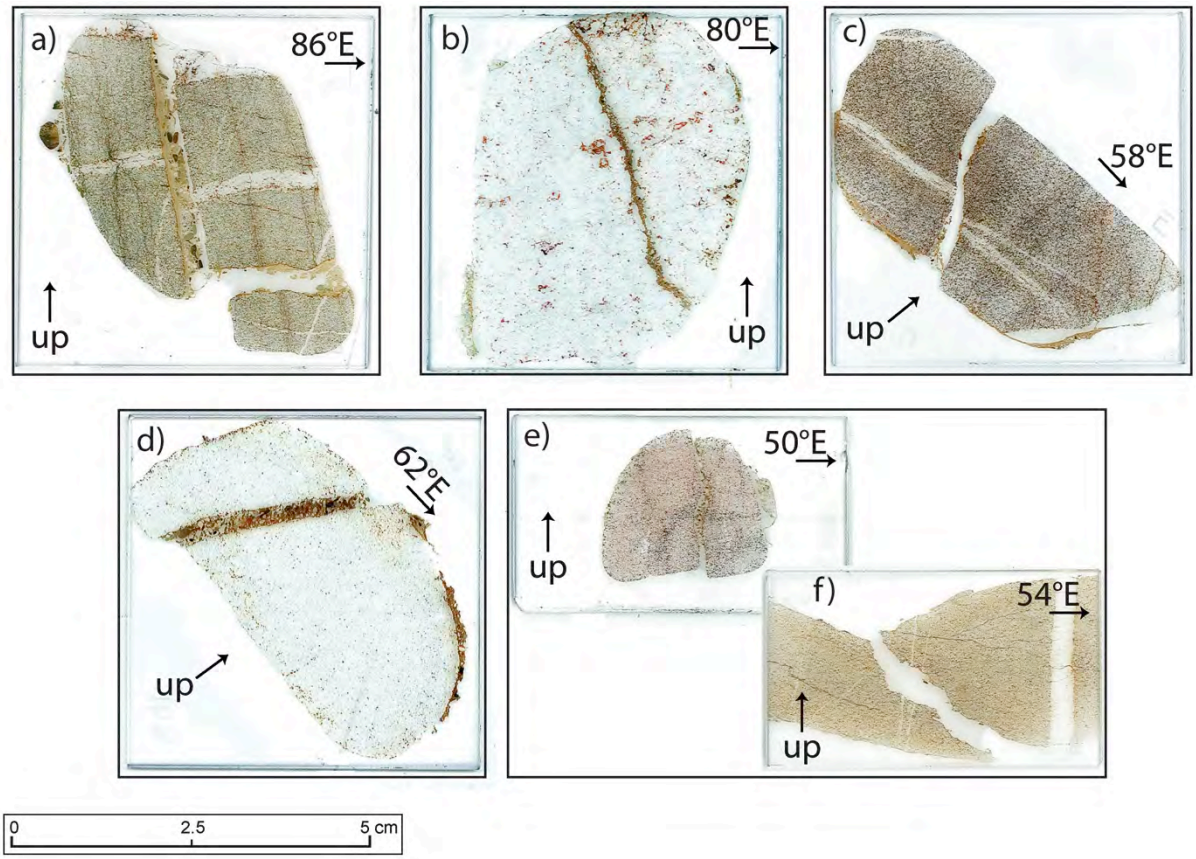


Figure 6.4: Oriented thin-sections of fractured clasts. The thin-sections exhibit tensile and shear fractures, respectively, and offsets of up to 6 mm. (a) Fractured and offset siltstone clast exhibiting displaced quartzite veins; (b) Fractured quartzite clast; (c) Fractured and offset sandstone exhibiting displaced quartzite veins; (d) Fractured and offset quartzite clast; (e) Fractured and offset sandstone clast; (f) Fractured mudstone clast.

Figure 6.5: Oriented thick-sections of fractured pebbles. (a) Thick-section (No. K37, 70 µm thick) of Buntsandstein-pebble, sampled from the lower level of the fault zone (Figure 2) exhibiting a complex fracture pattern; (b) thick-section (No. K23, 50 µm thick) of Buntsandstein-pebble, sampled from the upper level of the fault zone (Figure 2) exhibiting simple tensile fracturing.

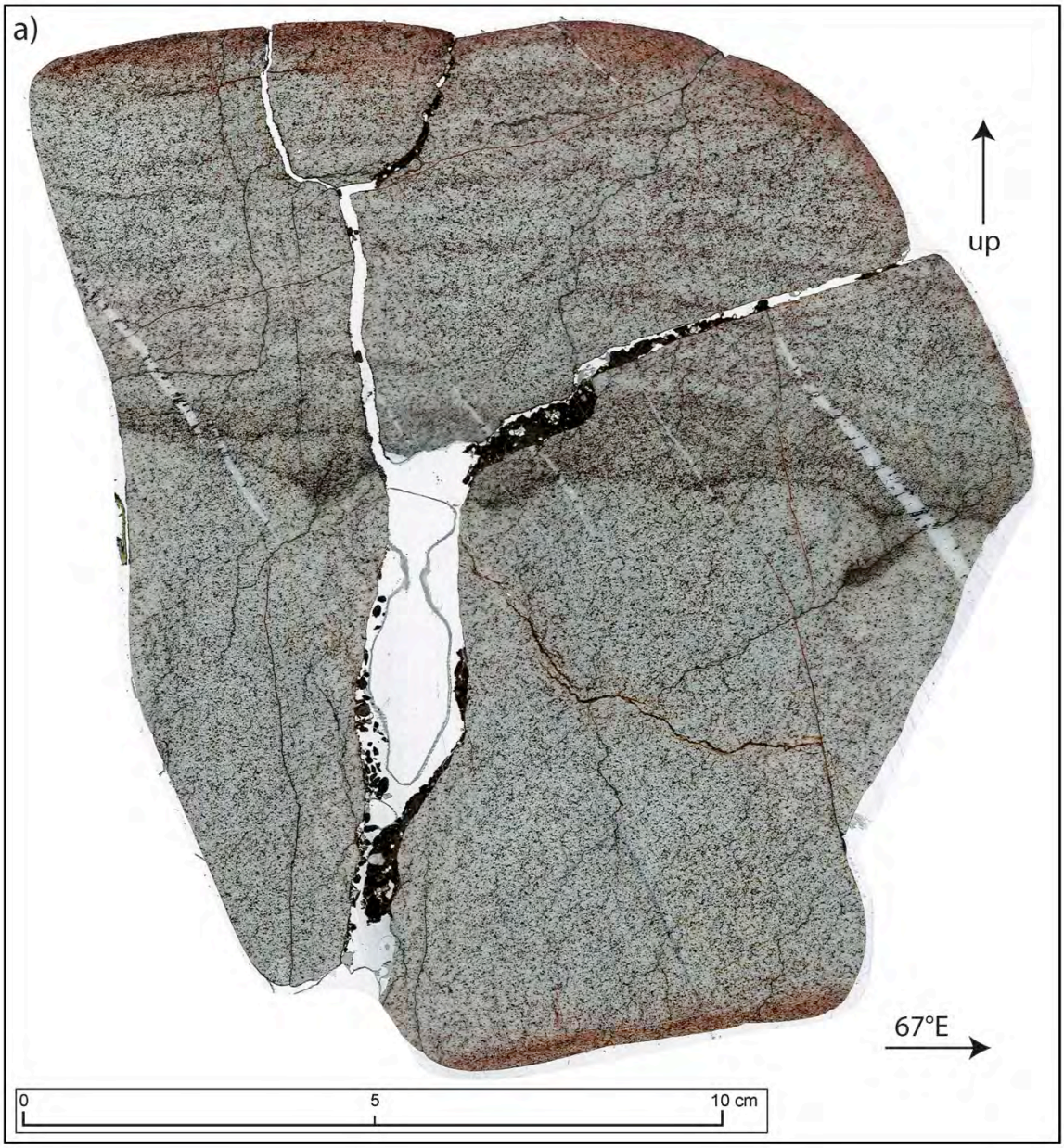
a)
up
67°E
0
5
10 cm


b)
up
70°E
0
5
10 cm

## 6.4 Results

### 6.4.1 Clast Characteristics

Results of our clast counts (Table 6.1) reveal that the most common lithologies of clasts are reddish middle and coarse sandstone (Buntsandstein, Lower Triassic, 84%), light-brown and grey silt- and mudstone (Heimbach Formation, Upper Lower Devonian, 11%) and light grey and white quartzite (Ems Formation, Upper Lower Devonian, 5%). The majority of sandstone and quartzite clasts are rounded to sub-rounded; siltstone clasts are commonly sub-angular to sub-rounded. The exposed gravels are typically prolate bodies. We measured the aspect ratio of the long-axes and short-axes of 91 clasts to determine the relationship of the lithology and clast shape (Appendix, Table III.2). Quartzite clasts in this study are the "roundest" clasts exposing the highest aspect ratios (0.67 - 0.86), sandstone clasts have highly varying aspect ratios (0.25 - 0.8), and mudstone clasts exhibit the lowest aspect ratios (0.16 - 0.3). Quartzite clasts do not exhibit any internal bedding or foliation. Sandstone and mudstone clasts commonly exhibit internal bedding structures that are predominately parallel to sub-parallel to the long axis (b-axis) of the clasts.

Due to the fluctuating groundwater table at the trench site, most clasts are coated with either reddish iron-rich or black manganese-rich patinas. This red-black color pattern is also visible in the matrix (Chapter 4, 5). Unit A is overlain by unit B, which is a clast- and matrix-supported gravel layer with a sandy and silt- and clay-rich matrix. Clasts are predominately of coarse gravel size but are commonly larger than 10 cm. Maximum clast sizes do not exceed 30 cm across. The lithological composition of unit B is similiar to unit A (Buntsandstein clasts 65%; Heimbach clasts 20%; Quartzites 15%, Table 6.1)

### 6.4.2 Fault Zone Architecture

Field observations reveal that the exposed fault segment is characterized by a > 40 m-wide fault zone characterized by distributed faulting along small faults within coarse gravel deposits (Figure 6.2). Mapping the location and orientation of fractured clasts reveals that the fault zone consists of two main structural units, which can be clearly distinguished considering the spatial distribution and orientation of fractured gravels (Appendix, Table III.3). Using the conventional terminology for fault zone architectural styles, originally

defined for bedrock fault zones, (e.g. Caine et al., 1996; Chester and Logan, 1986), we refer to the two units as "fault core" and "damage zone" (Figure 6.2a). The fault core is approximately 10 m wide and accommodates most of the fault displacement. Here, gravel deposits have the highest spatial density of fractured and offset clasts (up to 5 fractured clasts per $m^2$, Figure 6.6a). The damage zone is well recognizable about 10 - 15 m wide on either side of the fault zone. It also contains fractured clasts, but the frequency of occurrence decreases remarkably with distance to the fault zone (Figure 6.6b and Figure 6.6c). Orientation measurements also illustrate a clear difference in fault core and damage zone fractures (Figure 6.7). While the dip directions of fracture planes appear to be consistent for both structural units (Figure 6.7a), the fault core exhibits much smaller variations in the dip angles compared to the damage zone (Figure 6.7b).

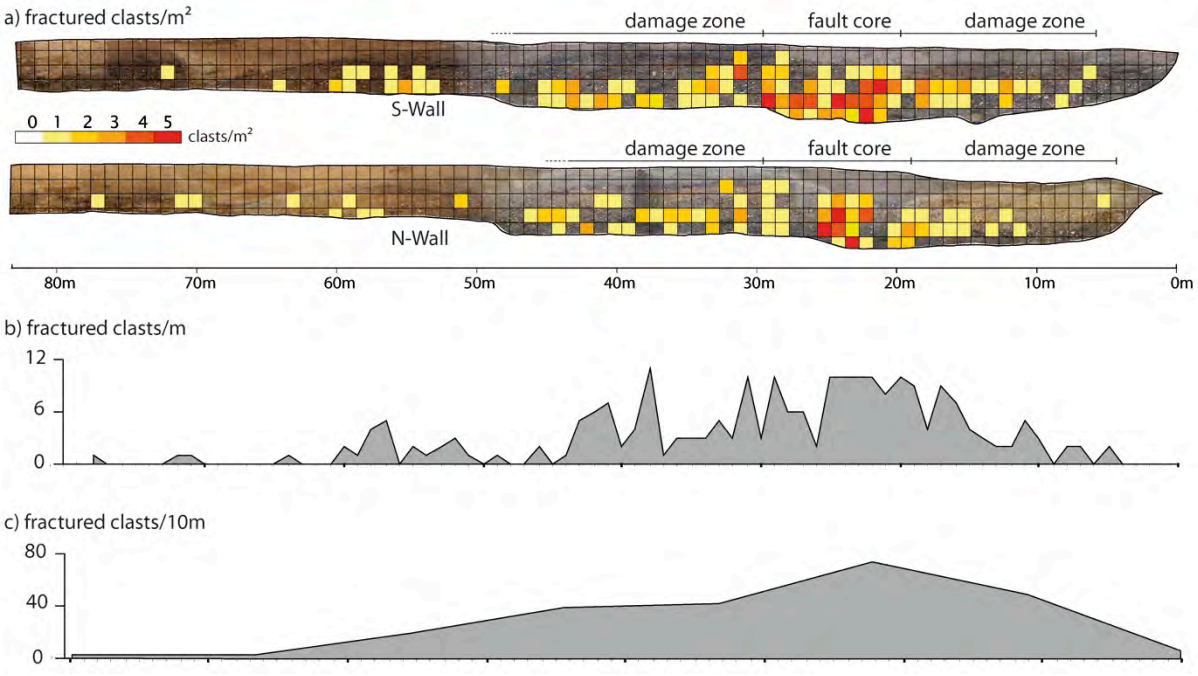


Figure 6.6: Density distribution of fractured clasts. (a) Spatial distribution of fractured clasts at both trench walls showing the number of fractured clasts per square meter, transparent squares indicate locations where no fractured clasts were observed; (b) Cumulative number of fractured clasts per square meter of both trench walls; (c) Cumulative number of fractured clasts per 10 square meters of both trench walls.

### 6.4.3 Fractures

Fractured clasts in the exposed gravel deposits are typically cut by one to five sub-parallel fractures. In the fault core over a distance of ~ 10 m, fractured pebbles are frequent within the unconsolidated gravel deposits and become significantly less frequent with increasing distance to the fault core (Figure 6.6). The fractures occur in the clasts but are absent in the surrounding matrix. The fractures usually have planar surfaces, fracture-parallel offsets occur on about 15% of the fractures, and offsets range from few mm to up to 4 cm (Appendix, Table III.1).

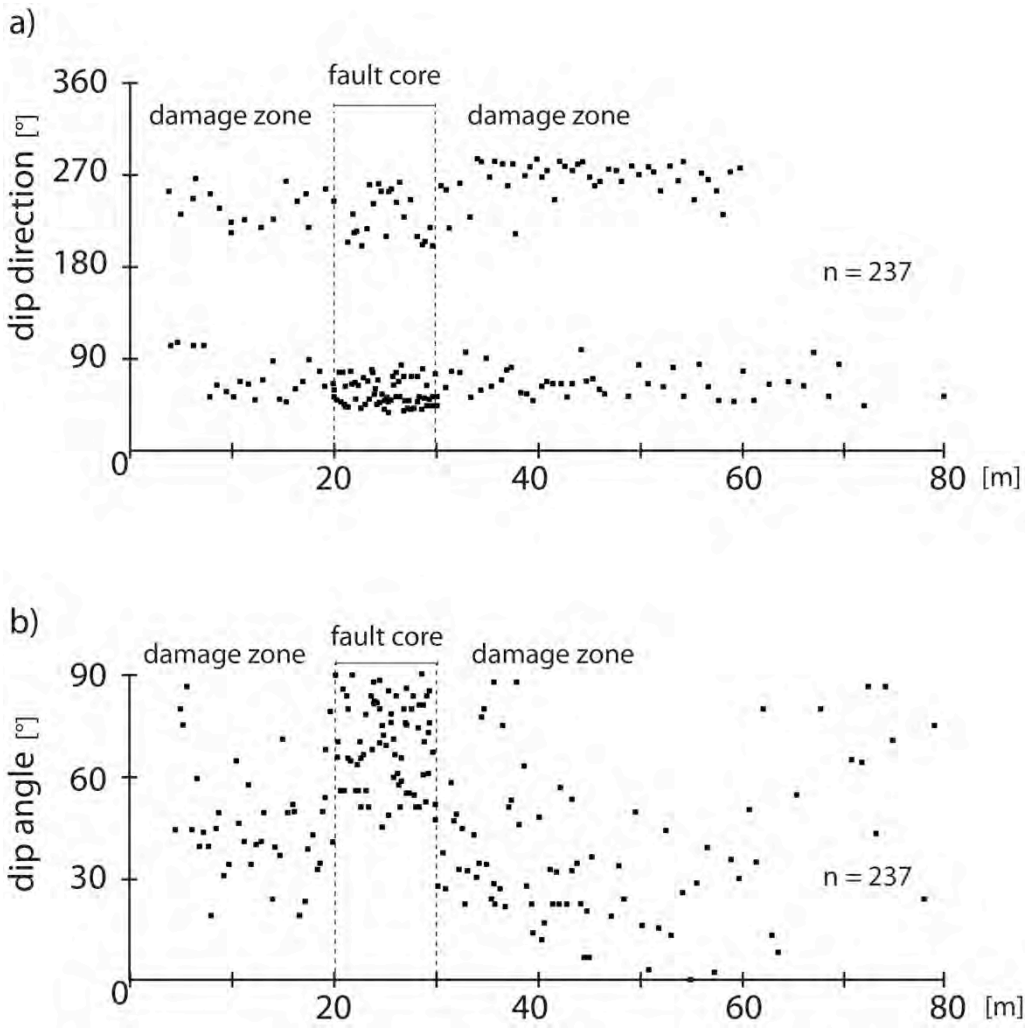


Figure 6.7: Scatter plots showing the variation in dip-direction and dip angle of the fracture planes, respectively. Dip values are plotted relative to their location in the trench. (a) Dip-direction values of fractured clasts, subdivided into westward dipping planes - upper point cloud, and eastward dipping planes - lower point cloud; (b) dip-angle values of fractured clasts. Note the higher frequency of fractured clasts in the fault core and the smaller variations in dip-angles of fault core fractures compared to those of the damage zone.

We mapped 237 fractured clasts in the gravel units A and B. The majority of fractures occur in Buntsandstein clasts (214 clasts, 90.3%), the percentage of fractured quartzite and

mudstone clasts are similar (mudstone: 11 clasts; 4.6%; quartzite: 12 clasts, 5.1%). The abundance of fractures in clasts of different lithology thus matches the general frequency distribution of lithologies in the trench (Table 6.1).

Results on fracture-orientation measurements with respect to the aspect ratios of the a- and b-axes of 91 fractured clasts reveal that the orientation of fractures does not show a recognizable relationship with the ellipticity of a clast (Figure 6.8). Fracture orientations of fault-core clasts appear to be also independent from the orientation of internal bedding of the sandstone and mudstone clasts, which is predominately parallel to sub-parallel to the clasts b-axes. Damage-zone clasts, however, commonly expose fractures sub-parallel to internal bedding (Figure 6.8).

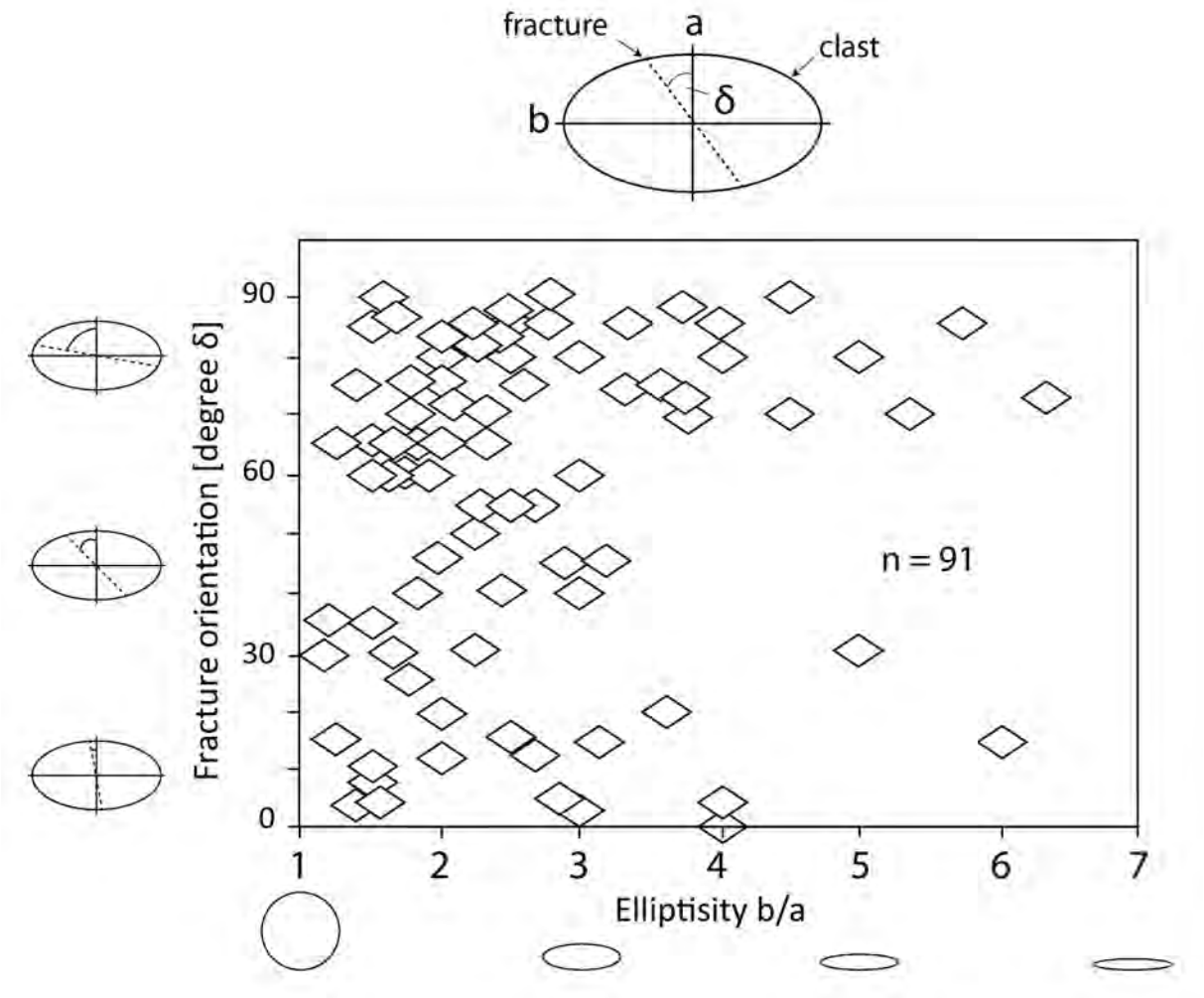


Figure 6.8: Relationship between clast shapes and fracture orientation. The x-axis displays the ratio of the clasts a-axis (short axis) and b-axis (long axis). Simplified corresponding clast shapes are shown below. The y-axis displays the maximum deviation of the fracture planes from the a-axis of the clasts. Corresponding examples are shown on the left-hand side of the diagram. For sandstone and mudstone clasts, the b-axis is usually sub-parallel to the orientation of internal bedding. Therefore, fractures sub parallel to the b-axis (upper points in the diagram) predominately represent bedding-parallel fractures.

Measuring the orientation of the fracture surfaces reveal a clear and consistent regional trend for the fracture planes. Most of the fractures dip to the northeast (mean dip direction 41°) dipping at angles of ~ 60° (Figure 6.7 and Figure 6.9). This trend is more pronounced in the fractures exposed in the fault core (Figure 9b). Fracture orientation is in good agreement with both the principal stress field of the region (Hinzen, 2003) and the suggested dip-angle of normal faults in the region (Dirkzwager et al., 2000; Duin et al., 2006; Vanneste et al., 2010). A second, smaller population of fractures is oriented in the opposite direction with dip directions predominately to the SW and dip-angles around 75° (Figure 6.7a and Figure 6.9a). Fault-core fractures are generally characterized by smaller variations in dip-angles compared to damage-zone fractures (Figure 6.7b).

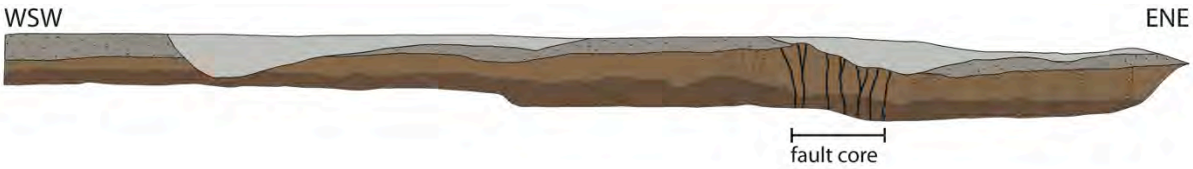


a) fracture plane orientation all clasts (N=237)

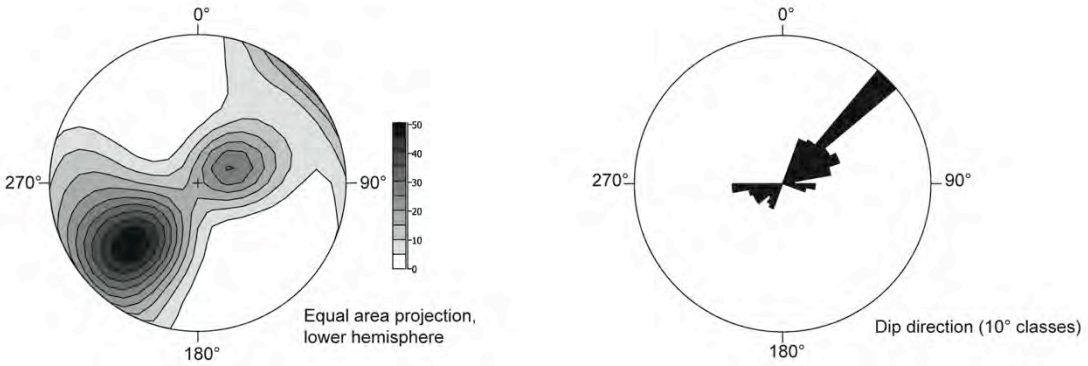


b) fracture plane orientation fault core (N=98)

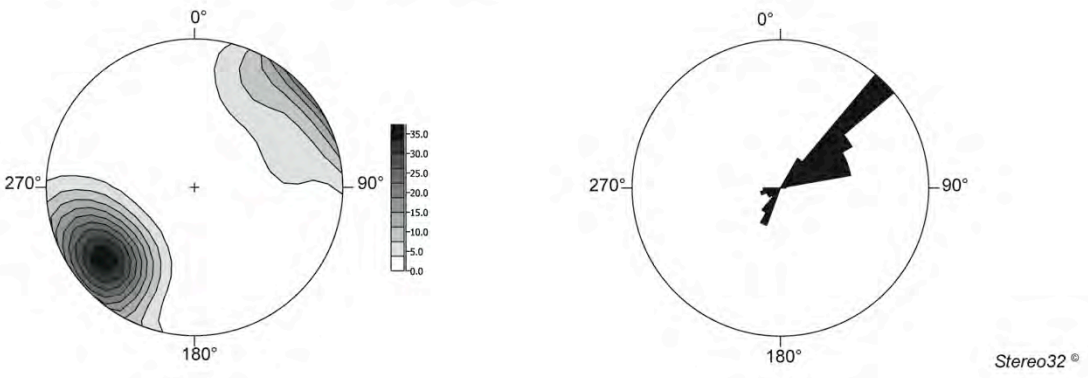

Figure 6.9: Stereonet diagrams showing the fracture-plane orientations of broken clasts. (a) Orientation of all fracture planes (237 measurements); (b) Orientation of fracture planes in the fault zone (98 measurements). The location of the fault core in the simplified trench log is shown in Figure 2.

The analysis of polished and scanned cross-sections reveal some complex fracture networks connecting multiple contact points (Figure 6.10 and Figure 6.11a), simple tensile fracturing exhibiting up to 2 cm of extension (Figure 6.10 and Figure 6.11a), and radial fractures at contact points (Figure 6.11b). Thick-section analysis reveals complex fracturing and local crushing at contact points of the clasts (Figure 6.11c). Thin- and thick-section analysis further allows for the detection of secondary cracks and grain-scale deformation. Trans-granular fractures predominately occur at small secondary cracks (Figure 6.12). Inter-granular fractures were commonly observed particularly at tensile cracks.

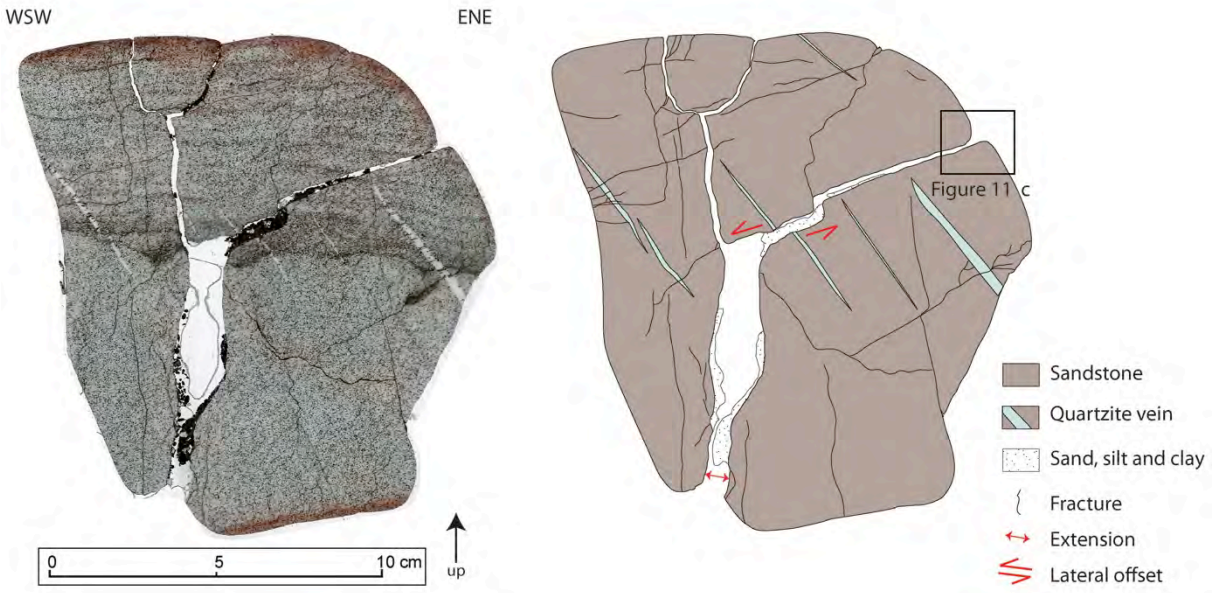


Figure 6.10: Results of structural mapping of a thick-section. The original thick-section (clast sample K37) is shown on the left-hand side, the mapped section is shown on the right-hand side.

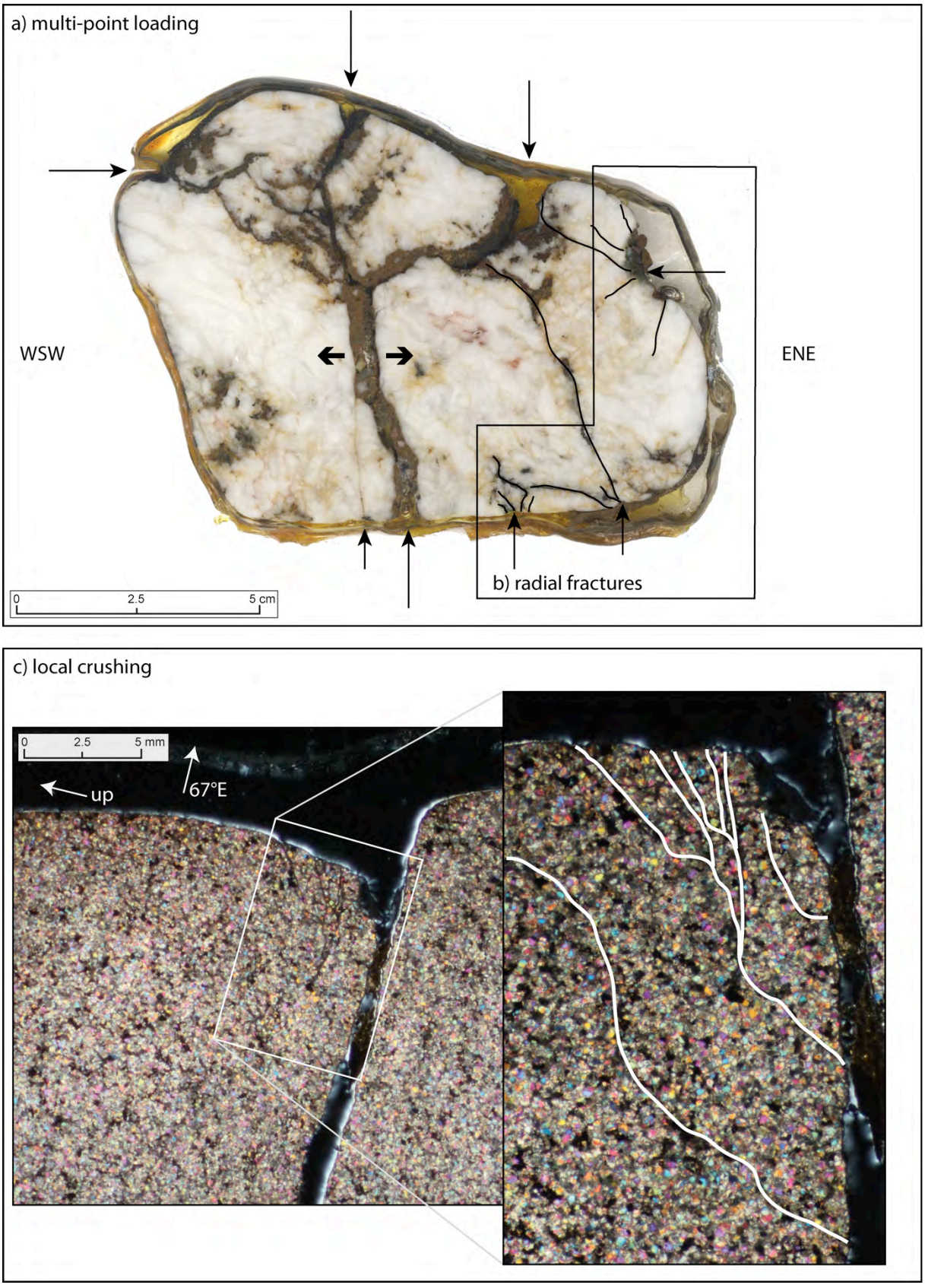


Figure 6.11: Deformation patterns of fractured clasts. (a) Polished cross-section of a quartzite clast exhibiting complex fracturing due to multi-point loading, and (b) radial fractures typical for impact-derived deformation; (c) cross-polarized microscope image showing local crushing and complex fracturing at the contact point of a fractured Buntsandstein clast.

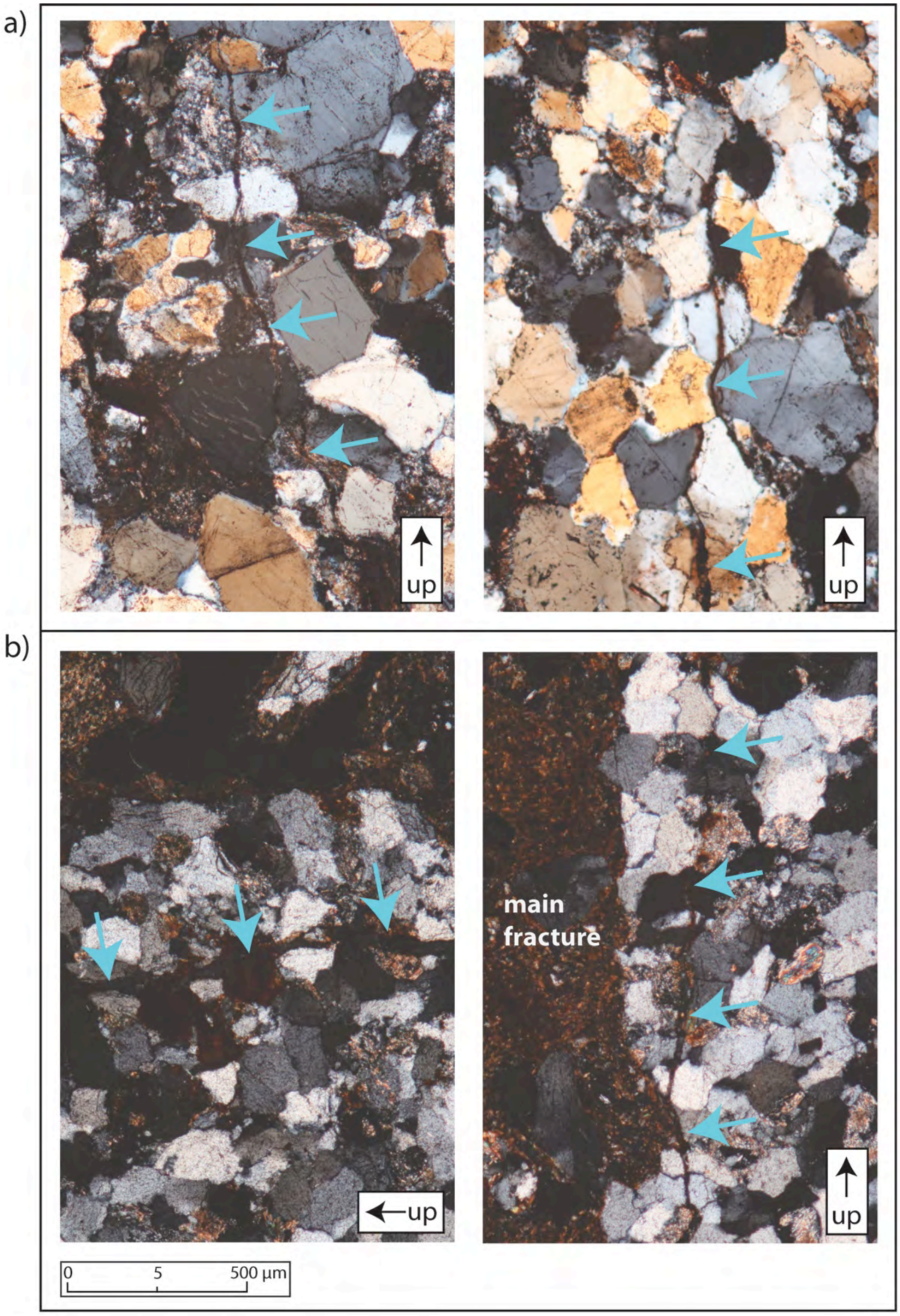


Figure 6.12: Polarization microscope images (magnification factor 50) of thin-sections showing trans-granular fractures observed on secondary fractures. (a) Thin-section of Buntsandstein clast, sample No. K23. (b) Thin-section of Buntsandstein clast, sample No. K23. The height of a single image is 1.8 mm.

## 6.5 Breakage Behaviour of Gravels

Based on our observations on the occurrence, distribution and orientation of fractured clasts in the exposed gravel deposits, we suggest a tectonic origin as process for clast fracturing. In the following, we critically examine different hypotheses of how the fractured clasts could have formed, and whether a coseismic or non-seismic origin of the fractured clasts is more likely. For the fracture process observed on our studied gravels we assume: (1) a low confining pressure due to the small sediment overburden; (2) the formation of new fractures is independent of lithology, clast size and internal bedding or cleavage; and (3) water-saturation of the clasts due to the presence of groundwater. Furthermore, we preclude permafrost processes as driving mechanism for clast breakage, because radiocarbon dates taken from paleosoil horizons exposed within the deformed gravels (Chapter 5) yielded mid to late Holocene ages and thus, preclude permafrost conditions for this region (Klostermann, 1992)

### 6.5.1 Clast Breakage under Various Loading Conditions

Due to the variety of shapes and sizes, the single clasts in a gravel deposit are subject to different loading conditions. Those include: point-to-point loading (the clast is loaded at two points), plane-to-plane loading (the clast is loaded at two planes), point-to-plane loading (one side of the pebble is loaded at a point, the other side at a plane) and multi-point loading (the clast is loaded at three points or more; Figure 6.13). All aforementioned loading conditions can be observed in the gravels exposed in our study site, yet point-to-point loading and multipoint-loading appear to be the most frequent configurations (Figure 6.10 and Figure 6.11).

Former numerical studies (Tang, 2004; Tuitz, 2012) show that particle (or clast-) breakage processes are highly dependent on the internal stress distribution, that is in turn controlled by the loading conditions. While point-to-point loading most likely leads to the formation of a fracture between the two contact points, the other loading configurations produce a much more complex internal stress field, which makes it difficult to predict how a fracture will form (Tang, 2004).

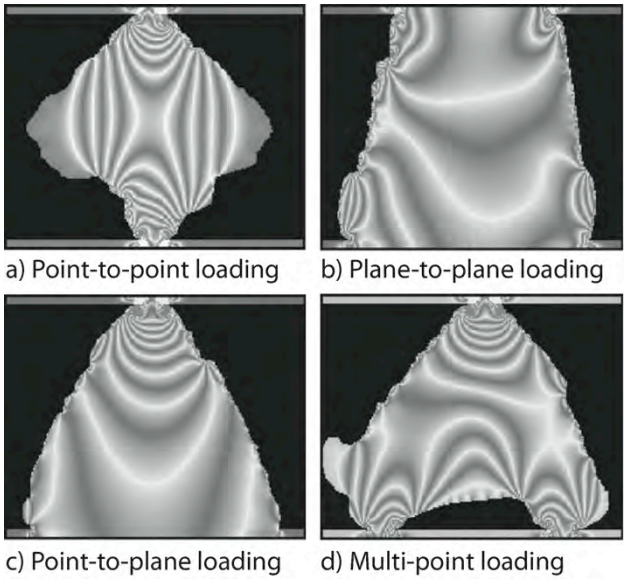


Figure 6.13: Quasi photo-elastic stress-fringe patterns of irregular particles. The figure is modified from Tang et al. (2004).

### 6.5.2 Impact Fracturing

Radial fractures and pockmarks (or "firing-pin structures") at contact points of fractured pebbles are deformation features, that indicate impact processes caused by high-velocity collision of pebbles within a gravel deposit (Strayer and Allen, 2008). Former studies suggest that either a meteorite impact (Ernston et al., 2001) or tectonic acceleration forces (Grützner et al., 2012) can be responsible for clast breakage. Observations on impact fractures in fault zone gravels have been made along the Pakua anticline in western Taiwan (Lee et al., 1996) as well as the Hayward fault in northern California (Strayer and Allen, 2008) and the Feldbiss fault zone in the Belgium part of the Lower Rhine Graben (Demoulin, 1996). In all these studies, the observed gravels exhibit radial fractures at the contact points of two gravels and systematic patterns of the main fracture planes coinciding with the regional stress field.

In our study, a few clasts exhibit radial fracture patterns (Figure 6.11b). Pockmarks, however, have not been observed on any of the exposed clasts either because groundwater processes have disguised any of those contact features or they have simply not been formed. The low number of impact-like features suggests that this process - if occurring - presumably plays only a minor role in the formation of fractured clasts observed in this study.

## 6.6 Fracture Toughness of Clasts

Rock-fracture toughness values quantify the ability of rock material to resist the propagation of cracks. In other words, fracture toughness is the consumption rate of fracture energy required to fracture rock (Tiryaki, 2006). Clasts in natural conglomerates are usually characterized by a high variability of material properties due to lithological differences. Also, the formation and abundance of small internal defects (e.g. micro-cracks) induced by fluvial transport or chemical weathering-processes differ from clast to clast. Therefore, fracture toughness moduli of rock types derived from laboratory tests are probably not fully assignable to the clasts of our study. However, they provide information on the expected stress magnitude necessary to fracture clasts of different lithologies. A useful classification system for the estimation of the strength properties of rock is the Geological Strength Index (GSI) developed particularly for natural rock exposures (Marino and Hoeck, 2000). The advantage of this system is that it adjusts strength values derived from laboratory tests to appropriate in-situ values.

As we expect mainly point-loading forces acting on our studied clasts, we have used Point Load Indices (PLI, measured in MPa) of the GSI. For rock types analog to those exposed in the studied fault zone (mudstone, sandstone and quartzite) critical point-load estimates range from 1 - 10 MPa based on field estimates of uniaxial compressive strength tests of intact rock (Marino and Hoeck, 2000). Accordingly, the weakest rock types in our gravel deposits are mudstone and siltstone clasts (PLI: 1 - 2 MPa), sandstone clasts are moderately strong (PLI: 2 - 4 MPa) quartzite clasts are very strong (PLI: 4-10 MPa).

The gravels in our study currently sit below the groundwater table. Therefore, the clasts may have also been water-saturated during fracturing. This is in particular relevant for the Buntsandstein clasts, as they represent the lithological group exhibiting the highest porosity (15 - 20%). It is known for porous silicatic rocks to become significantly weaker when exposed to an aqueous environment, an effect called hydrolytic weakening (Griggs, 1967). In comparison with dry rocks, the presence of pore water in water-saturated rocks produces an outward acting pore pressure. Furthermore, the penetration of water into the inter-granular boundaries reduces the cohesive strength of a rock. In siliciclastic rocks, water permeates also into the silicate grains leading to weakening of the crystal components of the rock (Griggs, 1967).

The hydrolytic weakening processes lead to significant (25 - 75%) lowering of the fracture toughness of a rock, as observed in uniaxial compression tests (Lin et al., 2005) and

impact experiments on wet sandstone (Kenkmann et al., 2011), as well as brittle-failure tests on tillites (Hiemstra and van den Meer, 1997). This means for our study that critical values leading to rock failure are presumably lower compared to the GSI values assigned for the different lithologies. The importance of groundwater as a reducer of fracture toughness of rock may also be an explanation for the rare observations of fractured clasts in exposed fault zones.

## 6.7 Sources of Stress

To produce well-organized fracture patterns in unconsolidated gravels as observed in our study, critical stress values must have exceeded several MPa. In the following, we examine different sources of stress and their likelihood of having produced the observed fractured clasts.

### 6.7.1 Sediment Overburden

Overburden stress acting on a clast is produced by the net weight of the sediment and increases with burial depth. Assuming a sediment bulk density of 2500 kg/m$^3$, the increase of overburden stress with depth would be ~ 1 MPa/40 m neglecting effects due to compaction and the presence of groundwater. Applying this to our studied clasts, a minimum sediment overburden of ~ 40 - 80 m would be necessary to fracture the weakest clasts (mudstones). Fracturing of sandstone clasts requires 80 - 160 m of overburden and quartzite clasts 160 - 400 m.

In our study, fractured clasts are exposed in depths of 0.5 - 4.5 m (Figure 6.2) corresponding to a vertical overburden stress of 1.25 - 11.25 kPa, which is several magnitudes below the critical value necessary for clast breakage, even for water-saturated weak rock types. Thus, the effect of sediment overburden can reliably be precluded as driving mechanism for producing the fractured clasts in this study.

### 6.7.2 Slow Tectonic Deformation

Aseismic and postseismic creep processes accommodate tectonic deformation by slow displacement rates (mm-cm/yr) without producing measurable coseismic events (Brune, 1968; Cowan, 1999; Stein and Lisowski, 1983). In deeply exhumed fault zones, fractured clasts have been observed and interpreted to be the result of slow tectonic deformation (Tanner, 1963, 1976). Other studies on fractured clasts in exhumed conglomerates (Eidelmann and Reches, 1992) suggest necessary burial depths of several hundreds of meters to enable in-situ fracturing of sandstone and limestone clasts. In near-surface gravels, the low confining pressure would most likely prevent clast breakage under slow tectonic deformation, and lead to the rotation of clasts. The lack of fractured particles in unconsolidated sediments cut by creeping faults has also been observed in deformed sand deposits of the creeping section of

the San Andreas Fault (Cashman et al., 2007). Here, sediment deformation is characterized by grain rotation along several minor faults without producing fractured grains. In contrast, deformation structures related to the 1906 earthquake rupture of the San Andreas Fault reveal both rotated and fractured grains and thus, the fracture process of grains appears to pose a diagnostic feature for coseismic rupture (Cashman et al., 2007). Applying the aforementioned observations on the gravels in our study, slow deformation appears to be highly unlikely to have produced the fractured clasts, as we observe abundant fractured clasts at minimum depths of 0.5 m (Figure 6.2).

### 6.7.3 Coseismic Deformation

Coseismic sediment deformation could be derived from either propagating P-, S-and surface-waves (shaking-related deformation) or the propagating rupture front (rupture-related deformation). Shaking related fracturing of pebbles has recently been reported from a paleoseismic study in southern Spain (Grützner et al., 2012). However, seismic wave-induced clast breakage would be expected to affect a large area depending on the earthquake magnitude. Similar to liquefaction phenomena, which are also the product of seismic shaking, shaking-induced deformation features may occur in an epicentral distance of 10 km and more for a $M_W$ 6 event covering several tens of $km^2$ (Obermeier, 1996; Silva and Rodríguez Pascua, 2008). This does not coincide with our observations.

A propagating coseismic rupture is often associated with a large dynamic increase of shear stress at the tip of the rupture (Bouchon and Campillo, 1998) with peak shear-stress values often exceeding several MPa (Dalguer et al., 2003; Di Toro et al., 2005; Freed, 2005; Lapusta and Rice, 2003; Madariaga et al., 2006). Fracture patterns induced by dynamic loading of a coseismic rupture would be expected to reflect the geometry of the fault plane and the direction of slip. As these conditions are achieved by the fractured clasts in our study, a coseismic rupture source appears to be the most likely process explaining the systematic rupture pattern in unconsolidated gravels.

## 6.8 Spatial Distribution of Different Fracture Types

The 237 fractured clasts are exposed in depths of 0.5 to 4.5 m. The near-surface clasts (0.5 - 2.0 m) are predominately cut by 1 - 2 fractures, while clasts buried at deeper levels are typically more intensively fractured with up to 5 main fractures (Figure 6.14). The number of fractures per clast increase remarkably at the contact between the upper and lower gravel deposit (Figure 6.14). In a former study (Chapter 4 and 5), this contact has been identified as the event horizon of the penultimate coseismic event. This implies that the older gravel unit has presumably experienced at least two earthquakes. Thus, a possible explanation for the increased fracture density of the older gravels would be that two generations of fractures are preserved in these clasts, while the younger gravels have only been deformed once.

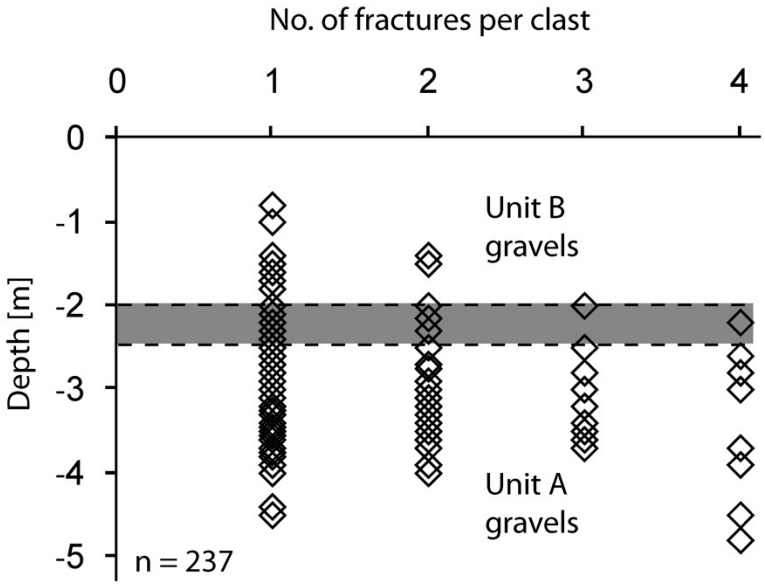


Figure 6.14: Diagram showing the relationship between the numbers of fractures observed on a single clast and the depth below the surface. The grey area depicts the transition zone between clasts exhibiting a maximum of 2 fractures at higher levels of the trench to clasts exhibiting up to 4 fractures at deeper levels of the trench.

Furthermore, the fracture types exposed in the fault core differ from those exposed in the damage zone of the exposed fault. Fault core fractures commonly cut the entire gravel independent of size, lithology and the orientation of internal bedding (Figure 6.15). Fractured clasts in the damage zone are often not fully fractured or fractured along planes of weakness, such as internal bedding or cleavage planes (Figure 6.15). Also, some damage-zone clasts

exhibit fracture deflection at bedding contacts. This indicates that the energy needed to propagate the fracture was too low to cause fracturing of the entire gravel perpendicular to its bedding (Snoke et al., 1998).

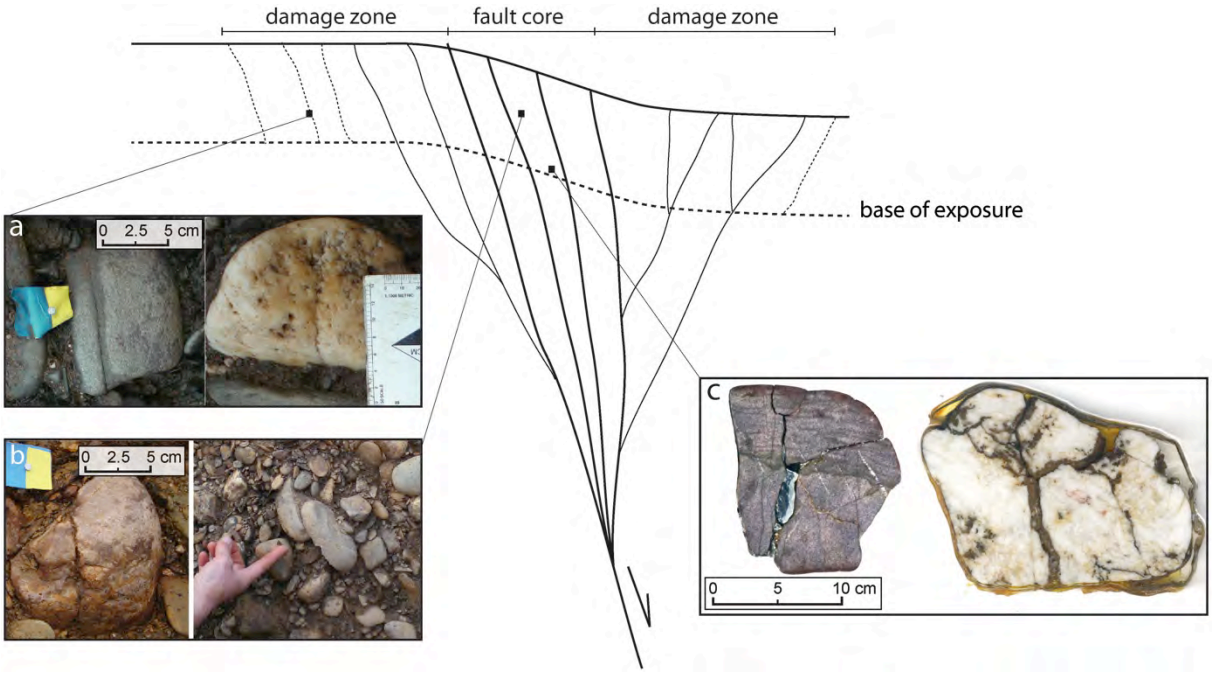


Figure 6.15: Spatial variations of different fracture types. (a) Fractured clasts found in the damage zone of the fault; fractures are commonly bedding-parallel or do not penetrate the entire clast; (b) Fractured clasts from the fault zone of the uppermost gravel unit; clasts are clearly cut by mostly one fracture, clasts commonly show dip-slip displacement; (c) Polished cross-sections from fractured clasts from the fault zone of the lowermost gravel unit; clasts are clearly cut often by multiple fractures. Fault zone sketch not drawn to scale.

## 6.9 Conclusions

On the basis of detailed fracture analysis on outcrop, macro- and microscale we evaluated the potential of fractured pebbles as indicator for coseismic rupture in an intraplate fault zone. Orientation measurements of fracture planes confirm that fractured clasts in fault zones are useful stress-field indicators. Furthermore, fractured clasts in unconsolidated near-surface deposits indicate coseismic rupture under these conditions:

1) Fractured clasts occur close to the surface (burial depth less than 40 m) and former sediment overburden can be excluded.
2) Periglacial or permafrost processes can be excluded to have affected the gravels.
3) The trend of the fracture planes coincides with the regional stress field and the orientation of the fault plane.
4) Fractures crosscut clasts independent of size, shape and internal bedding or cleavage.

In addition, the presence of groundwater presumably facilitates the formation of fractured clasts due to weakening effects on the rock. This implies that fractured clasts may occur predominately in humid regions, or locations with high water tables, respectively. The process of clast fracturing under dynamic loading requires stress values on the order of several MPa depending on the lithological composition. Thus, fractured clasts may also be used as a recorder for the seismological energy parameters during a coseismic rupture. Future research, including dynamic deformation experiments and modeling approaches may help to quantify the conditions under which dynamic clast fracture occurs.

## 6.10 References

Azanón, J. M., Azor, A., Booth-Rea, G., and Torcal, F., 2004, Small-scale faulting, topographic steps and seismic ruptures in the Alhambra (Granada, southeast Spain): Journal of Quaternary Science, v. 19, no. 3, p. 219-227.

Baran, R., Guest, B., and Friedrich, A. M., 2010, High-resolution spatial rupture pattern of a multiphase flower structure, Rex Hills, Nevada: New insights on scarp evolution in complex topography based on 3-D laser scanning Geological Society of America Bulletin, v. 122, p. 897-914.

Bouchon, M., and Campillo, M., 1998, Stress field associated with the rupture of the 1992 Landers, California, earthquake and its implications concerning the fault strength at the onset of the earthquake: Journal of Geophysical Reasearch, v. 103, no. B9, p. 21091-21097.

Brune, J. N., 1968, Seismic Moment, Seismicity, and Rate of Slip along Major Fault Zones: J. Geophys. Res., v. 73, no. 2, p. 777-784.

Caine, J. S., Evans, J. P., and Forster, C. B., 1996, Fault zone architecture and permeability structure: Geology, v. 24, no. 11, p. 1025-1028.

Cashman, S. M., Baldwin, J. M., Cashman, K. V., Swanson, K., and Crawford, R., 2007, Microstructures developed by coseismic and aseismic faulting in near-surface sediments, San Andreas fault, California: Geology, v. 35, no. 7, p. 611-614.

Chester, F., and Logan, J., 1986, Implications for mechanical properties of brittle faults from observations of the Punchbowl fault zone, California: Pure and Applied Geophysics, v. 124, no. 1-2, p. 79-106.

Cowan, D., S., 1999, Do faults preserve a record of seismic slip? A field geologist's opinion: Journal of Structural Geology, v. 21, p. 995-1001.

Dalguer, L. A., Irikura, K., and Riera, J., 2003, Simulation of tensile crack generation by three-dimensional dynamic shear rupture propagation during an earthquake: Journal of Geophysical Reasearch, v. 108.

Decker, K., and Peresson, H., 1996, Rollover and hanging-wall collapse during Sarmatian/pannonian synsedimentary extension in the Eisenstadt basin: Mitteilungen der Gesellschaft der Geologie und Bergbaustudenten in Österreich, v. 41, p. 45-52.

Demoulin, A., 1996, Clastic dykes in east Belgium: evidence for upper Pleistocene strong earthquakes west of the Lowr Rhine Rift segment: Journal of the Geological Society of London, v. 153, p. 803-810.

Di Toro, G., Nielsen, S., and Pennacchioni, G., 2005, Earthquake rupture dynamics frozen in exhumed ancient faults: Nature, v. 436, no. 18, p. 1009-1012.

Dirkzwager, J. B., Van Wees, J. D., Cloething, A. A. P. L., Geluk, M. C., Dost, B., and Beekman, F., 2000, Geo-mechanical and rheological modelling of upper crustal faults and their near-surface expression in the Netherlands: Global and Planetary Change, v. 27, p. 67-88.

Duin, E. J. T., Doornebal, J. C., Rijkers, R. H. B., Verbeek, J. W., and Wong, T. E., 2006, Subsurface structure of the Netherlands – results of recent onshore and offshore mapping: Geologie en Mijnbouw, v. 85, no. 4, p. 245-276.

Eidelmann, A., and Reches, Z., 1992, Fractured pebbles - a new stress indicator: Geology, v. 20, p. 307-310.

Ernston, K., Rampino, M. R., and Hiltl, M., 2001, Cratered cobbles in Triassic Bundsanstein conglomerates in Northeastern Spain: An indicator of shock deformation in the vicinity of large impacts: Geology, v. 29, p. 11-14.

Freed, A. M., 2005, Earthquake Triggering by Static, Dynamic, and Postseismic Stress Transfer: Annual Review of Earth and Planetary Sciences, v. 33, p. 335-367.

Griggs, D., 1967, Hydrolytic Weakening of Quartz and Other Silicates: Geophys. J. R. astr. Soc., v. 14, p. 19-31.

Grützner, C., Reicherter, K., Hübscher, C., and Silva, P. G., 2012, Active faulting and neotectonics in the Baelo Claudia area, Campo de Gibraltar (southern Spain): Tectonophysics, v. 554-557, p. 127-142.

Harker, R. I., 1993, Fracture patterns in clasts of diamictites (tillites): Journal of the Geological Society of London, v. 150, p. 251-254.

Hiemstra, J. F., and van den Meer, J. J. M., 1997, Pore-water controlled grain fracturing as an indicator for sub glacial shearing in tills: Journal of Glaciology, v. 43, no. 145, p. 446-454.

Hinzen, K. G., 2003, Stress field in the Northern Rhine area, Central Europe, from earthquake fault plane solutions: Tectonophysics, v. 377, p. 325-356.

Hippolyte, J. C., 2001, Paleostress and neotectonic analysis of sheared conglomerates: Southwest Alps and Southern Apennines: Journal of Structural Geology, v. 23, no. 2-3, p. 421-429.

Jerzykiewicz, T., 1985, Tectonically deformed pebbles in the Brazeau and Paskapoo formations, central Alberta Foothills, Canada: Sedimentary Geology, v. 42, no. 3-4, p. 159-180.

Kenkmann, T., Wünnemann, K., Deutsch, A., Poelchau, M. H., Schäfer, F., and Thoma, K., 2011, Impact cratering in sandstone: The MEMIN pilot study on the effect of pore water: Meteoritics & Planetary Science, v. 46, no. 6, p. 890-902.

Klostermann, J., 1992, Das Quartär der Niederrheinischen Bucht: Ablagerungen der letzten Eiszeit am Niederrhein. : Geological Survey of Northrhine-Westphalia, Krefeld, p. 1-200.

Kupsch, W. O., 1955, Drumlins with jointed boulders near Dollard, Saskatchewan: Geological Society of America Bulletin, v. 66, p. 327-338.

Lapusta, N., and Rice, J. R., 2003, Nucleation and early seismic propagation of small and large events in a crustal earthquake model: J. Geophys. Res., v. 108, no. B4, p. 2205-2223.

Lee, J. C., Lu, C. Y., Chu, H. T., Delcaillau, B., Angelier, J., and Deffontaines, B., 1996, Active Deformation and Paleostress Analysis in the Pakua Anticline Area of Western Taiwan: TAO, v. 7, no. 4, p. 431-446.

Lin, M. L., Jeng, F. S., Tsai, L. S., and Huang, T. H., 2005, Wetting weakening of tertiary sandstones—microscopic mechanism: Environmental Geology, v. 48, p. 265-275.

Madariaga, R., Ampuero, J. P., and Adda-Bedia, M., 2006, Seismic radiation from simple models of earthquakes, in: Earthquakes: Radiated Energy and Physics of faulting, Geophys. Monogr. Ser., v. 170, p. 223-236.

Marino, P., and Hoeck, E., 2000, A geologically friendly tool for rock mass strength estimation: Proc. GeoEng2000 Conference Melbourne, p. 1-19.

Obermeier, S., F., 1996, Use of liquefaction-induced features for paleoseismic analysis — An overview of how seismic liquefaction features can be distinguished from other features and how their regional distribution and properties of source sediment can be used to infer the location and strength of Holocene paleo-earthquakes: Engineering Geology, v. 44, no. 1-4, p. 1-76.

Ramsay, D. M., 1964, Deformation of Pebbles in Lower Old Red Sandstone Conglomerates Adjacent to the Highland Boundary Fault: Geological Magazine, v. 101, p. 228-248.

Silva, P. G., and Rodríguez Pascua, M. A., 2008, Catalogación de los effectos geológicos y ambientales de los terremotos en España en la Escala ESI-2007 y su aplicatión a los estudios paleseismológicos: Geotemas, v. 6, p. 1063-1066.

Snoke, A. W., Tullis, J., and Todd, V. R., 1998, Fault-Related Rocks: A Photographic Atlas Princeton University Press, p. 1-629.

Stein, R., and Lisowski, M., 1983, The 1979 Homestead Valley Earthquake Sequence, California: Control of Aftershocks and Postseismic Deformation: Journal of Geophysical Reasearch, v. 88, no. B8, p. 6477-6490.

Strayer, L. M., and Allen, J. R., 2008, The Oakland Conglomerate: a Hayward Fault Tectonite?: AGU Fall Meeting 2008, abstract #T51A-1862.

Tang, C. A., H. Y. Liu, W. C. Zhu, T. H. Yang, W. H. Li, L. Song, P. Lin, 2004, Numerical approach to particle breakage under different loading conditions: Powder Technology, v. 143-144, p. 130-143.

Tanner, W. F., 1963, Crushed Pebble Conglomerate of Southwestern Montana: The Journal of Geology, v. 71, no. 5, p. 637-641.

-, 1976, Tectonically significant pebble types: sheared, pocked and second-cycle examples: Sedimentary Geology, v. 16, p. 69-83.

Tapponier, P., Peltzer, G., and Armijo, R., 1986, On the mechanics of the collision between India and Asia. In: Coward, M. P. & Ries, A. C. (eds), Collision Tectonics: Geological Society of London, Special Publication, v. 19, p. 115-157.

Tiryaki, B., 2006, Evaluation of the indirect measures of rock brittleness and fracture toughness in rock cutting: The Journal of The South African Institute of Mining and Metallurgy, v. 106, p. 407-423.

Tokarski, A. T., and Swierczewska, A., 2005, Neofractures versus inherited fractures in structural analysis: a case study from Quaternary fluvial gravels (outer Carpathians, Poland): Annales Societatis Geologorum Poloniae, v. 75, p. 95-104.

Tokarski, A. T., Swierczewska, A., and Zuchiewicz, W., 2007, Fractured clasts in neotectonic reconstructions: an example from the Nowy Sacz Basin, Western Outer Carpathians, Poland: Studia Quaternaria, v. 24, p. 47-52.

Tuitz, C., U. Exner, M. Frehner, B. Grasemann, 2012, The impact of ellipsoidal particle shape on pebble breakage in gravel: International Journal of Rock Mechanics and Mining Sciences, v. 54, p. 70-79.

Vanneste, K., Verbeeck, K., Moreno, D. G., and Camelbeeck, T., 2010, A database of seismic sources for the Roer Valley Rift system: Proceedings of the European Seismological Commission 32nd General Assembly, September 6-10, Montpellier, France p. 1.

Zuchiewicz, W., Tokarski, A. K., Jarosinski, M., and Márton, E., 2002, Late Miocene to present day structural development of the Polish segment of the Outer Carpathians: EGU Stephan Mueller Special Publication Series v. 3, p. 185-202.

# Chapter 7

## *Conclusions and Outlook*

The focus of this thesis was to investigate the Holocene and historical fault activity of the Lower Rhine Graben (NW Germany) by combining paleoseismical approaches, analysis of high-resolution LiDAR data, and outcrop- to micro-scale analysis of coseismically deformed gravel deposits.

In the slowly-deforming Lower Rhine Graben, the tectonic imprint on young sediments, is difficult to identify. The reasons for this are (1) the long recurrence intervals of large earthquakes, relative to the sedimentation rates in the adjacent basins, and, (2) the extensive overprint of the landscape due to hillslope processes, soil erosion, and anthropogenic influence. The results from LiDAR-data analysis confirm that the landscape of the central Lower Rhine Graben is overprinted by man-made processes such as farming, urbanization and mining-induced subsidence. The LiDAR-analysis also showed, for the first time in paleoseismic research, the severe surface modification caused by aerial bombing, or so-called *bombturbation*. The sediment disturbance expected from such drastic incidents, as well as the associated hazard concerning future excavations due to unexploded bombs, thus call for more research to better understand the effects of *bombturbation* on the geomorphology of a region.

Former paleoseismological studies carried out in the Lower Rhine Graben had successfully identified earthquake-related deformation in Pleistocene sediments. Due to a lack of fault exposures in younger sediments, however, the present-day seismogenic potential of most of the faults in the Lower Rhine Graben is unknown. Seismic activity of the Schafberg fault, which is considered a subsidiary fault can be related to Holocene and historical surface rupture, as the youngest identified event in the trench most likely matches the 1756 AD Düren earthquake. This implies that at least one, perhaps neighboring faults, too, can produce coseismic surface ruptures.

The results of this study imply that future paleoseismic and tectonogeomorphic research in the Lower Rhine Graben must focus on faults concealed by Holocene sediments, rather than on analysis of the main border faults. Recurrence interval and slip-rate estimates on the Schafberg fault, as well as historical and instrumental earthquake records further imply that the tectonic activity of the Lower Rhine Graben is currently concentrated in the SW sector of the rift system. In order to better understand the spatio-temporal evolution of the

Lower Rhine Graben, however, additional paleoseismological studies, for example, in the eastern and central sectors of the region are needed.

Understanding coseismic rupture and aseismic creep processes, as well as their distinction in the geological record, are important tasks for earthquake geologists in both, intraplate and plate boundary settings. In particular, unconsolidated sediments cut by active faults often lack distinct features for differentiating aseismic and coseismic slip. In low-strain regions, however, most seismogenic ruptures barely reach the surface. Therefore, coseismic features are intrinsically small, such as those near the ends of large-magnitude rupture segments or those in the center of ruptures just large enough to break the surface..

We have developed a new approach, using 'fractured clasts' to analyze tectonically deformed gravel deposits. Systematic analysis of the spatial distribution of fractured clasts, as well as fracture-orientation measurements are valuable observables to detect seismogenic rupture processes in unconsolidated sediments. Under specific conditions, this approach may be useful for the identification of earthquake-related deformation in intraplate settings.
Elsewhere, the fractured-clast analysis may also be useful for potential supershear faults such as the Kunlun, Denali, or Dead Sea faults. Here, the distribution of fractured clasts may be used to pin point the relative timing between the propagating rupture on the one hand, and shaking-related deformation on the other hand.

The methods developed in this thesis expand the tools and strategies available for future paleoseismic research. Such strategies include trench site selection specifically in gravel deposits, as well as the combination of field observations of deformed gravels with laboratory tests and modeling approaches.

This study showed that at least one fault in the Lower Rhine Graben has been seismically active in historic time. I postulate that aseismic creep, if any, may result from near-surface motion of faults due to mining-induced subsidence and does not represent the dominant fault-slip mode in this region. However, a distinction between seismically and aseismically generated features in the geological record remains difficult for small-offset faults, and needs further investigation. The fractured-clast approach could be tested some of the larger faults in the central Lower Rhine Graben, e.g., at the Erft-, or Rurrand faults, where mining-induced near-surface creep overlaps with larger offset seismogenic ruptures.

Promising future paleoseismic approaches combine traditional trenching and high-resolution remote sensing analysis with micro-deformation analysis and modeling approaches.

# Appendix

## I. Trench Excavation Untermaubach

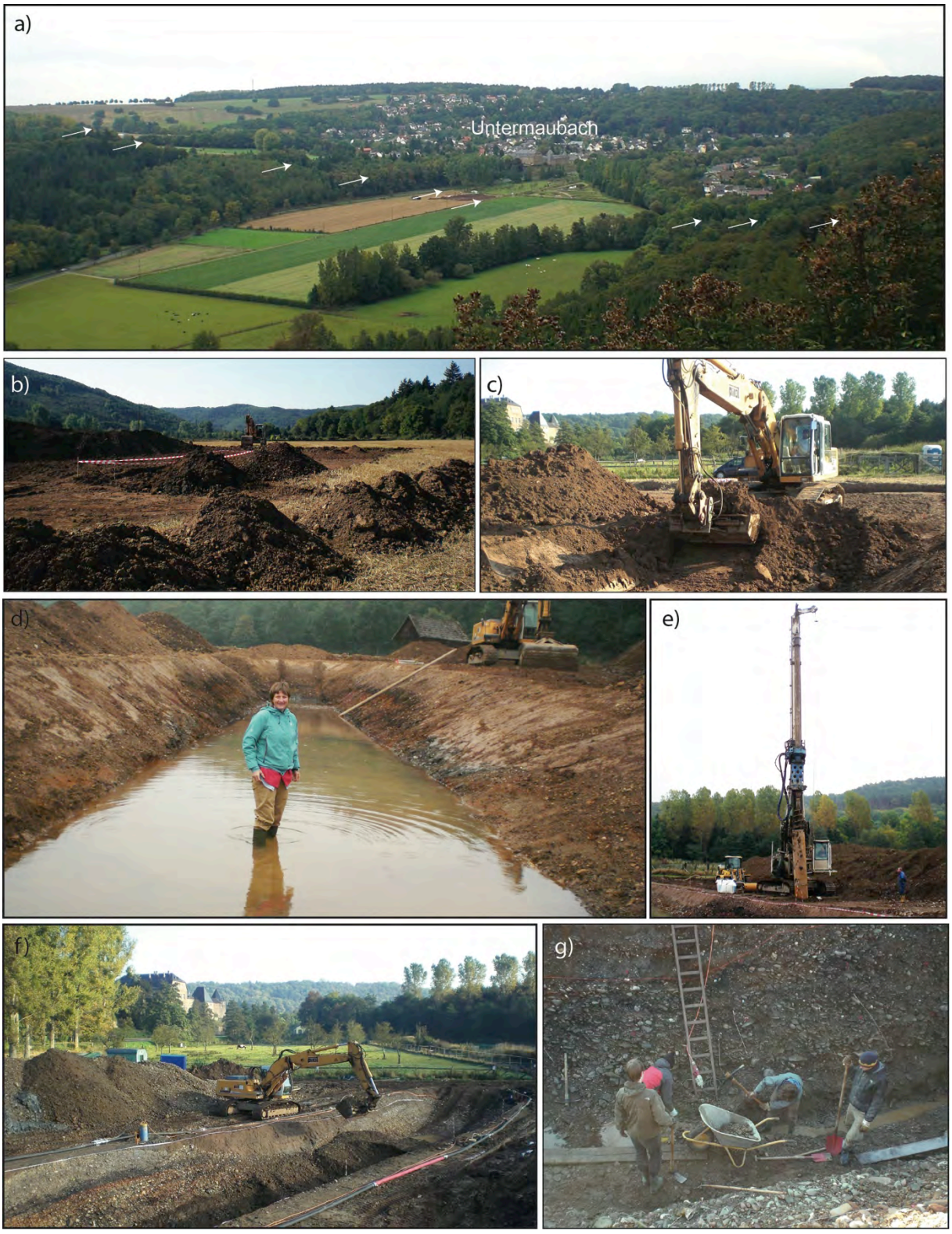


Figure I.1: Trench excavation at the Untermaubach site. (a) Overview of the Untermaubach trench site, view to the northeast. White arrows depict the suspected surface trace of the Schafberg fault; (b) removal and separate deposition of topsoil at the trench site before trench excavation; (c) start of trench excavation; (d) uncovered watertable at the Untermaubach trench site; (e) installation of wells for groundwater disposal. A total of six wells are installed using a drilling crane. The drill holes are equipped with perforated plastic tubes that are fixed on the outside with fine gravel. Tubes are then equipped with wet pit pumps; (f) excavation of the trench to its final depth of ~4.5 m and a length of 85 m. Note the installed drainage system connecting the wells. Disposed groundwater is discharged into a creek ~ 100 m north of the trench site; (g) partial manuel excavation to depth of > 5 m to evaluate the depth to the top of devonian basement rocks; (h) cleaning of trench walls; (i) sampling of trench walls; (j) Terrestrial laser scanner (Topcon GLS 1000) for high resolution 3D-scans of the trench; (k) orientation measurement of fractured clast; (l) trench inspection by researchers of the Seismological Observatory Bensberg; (m) students of the LMU Munich working in fully excavated trench.

# II. Trench Log and Radiocarbon Reports

Figure II.1: Full trench log of both trench walls and record of radiocarbon reports.

The complete trench log of the northern and southern trench wall (Adobe Illustrator Format, CS5.1) as well as the reports from radiocarbon dating are available on CD-ROM attached to the print version of this thesis.

# III. Fractured-Clast Data


Figure III.1: Polished cross-cuts of fractured fault-core clasts.

Sampled from the fault-core of the trench exposure. Clasts are fully fractured and cut by one or two main fractures, predominately independant of internal bedding.


Figure III.2: Polished cross-cuts of fractured damage-zone clasts.

Fractures are parallel to internal bedding.

Table III.1: Detailed log of fractured clasts of the Untermaubach trench.

Abbreviations: BS: Buntsandstein (Triassic); HB: mudstone of the Heimbach Formation (Devonian); Qz: Quartzite (Devonian); PO: point of origin; Fr: fracture; OS: offset; nm: not measurable.

| Trench wall | Distance from PO (m) | Depth (m) | Lith-ology | Size (cm) | Defor-mation | Fracture orien-tation | No. Of fractures |
|---|---|---|---|---|---|---|---|
| N | 36 | 3 | Qz | 8x4 | Fr | 210/45 | 1 |
| N | 39.5 | 3.7 | BS | 13,5x13 | Fr/OS | 182/25 | 1 |
| N | 46 | 3.3 | BS | 12,5x2,5 | Fr | 231/68 | 1 |
| S | 6 | 2 | BS | 7x6,5 | Fr | 22/80 | 1 |
| N | 25.5 | 2.7 | Qz | 11x5 | Fr | 26/75 | 1 |
| N | 31 | 2 | BS | 11x7,5 | Fr | 73/55 | 1 |
| N | 35 | 3.2 | BS | 10,5x6,5 | Fr | 270/60 | 1 |
| S | 32 | 1.7 | BS | 13x10 | Fr | 113/12 | 1 |
| N | 40 | 1.5 | BS | 14x12 | Fr/OS | 223/79 | 1 |
| N | 36 | 2.6 | BS | 9x3 | Fr | 212/05 | 1 |
| S | 22 | 2.3 | BS | 9,5x2,5 | Fr | 140/20 | 1 |
| S | 22 | 2.5 | BS | 5,5x4,5 | Fr | 156/45 | 1 |
| S | 20.7 | 2.6 | BS | 5x5,5 | Fr | 78/40 | 1 |
| S | 20.5 | 2.5 | BS | 9x4 | Fr | 130/15 | 1 |
| S | 20.5 | 1.8 | BS | 6x3,5 | Fr | 13/25 | 1 |
| S | 31.5 | 1 | BS | 16x4,5 | Fr | 210/60 | 1 |
| S | 31.2 | 1.6 | BS | 19x8 | Fr | 326/80 | 1 |
| S | 31.5 | 1.5 | BS | 3,5x2,5 | Fr | 178/10 | 1 |
| S | 33 | 2.7 | BS | 4x1,5 | Fr/OS | 122/20 | 1 |
| S | 33 | 2.7 | BS | 12x12,5 | Fr | 140/30 | 1 |
| S | 40 | 2.5 | BS | 14x2 | Fr | 238/20 | 1 |
| S | 41 | 3.2 | BS | 12x20 | Fr | 264/5 | 1 |
| S | 41 | 4.5 | BS | 5x2 | Fr | 182/10 | 1 |
| S | 42 | 1 | BS | 7,5x8 | Fr | 318/84 | 1 |
| S | 43 | 3.6 | BS | 8x2 | Fr/OS | 219/15 | 1 |
| S | 43 | 3.4 | BS | 8x7,5 | Fr/OS | 231/70 | 1 |
| S | 43 | 3.1 | BS | 6x2,5 | Fr | 164/20 | 1 |
| S | 59 | 2.3 | BS | 6,5x2,5 | Fr | 232/25 | 1 |
| S | 60.5 | 2.5 | BS | 9x3 | Fr/OS | 172/57 | 1 |
| S | 53 | 1.5 | BS | 10x6 | Fr | 112/20 | 1 |
| S | 54.5 | 1.5 | BS | 11x2,5 | Fr | 218/85 | 1 |
| S | 61 | 1 | BS | 12,5x1,5 | Fr | 232/15 | 1 |
| S | 66 | 2.7 | BS | 8x1,5 | Fr | 173/20 | 1 |
| S | 62 | 2 | BS | 8x8 | Fr | 152/50 | 1 |
| S | 48 | 2.5 | BS | 11x5 | Fr | 81/47 | 1 |
| S | 45 | 2.5 | BS | 7x3 | Fr | 272/65 | 1 |
| S | 54 | 1.8 | BS | 8x7 | Fr | 203/42 | 1 |
| S | 48 | 2.5 | BS | 10x4 | Fr/OS | 166/30 | 1 |
| S | 56 | 1.5 | BS | 12x6 | Fr | 70/66 | 1 |
| N | 23 | 1.4 | BS | 8x7 | Fr | 38/84 | 1 |
| N | 23.1 | 1.6 | BS | 2x3 | Fr | 196/81 | 1 |
| N | 23.1 | 3 | BS | 2x5 | Fr | 25/18 | 1 |
| N | 24 | 4 | BS | 4x6 | Fr/OS | 268/31 | 1 |
| N | 24.8 | 2.3 | BS | 12x6 | Fr | 298/32 | 1 |
| N | 60 | 2 | BS | 5x2,5 | Fr/OS | 308/70 | 1 |
| N | 59.5 | 2 | BS | 6x2 | Fr | 48/25 | 1 |
| N | 60 | 2.5 | BS | 6x10 | Fr | 208/42 | 1 |
| N | 80 | 2.5 | BS | 7x4 | Fr | 244/50 | 1 |
| N | 51 | 2.2 | BS | 10x7,5 | Fr | 37/64 | 1 |

| | | | | | | | |
|---|---|---|---|---|---|---|---|
| N | 74 | 2.3 | BS | 13,5x5 | Fr | 330/20 | 1 |
| N | 73 | 2.2 | Qz | 17x14 | Fr | 327/20 | 1 |
| N | 38 | 2.7 | BS | 9x7 | Fr | 40/42 | 1 |
| S | 45 | 3.2 | BS | 16x4 | Fr | 176/19 | 1 |
| S | 38 | 3.5 | BS | 15x6,5 | Fr | 198/10 | 1 |
| S | 8 | 3 | BS | 7x4 | Fr | 262/80 | 1 |
| S | 11 | 2.5 | Qz | 5,5x1,5 | Fr/OS | 196/25 | 1 |
| S | 11.5 | 2.6 | BS | 14x2,4 | Fr | 170/20 | 1 |
| S | 12 | 2.1 | BS | 13,5x3 | Fr | 232/15 | 1 |
| S | 14 | 3 | BS | 7x3 | Fr/OS | 94/43 | 1 |
| N | 37.5 | 2.5 | BS | 12x3 | Fr | 248/40 | 1 |
| N | 45 | 2.4 | BS | 9,5x4 | Fr | 246/60 | 1 |
| N | 44 | 3.2 | BS | 8x5 | Fr/OS | 210/38 | 1 |
| N | 57.5 | 2.5 | BS | 30x14 | Fr | 270/55 | 1 |
| N | 31 | 2.5 | BS | 12x4 | Fr | 336/18 | 1 |
| N | 31.5 | 3 | BS | 1,5x1 | Fr | 276/60 | 1 |
| S | 28 | 3.5 | BS | 14x12 | Fr/OS | 212/50 | 1 |
| S | 17.8 | 3.5 | BS | 10x2 | Fr/OS | 242/55 | 1 |
| S | 18 | 2.7 | BS | 5,5x0,7 | Fr | 231/12 | 1 |
| S | 18.5 | 2.8 | BS | 12x2 | Fr/OS | 88/50 | 1 |
| S | 18.4 | 2.5 | BS | 1,5x2 | Fr | 226/65 | 1 |
| N | 17 | 3.5 | BS | 21x12 | Fr | 216/24 | 1 |
| N | 18 | 2.2 | BS | 7x5 | Fr | 349/18 | 1 |
| N | 11 | 2.8 | BS | 8x7 | Fr | 231/66 | 1 |
| N | 20 | 3.8 | BS | 5x4 | Fr/OS | 293/74 | 1 |
| N | 13 | 3.6 | BS | 8,5x8 | Fr | 267/20 | 1 |
| N | 17 | 2.4 | BS | 6x4,5 | Fr | 88/55 | 1 |
| N | 8 | 2.5 | BS | 9x9 | Fr | 298/45 | 1 |
| N | 8 | 1.5 | BS | 12x11 | Fr | 46/25 | 1 |
| N | 24 | 3.5 | BS | 3x5 | Fr | 86/34 | 1 |
| N | 25 | 3.6 | BS | 5x4 | Fr/OS | 356/40 | 1 |
| N | 23 | 3.3 | BS | 13x12 | Fr | 38/21 | 1 |
| N | 24 | 2.7 | BS | 10x9 | Fr | 287/04 | 1 |
| S | 55 | 2 | BS | 12x3 | Fr | 173/25 | 1 |
| N | 62 | 2 | BS | 5x4 | Fr | 222/50 | 1 |
| S | 59 | 2 | BS | 7x2,5 | Fr | 179/37 | 1 |
| S | 60 | 2 | BS | 12x4 | Fr | 97/51 | 1 |
| N | 24 | 1 | BS | 8x4 | Fr | 329/36 | 1 |
| N | 24 | 1.5 | BS | 6x6 | Fr | 54/78 | 1 |
| N | 32 | 0.8 | BS | 5x2 | Fr | 284/50 | 1 |
| N | 25 | 1.5 | BS | 10x7,5 | Fr | 101/81 | 1 |
| S | 15.5 | 2.6 | BS | 13x3 | Fr | 214/10 | 1 |
| S | 17 | 2.5 | BS | 6,5x1 | Fr | 62/10 | 1 |
| S | 17.4 | 2.5 | BS | 6,5x2 | Fr | 142/15 | 1 |
| S | 18 | 2.7 | BS | 6x5 | Fr | 90/60 | 1 |
| S | 12.3 | 3.5 | BS | 8x7,5 | Fr | 112/20 | 1 |
| S | 20.5 | 3 | BS | 7x4 | Fr | 170/60 | 1 |
| S | 21 | 2.5 | BS | 6x15 | Fr | 84/20 | 1 |
| S | 21 | 2.8 | BS | 4,5x1,5 | Fr | 270/25 | 1 |
| S | 21 | 3.2 | BS | 16x3 | Fr | 192/35 | 1 |
| S | 21 | 3.25 | BS | 7x7 | Fr/OS | 76/25 | 1 |
| S | 21.5 | 3 | BS | 15x3,5 | Fr | 218/35 | 1 |
| S | 21.5 | 1.8 | Qz | 5x6 | Fr | 280/55 | 1 |
| S | 23 | 2 | BS | 10x5 | Fr | 28/25 | 1 |
| S | 23 | 2 | BS | 6,5x4,5 | Fr | 126/40 | 1 |
| N | 38 | 3 | BS | 7x5 | Fr | 322/15 | 1 |

| | | | | | | | |
|---|---|---|---|---|---|---|---|
| N | 33 | 3 | BS | 4x2 | Fr | 248/70 | 1 |
| N | 36 | 2.9 | BS | 8x2 | Fr | 330/07 | 1 |
| N | 31.5 | 2.7 | Qz | 10x3 | Fr | 224/84 | 1 |
| N | 35 | 3 | BS | 7x4,5 | Fr | 272/80 | 1 |
| N | 29.5 | 2.5 | BS | 7x5 | Fr/OS | 238/83 | 1 |
| N | 33 | 3.1 | BS | 12x6 | Fr | 316/28 | 1 |
| N | 44 | 2.5 | BS | 11x3 | Fr | 307/81 | 1 |
| N | 33 | 3.6 | BS | 12x10 | Fr | 238/46 | 1 |
| N | 43 | 2.5 | BS | 10x5 | Fr | 240/30 | 1 |
| N | 45 | 2.5 | BS | 4x4 | Fr | 53/67 | 1 |
| N | 42 | 3.2 | BS | 10x5 | Fr | 306/14 | 1 |
| S | 26 | 3.4 | BS | 5x1 | Fr | nm | 1 |
| S | 26 | 3.4 | BS | 5x2,5 | Fr | nm | 1 |
| S | 26 | 3.4 | BS | 6,5x3 | Fr | nm | 1 |
| S | 26 | 3.4 | HB | 7x2,5 | Fr | nm | 1 |
| S | 26.2 | 4.5 | HB | 2x0,5 | Fr | nm | 1 |
| S | 26.2 | 4.5 | BS | 2x2 | Fr | nm | 1 |
| S | 27 | 3.6 | Qz | 4x6 | Fr | 280/65 | 1 |
| S | 27.2 | 3.5 | BS | 8x2 | Fr | 228/84 | 1 |
| S | 21.1 | 4.4 | BS | 4x4 | Fr/OS | 66/82 | 1 |
| S | 28 | 3.45 | BS | 20x6 | Fr | 220/42 | 1 |
| S | 28 | 3.55 | BS | 7x2 | Fr | 124/52 | 1 |
| S | 29.5 | 3.5 | HB | 8x2 | Fr | 262/30 | 1 |
| S | 29.5 | 3.5 | HB | 8x1,5 | Fr | 240/34 | 1 |
| S | 29.5 | 3.5 | BS | 8,5x2 | Fr | 255/40 | 1 |
| S | 29.5 | 3.5 | BS | 7,5x2,5 | Fr | 268/28 | 1 |
| S | 29.5 | 3.5 | BS | 7x1 | Fr | 260/32 | 1 |
| S | 28 | 1.5 | BS | 11x6 | Fr | 202/74 | 1 |
| S | 33 | 1.6 | BS | 6x6 | Fr | 230/80 | 1 |
| S | 33.2 | 1.4 | BS | 2x3 | Fr | 302/84 | 1 |
| S | 34 | 3.5 | BS | 5x12 | Fr | nm | 1 |
| S | 34 | 2.4 | Qz | 7x6 | Fr | 262/88 | 1 |
| S | 34.5 | 2.9 | BS | 4x6 | Fr | 142/60 | 1 |
| S | 37 | 3.4 | BS | 12x1 | Fr | nm | 1 |
| S | 40 | 3.4 | BS | 2x1 | Fr | nm | 1 |
| S | 40 | 3.4 | BS | 3x1 | Fr | nm | 1 |
| S | 40 | 3.4 | BS | 3x1,5 | Fr | nm | 1 |
| S | 40 | 3.4 | BS | 6x4 | Fr | nm | 1 |
| S | 40 | 3.4 | BS | 8x3,5 | Fr | nm | 1 |
| S | 40 | 3.4 | BS | 12x12 | Fr | nm | 1 |
| S | 40 | 2.6 | BS | 10x8 | Fr | 74/32 | 1 |
| S | 43.5 | 2.6 | BS | 12x5 | Fr | 124/70 | 1 |
| S | 44 | 3.1 | BS | 7x3 | Fr | 64/50 | 1 |
| S | 59 | 2.5 | HB | 8x2 | Fr | 18/22 | 1 |
| S | 6 | 2 | BS | 4x1 | Fr | 204/84 | 1 |
| S | 16 | 2.8 | HB | 5x1 | Fr | 84/20 | 1 |
| S | 17 | 3.6 | BS | 15x10 | Fr/OS | 69/69 | 1 |
| S | 20.2 | 3.3 | BS | 2x10 | Fr | 100/86 | 1 |
| S | 24.5 | 2.4 | BS | 6x1 | Fr | 128/86 | 1 |
| S | 25.5 | 2.9 | BS | 12x3 | Fr | 190/45 | 1 |
| S | 25.8 | 3.8 | BS | 15x6 | Fr | 196/70 | 1 |
| S | 26.5 | 2.8 | BS | 5x2 | Fr | 199/25 | 1 |
| S | 26.5 | 2.9 | BS | 6x1 | Fr | 242/72 | 1 |
| S | 28.5 | 1.4 | BS | 12x7 | Fr | 198/68 | 1 |
| N | 16 | 3.4 | BS | 6x11 | Fr | 114/54 | 1 |
| N | 18 | 3.3 | BS | 15x6 | Fr | 102/44 | 1 |

| | | | | | | | |
|---|---|---|---|---|---|---|---|
| N | 18.5 | 3.9 | BS | 15x3 | Fr | 215/20 | 1 |
| N | 19 | 4 | BS | 10x15 | Fr | 13/48 | 1 |
| N | 19.5 | 3.7 | BS | 15x5 | Fr | 252/85 | 1 |
| N | 20 | 3.7 | HB | 7x2 | Fr | 210/26 | 1 |
| N | 20 | 3.75 | BS | 6x3 | Fr/OS | 44/89 | 1 |
| N | 22 | 1.8 | BS | 2x6 | Fr/OS | 192/50 | 1 |
| N | 21.9 | 2.2 | BS | 5x1 | Fr | nm | 1 |
| N | 22.3 | 2.3 | BS | 12x6 | Fr | 20/75 | 1 |
| N | 22 | 2.4 | Qz | 5x4 | Fr | nm | 1 |
| N | 21.9 | 2.8 | BS | 7x2 | Fr | 252/85 | 1 |
| N | 22.5 | 3 | BS | 5x3 | Fr | 280/86 | 1 |
| N | 22.4 | 4.4 | BS | 3x1 | Fr | 288/70 | 1 |
| N | 22.4 | 4.5 | BS | 12x4 | Fr | 208/50 | 1 |
| N | 40 | 2.7 | BS | 11x5 | Fr | 120/25; nm | 2 |
| N | 25.5 | 3.5 | BS | 5x3 | Fr | 210/86; nm | 2 |
| S | 31 | 3.6 | BS | 7x4,5 | Fr | 155/66; nm | 2 |
| N | 37 | 1.5 | BS | 11x9 | Fr | 295/20; nm | 2 |
| S | 45 | 2.5 | BS | 5x3,5 | Fr | 199/60; nm | 2 |
| S | 21 | 2 | BS | 13x6,5 | Fr/OS | 164/10; nm | 2 |
| S | 31.2 | 1.4 | Qz | 9x2,5 | Fr | 154/30; nm | 2 |
| S | 35 | 3.4 | BS | 9x1 | Fr | 195/5; nm | 2 |
| S | 35 | 2.3 | BS | 3,5x4 | Fr/OS | 250/40; nm | 2 |
| S | 43 | 2 | BS | 15x8,5 | Fr | 46/20; 267/32 | 2 |
| S | 57 | 2.15 | BS | 9,5x8,5 | Fr | 70/55; 196/35 | 2 |
| S | 55 | 1.4 | BS | 8,5x4 | Fr | 158/20; nm | 2 |
| S | 44 | 2.5 | BS | 6x5 | Fr | 205/15; nm | 2 |
| N | 23 | 3.9 | HB | 5x4 | Fr/OS | 220/35; nm | 2 |
| S | 24 | 3.5 | BS | 19,5x6,5 | Fr/OS | 352/5; nm | 2 |
| S | 9.5 | 2.5 | BS | 15x4 | Fr | 165/44; nm | 2 |
| S | 13.5 | 2.75 | BS | 12x6,5 | Fr | 128/25; nm | 2 |
| N | 44 | 3 | BS | 6x1,8 | Fr/OS | 115/50; nm | 2 |
| N | 26 | 3.1 | BS | 12x9 | Fr | 74/63; nm | 2 |
| S | 40 | 3.1 | BS | 14x12 | Fr/OS | 272/50; nm | 2 |
| S | 18.1 | 3.3 | BS | 0,7x3 | Fr/OS | 70/70; nm | 2 |
| N | 12 | 2.7 | BS | 13x11 | Fr | 13/15; nm | 2 |
| N | 25 | 3.4 | BS | 6x4 | Fr/OS | 28/39; nm | 2 |
| N | 25 | 3.4 | BS | 9x14 | Fr | 353/30; nm | 2 |
| N | 19 | 2.5 | BS | 14x7 | Fr | 313/31; nm | 2 |
| N | 25 | 2.9 | Qz | 3,5x3,5 | Fr | 23/52; nm | 2 |

| | | | | | | | |
|---|---|---|---|---|---|---|---|
| N | 33 | 3.2 | BS | 7x1 | Fr | 212/13; nm | 2 |
| S | 15 | 2 | BS | 14x5 | Fr | 245/18; nm | 2 |
| S | 16 | 3 | BS | 3x3 | Fr | 96/80; nm | 2 |
| S | 23.5 | 4 | BS | 14x10 | Fr/OS | 110/75; nm | 2 |
| S | 26.5 | 3.7 | HB | 6x1,5 | Fr | 152/22; nm | 2 |
| S | 28.2 | 2.5 | HB | 12x3 | Fr | 185/20 | 2 |
| S | 32.5 | 2.7 | BS | 12x6 | Fr | 98/64; nm | 2 |
| S | 33.1 | 3.4 | BS | 8x2 | Fr | 206/76; nm | 2 |
| N | 15 | 3.6 | BS | 5x5 | Fr | 208/72; nm | 2 |
| N | 18 | 3.1 | BS | 4x4 | Fr | 62/85; nm | 2 |
| N | 39 | 3.4 | BS | 7x8 | Fr/OS | 208/45; nm; nm | 3 |
| N | 59 | 2.5 | BS | 16x9 | Fr | 190/80; nm; nm | 3 |
| N | 44 | 3.6 | BS | 70x6 | Fr/OS | 273/84; nm; nm | 3 |
| N | 41.5 | 2 | BS | 11x6 | Fr | 285/5; nm; nm | 3 |
| S | 41.5 | 2 | BS | 12x7,5 | Fr | 70/90; nm; nm | 3 |
| S | 12.5 | 3.6 | BS | 13x5 | Fr | 176/35; nm | 3 |
| N | 31 | 3.5 | BS | 6x4 | Fr | 211/71; nm | 3 |
| N | 9 | 2.5 | BS | 10x5 | Fr | 144/02; nm | 3 |
| N | 24 | 3.6 | BS | 3x1 | Fr/OS | 228/35; nm; nm | 3 |
| N | 19 | 2.5 | BS | 13x6 | Fr | 298/63; nm; nm | 3 |
| S | 12.5 | 2.8 | BS | 7x3 | Fr/OS | 327/10; nm; nm | 3 |
| S | 43 | 3.6 | Qz | 12x10 | Fr | 112/85; nm; nm | 3 |
| S | 20.2 | 3.2 | BS | 13x7 | Fr | 110/75; ; nm; nm | 3 |
| S | 24.5 | 3.7 | BS | 15x11 | Fr | 222/75; nm; nm | 3 |
| N | 14.8 | 3 | BS | 15x3 | Fr | 244/48; nm; nm | 3 |
| S | 33 | 3 | BS | 6x3 | Fr | 18/40; nm; nm; nm | 4 |
| S | 54.5 | 2.8 | BS | 16x10 | Fr | 44/45; nm; nm; nm | 4 |
| S | 17.8 | 3.7 | BS | 12x7,5 | Fr/OS | 178/5; nm; nm; nm | 4 |
| N | 25 | 3.9 | BS | 12x8,5 | Fr | 292/27; nm; nm; nm | 4 |
| S | 16.5 | 2.6 | BS | 14x7 | Fr | 330/90; nm; nm; nm | 4 |
| S | 23.5 | 4.5 | BS | 20x12 | Fr | 76/88; nm; nm; nm | 4 |

| | | | | | | | |
|---|---|---|---|---|---|---|---|
| S | 23 | 4.8 | HB | 17x5 | Fr | 77/81; nm; nm; nm | 4 |
| N | 35 | 2.2 | BS | 26x14,5 | Fr | 314/60; nm; nm; nm | 4 |

Table III.2: Fracture orientation vs. Clast shape.

List of the short-axes (a-axes) and long-axes (b-axes) of 91 fractured clasts and the deviation of the fracture plane with respect to the a-axis.

| a-axis (cm) | b-axis(cm) | a/b | Max. fracture deviation from a-axis (°) | sample No. |
|---|---|---|---|---|
| 8 | 12 | 0,67 | 10 | 7198 |
| 2 | 9 | 0,22 | 90 | 7199 |
| 1,5 | 5 | 0,30 | 85 | 7200 |
| 4 | 6 | 0,67 | 8 | 7201 |
| 6 | 11 | 0,55 | 75 | 7202 |
| 3,5 | 13 | 0,27 | 88 | 7203 |
| 8 | 12,5 | 0,64 | 5 | 7204 |
| 8,5 | 14 | 0,61 | 86 | 7205 |
| 4 | 12 | 0,33 | 12 | 7206 |
| 1 | 4 | 0,25 | 0 | 7210 |
| 3 | 9 | 0,33 | 3 | 7211 |
| 5 | 6 | 0,83 | 35 | 7212 |
| 4 | 6,5 | 0,62 | 60 | 7213 |
| 5 | 10 | 0,50 | 45 | 7214 |
| 2 | 4,5 | 0,44 | 30 | 7215 |
| 1,5 | 9,5 | 0,16 | 73 | 7216 |
| 2 | 3 | 0,67 | 65 | 7217 |
| 1 | 1,5 | 0,67 | 85 | 7218 |
| 3 | 16 | 0,19 | 70 | 7219 |
| 5 | 7 | 0,71 | 4 | 7220 |
| 3 | 7,5 | 0,40 | 80 | 7221 |
| 0,7 | 2 | 0,35 | 5 | 7222 |
| 1,5 | 6 | 0,25 | 85 | 7223 |
| 2,5 | 4 | 0,63 | 90 | 7224 |
| 5 | 9 | 0,56 | 60 | 7225 |
| 7 | 13 | 0,54 | 40 | 7226 |
| 2,5 | 6 | 0,42 | 80 | 7227 |
| 3 | 6 | 0,50 | 75 | 7228 |
| 4 | 18 | 0,22 | 70 | 7229 |
| 1 | 4 | 0,25 | 3 | 7230 |
| 3 | 8 | 0,38 | 12 | 7231 |
| 5 | 12 | 0,42 | 78 | 7232 |

| | | | | |
|---|---|---|---|---|
| 5 | 9 | 0,56 | 70 | 7234 |
| 4 | 10 | 0,40 | 80 | 7235 |
| 2 | 5 | 0,40 | 85 | 7237 |
| 4 | 15 | 0,27 | 70 | 7238 |
| 10 | 19 | 0,53 | 60 | 7239 |
| 3 | 10 | 0,30 | 75 | 7240 |
| 7 | 16 | 0,44 | 55 | 7241 |
| 3 | 5 | 0,60 | 30 | 7242 |
| 4 | 11 | 0,36 | 85 | 7243 |
| 2,5 | 7 | 0,36 | 90 | 7244 |
| 2 | 3 | 0,67 | 60 | 7244 |
| 4 | 8 | 0,50 | 45 | 7245 |
| 3 | 15 | 0,20 | 30 | 7246 |
| 3,5 | 5 | 0,70 | 75 | 7247 |
| 2 | 6 | 0,33 | 60 | 7248 |
| 1 | 5 | 0,20 | 80 | 7249 |
| 3,5 | 7 | 0,50 | 65 | 7249 |
| 3 | 10 | 0,30 | 85 | 7250 |
| 4 | 8 | 0,50 | 80 | 7251 |
| 4,5 | 12 | 0,38 | 55 | 7252 |
| 6 | 14 | 0,43 | 70 | 7253 |
| 3,5 | 8 | 0,44 | 85 | 7254 |
| 4 | 7,5 | 0,53 | 65 | 7255 |
| 6 | 15 | 0,40 | 15 | 7256 |
| 2 | 4 | 0,50 | 83 | 7257 |
| 7 | 18 | 0,39 | 75 | 7258 |
| 6 | 10 | 0,60 | 62 | 7259 |
| 4 | 5 | 0,80 | 65 | 7260 |
| 2,5 | 9 | 0,28 | 20 | 7261 |
| 3,5 | 8,5 | 0,41 | 40 | 7262 |
| 2 | 3 | 0,67 | 35 | 7263 |
| 7 | 22 | 0,32 | 15 | 7265 |
| 3 | 5 | 0,60 | 65 | 7266 |
| 1,5 | 6 | 0,25 | 80 | 7267 |
| 4 | 15 | 0,27 | 73 | 7269 |
| 10 | 25 | 0,40 | 55 | 7270 |
| 2 | 12 | 0,17 | 15 | 7271 |
| 0,5 | 2 | 0,25 | 80 | 7272 |
| 0,7 | 4 | 0,18 | 85 | 7273 |
| 5 | 10 | 0,50 | 20 | 7274 |
| 3 | 7 | 0,43 | 65 | 7275 |
| 4 | 9 | 0,44 | 68 | 7276 |
| 3 | 9,5 | 0,32 | 45 | 7277 |

| | | | | |
|---|---|---|---|---|
| 3 | 3,5 | 0,86 | 30 | 7278 |
| 9 | 16 | 0,56 | 25 | 7279 |
| 6 | 7,5 | 0,80 | 15 | 7280 |
| 6 | 13,5 | 0,44 | 85 | 7281 |
| 1,5 | 4,5 | 0,33 | 80 | 7282 |
| 9 | 18,5 | 0,49 | 72 | 7283 |
| 6 | 17,5 | 0,34 | 45 | 7284 |
| 5 | 18 | 0,28 | 75 | 7285 |
| 4 | 8 | 0,50 | 12 | 7285 |
| 2 | 5 | 0,40 | 87 | 7286 |
| 1 | 4 | 0,25 | 80 | 7286 |
| 4,5 | 13,5 | 0,33 | 40 | 7287 |
| 3 | 7,5 | 0,40 | 15 | 7288 |
| 2 | 4,5 | 0,44 | 50 | 7289 |
| 2,5 | 5,5 | 0,45 | 82 | 7290 |

Table III.3: Data on fracture orientation of fractured clasts sorted by damage zone and fault zone.

Fault zone clasts are further subdivided into clasts deformed during the most recent event (MRE) and during the penultimate event (PUE).

| Fault zone all clasts | | Fault zone MRE | | Fault zone PUE | | Damage zone | |
|---|---|---|---|---|---|---|---|
| Dip direction | Dip angle | Dip direction | Dip angle | Dip direction | Dip angle | Dip direction | Dip angle |
| 42 | 55 | 51 | 68 | 42 | 55 | 30 | 45 |
| 51 | 68 | 50 | 60 | 73 | 55 | 28 | 45 |
| 73 | 55 | 62 | 75 | 43 | 79 | 22 | 80 |
| 50 | 60 | 50 | 90 | 49 | 60 | 26 | 75 |
| 43 | 79 | 78 | 80 | 48 | 40 | 30 | 86 |
| 49 | 60 | 51 | 70 | 43 | 55 | 32 | 45 |
| 48 | 40 | 52 | 75 | 78 | 80 | 30 | 60 |
| 43 | 55 | 70 | 66 | 39 | 65 | 18 | 40 |
| 62 | 75 | 52 | 65 | 46 | 70 | 45 | 45 |
| 50 | 90 | 66 | 60 | 70 | 55 | 70 | 40 |
| 78 | 80 | 70 | 70 | 38 | 85 | 28 | 20 |
| 39 | 65 | 51 | 66 | 52 | 55 | 84 | 45 |
| 51 | 70 | 54 | 78 | 38 | 84 | 42 | 50 |
| 46 | 70 | 50 | 60 | 46 | 81 | 47 | 32 |
| 70 | 55 | 68 | 70 | 40 | 80 | 46 | 35 |
| 52 | 75 | 58 | 83 | 48 | 65 | 44 | 45 |
| 38 | 85 | 53 | 67 | 37 | 64 | 25 | 65 |
| 52 | 55 | 66 | 82 | 82 | 80 | 61 | 47 |
| 70 | 66 | 50 | 80 | 50 | 55 | 23 | 42 |
| 38 | 84 | 69 | 69 | 74 | 63 | 25 | 58 |

| | | | | | | | |
|---|---|---|---|---|---|---|---|
| 46 | 81 | 62 | 72 | 62 | 55 | 40 | 35 |
| 40 | 80 | 62 | 85 | 48 | 50 | 68 | 41 |
| 48 | 65 | 63 | 66 | 46 | 65 | 28 | 42 |
| 37 | 64 | 60 | 80 | 36 | 64 | 64 | 50 |
| 70 | 90 | | | 48 | 55 | 40 | 42 |
| 82 | 80 | | | 38 | 61 | 46 | 25 |
| 52 | 65 | | | 44 | 50 | 68 | 40 |
| 66 | 60 | | | 44 | 84 | 30 | 38 |
| 50 | 55 | | | 76 | 88 | 31 | 71 |
| 74 | 63 | | | 77 | 81 | 32 | 50 |
| 62 | 55 | | | 48 | 81 | 51 | 52 |
| 70 | 70 | | | 42 | 88 | 48 | 50 |
| 48 | 50 | | | 42 | 75 | 87 | 20 |
| 46 | 65 | | | 40 | 45 | 46 | 25 |
| 36 | 64 | | | 46 | 70 | 28 | 39 |
| 51 | 66 | | | 48 | 68 | 46 | 44 |
| 48 | 55 | | | 64 | 48 | 46 | 34 |
| 38 | 61 | | | 72 | 85 | 48 | 35 |
| 54 | 78 | | | 76 | 76 | 42 | 50 |
| 50 | 60 | | | 40 | 78 | 23 | 52 |
| 44 | 50 | | | 40 | 59 | 32 | 43 |
| 68 | 70 | | | 40 | 71 | 34 | 40 |
| 44 | 84 | | | 42 | 84 | 65 | 48 |
| 58 | 83 | | | 76 | 61 | 62 | 40 |
| 53 | 67 | | | 45 | 57 | 50 | 25 |
| 76 | 88 | | | 75 | 57 | 42 | 35 |
| 77 | 81 | | | 224 | 60 | 76 | 25 |
| 48 | 81 | | | 245 | 66 | 38 | 35 |
| 66 | 82 | | | 236 | 80 | 28 | 55 |
| 50 | 80 | | | 228 | 84 | 84 | 44 |
| 42 | 88 | | | 262 | 54 | 58 | 46 |
| 69 | 69 | | | 242 | 50 | 60 | 30 |
| 42 | 75 | | | 255 | 50 | 40 | 42 |
| 40 | 45 | | | 253 | 74 | 45 | 20 |
| 46 | 70 | | | 208 | 63 | 42 | 30 |
| 62 | 72 | | | 254 | 50 | 60 | 34 |
| 48 | 68 | | | 261 | 81 | 75 | 40 |
| 64 | 48 | | | 240 | 90 | 48 | 28 |
| 62 | 85 | | | 260 | 60 | 40 | 32 |
| 72 | 85 | | | 217 | 81 | 22 | 74 |
| 76 | 76 | | | 200 | 75 | 26 | 76 |
| 40 | 78 | | | 214 | 52 | 74 | 32 |
| 40 | 59 | | | 212 | 84 | 48 | 22 |
| 40 | 71 | | | 232 | 60 | 24 | 84 |
| 63 | 66 | | | 202 | 85 | 44 | 20 |

| | | | | | | | |
|---|---|---|---|---|---|---|---|
| 42 | 84 | | | 214 | 70 | 49 | 25 |
| 76 | 61 | | | 64 | 50 | 28 | 72 |
| 45 | 57 | | | 200 | 75 | 35 | 20 |
| 75 | 57 | | | 218 | 86 | 43 | 48 |
| 224 | 60 | | | 204 | 54 | 28 | 50 |
| 245 | 66 | | | 201 | 75 | 92 | 65 |
| 236 | 80 | | | 209 | 54 | 93 | 84 |
| 228 | 84 | | | 47 | 65 | 94 | 43 |
| 262 | 54 | | | 52 | 58 | 96 | 60 |
| 242 | 50 | | | | | 92 | 50 |
| 255 | 50 | | | | | 260 | 25 |
| 253 | 74 | | | | | 255 | 20 |
| 208 | 63 | | | | | 203 | 12 |
| 254 | 50 | | | | | 230 | 20 |
| 261 | 81 | | | | | 246 | 45 |
| 240 | 90 | | | | | 254 | 10 |
| 260 | 60 | | | | | 220 | 15 |
| 217 | 81 | | | | | 268 | 10 |
| 200 | 75 | | | | | 244 | 30 |
| 214 | 52 | | | | | 262 | 20 |
| 212 | 84 | | | | | 230 | 30 |
| 232 | 60 | | | | | 254 | 20 |
| 202 | 85 | | | | | 262 | 54 |
| 214 | 70 | | | | | 252 | 20 |
| 64 | 50 | | | | | 263 | 20 |
| 200 | 75 | | | | | 242 | 50 |
| 218 | 86 | | | | | 256 | 30 |
| 204 | 54 | | | | | 258 | 32 |
| 201 | 75 | | | | | 240 | 20 |
| 209 | 54 | | | | | 237 | 20 |
| 47 | 65 | | | | | 245 | 5 |
| 52 | 58 | | | | | 266 | 19 |
| 60 | 80 | | | | | 262 | 5 |
| | | | | | | 255 | 44 |
| | | | | | | 260 | 20 |
| | | | | | | 266 | 35 |
| | | | | | | 218 | 25 |
| | | | | | | 255 | 50 |
| | | | | | | 246 | 18 |
| | | | | | | 268 | 5 |
| | | | | | | 259 | 18 |
| | | | | | | 248 | 45 |
| | | | | | | 53 | 15 |
| | | | | | | 262 | 27 |
| | | | | | | 234 | 2 |

| | | | | | | | |
|---|---|---|---|---|---|---|---|
| | | | | | | 263 | 30 |
| | | | | | | 266 | 40 |
| | | | | | | 247 | 4 |
| | | | | | | 263 | 25 |
| | | | | | | 269 | 37 |
| | | | | | | 223 | 31 |
| | | | | | | 97 | 51 |
| | | | | | | 239 | 36 |
| | | | | | | 96 | 80 |
| | | | | | | 232 | 15 |
| | | | | | | 237 | 10 |
| | | | | | | 202 | 20 |
| | | | | | | 100 | 55 |
| | | | | | | 216 | 40 |
| | | | | | | 232 | 15 |
| | | | | | | 92 | 80 |
| | | | | | | 226 | 28 |
| | | | | | | 216 | 14 |
| | | | | | | 242 | 22 |
| | | | | | | 100 | 65 |
| | | | | | | 98 | 64 |
| | | | | | | 100 | 86 |
| | | | | | | 102 | 44 |
| | | | | | | 100 | 86 |
| | | | | | | 108 | 70 |
| | | | | | | 101 | 81 |
| | | | | | | 108 | 77 |
| | | | | | | 98 | 64 |
| | | | | | | 220 | 25 |
| | | | | | | 201 | 75 |
| | | | | | | 93 | 60 |